Dissertation zur Erlangung des Doktorgrades

der Fakultät für Chemie und Pharmazie

der Ludwig-Maximilians-Universität München

Controlling Functionalization and Morphology of MOF Particles – employing Novel Characterization Techniques

Patrick Hirschle

aus

Ehingen (Donau), Deutschland

2020

Erklärung

Diese Dissertation wurde im Sinne von § 7 der Promotionsordnung vom 28. November 2011 von Herrn Prof. Dr. Thomas Bein betreut.

Eidesstattliche Versicherung

Diese Dissertation wurde eigenständig und ohne unerlaubte Hilfe erarbeitet.

München, 08.01.2020

Patrick Hirschle

Dissertation eingereicht am 09.01.2020

1. Gutachter: Prof. Dr. Thomas Bein
2. Gutachter: Prof. Dr. Stefan Wuttke

Mündliche Prüfung am 04.02.2020

Danksagung

Als Erstes bedanke ich mich bei meinem Doktorvater Prof. Dr. Thomas Bein. Danke, dass Du mich in Deine Gruppe aufgenommen hast. Du hast mir die Möglichkeit gegeben mich in Deinem Arbeitskreis zu verwirklichen, und mich sowohl finanziell, als auch mit Diskussionen und alternativen Blickwinkeln unterstützt.

Als Zweites möchte ich mich bei meinem Mentor Prof. Dr. Stefan Wuttke bedanken. Wir kennen uns jetzt seit 6 Jahren und haben ein vielschichtiges Verhältnis zueinander. In Deiner Funktion als mein Betreuer bin ich dankbar für das Potential, dass Du in mir gesehen hast, die zahlreichen Möglichkeiten, die Du mir aufgetan hast, und für Deine finanzielle Unterstützung. Du hast dich immer gut um mich gekümmert und warst als Ansprechpartner zur Stelle, wenn ich Rat gebraucht habe. Ich möchte Dir außerdem auch als Freund danken. Ich habe in Dir einen Menschen mit interessanten und offenen Blickwinkeln kennengelernt. Wir haben zusammen privat einiges erlebt und hatten eine schöne Zeit miteinander.

Ich bedanke mich außerdem bei Prof. Dr. Joachim Rädler und Prof. Dr. Ernst Wagner. Danke, dass Ihr mich beide finanziell lange gefördert habt. Ich habe die Zeit, in der ich eure Arbeitsgruppen kennen lernen durfte, genossen und konnte mich dadurch auch fachlich weiterbilden.

Ich möchte unserer Sektretärin Corinna Heidt danken. Danke für das Einführen in die korrekte Etikette im Büroalltag und hilfreiche Ratschläge beim Manövrieren meiner vielen Departments und Förderer. Ich möchte mich bei Tina Reuther bedanken. Danke für diverse Messungen an der TGA und BET die Du durchgeführt hast und Deine organisatorische Hilfe. Danke an Dr. Jaraslova Obel für das Durchführen von ICP Messungen.

Als nächstes möchte ich mich bei meinen zahlreichen Kooperationspartnern bedanken. Danke and Ulrich Lächelt, Miriam Höhn und Benjamin Steinborn aus dem Arbeitskreis Wagner. Ich schaue immer mal wieder gerne bei euch vorbei, auch um einfach nur zu plaudern. Danke an Hanna Engelke und Bernhard Illes für eine sehr unkomplizierte Kooperation und viele Ratschläge. Danke an Michael Peller und Konstantin Böll aus dem Universitätsklinikum für sehr zielstrebiges Zusammenarbeiten. Danke an Waldemar Schrimpf und Nader Danaf aus dem Arbeitskreis Lamb für eine lange Kooperation und für den obligatorischen Kaffee, den ich bei euch immer bekomme. Vielen Dank an Mario Modena und Professor Dr. Thomas Burg für eine schöne Zusammenarbeit und das Kennenlernen sehr ungewöhnlicher Methoden. I want to thank Zhe Ji and Prof. Dr. Omar Yaghi for giving me a nice excursion to the world of Berkeley. It was interesting getting to know you and I wish you all the best for your future. Danke an Markus Döblinger für eine sehr sorgfältige Zusammenarbeit und die Lehrstunden. Ein großer Dank geht an Evelyn Plötz und Adrian Fuchs für eure tatkräftige Hilfe. Adrian, vielen Dank auch für deine Freundschaft, die bald ihr Zehnjähriges hat.

Besonders bedanken möchte ich mich bei Dr. Steffen Schmidt. Ich hatte viel Spaß in der Zeit mit Dir im Büro und während der Messungen am SEM. Ohne Dich wäre diese Arbeit nicht möglich gewesen.

Ich möchte mich auch bei meinen Praktikanten Stefan Königl, Ralph Freund und Madeline Walden bedanken. Ich hatte großen Spaß mit euch zusammenzuarbeiten und habe ich mich durch jeden von euch weiterentwickelt.

Vielen Dank an den kompletten Arbeitskreis Bein für viele schöne Momente. Ich habe hier viele tolle Menschen kennen gelernt. Es ist etwas ganz Besonderes, Teil dieser Gruppe zu sein, in der jeder seinen Platz hat und alle willkommen sind. Besonderer Dank geht hier an alle meine Bürokollegen, die tapferen Tapper, und die Freunde vom Fruit-Sharing, die mich immer durchgefüttert haben.

Danke an meine Freunde Ralph Freund, Johnathan Sappl und Adrian Fuchs für das Begleiten durch das komplette Studium und die Promotion.

Ich möchte mich bei meinen Münchner Freunden bedanken, die mir die bayrische Kultur beigebracht haben. Danke für das Schafkopfen und die vielen gemeinsamen Momente. Ihr habt dafür gesorgt, dass München in den letzten 10 Jahren ein unvergessliches Zuhause war.

Vielen Dank an meine Freundin Sabrina. Ich finde Du bist ein toller Mensch und ich finde es immer gut Zeit mir dir zu verbringen. Meistens bist Du die erste, die mitbekommt, wenn ich schlechte Laune habe und päppelst mich dann auch immer gut wieder auf. Vielen Dank für deine Unterstützung und dass du an mich glaubst.

Dank geht auch an meinen Bruder Christian. Danke für die vielen lustigen Telefonate und die fachlichen Diskussionen, die es letztendlich auch in diese Arbeit geschafft haben.

Als letztes möchte ich mich bei meinen Eltern bedanken. Danke, dass Ihr mich während meines ganzen Studiums und während meiner Doktorarbeit finanziell unterstützt habt, dass Ihr immer an mich geglaubt habt, und die Werte, die Ihr mir mitgegeben habt.

Abstract

Reticular science of metal-organic frameworks (MOFs) has turned into an advanced research field recognized as a driver for the development of key technologies incorporating novel functional materials. This field has proved to be potentially useful for various applications such as storage, separation, catalysis, sensing, and energy technologies. However, to translate their performance benefit measured in laboratories into real-world applications it is essential to have structural and functional control across molecular, nano, meso, and bulk regimes. Moreover, the exponential growth of MOF materials and their use for different purposes requires detailed characterization. To be able to correlate the physicochemical properties of MOF materials with their performance in a specific task, characterization needs to be both accurate and precise.

Work described in this thesis intends (1) to optimize the synthesis of MOF nano and microparticles using solvothermal, microwave assisted, and microfluidic techniques, (2) to establish functionalization approaches that specifically alter the inner or external surface of particles, (3) to characterize the physicochemical properties of MOFs and develop new characterization methods, and (4) to systematically study the relationship between MOF particles and their performance in cell cultures. This work highlights the strong mutual connection between materials science, nanotechnology and biomedicine and suggests a systematic approach in the effort to synthesize, functionalize, characterize and ultimately apply MOF materials in biomedical applications.

The first chapter of this thesis introduces different aspects of the MOF field and describes different concepts for their refinement into functional materials. In the second chapter, the principles of MOF characterization techniques used in this thesis are explained.

In chapter three fundamental properties of MOF nanoparticles are discussed. The potential of the newly developed method “nanomechanical mass correlation spectroscopy” in the characterization of porous nanosystems was demonstrated. In this study the mass-density of MIL-101(Cr) particles was studied in solution, and it was found that the density of the particles changes depending on the particles’ environment. It was observed that the density of the particles not only differs when measured in solution and in air, but also that the density

changes when measured in different solvent systems. Additionally, the solvent uptake of these particles was quantified in several mixed solvent systems. Depending on the polarity of the pores of the structure, MOF nanoparticles exhibit a preferential uptake of polarity-matched solvents. The density and polarity of MIL-101(Cr) was then manipulated via coordinative functionalization, and the quantitative uptake of different solvents was used to measure the internal polarity of the framework.

Chapter four describes how iron(III) fumarate was used to demonstrate the refinement of MOF materials into functional objects for biomedical applications. Iron-fumarate is composed of biocompatible building blocks, has high porosity, is easily functionalized, and is magnetic resonance imaging active, so it is intrinsically suited for biomedical applications. In the first part of this chapter, several surfactant-free methods to produce monodisperse iron(III) fumarate nano- and microparticles are described (specifically room temperature precipitation, and solvothermal, microwave, or microfluidic heating methods). Using these techniques, four variants of iron(III) fumarate particles with distinct morphologies and diameters ranging from tens of nanometers to several micrometers in size were isolated and characterized. Structural characterization via electron diffraction and pair distribution function analysis revealed that all of these iron(III) fumarate variants exhibit the characteristic MOF structure of MIL-88A, including the smallest X-ray amorphous particles. Despite their identical structure, these particles exhibit drastic differences in suitability as MRI contrast agents. When comparing the different iron(III) fumarate types to each other, their r_1 relaxivities are quadrupled and their r_2 relaxivities are tripled in dependency of the particles' size and crystallinity. This puts them in the same range as commercially available T_1 contrast agents such as Dotarem.

While chapter four explores the potential of iron(III) fumarate in biomedical applications, chapter five describes a specific study in which such nanoparticles (NP) were used as a drug delivery system. In this system, the MOF pores were loaded with either fluorescent or biologically active molecules, and then the particles were coated with exosomes to improve their interaction with targeted cells. The study shows the efficiency of this system provided by the high loading capacity of the MOF NPs and their biocompatible coating. This is demonstrated by the facile delivery and subsequent release of their cargo, which is not affected by endosomal entrapment.

In chapter six, a study addressing the distribution of functionalized linker molecules within MOF particles is presented. UiO-67 nanoparticles were fluorescently-functionalized either *de-novo* during synthesis or post-synthetically via linker-exchange. While the distribution of the functionalized linker molecules appeared homogeneous on a bulk scale, fluorescence lifetime microscopy showed that individual particles within a single sample had vastly different degrees of functionalization, and that higher degrees of functionalization correlated strongly with a higher density of crystal defects among different particles in a single sample. Furthermore, the study relates the influence of the functionalization approach (*de-novo* and post-synthetic) to the density of crystal defects.

In the appendix, an additional study performed mostly during the author's masters' thesis work is presented. It is included in this thesis as it complements the overall theme of MOF nanoparticle characterization. Chapter three addresses basic questions regarding the internal polarity and density of MOF nanoparticles. Appendix chapter eight focuses on methods for determining nanoparticle size. Although size measurements are often trivial on larger scales, measuring the diameter of nanoparticles is more difficult; not only are there several different definitions of size such as hydrodynamic size, crystallite size and size based on image contrast in microsocopy, but the data reported are dependent on the conditions of the measurement and the underlying physical principle of the analytical technique used. The size of MOF nanoparticles is a crucial parameter in defining these materials as they feature size-dependent properties such as an increased amount of surface defects, a higher reactivity, and improved sorption kinetics. To address this challenge, Zr-*fum* nanoparticles were prepared and characterized using common physical characterization tools. The results of several solid-state methods (including X-ray diffraction, atomic force microscopy, scanning electron microscopy and transmission electron microscopy) were compared to dispersion-based methods (such as fluorescence correlation spectroscopy and dynamic light scattering) and overall guidelines for the measurement of MOF nanoparticles are given.

Table of Contents

1 Introduction 1

1.1 Metal Organic Frameworks 1

1.2 Controlling Properties beyond the Structure 2

1.3 Control of Material Properties with Bulk-Processing 3

1.4 Control of Material Properties with Particle Morphology 4

1.5 Special Focus: MOF Nanoparticle Synthesis 7

1.6 Control of Material Properties with Post-synthetic Modification 14

1.7 Metal-Organic Framework Applications 18

1.8 Scope of this Thesis 23

2 Characterization Methods 39

2.1 X-Ray Diffraction 39

2.2 Nitrogen sorption 42

2.3 Thermogravimetric Analysis 47

2.4 Electron Microscopy 47

2.5 Dynamic Light Scattering 50

2.6 Zeta Potential Measurements 51

2.7 Vibrational Spectroscopy 53

2.8 Fluorescence Spectroscopy 55

2.9 Confocal Microscopy 57

2.10 Magnetic Resonance Imaging 58

2.11 Nanomechanical Mass Correlation Spectroscopy 60

3 Mass Measurements Reveal Preferential Sorption of Mixed Solvent Components in Porous Nanoparticles 65

3.1 Introduction 65

3.2 Results 67

3.3 Discussion 70

3.4 Experimental Methods 73

3.5 Supplementary Information 76

4 The Need for Material Optimization of Nanoparticles in Biomedicine: The Example of Iron(III) fumarate 99

4.1 Introduction 99

4.2 Results: Morphological Control of Iron(III) Fumarate 103

4.3 Results: Material Characterization 106

4.4 MRI measurements 113

4.5 Results: Biological Characterization 114

4.6 Conclusion 116

4.7 Supplementary Information 123

5 Exosome-coated Metal-Organic Framework Nanoparticles: An Efficient Drug Delivery Platform 159

5.1 Introduction 159

5.2 Results 161

5.3 Conclusion 166

5.4 Supporting Information 169

6 Chemical diversity in a metal-organic framework revealed by fluorescence lifetime imaging 197

6.1 Introduction 197

6.2 Results 198

6.3 Discussion 210

6.4 Experimental Methods 211

6.5 Supporting Information 222

7 Conclusion and Outlook 233

8 Appendix: Exploration of MOF nanoparticle sizes using various physical characterization methods – is what you measure what you get? 237

8.1 Introduction 237

8.2 Results 239

8.3 Discussion 246

8.4 Conclusion 249

8.5 Supplementary Information 256

9 Curriculum Vitae Error! Bookmark not defined.

1 Introduction

This chapter is based on the following review:

Hirschle P, Haase F, Freund R, Furukawa S, Ji Z, Wuttke S. *Beyond Frameworks: Structuring Reticular Materials across Nano, Meso, and Bulk Regimes.* Angew. Chem. Int Ed. 2019, **submitted.**

1.1 Metal Organic Frameworks

Metal-Organic frameworks (MOFs) are crystalline materials composed of organic molecules bridging inorganic ions or clusters through coordination bonds. This simple construction principle grants high structural and chemical diversity; currently, there are nearly 70.000 structures published in the Cambridge database of crystallography.[1] MOF structures are defined by two properties: their topology and the chemistry of their constituents. The topology of a MOF describes the abstract network in which the building units (organic molecules and metal-oxo clusters) are connected. It is mainly directed by the geometry and connectivity of the organic linkers, while the coordination chemistry of the metal clusters plays a much smaller role.[2] The detailed knowledge of organic synthesis that has accumulated over the last 150 years allows for the creation of virtually any stable molecular building unit that can be imagined, only limited by the time and resources required for the synthesis. Consequently, there is essentially an endless number of possible MOF structures waiting to be generated, as demonstrated in the well-known isoreticular IRMOF series.[3]

MOFs share a number of features that result from their periodic lattice structure and are considered “bulk properties,” as they describe the materials at a macroscale. Most MOFs are categorized as microporous materials. Depending on the design of their crystal structure, they can feature BET surface areas of up to 7000 m^2/g and greater.[4] Generally, MOFs have low mechanical stability, with shear moduli around 1-10 GPa and bulk moduli around 7 to 40 GPa.[5] The rigidity of MOFs is related to their crystal structure; increasing the number of connections between molecular building blocks and/or strengthening the bond energy of the linkages increases the stability of the material. The porous structure of MOFs is responsible for their low thermal conductivity (around 0.1 W/m K).[6] Heat in MOFs is transported primarily along their chemical bonds and is limited by the low atomic density of the crystal structure.[7]

1.2 Controlling Properties beyond the Structure

The properties of MOFs in conjunction with their large structural variability make MOFs attractive materials for numerous applications. However, the successful implementation of MOFs in fields such as catalysis, molecular storage, and biomedicine requires further refinement of the raw MOF into functional tools. Considerable efforts have been made to enhance the properties of MOFs beyond their crystal structure. These can be categorized into three approaches: bulk-processing, morphological optimization, and post-synthetic modification.

The characteristics of macroscopic MOF materials are influenced by manufacturing processes. Typical MOF synthesis conditions produce loose powders that are difficult to process and have poorly defined external interfaces. These problems can be addressed by using bulk-processing techniques such as pressing, casting and 3D-printing. Processing MOFs can tailor the materials' crystallinity, proton and thermal conductivity, elasticity, porosity, adsorption/desorption kinetics, and improve their interfaces with other components in macroscopic devices.

The goal of morphological optimization is to yield a material with a defined shape and precise physical and chemical properties. The external surface area increases exponentially with the decrease of particle size, so the effects of this optimization technique are especially pronounced when the material is confined to the nanoregime. Anisotropic spatial confinement and the introduction of hierarchy lead to mesoparticles, materials that feature both large external surface areas and bulk characteristics.

Post-synthetic modification introduces new functionalities to a completed MOF crystal to further refine it for a specific application. Two types of post-synthetic modification are discussed: Internal modifications, which affect the properties of MOFs throughout their entire structure, and external post-synthetic modifications, which only change the surface of MOF crystals (and therefore affect the interface of MOFs with their surrounding medium).

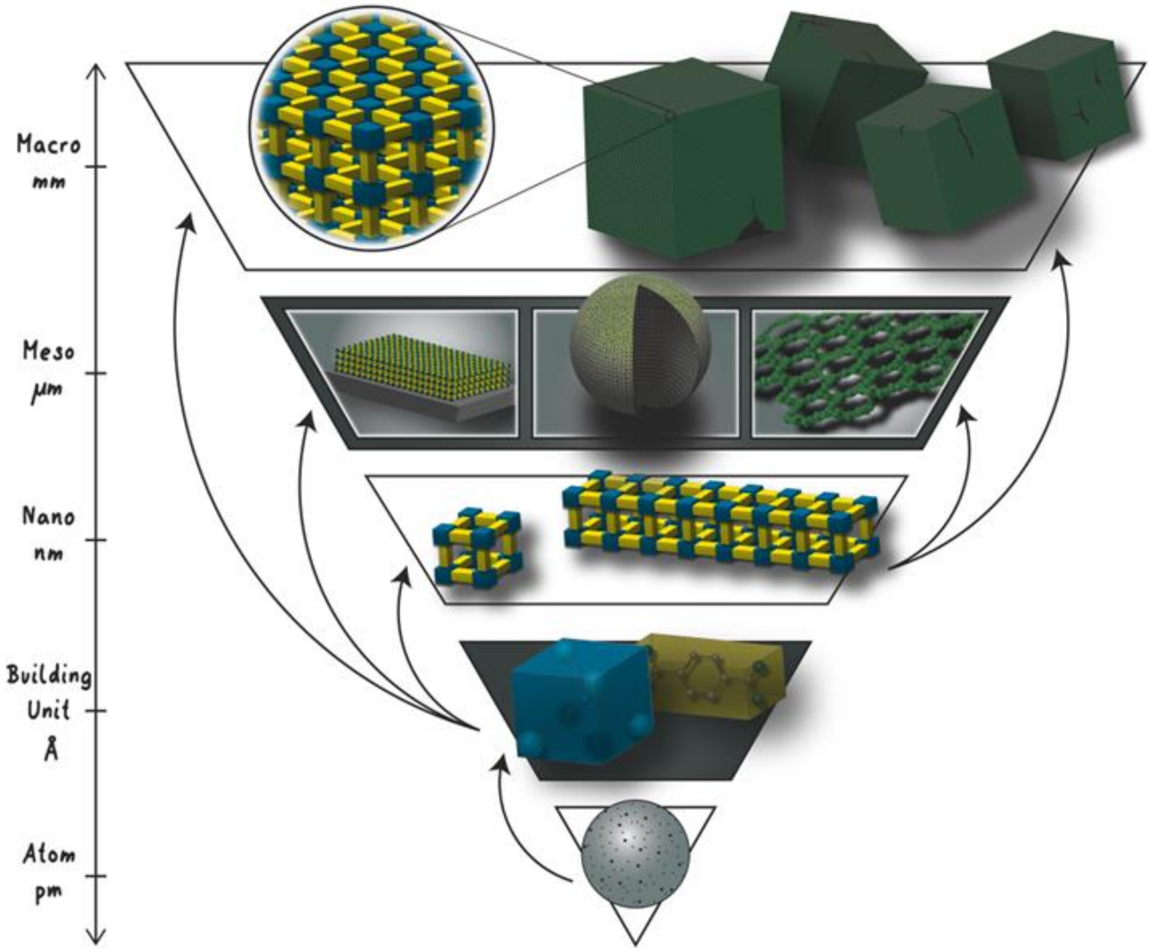

Figure 1.1. Schematic illustration of building-up MOF materials on all length scales. Morphological control and bulk-processing methods result in the formation of nano, meso and bulk structures either by self-assembly or via external control. The strategies that result in these materials and the properties that dominate their behavior are discussed below.

1.3 Control of Material Properties with Bulk-Processing

For a chemist, the optimization of reaction parameters is the most intuitive method to fine-tune the characteristics of a MOF.[8] The main challenge of refining MOF bulk materials for specific applications requires overcoming the instability and poor interface properties associated with loose MOF powders. Therefore, a variety of different processing techniques have been adapted for MOFs. Pelleting compresses material into small wafers, which can either be pure MOF[9], of MOF crystals held together by a binding agent, usually a polymer[10,11]. This increases the materials' volumetric density and makes them easier to handle (which is especially important when working with toxic substances). This strategy has also been used to improve the mechanical stability[12] and thermal conductivity[6] of MOFs. Monoliths are free standing structures with macroscopic pores that are used to support catalytically active species. Their pores facilitate heat and mass transfer with low flow resistance, and their structures exhibit high mechanical stability.[13] Suitable approaches towards the production of monoliths are based on wetting solid precursor mixtures[14], evaporation[15], extrusion[16] and via pressing the powder into monolith shape.[17] Additionally, heterogeneous growth of MOFs on monolith surfaces[18,19] and 3D-printing have been used to generate reticular monoliths.[20,21] Typically these monoliths are composed of a large proportion of MOFs mixed with a small proportion of binders.[22] The resulting structures combine the advantages of monoliths with the high surface areas of MOFs, while providing improved adsorption/desorption kinetics due to their macroporous structuring.[21]

Glasses are amorphous structures that exhibit a disordered arrangement of their chemical building blocks. Similarly, MOF glasses show a lack of long range periodic order, while still preserving the short-range order in the connection of their building units. They can be synthesized directly through the use of modulating and high-viscosity solvents,[23] however the majority of MOF glasses have been manufactured by the amorphization of their parent framework structures via applying high-pressure[24] or melting and quenching.[25,26] Compared to their parent compounds, MOF glasses display transparency, improved mechanical stability, and an increased density,[27] but can still remain microporous.[28]

MOFs have also been used to create soft materials such as cloth, foam and sponges that exhibit both porosity and and flexibility. These materials have been synthesized by introducing MOF particles into foam-precursor mixtures,[29] dip-coating preexisting structures with presynthesized MOF nanoparticles,[30] synthesizing MOFs in the cavities of foams,[31] or by nucleating MOF crystals on fabrics. [32-34]

1.4 Control of Material Properties with Particle Morphology

Decreasing the size of particles leads to an exponential increase of their exterior surface area, a principle ardently exploited in the creation of nano-sized frameworks. The characteristics of MOF materials in the nano-regime are strongly influenced by particle size, but measuring particles at the scale is not trivial: different physical characterization techniques yield different measurements describing either the crystallite/domain size, particle size, or hydrodynamic radius.[35] MOF nanoparticles inherit properties that are typical for bulk MOFs, such as ultrahigh porosity and internal surface areas, but also display new properties that dominate the nanoscale, including short diffusion distances, abundant surface defects, facile chemical functionalization, and higher chemical reactivity and improved sorption dynamics. While the material's overall adsorption capacities are almost unchanged, adsorption and desorption kinetics increase significantly.[36] Similarly, catalytic conversion rates of MOF nanomaterials are increased multifold in comparison to their bulk counterparts, as higher pore accessibility leads to higher performance.[37] Many MOFs feature flexible crystal structures that undergo reversible changes, such as conversion between "guest-stabilized open" and "non-porous closed" forms. Reducing the crystals to the nanoscale gives access to transient, otherwise inaccessible, metastable structures (such as stable open frameworks) even after removal of guest molecules.[38]

The tailorable nature of the individual building blocks of MOF materials provides them with a high functional efficiency that can be increased even further in nano-species. Grafting different functional groups on the external surface of framework nanoparticles can introduce the multivariate functionalities of a single particle. These functionalities, such as fluorescence, magnetism, charge, and molecule recognition capabilities, can be exploited both alone and synergistically, widening the applications of MOF NPs to include sophisticated nanoparticles that perform multiple tasks required by demanding applications.[39]

Meso-objects exhibit chemistry that bridges the material's nano and bulk properties. Typically, meso objects are characterized by hierarchical structuring, where the morphology and spatial arrangement of subunits lead to enhanced and even new properties that are not present in the crystal structure alone. Depending on their synthesis, mesostructures can be single or polycrystalline.[40-43] The spatial arrangement of mesostructures is used to classify these materials as zero-dimensional, one-dimensional, two-dimensional or three-dimensional systems.

Zero-dimensional (0D) MOF mesostructures combine the properties of nanoparticles with higher level structural characteristics such as compartmentalization. Some of the most common examples of this class of mesostructures are hollow particles and core shell structures. These MOF materials can be synthesized by a number of methods.[44-47] In template-free approaches, morphology can be controlled by surface-energy-driven mechanisms,[47] modulating surfactants,[48] etching[49,50] or self-templating.[51] Templated approaches generally rely on heterogeneous nucleation or assembly on the surface of the template (thus replicating the template's morphology).[40-43,52-55] Depending on the synthetic route, these templates then need to be removed in a subsequent step.[56]

One-dimensional (1D) mesostructures include helical and needle morphologies as their synthesis is mostly performed by electrospinning[57,58] or alternatively template-directed crystallization. This process uses either a dissolvable template with hollow channels to grow the MOF, [59,60] or heterogeneous nucleation on 1D objects.[61,62] Other approaches rely on sacrificial templates to grow 1D MOFs on surfaces.[63] Similar to 0D mesostructures, the templated synthesis of 1D reticular materials allows for the transfer of template morphology onto the resulting meso-object, which can either be used to increase the external surface area of the materials[63] or to introduce specific functionality (such as chirality).[61]

Two-dimensional (2D) MOF mesostructures include free-standing membranes and surface-supported films. Free standing 2D mesostructures can be made by either exfoliating 2D stacked frameworks into well-dispersed layers by mechanical techniques (sonication[64]) or by chemical methods (introduction of non-bridging ligands to remove single sheets of MOF films).[65] Surface-supported films have a large interface with the substrate surface as well as the adjacent medium. 2D mesostructures are often used to functionalize a surface with a crystalline film.[66] For example, self-assembled monolayers provide functional groups such as carboxylic moieties that enable crystal growth on many different surfaces and can even direct the crystallographic orientation of MOF-based films grown on the substrate.[67] The spatial dimension perpendicular to the substrate surface of thin films can be confined to the nanoscale during synthesis. This produces thin films with short diffusion distances in this nano-dimension. Compared to their bulk equivalents, MOF thin films have a much greater interface with their adjacent medium, and a high concentration of coordinatively unsaturated metal sites.[68] Generally, the growth of thin films on substrate surfaces is accompanied by interfacial strain.[69] In the case of MOF nano-films, this can be used to access otherwise only metastable structures. Lattice parameters of these MOF films can deviate from their bulk counterparts depending on the extent of this strain, leading to an increase in the structural symmetry of MOF films [70] and enabling the stabilization of non-interpenetrated structures.[71] Confining reticular materials to thin films can also alter their sorption properties. Reticular thin films show increased rigidity that can inhibit the expansion of the crystal structure upon guest uptake, so called “breathing”.[72]

3D meso-structures, which are often called superstructures, exhibit a hierarchical arrangement of morphologically distinguishable components, which differentiates them from bulk materials.[73] They have been realized in form of single objects or extended assemblies of MOF components. Synthesis of 3D meso-structures has been developed by self-assembling objects with lower dimensionality such as nanoparticles,[74-76] 1D helices,[61] and those capable of self-templating[77]. External means to produce 3D meso-structures include templating,[78-80] using external electric fields to produce 1D particle strings,[81] and manually stacking thin-film layers into 3D architectures[82]. The ordered arrangement of these constituents into superstructures can provide the resulting material with textural pores and other large cavities,[83,84] leading to better accessibility for guest molecules. 3D meso-structuring of MOFs can additionally increase mechanical stability and provide improved flexilibity.[85]

1.5 Special Focus: MOF Nanoparticle Synthesis

The materials examined in this thesis are largely confined to the nano-scale. Over the years, many strategies have been developed for MOF nanoparticle synthesis. To achieve morphological control, it is important to understand the underlying principles on which these methods rely. The synthesis of MOF nanoparticles must ensure crystallinity, homogenous morphology, narrow particle size distributions, and (as most of their applications are solvent-based) colloidal stability. Most commonly, MOF nanoparticles are synthesized by wet methods. Under these conditions, the formation of MOF nanoparticles is approximated with a LaMer mechanism[86] according to a three step process: First, the dissolution of precursors leads to supersaturation of the reaction solution. Second, precursor concentrations further increase until the solution reaches a critical point, where rapid nucleation of crystal seeds begins. Finally, after the dissolved reactants are consumed, nucleation slows to a halt and the reaction transitions into a growth phase. During this time the nuclei grow steadily larger until precursors and crystals are eventually in an equilibrium.[87] The LaMer process is influenced by changing solvents, precursors, temperatures, and/or concentrations, or by introducing modulating agents. Other factors that contribute to the final size and shape of MOF crystals include further equilibria such as linker deprotonation, solvent degradation, and Ostwald (or digestive) ripening.[88]

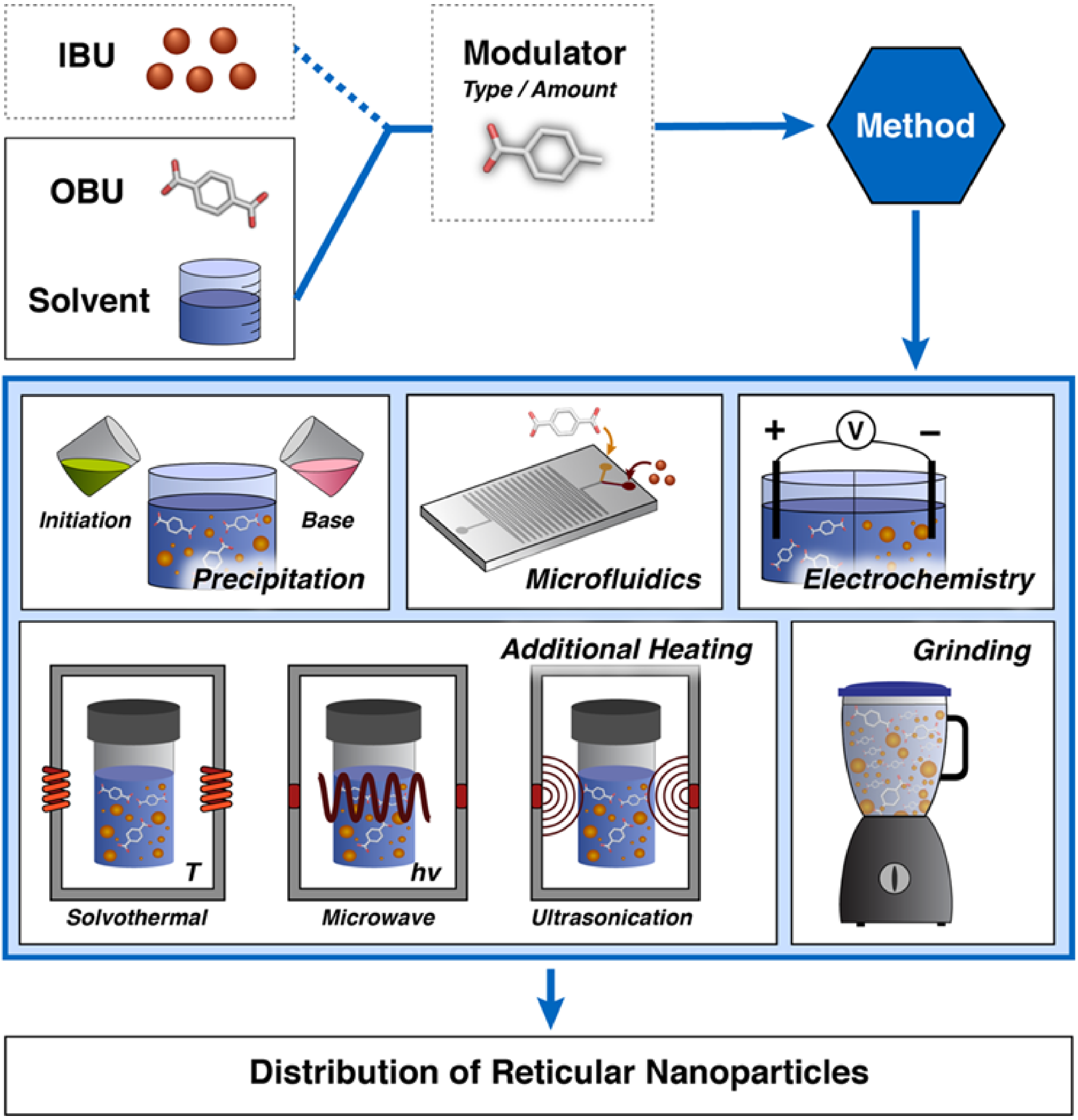

Figure 1.2. Depiction of the most relevant strategies used in the synthesis of MOF nanoparticles. Generally, these strategies rely on reaction mixtures that are based on specific combinations of solvent, metal source to provide the inorganic building unit (IBU) and ligand to from the organic building unit (OBU). Often the syntheses are performed in conjunction with morphology- and crystallinity-modulating additives. The reaction mixtures are then subjected to different reaction methods, resulting in the formation of nanoparticles.[89]

In its most simple form, the wet chemistry approach requires two precursor solutions – a metal source and a ligand source- that are mixed and reacted at room temperature. For certain frameworks, most famously HKUST-1, ZIF-8, and MOF-5, this simple process creates highly crystalline particles. In this method, particle morphology is controlled by altering nucleation and crystal growth periods. Studies have shown that particle size and crystallinity of ZIF-8 frameworks are decreased when precursors have a large ligand surplus,[90] and that longer reaction times favor larger particles.[91] Adaptations of this spontaneous precipitation approach have also shown that it is possible to slow HKUST-1 growth by using pre-cooled reactants or to stop crystal growth completely by freeze-drying, both of which result in smaller particles.[92]

Solvothermal MOF synthesis adds further parameters to spontaneous precipitation by introducing additional heating steps. This synthesis procedure can be performed via reflux condensing,[93] but typically the reaction is performed under pressure in closed reactors.[94] In solvothermal MOF nanoparticle synthesis, heating is either required for initiating the chemical reaction or to accelerate crystal growth.[95] Applying heat to a MOF reaction mixture can also speed nucleation during LaMer growth, resulting in overall smaller particles due to the increased depletion of the precursors as shown for ZIF-8.[96] In addition to heating temperature and reaction time, choosing optimized precursors facilitates the formation of MOF structures.[97] Precursor selection is therefore crucial during the synthesis of MOF nanoparticles: Depending on the system, changing metal salts from a chloride to a bromide can result in different crystal structures with unique morphologies and particle sizes.[98] Similarly, choosing a suitable solvent is another important aspect in solvothermal MOF nanoparticle synthesis; in the solvothermal synthesis of NH_2-MIL-53(Fe), particle morphology can be controlled by changing the ratio of water and DMF.[99]

Microwave-assisted synthesis is a common technique for the generation of MOF nanoparticles. In solids, oscillating electromagnetic waves induce currents that cause resistive heating. Microwaves can interact with polar solvent molecules or ions causing the molecules to constantly realign. This leads to collision between the molecules and increases the system's kinetic energy, ultimately heating the reaction mixture. MOF nanoparticle synthesis in a microwave reactor has several advantages. Unlike solvothermal heating, where heat is transported from the outside to the inside of a reaction vessel, microwave heating is more uniform, and typically reaches the desired temperature within a shorter time interval.[100] As shown in quantitative theoretical and experimental studies, for many MOFs microwave heating can accelerate nucleation and crystal growth up to 30 times compared to conventional heating, a phenomenon attributed to a reduced activation free energy caused by higher entropy intermediates formed during the reaction.[101] This can be used to produce significantly smaller particles. Important studies include the MOFs MIL-88A[102] and MIL-101(Cr) nanoparticles,[103] where particle size and crystallinity were altered by varying microwave reaction temperatures, irradiation times, precursor concentrations, and reaction pressure.

Ultrasound irradiation is another heating technique used to generate MOF nanoparticles. When subjecting a reaction mixture to ultrasonic waves, transient cavities are formed that quickly (after a few microseconds) collapse. These short lived "bubbles" are responsible for hot-spots of high temperature (5000 K) and pressure (1000 bar) in the mixture and thereby can enhance the rate of MOF formation.[104,105] As shown in an extensive study on MIL-53, in comparison to conventional or microwave heating, ultrasound-synthesis is the fastest route to a crystalline product. In this study, ultrasound-based synthesis exhibited reaction rates that were up to a 100 times higher than for conventional heating at comparable temperatures. Additionally, the method yielded the smallest nanoparticles.[106] Another study on MIL-88A showed that the resulting nanoparticles are dependent on the type of ultrasound delivery. In these experiments, an ultrasonic bath produced microparticles that became smaller as sonication time increased. In contrast, pulsed and continuous ultrasonic probes resulted in nanoparticles with unique size and width ratios, but which also grew smaller with longer exposure times.[107] Sonication can also be used to break up larger MOF structures such as hollow spheres into smaller MOF nanoparticles, as shown for HKUST-1.[46]

One of the most common approaches to controlling the size and morphology of MOF nanoparticles is adding modulating agents to the reaction mixture. A plethora of studies have been conducted with zirconium-based frameworks, especially for UiO-66. In this system, weak bases such as triethylamine can be used to precisely tune the nanoparticle size by deprotonating linker molecules resulting in higher nucleation rates, leading to more nuclei and smaller particles.[108] DMF-based synthesis of UiO-66 and UiO-67 specifically opens up the possibility of modulation with hydrochloric acid. Microwave-synthesized UiO-66 nanoparticles modulated with this method increased in size as the amount of acid was increased.[109] The role of hydrochloric acid is not fully explained yet. It is speculated to either reduce the basic solvent impurities or to help in the formation of hexa-Zr clusters resulting in faster nucleation.[110] Most commonly though, modulating agents are short-chain monocarboxylic acids that compete with organic ligands for coordination with the metal-centers. For UiO-66[111] and many other MOFs,[87] coordination-modulation can be done with acetic acid, benzoic acid, trifluoracetic acid, and dichloracetic acid, any of which can be used to increase particle size and crystallinity. Side effects of these modulating agents include their accumulation on the particle surface, changing its functionality[112] and introducing defect sites to the framework.[113]

Even surfactants can be considered a special class of modulating molecules added during MOF synthesis. Surfactants used here are often long, apolar alkyl chains terminated with a polar group. In solution, the surfactants form colloids called micelles that minimize the interactions of the apolar tails with the polar solvent (or vice versa). Surfactants can be used to stabilize nano-sized droplets by forming a layer at the interface of two immiscible phases. Depending on the ratio of the individual components and the nature of the surfactants, the shape of these droplets can be adjusted. In MOF nanoparticle synthesis, microemulsion droplets can be used as nano-reactors. Water/oil based microemulsion, for example, has been used to generate rare-earth MOF nanoparticles, where the shape and size of the resulting nanoparticles is controlled by the surfactant/solvent ratio.[114,115] The synthesis of La-BTC MOF with various morphologies in an ionic liquid/water/surfactant system was explained by the interfacial reaction of La^{3+} ions dissolved in the aqueous layer with linker molecules dissolved in the ionic liquid droplets. The shapes of these droplets were dictating the shape of the nuclei that grew larger into different MOF nano- and micromorphologies.[116] There are many variations of microemulsion-based MOF nanoparticle synthesis, such as the liquid-solid-solution (LSS) growth technique that was used in the size-controlled synthesis of HKUST-1 nanoparticles. In this technique, copper-ions and benzene-1,3,5-tricarboxylate (BTC) linkers were successively added to an oleic acid/oil-phase/aqueous-phase microemulsion. This first led to the formation of Cu-oleic acid clusters which then reacted at the water/oil interface with BTC ligands to form HKUST-1 nanoparticles with hydrophobic coatings.[117] Surfactants additionally open up the possibility of templated structuring during MOF nanoparticle synthesis. For MIL-101(Cr), adding CTAB to the aqueous synthesis mixture resulted in mesoporous nanoparticles because the framework crystallized around the micelles.[118]

In addition to these ‘common’ synthesis methods for MOFs nanoparticles, several more specialized ‘boutique’ synthesis procedures have been developed in recent years. In some cases, special solvents such as ionic liquids are used as structural directing agents or to accelerate reaction times of MOF nanoparticle synthesis. The synthesis of Zn-BDC MOF nanoparticles in a supercritical CO_2/ionic liquid/surfactant system resulted in hexagonally meso-porous Zn-BDC MOF nanoparticles.[119] This synthesis was based on templating the MOF by cylindrically self-assembled micelles formed by the surfactant molecules in the system. Another example is the synthesis of UiO-66 nanoparticles during a study of ionic-liquid reaction conditions on the resulting particles’ properties. Compared to solvothermal methods, the particles grew much faster under these conditions. This phenomenon was explained by the strong hydrogen bonding interactions between the ionic liquids and the modulating agent acetic acid. The hydrogen bonds were proposed to enable rapid exchange of modulator for linker molecules in the initial metal clusters that were formed by the reaction and therefore increased nucleation rate.[120]

Electrochemical synthesis of MOF nanoparticles was shown for IRMOF-3 in a DMF/ethanol/tetrabutylammonium bromide electrolyte. In this method, linker molecules are deprotonated at a copper cathode leading to the formation of molecular and move to the anode for MOF assembly. The zinc anode is oxidized, producing the Zn^{2+} ions required for MOF synthesis. The size of the resulting nanoparticles was modulated by either altering the voltage or changing the DMF/ethanol solvent ratio. [121]

A recent study demonstrated the synthesis of MIL-100(Fe) nanoparticles via heterogeneous nucleation on polystyrene nanospheres. In the first step of this synthesis, polystyrene nanocolloids were functionalized with linker molecules by simple immersion in an aqueous solution. Subsequent addition of iron(III) precursors and solvothermal treatment led to the growth of MIL-100(Fe) nanoparticles on the bead surface. Removal of the polystyrene beads via washing in DMF produced MOF nanoparticles that were smaller than conventionally synthesized particles and that could be size-tuned by varying the amount and size of polymer colloids in the reaction mixture.[122]

Many MOF nanoparticles have also been synthesized by dry-chemical approaches. Especially noteworthy is the synthesis of MIL-101(Cr), which was performed by solvent-free grinding and then dry heating.[123] The resulting phase-pure nanoparticles were smaller than particles produced by solvothermal methods; however, the nanoparticles were also aggregated and lost their homogeneous morphology. Liquid assisted grinding, which uses catalytic amounts of solvents, has also successfully produced MOFs. For example, phase-pure NH_2-UiO-66 nanoparticles were synthesized by this method in less than 2 hours, of by exposing ground precursors of the MOF to methanol vapors for 3 days at elevated temperature. The colloidal stability of the resulting particles was proven in aqueous dynamic light scattering experiments[124] Another more recent study has shown that Pd-loaded ZIF-8 nanoparticles can be synthesized at room temperature via ball-milling. The synthesis was based on sacrificial ZnO nanoparticle templates that were completely converted to ZIF-8 nanoparticles using catalytic amounts of solvent.[125]

Recently, microfluidic flow-reactors have gained popularity in the synthesis of MOF nanoparticles and are of special interest in this work. In these setups, reaction solutions are pressed through narrow channels, either in tubing or on a chip, with diameters of a few hundreds of micrometers. While traversing the reactor-channel, a reaction mixture passes through heated segments; the narrow channels ensure fast heat transfer, resulting in good control over nucleation and crystal growth. For MOFs, this can result in smaller particle sizes and reaction rates up to 400 times faster than conventional solvothermal heating.[126] Heating time is controlled by the speed at which the reaction solution passes through the heated section and can be precisely tuned to fractions of seconds. This allows for the fine-tuning of nanoparticle sizes (as shown for UiO-66[127] and other MOFs).[128] Microfluidic setups have many advantages: they are easily customized, and pressure regulators and heat resistant equipment allow for solvothermal MOF syntheses under pressurized conditions (as shown for cerium(III) terephthalate MOF nanoparticles).[129] Surfactants and non-miscible solvents are required in droplet-microfluidic setups, simulating micro-emulsions that produce well-defined droplet sizes. These setups can be used to limit precursor supply or to perform interfacial chemical reactions.[130] Using such a setup, nanoparticles of the MOFs Ru_3BTC_2 and UiO-66[131] have been synthesized, and size modulation has been demonstrated for MIL-88B[132]

1.6 Control of Material Properties with Post-synthetic Modification

1.6.1 Internal Modification

Internal modification of MOFs is carried out by introducing to organic linkers and metal nodes desired functionalities through the formation of new covalent bonds or coordination bonds.[133-137] Internal modification of MOFs takes place at the inner periodic scaffold of the material. It includes functionalization of their inner surface and results in changes to bulk properties. Other modification techniques such as linker-exchange and trans-metalation rely on the substitution of either the organic or inorganic building units. Internal post-synthetic modification is performed to influence bulk characteristics such as porosity, magnetic, optical and electronic properties,[138] and can influence the flexibility[139] of a structure, change its polarity[140] and introduce functionalities such as biologically active groups. [141]

Modification of the inorganic building units requires accessible under-coordinated metal sites, [142] where these Lewis-acidic metal-centers are used to pull small Lewis-basic molecules such as imines or pyridines[94] into the framework structure. The opposite approach of this technique is post-metalation, where either defect sites in the framework[143] or electron-rich linker-molecules (like carboxylic groups or pyridine-rings) can be used for metal-capture.[144]

Covalent internal functionalization requires linker molecules with reactive groups. While common groups such as azides or halides and multivalent bonds[139,145] are open to many kinds of reactions, amines are especially popular for post-synthetic modifications in MOFs.[146] Amine groups enable, amongst other things, chemistry that is easy on the material: It is compatible with the well-defined chemistry of peptide coupling reagents and can be performed at room temperature.[147]

An alternative internal modification strategy is the substitution of inorganic and organic building units. Solvent-assisted linker exchange can be used to incorporate functional linker molecules into already crystallized MOFs. During this process, the modified linker molecules diffuse through the scaffold and bind to the metal centers, permanently recrystallizing the framework without destroying it. Solvent assisted linker exchange opens up the possibility of incorporating large molecules into a MOF structure that would otherwise not be able to enter the MOFs pore openings.[148] Post-synthetic metal-exchange of the inorganic building units is called trans-metalation.[149] Metal-exchange exploits the coordination chemistry of the metal, which facilitates the substitution of metal-ions with species featuring a higher ligand-affinity with similar ionic radii and coordination chemistry.

The methods of modifying the internal surfaces of MOFs that have been discussed so far are intended to introduce uniform functionalization to their crystal structure, but it is also possible to use diffusion and sterically controlled reactions or external triggers to produce localized modifications and create hierarchical MOF mesomaterials. An elegant variation of this approach are light-induced post-synthetic reactions such as the thiolene click reactions that have been used to crosslink organic linkers within a framework.[150] Similar reactions have been controlled by layer-by-layer epitaxy that allows for 2-dimensional functionalization.[151,152] This approach can also be used to selectively dissolve any remaining non-crosslinked MOF to obtain structured gels based on previous patterning. Another prominent means of introducing spatially controlled functionality in MOFs through PSM uses the inherent diffusion limitation of post-synthetic reactions, which typically start at the faces of a crystallite in contact with the solvent and then penetrate further into the crystallite. This effect has been demonstrated in post-synthetic topotactic linker exchange and has been visualized by fluorescence[148] and Raman microscopy.[153] This type of PSM can be used to generate well-defined core-shell type structures. Similarly, the metal of a MOF can be exchanged in anisotropic crystallites leading to sandwich[154] or core-shell structures[155]. The spatially selective covalent post-synthetic modification of linkers can be achieved by the use of bulky molecules in post-synthetic functionalization, leading to preferred functionalization of the MOF crystallites close to the external surface.[156] This method is in essence similar to modification schemes covered in the next section that intend to only functionalize the external surface area. Through this approach, initially uniform materials can be converted to functionally graded materials and composites with spatially abrupt changes in their properties.

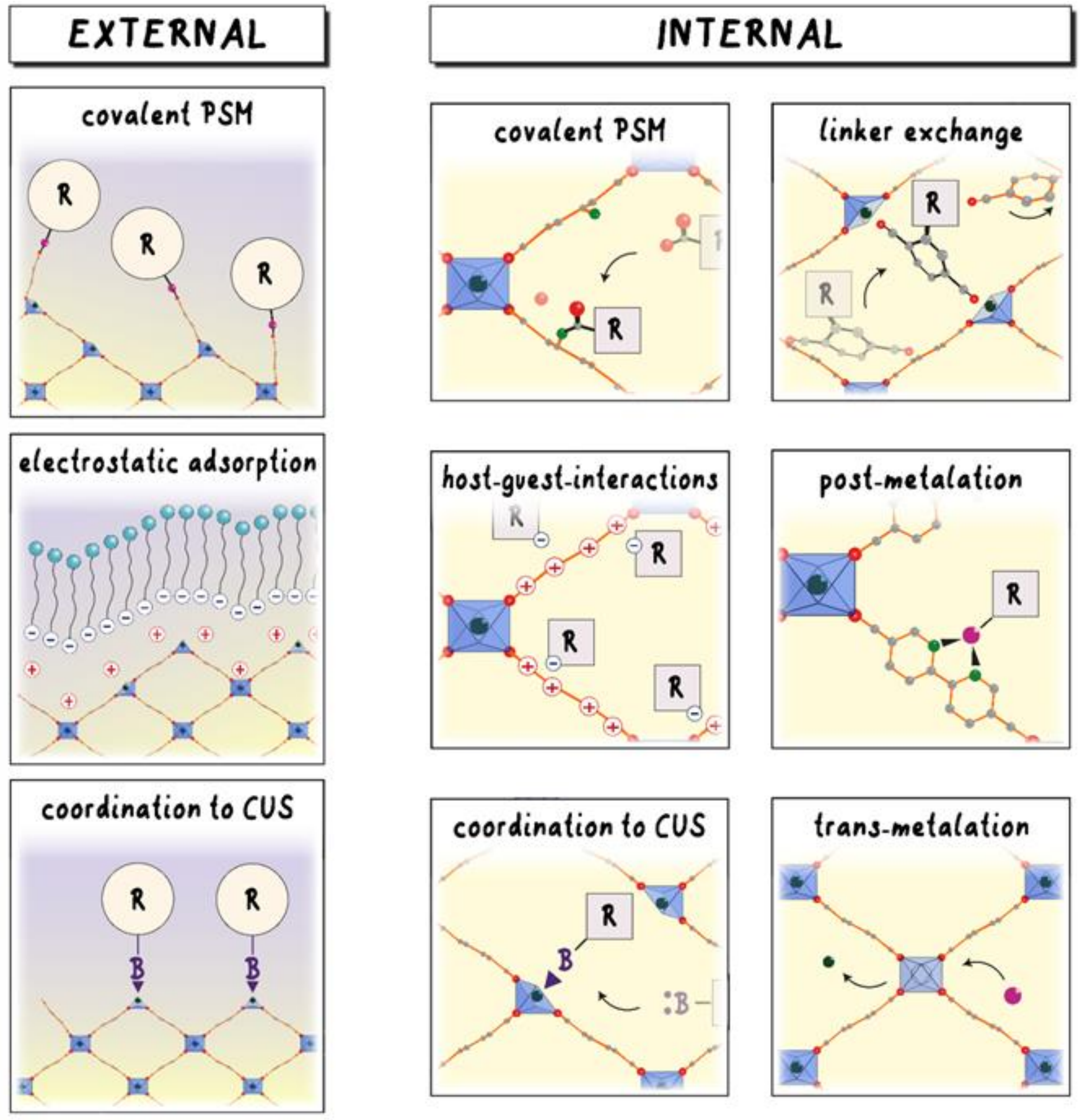

Figure 1.3. Schematic representation of different post-synthetic modification strategies (PSM) used for the introduction of functionality. Two general concepts are shown: selective functionalization of the external surface and the internal modification of the periodic lattice.

1.6.2 External Modification

External modification affects the chemistry at the interface between a structure and its surrounding medium. In the case of the porous structures of MOFs, this implies the area that is shared by the outer surface of the framework with its surroundings. The modification of the external surface presents an essentially two-dimensional modification and is mostly performed on nanoparticles and mesostructured materials because their properties are determined to a great extent by their high surface-to-volume ratio.

External functionalization of MOFs is done for a variety of reasons: Binding long molecules to the outer surface of particles can improve their colloidal stability via steric stabilization. The polarity of nanoparticles can be changed by introducing hydrophobic coatings, leading to improved chemical stability in water and colloidal stability in non-polar solvents.[157,158] Molecules can be introduced to the particle surface that either exhibit functionality or carry active groups for further functionalization.

To specifically functionalize the outer surface of MOFs, two complimentary methods have been developed: either reactive centers exclusive to the outer surface[159] are targeted for functionalization or functionalization reagents need to be hindered from entering the framework.[160] The former strategy relies on the accumulation of crystal defects, such as coordinatively unsaturated metal sites (CUS),[161] and dangling uncoordinated carboxyl groups on the external surface of nano- and meso-structures. The second coating method generally relies on size exclusion, but can also exploit hydrophilic/hydrophobic interactions,[162] electrostatic adsorption,[163] linker exchange,[148] or covalent binding[146] to limit alterations of the internal surface.

The majority of external modification techniques rely on the accumulation of coordinatively unsaturated metal sites on the MOF surface. Due to their Lewis-acidity, they can act as anchor-points for Lewis-basic molecules. The coordinative nature of this modification technique requires mild reaction conditions, so this method is widely used to modify biocompatible MOFs with biologically active molecules or molecules relevant for imaging. Popular Lewis-basic anchor groups include carboxylic acids,[144] histidines[161], phosphates,[164,165] and phenols[166].

Another surface-defect-driven modification technique targeting the external surface of MOFs is the covalent bonding of organic molecules to the particle surface. Inherent uncoordinated linker molecules that accumulate on the external surface of MOF nanoparticles provide active moieties such as carboxylic groups for further surface-selective modification.[167] Additional anchor points for selective functionalization of MOFs can be introduced by using capping ligands during the synthesis; their low connectivity leads to accumulation of these molecules on the MOF surface, providing additional functionalities such as azide groups.[168]

Finally, outer surface nanostructures can be functionalized by encapsulation of particles in preformed compartments. An example for this principle can be seen in the confinement of MOF nanoparticles in liposomes[169] and exosomes[170] using lipid-fusion. This functionalization approach results in an additional interface in the form of a membrane wall that can block further molecular access to the inside of the particles.

1.7 Metal-Organic Framework Applications

The application of MOFs is highly dependent on their structuring across all length scales (**Figure 1.4**). The following section therefore describes the most important application fields for reticular nano- meso- and bulk-objects.

1.7.1 Specific Applications at the Nanoscale

Combining the versatile chemistry of MOFs with the properties of the nanoworld opens a door for a large variety of applications for MOF nanoparticles.[171] These properties include short diffusion paths, fast sorption/desorption kinetics and sorption properties, as well as size-dependent optical, electrical, and magnetic properties.

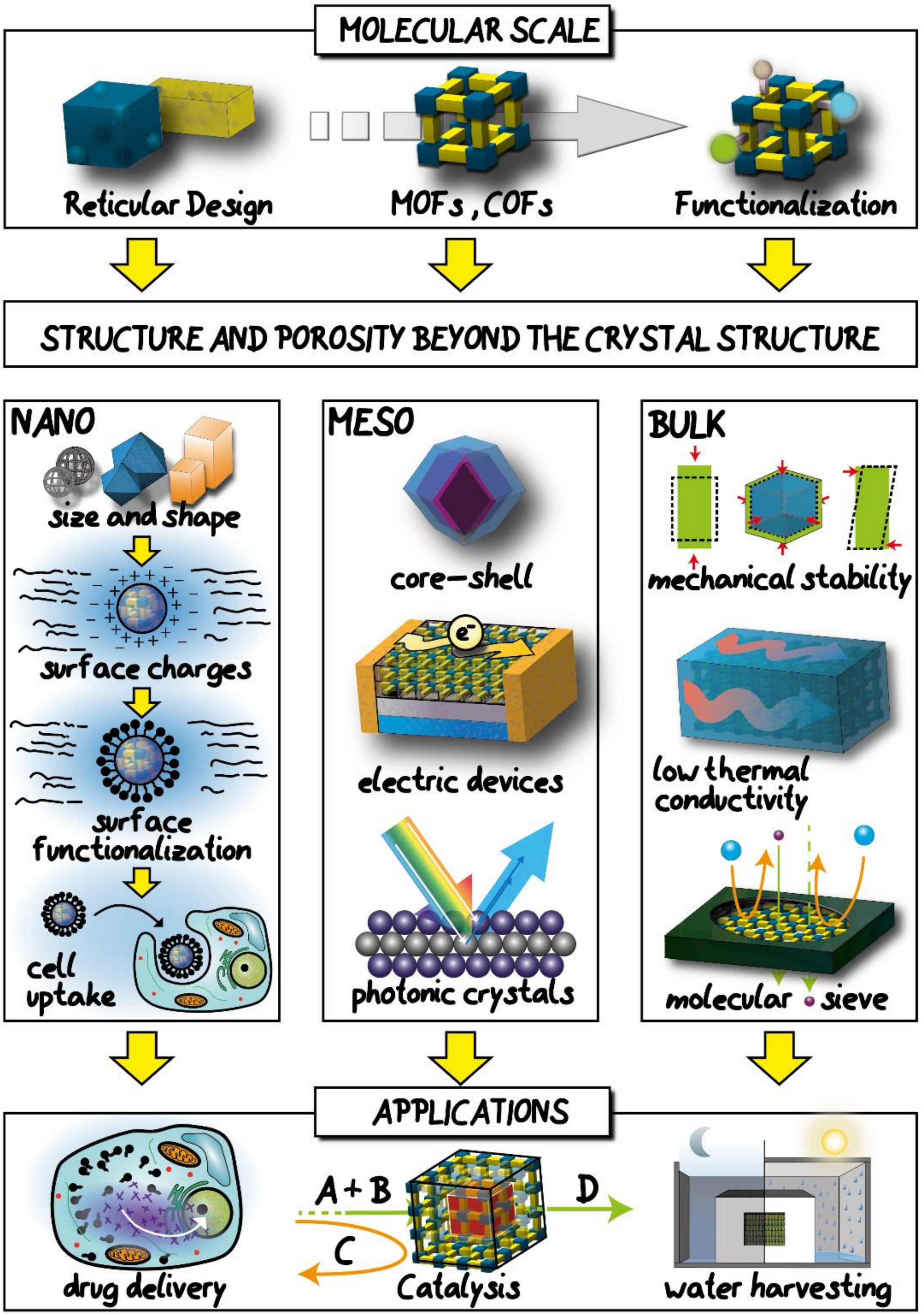

Figure 1.4. Schematic depiction of the concept of going *beyond* the crystal structure of MOFs. While many features of MOFs can be designed through crystal engineering, their successful use in specialized applications requires further optimization, namely functionalization, morphological optimization in form of nano- and meso-structuring, as well as bulk-processing.

Due to their enhanced conversion rates and sorption kinetics, MOF nanoparticles find applications in fields such as catalysis[36,172] and adsorption,[37] as well as in electrical applications, *e.g.* as composite materials in supercapacitors[37].

The main focus of MOF nanoparticle applications lies in the field of biomedicine.[173] Nanosized particles are favorable in biomedical applications as they exhibit improved endocytosis and can be well dispersed in body fluids. MOF nanoparticles are being investigated in this field due to their porosity and functionalizability. Straightforward functionalization allows one to not only use MOF nanoparticles as transport vehicle, but can turn their scaffold into an active component for cancer treatment,[174-180] different biomedical imaging techniques (*e.g.* positron emission tomography, magnetic resonance imaging),[167,181-185] drug delivery,[186-190] or a combination of these[191-194]. The size of MOF nanoparticles provides for easy cell uptake, which can be further enhanced by coating strategies, such as polymer or lipid coatings.[167,170,195] Finally, luminescent functionalization allows one to use the MOF as chemical sensors[93,196-198] and easy monitoring of their pathways and metabolism within living cells[199]. Further, the tailorable nature of MOFs allows the use of biocompatible building blocks, offering the prospect of efficient biodegradability and biocompatibility, as the toxicity of MOF nanoparticles can be independently influenced by choice of the metal- and the organic components, respectively.[200] Importantly, the toxicity of nanoparticles also strongly depends on size, shape, surface area, surface charge and dose and cannot be associated with composition only.[39,201]

1.7.2 Specific Applications of the Mesoscale

Applications of MOF mesostructures rely on the nature of the hierarchy in their respective systems. 0D MOF mesostructures offer both compartmentalization and a large external surface area for functionalization, which is why they are mainly examined for catalysis,[52,53] and in drug delivery[202]. On the other hand, 3D reticular mesostructures can be used as precursor materials for the generation of sophisticated catalysts.[9] Additional assemblies of 3-D mesostructures have been used for filtering applications[203] and in sensors, based on changes of the materials’ optical properties upon guest uptake.[204]

The majority MOF mesostructure-applications, however, are film-based. Here, 1D spatial confinement results in reduced transport distances for electron and ion conduction.

Additionally, mesomaterials provide an increased interface between a surface and its surrounding medium, which is beneficial for catalytic applications. The growth of MOF films on supports is a straightforward method to augment a carrier material, for example a metal surface[205], with features such as porosity, crystallinity, ion conductivity and new optical properties. These properties make thin film framework materials interesting for sensing applications.[206-208] The porous nature allows for the inclusion of guest molecules within the frameworks, which then cause, for example, changed absorption spectra and altered refractive indices that can be read out optically, leading to potential uses in small molecule detection.

Porosity, a large interface to the surrounding medium and a high concentration of reactive sites are reasons for the use of MOF films in catalysis.[209] Similarly, a framework-based surface coating can enhance the performance of electrodes. For example a Fe_2O_3:Ti electrode with a thin film coating of the MOF NH_2-MIL-101(Fe) MOF exhibits an improved performance in the photoelectrochemical oxidation of water. This is based on a shifted absorption spectrum due to the electrodes' MOF coating as well as due to an improved incident-photon-to-electron conversion efficiency based on the facile charge-transfer between Fe_2O_3 and the MOF.[210]

MOF thin films have also been examined for ion conduction such as for lithium ions and protons: Their porous structure can either be functionalized with proton-conducting surface dangling groups such as sulfonate-moieties or be loaded with proton-conducting guest molecules such as imidazole or histamine.[211] [212]

The combination of the porous structure and large interfacial area of 2D MOF meso-structures is strongly related to their applications in water purification[213] and gas separation[214]. Films of MOF nanosheets can selectively separate mixtures of gas molecules such as H_2 or CO_2. Selection criteria include the size of the gas molecules or their chemical nature as they have to interact with the pores of the material. This advantage can be further enhanced via post-modification of pore size or via the introduction of functional groups such as amino groups into the pores leading to improved selectivity.[215]

In the past, MOF have been viewed as not suitable as electron conductors due to their metal centers generally preventing electron resonance delocalization and due to the lack of redox-active ligands. This is slowly changing with the development of new electron-rich linker molecules, the inclusion of suitable guest molecules and the development of MOFs with "through-space" mechanisms such as pi-pi stacking, features that have opened up the use of MOF films for electronic applications.[216-218] Frameworks with improved charge carrier mobility have also been realized by the synthesis of mixed-valence frameworks[219] and by the introduction of charge-transport pathways along heteroatoms such as sulfur.[220,221]

1.7.3 Specific Applications at the Bulkscale

MOF materials that are used in bulk-scale applications rely mainly on properties that originate from their framework structure. The extension of the framework dimensions to the bulk regime converts the physical behavior of a unit cell to the collective performance of the whole material. Often the corresponding applications require a specific macroscopic shape, such as column and reaction bed, into which framework material can be packed. MOF bulk materials offer diverse applications in heterogeneous catalysis. On the one hand, their porous structure allows for the loading with catalytically active species such as metal- nanoparticles[222] or single-site metal complexes[223] into their pores, making them excellent carrier materials. On the other hand, the heterogeneous construction of the scaffold structure can provide catalytically active centers, both at the metal-based nodes and at the linker molecules.[224] The precisely defined pores of a MOF structure reveal their catalytic potential by providing the material with a structural selectivity towards both educts and products, filtering molecules by size[225] and even by chirality[226].

New gas storage technologies are urgently sought after, as they are especially relevant in fuel technology. Materials that are used in this field need to exhibit a combination of high storage capacity, high cycling stability, low adsorption/desorption enthalpies, a high thermal conductivity and a high safety standard. Fuel tanks based on MOFs can meet many of these criteria: the adsorption of gas molecules such as hydrogen[227] and methane[228] into the porous structures allows for high volumetric storage capacities at reduced pressures (relative to the gas), which can result in easier refueling and increased safety due to the lower pressurization of the fuel container.

The porous architecture of MOFs has opened the field of heat transfer to MOFs. While heat in MOFs is transported primarily along the chemical bonds in the scaffold of their porous structure and the low atomic density of their crystal structure results in a low thermal conductivity (around 0.1 W/m K),[6] the structures can act as heat pumps distributing energy via the adsorption and desorption enthalpies of small molecules. In these studies MOFs are already surpassing benchmark materials [229] Research in this field is most advanced in the case of water harvesting from air where materials with a sufficiently small desorption enthalpy can even be used to extract water from air via solar-powering.[230] Similarly, these sorption properties have resulted in MOFs being used in air dehumification.[231]

1.8 Scope of this Thesis

This thesis explores the refinement of MOFs from raw materials to specialized materials. The crystalline architecture of MOFs gives every MOF uniquely defined porosity. Additional versatility of this material is obtained by employing some of the countless optimization techniques that can be used to change its properties. Morphological control, post-synthetic functionalization, and specialized processing create an unmatched variety of functional materials.

The projects presented in thesis show how different optimization techniques influence the properties of different MOF nano- and microparticles. By post-synthetic functionalization and exerting morphological control the particles' internal polarity, their behavior in MRI applications, as well as Raman and fluorescence imaging can be changed. The resulting functional materials were analyzed with state-of the art analytical spectroscopy and microfluidic methods in collaboration with various groups. These novel and specialized techniques include mass correlation spectroscopy, Raman microscopy and magnetic resonance imaging. We additionally address fundamental features of MOF nanoparticles, including their crystallinity, porosity and density. The applicability of these particles, especially in biomedicine, was further demonstrated in *in-vitro* experiments that were performed in cooperation with research groups in pharmacy and medicine.

References

1 Moghadam, P. Z. *et al.* Development of a Cambridge Structural Database Subset: A Collection of Metal–Organic Frameworks for Past, Present, and Future. *Chem. Mater.* **29**, 2618-2625, doi:10.1021/acs.chemmater.7b00441 (2017).

2 Yaghi, O. M. *et al.* Reticular synthesis and the design of new materials. *Nature* **423**, 705-714, doi:10.1038/nature01650 (2003).

3 Eddaoudi, M. *et al.* Systematic design of pore size and functionality in isoreticular MOFs and their application in methane storage. *Science* **295**, 469-472, doi:10.1126/science.1067208 (2002).

4 Farha, O. K. *et al.* Metal–Organic Framework Materials with Ultrahigh Surface Areas: Is the Sky the Limit? *J. Am. Chem. Soc.* **134**, 15016-15021, doi:10.1021/ja3055639 (2012).

5 Wu, H., Yildirim, T. & Zhou, W. Exceptional Mechanical Stability of Highly Porous Zirconium Metal-Organic Framework UiO-66 and Its Important Implications. *J Phys Chem Lett* **4**, 925-930, doi:10.1021/jz4002345 (2013).

6 Liu, D. *et al.* MOF-5 composites exhibiting improved thermal conductivity. *Int. J. Hydrogen Energy* **37**, 6109-6117, doi:10.1016/j.ijhydene.2011.12.129 (2012).

7 Babaei, H., McGaughey, A. J. H. & Wilmer, C. E. Effect of pore size and shape on the thermal conductivity of metal-organic frameworks. *Chem Sci* **8**, 583-589, doi:10.1039/c6sc03704f (2017).

8 Mulyati, T. A., Ediati, R. & Rosyidah, A. Influence of Solvothermal Temperatures and Times on Crystallinity and Morphology of MOF-5. *Indonesian Journal of Chemistry* **15**, 101, doi:10.22146/ijc.21202 (2015).

9 Avci-Camur, C. *et al.* Aqueous production of spherical Zr-MOF beads via continuous-flow spray-drying. *Green Chemistry* **20**, 873-878, doi:10.1039/c7gc03132g (2018).

10 O'Neill, L. D., Zhang, H. & Bradshaw, D. Macro-/microporous MOF composite beads. *J. Mater. Chem.* **20**, 5720, doi:10.1039/c0jm00515k (2010).

11 Cousin-Saint-Remi, J. *et al.* Highly Robust MOF Polymeric Beads with a Controllable Size for Molecular Separations. *ACS Appl Mater Interfaces* **11**, 13694-13703, doi:10.1021/acsami.9b00521 (2019).

12 Ren, J. *et al.* A more efficient way to shape metal-organic framework (MOF) powder materials for hydrogen storage applications. *Int. J. Hydrogen Energy* **40**, 4617-4622, doi:10.1016/j.ijhydene.2015.02.011 (2015).

13 Küsgens, P., Zgaverdea, A., Fritz, H.-G., Siegle, S. & Kaskel, S. Metal-Organic Frameworks in Monolithic Structures. *J. Am. Ceram. Soc.* **93**, 2476-2479, doi:10.1111/j.1551-2916.2010.03824.x (2010).

14 Ahmed, A., Forster, M., Clowes, R., Myers, P. & Zhang, H. Hierarchical porous metal-organic framework monoliths. *Chem Commun (Camb)* **50**, 14314-14316, doi:10.1039/c4cc06967f (2014).

15 Vilela, S. M. F. *et al.* A robust monolithic metal-organic framework with hierarchical porosity. *Chem Commun (Camb)* **54**, 13088-13091, doi:10.1039/c8cc07252c (2018).

16 Hong, W. Y., Perera, S. P. & Burrows, A. D. Manufacturing of metal-organic framework monoliths and their application in CO 2 adsorption. *Microporous Mesoporous Mater.* **214**, 149-155, doi:10.1016/j.micromeso.2015.05.014 (2015).

17 Plaza, M. G. *et al.* Propane/propylene separation by adsorption using shaped copper trimesate MOF. *Microporous Mesoporous Mater.* **157**, 101-111, doi:10.1016/j.micromeso.2011.06.024 (2012).

18 Rezaei, F. *et al.* MOF-74 and UTSA-16 film growth on monolithic structures and their CO2 adsorption performance. *Chem. Eng. J.* **313**, 1346-1353, doi:10.1016/j.cej.2016.11.058 (2017).

19 Pang, J., Liao, Y., Huang, X., Ye, Z. & Yuan, D. Metal-organic framework-monolith composite-based in-tube solid phase microextraction on-line coupled to high-performance liquid

chromatography-fluorescence detection for the highly sensitive monitoring of fluoroquinolones in water and food samples. *Talanta* **199**, 499-506, doi:10.1016/j.talanta.2019.03.019 (2019).

20 Lim, G. J. H. *et al.* 3D-Printing of Pure Metal–Organic Framework Monoliths. *ACS Materials Letters* **1**, 147-153, doi:10.1021/acsmaterialslett.9b00069 (2019).

21 Thakkar, H., Eastman, S., Al-Naddaf, Q., Rownaghi, A. A. & Rezaei, F. 3D-Printed Metal-Organic Framework Monoliths for Gas Adsorption Processes. *ACS Appl Mater Interfaces* **9**, 35908-35916, doi:10.1021/acsami.7b11626 (2017).

22 Shan, M., Seoane, B., Andres-Garcia, E., Kapteijn, F. & Gascon, J. Mixed-matrix membranes containing an azine-linked covalent organic framework: Influence of the polymeric matrix on post-combustion CO 2 -capture. *Journal of Membrane Science* **549**, 377-384, doi:10.1016/j.memsci.2017.12.008 (2018).

23 Zhao, Y., Lee, S. Y., Becknell, N., Yaghi, O. M. & Angell, C. A. Nanoporous Transparent MOF Glasses with Accessible Internal Surface. *J. Am. Chem. Soc.* **138**, 10818-10821, doi:10.1021/jacs.6b07078 (2016).

24 Widmer, R. N. *et al.* Pressure promoted low-temperature melting of metal-organic frameworks. *Nat Mater* **18**, 370-376, doi:10.1038/s41563-019-0317-4 (2019).

25 Bennett, T. D. & Cheetham, A. K. Amorphous metal-organic frameworks. *Acc. Chem. Res.* **47**, 1555-1562, doi:10.1021/ar5000314 (2014).

26 Tuffnell, J. M. *et al.* Novel metal-organic framework materials: blends, liquids, glasses and crystal-glass composites. *Chem Commun (Camb)* **55**, 8705-8715, doi:10.1039/c9cc01468c (2019).

27 Bennett, T. D. *et al.* Structure and properties of an amorphous metal-organic framework. *Phys. Rev. Lett.* **104**, 115503, doi:10.1103/PhysRevLett.104.115503 (2010).

28 Zhou, C. *et al.* Metal-organic framework glasses with permanent accessible porosity. *Nat Commun* **9**, 5042, doi:10.1038/s41467-018-07532-z (2018).

29 Chen, Y. *et al.* Shaping of Metal-Organic Frameworks: From Fluid to Shaped Bodies and Robust Foams. *J. Am. Chem. Soc.* **138**, 10810-10813, doi:10.1021/jacs.6b06959 (2016).

30 Andrew Lin, K.-Y. & Chang, H.-A. A zeolitic imidazole framework (ZIF)–sponge composite prepared via a surfactant-assisted dip-coating method. *Journal of Materials Chemistry A* **3**, 20060-20064, doi:10.1039/c5ta04427h (2015).

31 Pinto, M. L., Dias, S. & Pires, J. Composite MOF foams: the example of UiO-66/polyurethane. *ACS Appl Mater Interfaces* **5**, 2360-2363, doi:10.1021/am303089g (2013).

32 Zhou, S., Stromme, M. & Xu, C. Highly Transparent, Flexible, and Mechanically Strong Nanopapers of Cellulose Nanofibers @Metal-Organic Frameworks. *Chemistry* **25**, 3515-3520, doi:10.1002/chem.201806417 (2019).

33 Ma, K. *et al.* Facile and Scalable Coating of Metal-Organic Frameworks on Fibrous Substrates by a Coordination Replication Method at Room Temperature. *ACS Appl Mater Interfaces* **11**, 22714-22721, doi:10.1021/acsami.9b04780 (2019).

34 Ma, X., Lou, Y., Chen, X.-B., Shi, Z. & Xu, Y. Multifunctional flexible composite aerogels constructed through in-situ growth of metal-organic framework nanoparticles on bacterial cellulose. *Chem. Eng. J.* **356**, 227-235, doi:10.1016/j.cej.2018.09.034 (2019).

35 Hirschle, P. *et al.* Exploration of MOF nanoparticle sizes using various physical characterization methods – is what you measure what you get? *CrystEngComm* **18**, 4359-4368, doi:10.1039/c6ce00198j (2016).

36 Tanaka, D. *et al.* Rapid preparation of flexible porous coordination polymer nanocrystals with accelerated guest adsorption kinetics. *Nature Chemistry* **2**, 410-416, doi:10.1038/nchem.627 (2010).

37 Li, P. *et al.* Synthesis of nanocrystals of Zr-based metal-organic frameworks with csq-net: significant enhancement in the degradation of a nerve agent simulant. *Chem Commun (Camb)* **51**, 10925-10928, doi:10.1039/c5cc03398e (2015).

38 Sakata, Y. *et al.* Shape-Memory Nanopores Induced in Coordination Frameworks by Crystal Downsizing. *Science* **339**, 193-196, doi:10.1126/science.1231451 (2013).

39 Freund, R., Lachelt, U., Gruber, T., Ruhle, B. & Wuttke, S. Multifunctional Efficiency: Extending the Concept of Atom Economy to Functional Nanomaterials. *ACS Nano* **12**, 2094-2105, doi:10.1021/acsnano.8b00932 (2018).

40 Kim, H. *et al.* Single crystalline hollow metal-organic frameworks: a metal-organic polyhedron single crystal as a sacrificial template. *Chem Commun (Camb)* **51**, 3678-3681, doi:10.1039/c4cc10051d (2015).

41 Kuo, C.-H. *et al.* Yolk–Shell Nanocrystal@ZIF-8 Nanostructures for Gas-Phase Heterogeneous Catalysis with Selectivity Control. *J. Am. Chem. Soc.* **134**, 14345-14348, doi:10.1021/ja306869j (2012).

42 Zhang, Z. *et al.* Hierarchical Zn/Ni-MOF-2 nanosheet-assembled hollow nanocubes for multicomponent catalytic reactions. *Angew. Chem. Int. Ed. Engl.* **53**, 12517-12521, doi:10.1002/anie.201406484 (2014).

43 Zhang, W. *et al.* Hollow carbon nanobubbles: monocrystalline MOF nanobubbles and their pyrolysis. *Chem Sci* **8**, 3538-3546, doi:10.1039/c6sc04903f (2017).

44 Ameloot, R. *et al.* Interfacial synthesis of hollow metal–organic framework capsules demonstrating selective permeability. *Nature Chemistry* **3**, 382-387, doi:10.1038/nchem.1026 (2011).

45 Li, A.-L. *et al.* Controllable synthesis of metal–organic framework hollow nanospheres by a versatile step-by-step assembly strategy. *CrystEngComm* **15**, 3554, doi:10.1039/c2ce26636a (2013).

46 Carné-Sánchez, A., Imaz, I., Cano-Sarabia, M. & Maspoch, D. A spray-drying strategy for synthesis of nanoscale metal–organic frameworks and their assembly into hollow superstructures. *Nature Chemistry* **5**, 203-211, doi:10.1038/nchem.1569 (2013).

47 Kim, H. & Lah, M. S. Templated and template-free fabrication strategies for zero-dimensional hollow MOF superstructures. *Dalton Trans* **46**, 6146-6158, doi:10.1039/c7dt00389g (2017).

48 Deng, Z. *et al.* Ferrocenyl metal-organic framework hollow microspheres for in situ loading palladium nanoparticles as a heterogeneous catalyst. *Dalton Trans* **48**, 8995-9003, doi:10.1039/c9dt01406c (2019).

49 Avci, C. *et al.* Post-Synthetic Anisotropic Wet-Chemical Etching of Colloidal Sodalite ZIF Crystals. *Angew. Chem.* **127**, 14625-14629, doi:10.1002/ange.201507588 (2015).

50 Lupica-Spagnolo, L., Ward, D. J., Marie, J. J., Lymperopoulou, S. & Bradshaw, D. Pollen-like ZIF-8 colloidosomes via emulsion templating and etching. *Chem Commun (Camb)* **54**, 8506-8509, doi:10.1039/c8cc03511c (2018).

51 Chuan Tan, Y. & Chun Zeng, H. Self-templating synthesis of hollow spheres of MOFs and their derived nanostructures. *Chem Commun (Camb)* **52**, 11591-11594, doi:10.1039/c6cc05699g (2016).

52 Zhang, S. L., Guan, B. Y. & Lou, X. W. D. Co-Fe Alloy/N-Doped Carbon Hollow Spheres Derived from Dual Metal-Organic Frameworks for Enhanced Electrocatalytic Oxygen Reduction. *Small* **15**, e1805324, doi:10.1002/smll.201805324 (2019).

53 Chen, H., Yang, T., Liu, F. & Li, W. Electrodeposition of gold nanoparticles on Cu-based metal-organic framework for the electrochemical detection of nitrite. *Sensors and Actuators B: Chemical* **286**, 401-407, doi:10.1016/j.snb.2018.10.036 (2019).

54 Luo, T. Y. *et al.* Multivariate Stratified Metal-Organic Frameworks: Diversification Using Domain Building Blocks. *J. Am. Chem. Soc.* **141**, 2161-2168, doi:10.1021/jacs.8b13502 (2019).

55 Tan, Y. C. & Zeng, H. C. Defect Creation in HKUST-1 via Molecular Imprinting: Attaining Anionic Framework Property and Mesoporosity for Cation Exchange Applications. *Adv. Funct. Mater.* **27**, 1703765, doi:10.1002/adfm.201703765 (2017).

56 Choi, S. & Oh, M. Well-Arranged and Confined Incorporation of PdCo Nanoparticles within a Hollow and Porous Metal-Organic Framework for Superior Catalytic Activity. *Angew. Chem. Int. Ed. Engl.* **58**, 866-871, doi:10.1002/anie.201812827 (2019).

57 Zhang, C.-L. *et al.* Electrospun metal-organic framework nanoparticle fibers and their derived electrocatalysts for oxygen reduction reaction. *Nano Energy* **55**, 226-233, doi:10.1016/j.nanoen.2018.10.029 (2019).

58 Zhong, R. *et al.* Fabricating hierarchically porous and Fe3C-embeded nitrogen-rich carbon nanofibers as exceptional electocatalysts for oxygen reduction. *Carbon* **142**, 115-122, doi:10.1016/j.carbon.2018.10.040 (2019).

59 Gualino, M., Roques, N., Brandès, S., Arurault, L. & Sutter, J.-P. From ZIF-8@Al2O3 Composites to Self-Supported ZIF-8 One-Dimensional Superstructures. *Crystal Growth & Design* **15**, 3552-3555, doi:10.1021/acs.cgd.5b00687 (2015).

60 Arbulu, R. C., Jiang, Y.-B., Peterson, E. J. & Qin, Y. Metal-Organic Framework (MOF) Nanorods, Nanotubes, and Nanowires. *Angew. Chem.* **130**, 5915-5919, doi:10.1002/ange.201802694 (2018).

61 Wang, H. *et al.* Helically structured metal-organic frameworks fabricated by using supramolecular assemblies as templates. *Chem Sci* **6**, 1910-1916, doi:10.1039/c4sc03278k (2015).

62 Xu, H. *et al.* Stringing MOF-derived nanocages: a strategy for the enhanced oxygen evolution reaction. *Journal of Materials Chemistry A* **7**, 8284-8291, doi:10.1039/c9ta00624a (2019).

63 Cai, G., Zhang, W., Jiao, L., Yu, S.-H. & Jiang, H.-L. Template-Directed Growth of Well-Aligned MOF Arrays and Derived Self-Supporting Electrodes for Water Splitting. *Chem* **2**, 791-802, doi:10.1016/j.chempr.2017.04.016 (2017).

64 Xia, Z. *et al.* Pt nanoparticles embedded metal-organic framework nanosheets: A synergistic strategy towards bifunctional oxygen electrocatalysis. *Applied Catalysis B: Environmental* **245**, 389-398, doi:10.1016/j.apcatb.2018.12.073 (2019).

65 Deng, J. H. *et al.* Facile Exfoliation of 3D Pillared Metal-Organic Frameworks (MOFs) to Produce MOF Nanosheets with Functionalized Surfaces. *Inorg. Chem.* **58**, 11020-11027, doi:10.1021/acs.inorgchem.9b01564 (2019).

66 Virmani, E. *et al.* On-Surface Synthesis of Highly Oriented Thin Metal-Organic Framework Films through Vapor-Assisted Conversion. *J. Am. Chem. Soc.* **140**, 4812-4819, doi:10.1021/jacs.7b08174 (2018).

67 Biemmi, E., Scherb, C. & Bein, T. Oriented growth of the metal organic framework Cu(3)(BTC)(2)(H(2)O)(3).xH(2)O tunable with functionalized self-assembled monolayers. *J. Am. Chem. Soc.* **129**, 8054-8055, doi:10.1021/ja0701208 (2007).

68 Ning, Y., Lou, X., Li, C., Hu, X. & Hu, B. Ultrathin Cobalt-Based Metal–Organic Framework Nanosheets with Both Metal and Ligand Redox Activities for Superior Lithium Storage. *Chemistry – A European Journal* **23**, 15984-15990, doi:doi:10.1002/chem.201703077 (2017).

69 Haraguchi, T., Otsubo, K. & Kitagawa, H. Emergence of Surface- and Interface-Induced Structures and Properties in Metal-Organic Framework Thin Films. *Eur. J. Inorg. Chem.* **2018**, 1697-1706, doi:10.1002/ejic.201701234 (2018).

70 Sakaida, S. *et al.* Fabrication and Structural Characterization of an Ultrathin Film of a Two-Dimensional-Layered Metal-Organic Framework, {Fe(py)2[Ni(CN)4]} (py = pyridine). *Inorg. Chem.* **56**, 7606-7609, doi:10.1021/acs.inorgchem.7b01113 (2017).

71 Liu, J. *et al.* A novel series of isoreticular metal organic frameworks: realizing metastable structures by liquid phase epitaxy. *Sci Rep* **2**, 921, doi:10.1038/srep00921 (2012).

72 Wannapaiboon, S. *et al.* Control of structural flexibility of layered-pillared metal-organic frameworks anchored at surfaces. *Nat Commun* **10**, 346, doi:10.1038/s41467-018-08285-5 (2019).

73 Zhang, G. *et al.* Construction of a Hierarchical Architecture of Covalent Organic Frameworks via a Postsynthetic Approach. *J. Am. Chem. Soc.* **140**, 2602-2609, doi:10.1021/jacs.7b12350 (2018).

74 Yang, H. *et al.* Hierarchical pore architectures from 2D covalent organic nanosheets for efficient water/alcohol separation. *Journal of Membrane Science* **561**, 79-88, doi:10.1016/j.memsci.2018.05.036 (2018).

75 Avci, C. *et al.* Self-assembly of polyhedral metal-organic framework particles into three-dimensional ordered superstructures. *Nat Chem* **10**, 78-84, doi:10.1038/nchem.2875 (2018).

76 Avci, C. *et al.* Self-assembly of polyhedral metal-organic framework particles into three-dimensional ordered superstructures. *Nat Chem* **10**, 78-84, doi:10.1038/nchem.2875 (2017).

77 Feng, L., Li, J.-L., Day, G. S., Lv, X.-L. & Zhou, H.-C. Temperature-Controlled Evolution of Nanoporous MOF Crystallites into Hierarchically Porous Superstructures. *Chem* **5**, 1265-1274, doi:10.1016/j.chempr.2019.03.003 (2019).

78 Sun, S. *et al.* 3D hierarchical porous Co1−xS@C derived from a ZIF-67 single crystals self-assembling superstructure with superior pseudocapacitance. *Journal of Materials Chemistry A* **7**, 17248-17253, doi:10.1039/c9ta04503a (2019).

79 Shen, K. *et al.* Ordered macro-microporous metal-organic framework single crystals. *Science* **359**, 206-210, doi:10.1126/science.aao3403 (2018).

80 Zhao, X. *et al.* Macro/Microporous Covalent Organic Frameworks for Efficient Electrocatalysis. *J. Am. Chem. Soc.* **141**, 6623-6630, doi:10.1021/jacs.9b01226 (2019).

81 Yanai, N., Sindoro, M., Yan, J. & Granick, S. Electric field-induced assembly of monodisperse polyhedral metal-organic framework crystals. *J. Am. Chem. Soc.* **135**, 34-37, doi:10.1021/ja309361d (2013).

82 Zhong, Y. *et al.* Wafer-scale synthesis of monolayer two-dimensional porphyrin polymers for hybrid superlattices. *Science*, doi:10.1126/science.aax9385 (2019).

83 Pang, M. *et al.* Synthesis and integration of Fe-soc-MOF cubes into colloidosomes via a single-step emulsion-based approach. *J. Am. Chem. Soc.* **135**, 10234-10237, doi:10.1021/ja403994u (2013).

84 Garzon-Tovar, L. *et al.* A MOF@COF Composite with Enhanced Uptake through Interfacial Pore Generation. *Angew. Chem. Int. Ed. Engl.* **58**, 9512-9516, doi:10.1002/anie.201904766 (2019).

85 Yan, Y. *et al.* Facile synthesis of an accordion-like Ni-MOF superstructure for high-performance flexible supercapacitors. *Journal of Materials Chemistry A* **4**, 19078-19085, doi:10.1039/c6ta08331e (2016).

86 LaMer, V. K. & Dinegar, R. H. Theory, Production and Mechanism of Formation of Monodispersed Hydrosols. *J. Am. Chem. Soc.* **72**, 4847-4854, doi:10.1021/ja01167a001 (1950).

87 Wang, S., McGuirk, C. M., d'Aquino, A., Mason, J. A. & Mirkin, C. A. Metal-Organic Framework Nanoparticles. *Adv. Mater.* **30**, e1800202, doi:10.1002/adma.201800202 (2018).

88 Barros, B. S., de Lima Neto, O. J., de Oliveira Frós, A. C. & Kulesza, J. Metal-Organic Framework Nanocrystals. *ChemistrySelect* **3**, 7459-7471, doi:10.1002/slct.201801423 (2018).

89 Ploetz, E., Engelke, H., Lächelt, U. & Wuttke, S. Functionalization chemistry of porous materials. *Adv. Funct. Mater.*, In Revision (2019).

90 Pan, Y., Liu, Y., Zeng, G., Zhao, L. & Lai, Z. Rapid synthesis of zeolitic imidazolate framework-8 (ZIF-8) nanocrystals in an aqueous system. *Chem Commun (Camb)* **47**, 2071-2073, doi:10.1039/c0cc05002d (2011).

91 Cravillon, J. *et al.* Rapid Room-Temperature Synthesis and Characterization of Nanocrystals of a Prototypical Zeolitic Imidazolate Framework. *Chem. Mater.* **21**, 1410-1412, doi:10.1021/cm900166h (2009).

92 Wee, L. H., Lohe, M. R., Janssens, N., Kaskel, S. & Martens, J. A. Fine tuning of the metal–organic framework Cu3(BTC)2 HKUST-1 crystal size in the 100 nm to 5 micron range. *J. Mater. Chem.* **22**, 13742, doi:10.1039/c2jm31536j (2012).

93 Sheta, S. M., El-Sheikh, S. M. & Abd-Elzaher, M. M. Promising photoluminescence optical approach for triiodothyronine hormone determination based on smart copper metal-organic framework nanoparticles. *Appl. Organomet. Chem.*, e5069, doi:10.1002/aoc.5069 (2019).

94 Mohammadi Nilash, M., Hashemzadeh, A., Fakhari, A. R. & Amini, M. M. Novel Schiff base-functionalized metal–organic framework nanoparticles for dispersive solid phase extraction of copper ions from vegetable and water samples. *Analytical Methods* **11**, 2683-2691, doi:10.1039/c9ay00304e (2019).

95 Horcajada, P. *et al.* Porous metal-organic-framework nanoscale carriers as a potential platform for drug delivery and imaging. *Nat Mater* **9**, 172-178, doi:10.1038/nmat2608 (2010).

96 Tsai, C.-W. & Langner, E. H. G. The effect of synthesis temperature on the particle size of nano-ZIF-8. *Microporous Mesoporous Mater.* **221**, 8-13, doi:10.1016/j.micromeso.2015.08.041 (2016).

97 Surble, S., Serre, C., Mellot-Draznieks, C., Millange, F. & Ferey, G. A new isoreticular class of metal-organic-frameworks with the MIL-88 topology. *Chem Commun (Camb)*, 284-286, doi:10.1039/b512169h (2006).

98 Shankar, S. *et al.* Metal-organic microstructures: from rectangular to stellated and interpenetrating polyhedra. *J. Am. Chem. Soc.* **137**, 226-231, doi:10.1021/ja509428a (2015).

99 Cheng, X. *et al.* Size- and morphology-controlled NH2-MIL-53(Al) prepared in DMF-water mixed solvents. *Dalton Trans* **42**, 13698-13705, doi:10.1039/c3dt51322j (2013).

100 Klinowski, J., Paz, F. A., Silva, P. & Rocha, J. Microwave-assisted synthesis of metal-organic frameworks. *Dalton Trans* **40**, 321-330, doi:10.1039/c0dt00708k (2011).

101 Haque, E., Khan, N. A., Kim, C. M. & Jhung, S. H. Syntheses of Metal–Organic Frameworks and Aluminophosphates under Microwave Heating: Quantitative Analysis of Accelerations. *Crystal Growth & Design* **11**, 4413-4421, doi:10.1021/cg200594e (2011).

102 Chalati, T., Horcajada, P., Gref, R., Couvreur, P. & Serre, C. Optimisation of the synthesis of MOF nanoparticles made of flexible porous iron fumarate MIL-88A. *J. Mater. Chem.* **21**, 2220-2227, doi:10.1039/c0jm03563g (2011).

103 Jhung, S. H. *et al.* Microwave Synthesis of Chromium Terephthalate MIL-101 and Its Benzene Sorption Ability. *Adv. Mater.* **19**, 121-124, doi:10.1002/adma.200601604 (2007).

104 Masoomi, M. Y., Morsali, A. & Junk, P. C. Ultrasound assisted synthesis of a Zn(ii) metal–organic framework with nano-plate morphology using non-linear dicarboxylate and linear N-donor ligands. *RSC Adv.* **4**, 47894-47898, doi:10.1039/c4ra09186h (2014).

105 Burgaz, E., Erciyes, A., Andac, M. & Andac, O. Synthesis and characterization of nano-sized metal organic framework-5 (MOF-5) by using consecutive combination of ultrasound and microwave irradiation methods. *Inorg. Chim. Acta* **485**, 118-124, doi:10.1016/j.ica.2018.10.014 (2019).

106 Haque, E., Khan, N. A., Park, J. H. & Jhung, S. H. Synthesis of a metal-organic framework material, iron terephthalate, by ultrasound, microwave, and conventional electric heating: a kinetic study. *Chemistry* **16**, 1046-1052, doi:10.1002/chem.200902382 (2010).

107 Amaro-Gahete, J. *et al.* Fast ultrasound-assisted synthesis of highly crystalline MIL-88A particles and their application as ethylene adsorbents. *Ultrason. Sonochem.* **50**, 59-66, doi:10.1016/j.ultsonch.2018.08.027 (2019).

108 Zhao, Y., Zhang, Q., Li, Y., Zhang, R. & Lu, G. Large-Scale Synthesis of Monodisperse UiO-66 Crystals with Tunable Sizes and Missing Linker Defects via Acid/Base Co-Modulation. *ACS Appl Mater Interfaces* **9**, 15079-15085, doi:10.1021/acsami.7b02887 (2017).

109 Vakili, R. *et al.* Microwave-assisted synthesis of zirconium-based metal organic frameworks (MOFs): Optimization and gas adsorption. *Microporous Mesoporous Mater.* **260**, 45-53, doi:10.1016/j.micromeso.2017.10.028 (2018).

110 Katz, M. J. *et al.* A facile synthesis of UiO-66, UiO-67 and their derivatives. *Chem Commun (Camb)* **49**, 9449-9451, doi:10.1039/c3cc46105j (2013).

111 Morris, W. *et al.* Role of Modulators in Controlling the Colloidal Stability and Polydispersity of the UiO-66 Metal-Organic Framework. *ACS Appl Mater Interfaces* **9**, 33413-33418, doi:10.1021/acsami.7b01040 (2017).

112 McGuire, C. V. & Forgan, R. S. The surface chemistry of metal-organic frameworks. *Chem Commun (Camb)* **51**, 5199-5217, doi:10.1039/c4cc04458d (2015).

113 Vermoortele, F. *et al.* Synthesis modulation as a tool to increase the catalytic activity of metal-organic frameworks: the unique case of UiO-66(Zr). *J. Am. Chem. Soc.* **135**, 11465-11468, doi:10.1021/ja405078u (2013).

114 Rieter, W. J., Taylor, K. M. & Lin, W. Surface modification and functionalization of nanoscale metal-organic frameworks for controlled release and luminescence sensing. *J. Am. Chem. Soc.* **129**, 9852-9853, doi:10.1021/ja073506r (2007).

115 Rieter, W. J., Taylor, K. M., An, H., Lin, W. & Lin, W. Nanoscale metal-organic frameworks as potential multimodal contrast enhancing agents. *J. Am. Chem. Soc.* **128**, 9024-9025, doi:10.1021/ja0627444 (2006).

116 Shang, W. *et al.* Shape and size controlled synthesis of MOF nanocrystals with the assistance of ionic liquid mircoemulsions. *Langmuir* **29**, 13168-13174, doi:10.1021/la402882a (2013).

117 Cai, X., Xie, Z., Pang, M. & Lin, J. Controllable Synthesis of Highly Uniform Nanosized HKUST-1 Crystals by Liquid–Solid–Solution Method. *Crystal Growth & Design* **19**, 556-561, doi:10.1021/acs.cgd.8b01695 (2019).

118 Huang, X.-X. *et al.* Hierarchically mesostructured MIL-101 metal–organic frameworks: supramolecular template-directed synthesis and accelerated adsorption kinetics for dye removal. *CrystEngComm* **14**, 1613-1617, doi:10.1039/c1ce06138k (2012).

119 Zhao, Y. *et al.* Metal-organic framework nanospheres with well-ordered mesopores synthesized in an ionic liquid/CO2/surfactant system. *Angew. Chem. Int. Ed. Engl.* **50**, 636-639, doi:10.1002/anie.201005314 (2011).

120 Sang, X. *et al.* Ionic liquid accelerates the crystallization of Zr-based metal-organic frameworks. *Nat Commun* **8**, 175, doi:10.1038/s41467-017-00226-y (2017).

121 Wei, J. Z. *et al.* Rapid and Large-Scale Synthesis of IRMOF-3 by Electrochemistry Method with Enhanced Fluorescence Detection Performance for TNP. *Inorg. Chem.* **57**, 3818-3824, doi:10.1021/acs.inorgchem.7b03174 (2018).

122 Nandiyanto, A. B. D., He, X. & Wang, W.-N. Colloid-assisted growth of metal–organic framework nanoparticles. *CrystEngComm* **21**, 2268-2272, doi:10.1039/c9ce00033j (2019).

123 Leng, K., Sun, Y., Li, X., Sun, S. & Xu, W. Rapid Synthesis of Metal–Organic Frameworks MIL-101(Cr) Without the Addition of Solvent and Hydrofluoric Acid. *Crystal Growth & Design* **16**, 1168-1171, doi:10.1021/acs.cgd.5b01696 (2016).

124 Uzarevic, K. *et al.* Mechanochemical and solvent-free assembly of zirconium-based metal-organic frameworks. *Chem Commun (Camb)* **52**, 2133-2136, doi:10.1039/c5cc08972g (2016).

125 Li, X. *et al.* Mechanochemistry-assisted encapsulation of metal nanoparticles in MOF matrices via a sacrificial strategy. *Journal of Materials Chemistry A* **7**, 14504-14509, doi:10.1039/c9ta03578h (2019).

126 Echaide-Górriz, C., Clément, C., Cacho-Bailo, F., Téllez, C. & Coronas, J. New strategies based on microfluidics for the synthesis of metal–organic frameworks and their membranes. *Journal of Materials Chemistry A* **6**, 5485-5506, doi:10.1039/c8ta01232f (2018).

127 Tai, S. *et al.* Facile preparation of UiO-66 nanoparticles with tunable sizes in a continuous flow microreactor and its application in drug delivery. *Microporous Mesoporous Mater.* **220**, 148-154, doi:10.1016/j.micromeso.2015.08.037 (2016).

128 Rubio-Martinez, M. *et al.* Versatile, high quality and scalable continuous flow production of metal-organic frameworks. *Sci Rep* **4**, 5443, doi:10.1038/srep05443 (2014).

129 D'Arras, L. *et al.* Fast and continuous processing of a new sub-micronic lanthanide-based metal–organic framework. *New J. Chem.* **38**, 1477-1483, doi:10.1039/c3nj01371e (2014).

130 Jeong, G.-Y. *et al.* Bioactive MIL-88A Framework Hollow Spheres via Interfacial Reaction In-Droplet Microfluidics for Enzyme and Nanoparticle Encapsulation. *Chem. Mater.* **27**, 7903-7909, doi:10.1021/acs.chemmater.5b02847 (2015).

131 Faustini, M. *et al.* Microfluidic approach toward continuous and ultrafast synthesis of metal-organic framework crystals and hetero structures in confined microdroplets. *J. Am. Chem. Soc.* **135**, 14619-14626, doi:10.1021/ja4039642 (2013).

132 Paseta, L. *et al.* Accelerating the controlled synthesis of metal-organic frameworks by a microfluidic approach: a nanoliter continuous reactor. *ACS Appl Mater Interfaces* **5**, 9405-9410, doi:10.1021/am4029872 (2013).

133 Modena, M. M., Hirschle, P., Wuttke, S. & Burg, T. P. Mass Measurements Reveal Preferential Sorption of Mixed Solvent Components in Porous Nanoparticles. *Small* **14**, e1800826, doi:10.1002/smll.201800826 (2018).

134 Yin, Z., Wan, S., Yang, J., Kurmoo, M. & Zeng, M.-H. Recent advances in post-synthetic modification of metal–organic frameworks: New types and tandem reactions. *Coord. Chem. Rev.* **378**, 500-512, doi:10.1016/j.ccr.2017.11.015 (2019).

135 Cohen, S. M. Postsynthetic methods for the functionalization of metal-organic frameworks. *Chem. Rev.* **112**, 970-1000, doi:10.1021/cr200179u (2012).

136 Yusran, Y., Fang, Q. & Qiu, S. Postsynthetic Covalent Modification in Covalent Organic Frameworks. *Isr. J. Chem.* **58**, 971-984, doi:10.1002/ijch.201800066 (2018).

137 Segura, J. L., Royuela, S. & Mar Ramos, M. Post-synthetic modification of covalent organic frameworks. *Chem. Soc. Rev.* **48**, 3903-3945, doi:10.1039/c8cs00978c (2019).

138 Yin, W. *et al.* The Tuning of Optical Properties of Nanoscale MOFs-Based Thin Film through Post-Modification. *Nanomaterials (Basel)* **7**, doi:10.3390/nano7090242 (2017).

139 Marshall, R. J., Griffin, S. L., Wilson, C. & Forgan, R. S. Single-Crystal to Single-Crystal Mechanical Contraction of Metal-Organic Frameworks through Stereoselective Postsynthetic Bromination. *J. Am. Chem. Soc.* **137**, 9527-9530, doi:10.1021/jacs.5b05434 (2015).

140 Wickenheisser, M., Jeremias, F., Henninger, S. K. & Janiak, C. Grafting of hydrophilic ethylene glycols or ethylenediamine on coordinatively unsaturated metal sites in MIL-100(Cr) for improved water adsorption characteristics. *Inorg. Chim. Acta* **407**, 145-152, doi:10.1016/j.ica.2013.07.024 (2013).

141 Mortada, B. *et al.* Postmetalated Zirconium Metal Organic Frameworks as a Highly Potent Bactericide. *Inorg. Chem.* **56**, 4740-4745, doi:10.1021/acs.inorgchem.7b00429 (2017).

142 Liu, J. *et al.* Applications of metal-organic frameworks in heterogeneous supramolecular catalysis. *Chem. Soc. Rev.* **43**, 6011-6061, doi:10.1039/c4cs00094c (2014).

143 Abdel-Mageed, A. M. *et al.* Highly Active and Stable Single-Atom Cu Catalysts Supported by a Metal-Organic Framework. *J. Am. Chem. Soc.* **141**, 5201-5210, doi:10.1021/jacs.8b11386 (2019).

144 Chen, Y. *et al.* Catalase-like metal-organic framework nanoparticles to enhance radiotherapy in hypoxic cancer and prevent cancer recurrence. *Chem Sci* **10**, 5773-5778, doi:10.1039/c9sc00747d (2019).

145 Gao, D. *et al.* CrPd nanoparticles on NH2-functionalized metal-organic framework as a synergistic catalyst for efficient hydrogen evolution from formic acid. *Chem. Eng. J.* **361**, 953-959, doi:10.1016/j.cej.2018.12.158 (2019).

146 Chen, W.-H., Luo, G.-F., Sohn, Y. S., Nechushtai, R. & Willner, I. Enzyme-Driven Release of Loads from Nucleic Acid-Capped Metal-Organic Framework Nanoparticles. *Adv. Funct. Mater.* **29**, 1805341, doi:10.1002/adfm.201805341 (2019).

147 Hintz, H. & Wuttke, S. Postsynthetic modification of an amino-tagged MOF using peptide coupling reagents: a comparative study. *Chem. Commun.* **50**, 11472-11475, doi:10.1039/c4cc02650k (2014).

148 Schrimpf, W. *et al.* Chemical diversity in a metal-organic framework revealed by fluorescence lifetime imaging. *Nat Commun* **9**, 1647, doi:10.1038/s41467-018-04050-w (2018).

149 Lalonde, M. *et al.* Transmetalation: routes to metal exchange within metal–organic frameworks. *Journal of Materials Chemistry A* **1**, 5453, doi:10.1039/c3ta10784a (2013).

150 Schmitt, S. *et al.* Localized Conversion of Metal–Organic Frameworks into Polymer Gels via Light-Induced Click Chemistry. *Chem. Mater.* **29**, 5982-5989, doi:10.1021/acs.chemmater.7b01677 (2017).

151 Ishiwata, T. *et al.* Box-like gel capsules from heterostructures based on a core-shell MOF as a template of crystal crosslinking. *Chem Commun (Camb)* **54**, 1437-1440, doi:10.1039/c7cc07158b (2018).

152 Tsotsalas, M. *et al.* Fabrication of highly uniform gel coatings by the conversion of surface-anchored metal-organic frameworks. *J. Am. Chem. Soc.* **136**, 8-11, doi:10.1021/ja409205s (2014).

153 Boissonnault, J. A., Wong-Foy, A. G. & Matzger, A. J. Core-Shell Structures Arise Naturally During Ligand Exchange in Metal-Organic Frameworks. *J. Am. Chem. Soc.* **139**, 14841-14844, doi:10.1021/jacs.7b08349 (2017).

154 Liu, L. *et al.* Harnessing Structural Dynamics in a 2D Manganese-Benzoquinoid Framework To Dramatically Accelerate Metal Transport in Diffusion-Limited Metal Exchange Reactions. *J. Am. Chem. Soc.* **140**, 11444-11453, doi:10.1021/jacs.8b06774 (2018).

155 Song, X. *et al.* Post-Synthetic Modifications of Framework Metal Ions in Isostructural Metal–Organic Frameworks: Core–Shell Heterostructures via Selective Transmetalations. *Chem. Mater.* **24**, 3065-3073, doi:10.1021/cm301605w (2012).

156 Zhang, H.-F. *et al.* Fine-tuning metal–organic framework performances by spatially-differentiated postsynthetic modification. *Journal of Materials Chemistry A* **6**, 4260-4265, doi:10.1039/c7ta09969j (2018).

157 Jeong, U. *et al.* Inversion of Dispersion: Colloidal Stability of Calixarene-Modified Metal-Organic Framework Nanoparticles in Nonpolar Media. *J. Am. Chem. Soc.* **141**, 12182-12186, doi:10.1021/jacs.9b04198 (2019).

158 Castells-Gil, J. *et al.* Surface Functionalization of Metal-Organic Framework Crystals with Catechol Coatings for Enhanced Moisture Tolerance. *ACS Appl Mater Interfaces* **9**, 44641-44648, doi:10.1021/acsami.7b15564 (2017).

159 Gadzikwa, T. *et al.* Covalent surface modification of a metal-organic framework: selective surface engineering via Cu(I)-catalyzed Huisgen cycloaddition. *Chem Commun (Camb)*, 5493-5495, doi:10.1039/b805101a (2008).

160 Rowe, M. D., Thamm, D. H., Kraft, S. L. & Boyes, S. G. Polymer-modified gadolinium metal-organic framework nanoparticles used as multifunctional nanomedicines for the targeted imaging and treatment of cancer. *Biomacromolecules* **10**, 983-993, doi:10.1021/bm900043e (2009).

161 Roder, R. *et al.* Multifunctional Nanoparticles by Coordinative Self-Assembly of His-Tagged Units with Metal-Organic Frameworks. *J. Am. Chem. Soc.* **139**, 2359-2368, doi:10.1021/jacs.6b11934 (2017).

162 Zhao, Y., Li, Y., Pang, H., Yang, C. & Ngai, T. Controlled synthesis of metal-organic frameworks coated with noble metal nanoparticles and conducting polymer for enhanced catalysis. *J. Colloid Interface Sci.* **537**, 262-268, doi:10.1016/j.jcis.2018.11.031 (2019).

163 Tay, C. Y., Setyawati, M. I., Xie, J., Parak, W. J. & Leong, D. T. Back to Basics: Exploiting the Innate Physico-chemical Characteristics of Nanomaterials for Biomedical Applications. *Adv. Funct. Mater.* **24**, 5936-5955, doi:10.1002/adfm.201401664 (2014).

164 Wang, S. *et al.* Surface-Specific Functionalization of Nanoscale Metal-Organic Frameworks. *Angew. Chem. Int. Ed. Engl.* **54**, 14738-14742, doi:10.1002/anie.201506888 (2015).

165 Wang, S. *et al.* DNA-Functionalized Metal-Organic Framework Nanoparticles for Intracellular Delivery of Proteins. *J. Am. Chem. Soc.* **141**, 2215-2219, doi:10.1021/jacs.8b12705 (2019).

166 Zhu, W. *et al.* Versatile Surface Functionalization of Metal-Organic Frameworks through Direct Metal Coordination with a Phenolic Lipid Enables Diverse Applications. *Adv. Funct. Mater.* **28**, 1705274, doi:10.1002/adfm.201705274 (2018).

167 Zimpel, A. *et al.* Imparting Functionality to MOF Nanoparticles by External Surface Selective Covalent Attachment of Polymers. *Chem. Mater.* **28**, 3318-3326, doi:10.1021/acs.chemmater.6b00180 (2016).

168 Abanades Lazaro, I. *et al.* Selective Surface PEGylation of UiO-66 Nanoparticles for Enhanced Stability, Cell Uptake, and pH-Responsive Drug Delivery. *Chem* **2**, 561-578, doi:10.1016/j.chempr.2017.02.005 (2017).

169 Illes, B., Wuttke, S. & Engelke, H. Liposome-Coated Iron Fumarate Metal-Organic Framework Nanoparticles for Combination Therapy. *Nanomaterials (Basel)* **7**, doi:10.3390/nano7110351 (2017).

170 Illes, B. *et al.* Exosome-Coated Metal–Organic Framework Nanoparticles: An Efficient Drug Delivery Platform. *Chem. Mater.* **29**, 8042-8046, doi:10.1021/acs.chemmater.7b02358 (2017).

171 Carné, A., Carbonell, C., Imaz, I. & Maspoch, D. Nanoscale metal–organic materials. *Chem. Soc. Rev.* **40**, 291-305, doi:10.1039/c0cs00042f (2011).

172 Archana, K., Pillai, N. G., Rhee, K. Y. & Asif, A. Super paramagnetic ZIF-67 metal organic framework nanocomposite. *Composites Part B: Engineering* **158**, 384-389, doi:10.1016/j.compositesb.2018.10.005 (2019).

173 Horcajada, P. *et al.* Metal–Organic Frameworks in Biomedicine. *Chem. Rev.* **112**, 1232-1268, doi:10.1021/cr200256v (2012).

174 Fu, C. *et al.* Microwave-Activated Mn-Doped Zirconium Metal-Organic Framework Nanocubes for Highly Effective Combination of Microwave Dynamic and Thermal Therapies Against Cancer. *ACS Nano* **12**, 2201-2210, doi:10.1021/acsnano.7b08868 (2018).

175 Liu, D., Poon, C., Lu, K., He, C. & Lin, W. Self-assembled nanoscale coordination polymers with trigger release properties for effective anticancer therapy. *Nat Commun* **5**, 4182, doi:10.1038/ncomms5182 (2014).

176 Lismont, M., Dreesen, L. & Wuttke, S. Metal-Organic Framework Nanoparticles in Photodynamic Therapy: Current Status and Perspectives. *Adv. Funct. Mater.* **27**, 1606314, doi:10.1002/adfm.201606314 (2017).

177 Liu, J. *et al.* Nanoscale metal-organic frameworks for combined photodynamic & radiation therapy in cancer treatment. *Biomaterials* **97**, 1-9, doi:10.1016/j.biomaterials.2016.04.034 (2016).

178 Lu, K., He, C. & Lin, W. Nanoscale metal-organic framework for highly effective photodynamic therapy of resistant head and neck cancer. *J. Am. Chem. Soc.* **136**, 16712-16715, doi:10.1021/ja508679h (2014).

179 Lan, G. *et al.* Titanium-Based Nanoscale Metal-Organic Framework for Type I Photodynamic Therapy. *J. Am. Chem. Soc.* **141**, 4204-4208, doi:10.1021/jacs.8b13804 (2019).

180 Zhao, X. *et al.* Postsynthetic Ligand Exchange of Metal-Organic Framework for Photodynamic Therapy. *ACS Appl Mater Interfaces* **11**, 7884-7892, doi:10.1021/acsami.9b00740 (2019).

181 Chowdhury, M. A. Metal-Organic-Frameworks as Contrast Agents in Magnetic Resonance Imaging. *ChemBioEng Reviews* **4**, 225-239, doi:10.1002/cben.201600027 (2017).

182 Della Rocca, J. & Lin, W. Nanoscale Metal-Organic Frameworks: Magnetic Resonance Imaging Contrast Agents and Beyond. *Eur. J. Inorg. Chem.* **2010**, 3725-3734, doi:10.1002/ejic.201000496 (2010).

183 Böll, K., Zimpel, A., Dietrich, O., Wuttke, S. & Peller, M. Clinically Approved MRI Contrast Agents as Imaging Labels for a Porous Iron-Based MOF Nanocarrier: A Systematic Investigation in a Clinical MRI Setting. *Advanced Therapeutics*, 1900126, doi:10.1002/adtp.201900126 (2019).

184 Chen, D. *et al.* In Vivo Targeting and Positron Emission Tomography Imaging of Tumor with Intrinsically Radioactive Metal-Organic Frameworks Nanomaterials. *ACS Nano* **11**, 4315-4327, doi:10.1021/acsnano.7b01530 (2017).

185 Ma, X. *et al.* Multifunctional iron-based Metal-Organic framework as biodegradable nanozyme for microwave enhancing dynamic therapy. *Biomaterials* **214**, 119223, doi:10.1016/j.biomaterials.2019.119223 (2019).

186 Wu, M. X. & Yang, Y. W. Metal-Organic Framework (MOF)-Based Drug/Cargo Delivery and Cancer Therapy. *Adv. Mater.* **29**, doi:10.1002/adma.201606134 (2017).

187 Della Rocca, J., Liu, D. & Lin, W. Nanoscale metal-organic frameworks for biomedical imaging and drug delivery. *Acc. Chem. Res.* **44**, 957-968, doi:10.1021/ar200028a (2011).

188 Dong, K. *et al.* Facile preparation of metal-organic frameworks-based hydrophobic anticancer drug delivery nanoplatform for targeted and enhanced cancer treatment. *Talanta* **194**, 703-708, doi:10.1016/j.talanta.2018.10.101 (2019).

189 Xue, Q., Ye, C., Zhang, M., Hu, X. & Cai, T. Glutathione responsive cubic gel particles cyclodextrin metal-organic frameworks for intracellular drug delivery. *J. Colloid Interface Sci.* **551**, 39-46, doi:10.1016/j.jcis.2019.04.096 (2019).

190 Liang, W. *et al.* Enhanced Activity of Enzymes Encapsulated in Hydrophilic Metal-Organic Frameworks. *J. Am. Chem. Soc.* **141**, 2348-2355, doi:10.1021/jacs.8b10302 (2019).

191 He, Z. *et al.* Hybrid Nanomedicine Fabricated from Photosensitizer-Terminated Metal-Organic Framework Nanoparticles for Photodynamic Therapy and Hypoxia-Activated Cascade Chemotherapy. *Small* **15**, e1804131, doi:10.1002/smll.201804131 (2019).

192 Liang, K. *et al.* Biomimetic mineralization of metal-organic frameworks as protective coatings for biomacromolecules. *Nature Communications* **6**, 7240, doi:10.1038/ncomms8240 (2015).

193 Yang, P. *et al.* Metal-Organic Framework Nanoparticles with Near-Infrared Dye for Multimodal Imaging and Guided Phototherapy. *ACS Appl Mater Interfaces* **11**, 11209-11219, doi:10.1021/acsami.9b01286 (2019).

194 Feng, J. *et al.* Stimuli-responsive multifunctional metal–organic framework nanoparticles for enhanced chemo-photothermal therapy. *Journal of Materials Chemistry B* **7**, 994-1004, doi:10.1039/c8tb02815j (2019).

195 Zimpel, A. *et al.* Coordinative Binding of Polymers to Metal-Organic Framework Nanoparticles for Control of Interactions at the Biointerface. *ACS Nano* **13**, 3884-3895, doi:10.1021/acsnano.8b06287 (2019).

196 Hu, Z., Deibert, B. J. & Li, J. Luminescent metal-organic frameworks for chemical sensing and explosive detection. *Chem. Soc. Rev.* **43**, 5815-5840, doi:10.1039/c4cs00010b (2014).

197 Kreno, L. E. *et al.* Metal–Organic Framework Materials as Chemical Sensors. *Chem. Rev.* **112**, 1105-1125, doi:10.1021/cr200324t (2012).

198 Wang, S. *et al.* Enhancing Luminol Electrochemiluminescence by Combined Use of Cobalt-Based Metal Organic Frameworks and Silver Nanoparticles and Its Application in Ultrasensitive Detection of Cardiac Troponin I. *Anal. Chem.* **91**, 3048-3054, doi:10.1021/acs.analchem.8b05443 (2019).

199 Cui, Y., Yue, Y., Qian, G. & Chen, B. Luminescent functional metal-organic frameworks. *Chem. Rev.* **112**, 1126-1162, doi:10.1021/cr200101d (2012).

200 Sajid, M. Toxicity of nanoscale metal organic frameworks: a perspective. *Environmental Science and Pollution Research* **23**, 14805-14807, doi:10.1007/s11356-016-7053-y (2016).

201 Jiang, J., Oberdörster, G. & Biswas, P. Characterization of size, surface charge, and agglomeration state of nanoparticle dispersions for toxicological studies. *J. Nanopart. Res.* **11**, 77-89, doi:10.1007/s11051-008-9446-4 (2008).

202 Gao, X., Hai, X., Baigude, H., Guan, W. & Liu, Z. Fabrication of functional hollow microspheres constructed from MOF shells: Promising drug delivery systems with high loading capacity and targeted transport. *Sci Rep* **6**, 37705, doi:10.1038/srep37705 (2016).

203 Yu, B., Ye, G., Chen, J. & Ma, S. Membrane-supported 1D MOF hollow superstructure array prepared by polydopamine-regulated contra-diffusion synthesis for uranium entrapment. *Environ. Pollut.* **253**, 39-48, doi:10.1016/j.envpol.2019.06.114 (2019).

204 Luo, W., Zheng, Y., Yan, J. & Chen, Y. Three-Dimensional Ordered Structures of Metal-Organic Frameworks for Carbon Tetrachloride Sensing and Comparative Study. *ChemistrySelect* **4**, 3936-3939, doi:10.1002/slct.201803706 (2019).

205 Sablowski, J. *et al.* Electrodeposited metal-organic framework films as self-assembled hierarchically superstructured supports for stable omniphobic surface coatings. *Sci Rep* **8**, 15400, doi:10.1038/s41598-018-33542-4 (2018).

206 Wu, Y. N. *et al.* Metal-organic frameworks with a three-dimensional ordered macroporous structure: dynamic photonic materials. *Angew. Chem. Int. Ed. Engl.* **50**, 12518-12522, doi:10.1002/anie.201104597 (2011).

207 Dou, Z. *et al.* Luminescent metal-organic framework films as highly sensitive and fast-response oxygen sensors. *J. Am. Chem. Soc.* **136**, 5527-5530, doi:10.1021/ja411224j (2014).

208 Falcaro, P. *et al.* Centimetre-scale micropore alignment in oriented polycrystalline metal-organic framework films via heteroepitaxial growth. *Nat Mater* **16**, 342-348, doi:10.1038/nmat4815 (2017).

209 Ye, L. *et al.* Highly oriented MOF thin film-based electrocatalytic device for the reduction of CO2 to CO exhibiting high faradaic efficiency. *Journal of Materials Chemistry A* **4**, 15320-15326, doi:10.1039/c6ta04801c (2016).

210 Dong, Y.-J. *et al.* Conformal Coating of Ultrathin Metal-Organic Framework on Semiconductor Electrode for Boosted Photoelectrochemical Water Oxidation. *Applied Catalysis B: Environmental*, doi:10.1016/j.apcatb.2018.05.059 (2018).

211 Otsubo, K. & Kitagawa, H. Metal–organic framework thin films with well-controlled growth directions confirmed by x-ray study. *APL Materials* **2**, 124105, doi:10.1063/1.4899295 (2014).

212 Xu, G., Otsubo, K., Yamada, T., Sakaida, S. & Kitagawa, H. Superprotonic Conductivity in a Highly Oriented Crystalline Metal–Organic Framework Nanofilm. *J. Am. Chem. Soc.* **135**, 7438-7441, doi:10.1021/ja402727d (2013).

213 Peng, Y., Yao, R. & Yang, W. A poly(amidoamine) nanoparticle cross-linked two-dimensional metal-organic framework nanosheet membrane for water purification. *Chem Commun (Camb)* **55**, 3935-3938, doi:10.1039/c9cc00349e (2019).

214 Kang, Z., Fan, L. & Sun, D. Recent advances and challenges of metal–organic framework membranes for gas separation. *Journal of Materials Chemistry A* **5**, 10073-10091, doi:10.1039/c7ta01142c (2017).

215 Wang, N., Mundstock, A., Liu, Y., Huang, A. & Caro, J. Amine-modified Mg-MOF-74/CPO-27-Mg membrane with enhanced H 2 /CO 2 separation. *Chem. Eng. Sci.* **124**, 27-36, doi:10.1016/j.ces.2014.10.037 (2015).

216 Talin, A. A. *et al.* Tunable electrical conductivity in metal-organic framework thin-film devices. *Science* **343**, 66-69, doi:10.1126/science.1246738 (2014).

217 Sun, L., Campbell, M. G. & Dinca, M. Electrically Conductive Porous Metal-Organic Frameworks. *Angew. Chem. Int. Ed. Engl.* **55**, 3566-3579, doi:10.1002/anie.201506219 (2016).

218 Cai, D. *et al.* A Highly Conductive MOF of Graphene Analogue Ni3 (HITP)2 as a Sulfur Host for High-Performance Lithium-Sulfur Batteries. *Small*, e1902605, doi:10.1002/smll.201902605 (2019).

219 Aubrey, M. L. *et al.* Electron delocalization and charge mobility as a function of reduction in a metal-organic framework. *Nat Mater* **17**, 625-632, doi:10.1038/s41563-018-0098-1 (2018).

220 Pathak, A. *et al.* Integration of a (-Cu-S-)n plane in a metal-organic framework affords high electrical conductivity. *Nat Commun* **10**, 1721, doi:10.1038/s41467-019-09682-0 (2019).

221 Sun, L., Miyakai, T., Seki, S. & Dinca, M. Mn2(2,5-disulfhydrylbenzene-1,4-dicarboxylate): a microporous metal-organic framework with infinite (-Mn-S-)infinity chains and high intrinsic charge mobility. *J. Am. Chem. Soc.* **135**, 8185-8188, doi:10.1021/ja4037516 (2013).

222 Pascanu, V. *et al.* Sustainable catalysis: rational Pd loading on MIL-101Cr-NH2 for more efficient and recyclable Suzuki-Miyaura reactions. *Chemistry* **19**, 17483-17493, doi:10.1002/chem.201302621 (2013).

223 Dybtsev, D. N. *et al.* Reversible sorption of hydrogen on the novel hybrid material based on mesoporous chromium(iii) terephthalate with included rhenium clusters. *Russ. Chem. Bull.* **58**, 1623-1626, doi:10.1007/s11172-009-0223-z (2010).

224 Isaeva, V. I. & Kustov, L. M. The application of metal-organic frameworks in catalysis (Review). *Petroleum Chemistry* **50**, 167-180, doi:10.1134/s0965544110030011 (2010).

225 Luan, Y. *et al.* A general post-synthetic modification approach of amino-tagged metal–organic frameworks to access efficient catalysts for the Knoevenagel condensation reaction. *Journal of Materials Chemistry A* **3**, 17320-17331, doi:10.1039/c5ta00816f (2015).

226 Wang, C., Zheng, M. & Lin, W. Asymmetric Catalysis with Chiral Porous Metal–Organic Frameworks: Critical Issues. *The Journal of Physical Chemistry Letters* **2**, 1701-1709, doi:10.1021/jz200492d (2011).

227 Balderas-Xicohténcatl, R., Schlichtenmayer, M. & Hirscher, M. Volumetric Hydrogen Storage Capacity in Metal-Organic Frameworks. *Energy Technology* **6**, 578-582, doi:10.1002/ente.201700636 (2018).

228 Li, B., Wen, H.-M., Zhou, W., Xu, Jeff Q. & Chen, B. Porous Metal-Organic Frameworks: Promising Materials for Methane Storage. *Chem* **1**, 557-580, doi:10.1016/j.chempr.2016.09.009 (2016).

229 de Lange, M. F., Verouden, K. J., Vlugt, T. J., Gascon, J. & Kapteijn, F. Adsorption-Driven Heat Pumps: The Potential of Metal-Organic Frameworks. *Chem. Rev.* **115**, 12205-12250, doi:10.1021/acs.chemrev.5b00059 (2015).

230 Service, R. This new solar-powered device can pull water straight from the desert air. *Science*, doi:10.1126/science.aal1051 (2017).

231 AbdulHalim, R. G. *et al.* A Fine-Tuned Metal-Organic Framework for Autonomous Indoor Moisture Control. *J. Am. Chem. Soc.* **139**, 10715-10722, doi:10.1021/jacs.7b04132 (2017).

2 Characterization Methods

2.1 X-Ray Diffraction

X-ray diffraction is a destruction-free analytical method that is mainly used for the identification and characterization of crystalline materials.

In laboratory setups, X-rays are typically generated in a X-ray tube.[1] By applying a high voltage, electrons are generated at a cathode and directed towards a metallic anode where the electron-anode interaction leads to the emission of emission of electromagnetic waves with wavelengths of X-rays. This spectrum is comprised of mainly two components: Bremsstrahlung and characteristic X-rays.[2] The former is generated by the slowing-down of the electrons due to their interaction with the positively charged metal centers of the anode and leading to a continuous spectrum of X-rays with a minimum wavelength. For the latter the impinging electrons push out anode inner electrons from their shells. The resulting vacancies are filled by outer-shell electrons and the energy difference is emitted in form of characteristic X-rays. After passing a monochromator or filter to select radiation with a desired wavelength, these X-rays are directed on the sample.

In case of a crystalline sample, the interaction of the X-ray electromagnetic waves with the materials' electrons leads to a special form of elastic scattering called diffraction.[3] It is the result of positive and negative interference effects of the outgoing electromagnetic waves and can be interpreted with the Bragg-equation (**Equation 1**) as illustrated in **Figure 2.1**. Here, d corresponds to the interplane distance of the lattice, Θ to the diffraction angle, λ the wavelength and n the diffraction order. Each crystalline substance exhibits a characteristic diffraction pattern with signals centered around the reflection angles that correspond to a path difference that is a multiple integer of the wavelength of the X-ray waves.

Equation 1

$$2d\sin\Theta = n\lambda$$

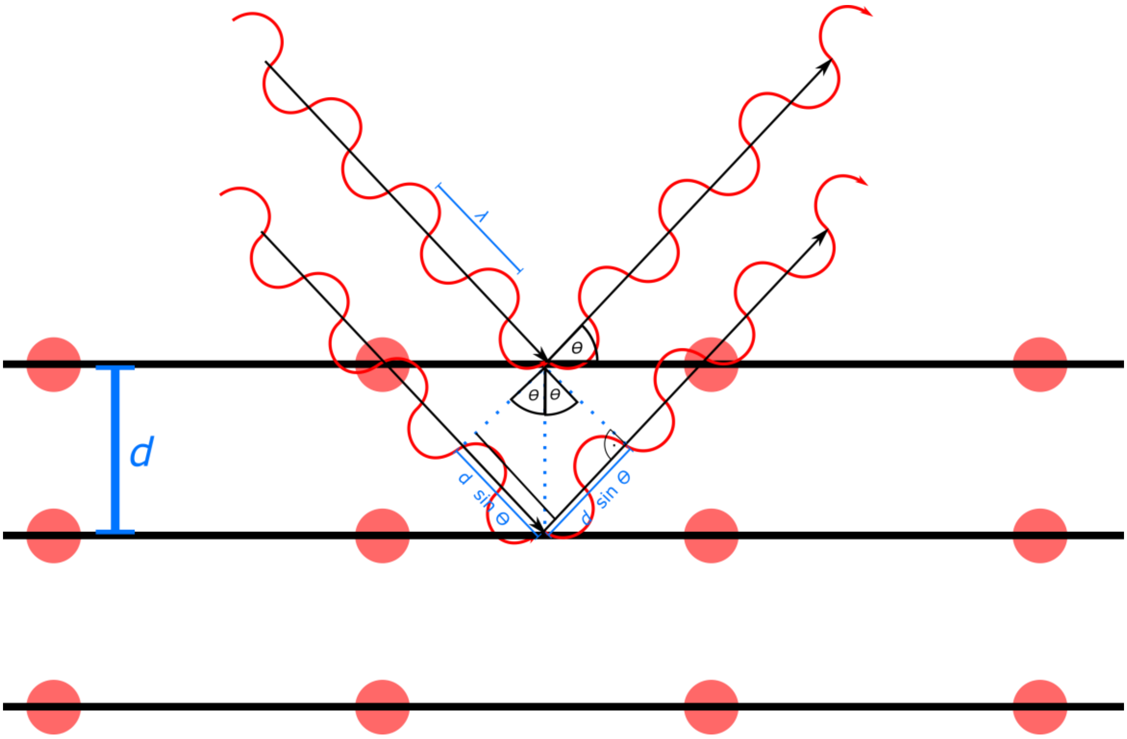

Figure 2.1. Depiction of the geometry of the Bragg conditions

A different way of describing this diffraction condition is given by the Laue equation (**Equation 2**).[4] Here it is necessary to use a reciprocal lattice, in which each point corresponds to a lattice plane in the real space. The diffraction conditions are met when the difference of the incoming wavevector $\vec{k}_{\mathrm{in}}$ and outgoing wavevector $\vec{k}_{\mathrm{out}}$ are equal to a reciprocal lattice vector $\vec{G}$ of a crystal.

Equation 2

$$\overrightarrow{\Delta k} = \vec{k}_{\mathrm{in}} - \vec{k}_{\mathrm{out}} = \vec{G}$$

It is possible to visualize this relationship by using the so-called Ewald construction (**Figure 2.2**). It utilizes the Ewald sphere, a sphere centered on the origin of real space $O_{[000]}$ (the sample) that intersects the origin of reciprocal space $O_{(000)}$ at the radius $1/\lambda$, which is equal to the magnitude of the wavevector of the incident wave $\vec{k}_{\mathrm{in}}$ and the outgoing wave $\vec{k}_{\mathrm{out}}$. Diffraction conditions are met for a lattice plane when its corresponding point in reciprocal space intersects the Ewald sphere.

Powder and dispersion-based X-ray diffraction patterns in this work were measured in Debye-Scherrer Geometry. The crystallites of these materials are randomly aligned, which is why the outgoing diffracted radiation of a single type of lattice plane propagates on the surface of a cone with an aperture of 2Θ instead of a single point. In Debye-Scherrer geometry, the angle at which the incident X-rays are directed onto the sample is fixed. A detector is moving in a circular motion behind the sample, recording the angles at which it intersects the cones. From this resulting diffraction angle it is possible to determine the lattice plane distances d in a crystalline sample.

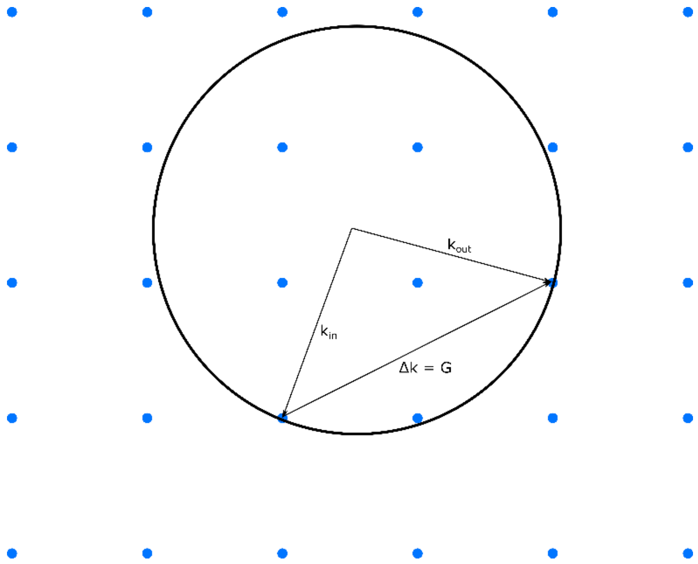

Figure 2.2. Ewald construction to illustrate the Laue conditions. The wave vectors of incident and outgoing X-rays construct a sphere in the reciprocal space. For positive interference the difference of these wave vectors needs to coincide with a wavevector of the reciprocal lattice, therefore the sphere needs to intersect two points of the reciprocal lattice.

If the extent of the crystalline areas in a material is limited to the nanosize this causes a line broadening in the corresponding diffraction pattern in addition to reflection broadening caused by the instrument and strain. This effect is important for nanoparticle characterization as the crystalline areas in such materials are restricted by the particles' size. A simplified relationship between the peak-broadening and the extent of the crystalline areas is given by the Scherrer equation (**Equation 3**).[5]

Equation 3

$$L = \frac{K \cdot \lambda}{\Delta(2\theta) \cdot \cos\theta_0}$$

In this equation, the diameter of a crystalline area L is given by the reflection integral breadth $\Delta(2\theta)$, the X-ray wavelength λ, the angle of the reflection θ and a shape factor K that is depending on the grain size, fit of the reflection and symmetry of the crystal structure.[6]

In case of an even lower crystallinity, such as in glasses, it is still possible to extract structural information via X-ray diffraction with pair distribution function analysis.[7] In this method high-energy X-rays that are typically generated at a synchrotron can be used to scan a large range of the reciprocal space. In addition to Bragg reflections, the data from diffuse scattering, which is usually treated as background noise, are taken into consideration. These data are then converted to a pair distribution function that gives a measure of the probability of atoms being separated by a given interatomic distance and, thus, enables the analysis of short range ordering. In amorphous solids, it can be used to determine the distribution of atomic distances in a solid. If certain atom distances are more abundant this indicates a local ordering of the structure. Similar to the Scherrer equation, this can give insight to the extent of crystalline areas in a sample.

Experiments in this thesis where performed on machines that are working in a variation of the Debye-Scherrer geometry. X-ray diffraction experiments were performed on a *STOE Transmissions-Diffraktometer System STADI P* with Ge(111) primary monochromator and Cu-$K_{\alpha1}$-radiation in transmission geometry. In case of powder measurements, dried samples were fixated between two polymer foils. In case of dispersions measurements, the particle dispersions were sealed in glass capillary tubes. For Pair Distribution Function Analysis, experiments were performed at the synchrotron I15-1 beamline at the Diamond Light Source in the UK that was operating with a wavelength of λ = 0.161669 Å at 72 keV. For measurements, the samples were vacuum-dried for 2 h at room temperature and finely ground before packing into sealed 1.17 mm (inner) diameter borosilicate capillaries.

2.2 Nitrogen sorption

One of the defining features of MOFs is given by their porosity.[8] The standard procedure for characterizing this property is based on nitrogen sorption.[9] From the amount of gas adsorbed to a materials surface, conclusions on its surface area and pore size distribution can be drawn. In this section, the fundamentals of this approach as recently defined by IUPAC[10] are elaborated and the terms that are used for MOF sorption experiments explained.

Generally, MOF sorption experiments are based on the adsorptive gas nitrogen that is interacting with the surface of the adsorbent sample. This process is based on physisorption and relies on weak interactions that are mainly caused by van der Waals forces. In case of MOF nanoparticle samples, two factors that contribute to their surface area have to be differentiated: On the one hand there is the surface at the interface of a MOF nanoparticle and its surrounding medium which is called external surface. On the other hand MOFs possess an internal surface caused by their porous coordination network. Decreasing the particle size leads to an exponential increase of the external surface in relation to its volume, and therefore particle-mass[11]. Depending on their pore size distribution, porous materials are assigned according to the IUPAC definitions presented in Table 2.1.

Table 2.1. Categorization of porous materials depending on their pore sizes.

Classification	**Pore Size**
Microporous	<2 nm
Mesoporous	>2 – 50 nm
Macroporous	>50 nm

In typical MOF sorption experiments a defined sample mass is stored in an evacuated chamber and subjected to small doses of nitrogen gas at low temperatures (77 K). The amount of gas adsorbed to the surface is most often determined in volumetric measurements. The adsorption of nitrogen to the MOF surface causes deviations in the pressure of the calibrated chamber which can be used to calculate the amount of gas adsorbed to the material's surface.

The data from these experiments are usually depicted in sorption isotherms, where the amount of adsorbate bound to the material surface is related to the ratio of the chamber's equilibrium pressure and the respective saturation vapor pressure of the nitrogen gas. Depending on their shape, sorption isotherms are classified in 8 different categories according to IUPAC.[10]

Type I isotherms result from microporous materials with almost no external surface area. Therefore the sorption isotherm becomes quickly nearly saturated after its micropore volume is filled at low pressures. Depending on the pore diameter, strong adsorbent/adsorptive interactions in small micropores with a diameter of <1 nm lead to Type I(a) isotherms while larger micropores lead to Type I(b) isotherms.

Type II isotherms result from non-porous and macroporous samples. As these materials lack noticeable surface from pores, their sorption behavior is dominated by monolayer/multilayer adsorption on their external surface. In **Figure 2.3** the completion of monolayer formation followed by multilayer adsorption is marked at point **B**, at which the curvature of the graph transitions into a linear slope.

Type III isotherms originate from non-porous materials that feature weak adsorbent/adsorbate interactions. Due to this unsubstantial interaction, adsorbed molecules do not exhibit monolayer formation. Instead, they are adsorbed in form of clusters to preferential sites on the material surface.

Type IV isotherms result from mesoporous materials. Similar to Type II isotherms, at low pressures, gas molecules are first adsorbed in form of a monolayer. After this monolayer formation is complete, increasing the pressure further leads to the condensation of adsorptive in the pores of the sample resulting in a steep increase of uptake by the sample. Depending on the desorption of the adsorbate inside the pores, two isotherm types are referred to: If the pores are wider than a critical diameter (about 4 nm), this results in a hysteresis loop and the material is to be classified as Type IVa. In case of smaller mesopores and certain pore geometries no hysteresis loop can be monitored, resulting in Type IVb isotherms.

Type V isotherms result from mesoporous materials that feature weak adsorbent/adsorbate interactions. Similar to a type III isotherm, at lower pressures, gas molecules adsorbed to the materials surface are clustered without monolayer formation. Increasing pressure leads to the condensation of adsorptive in the pores, similar to the behavior of Type IVa isotherms.

Type VI isotherms depict layer-by-layer adsorption. In this case, the material features a uniform nonporous surface. Molecules that are adsorbed to this surface form one completed layer after another, represented by each step in the graph.

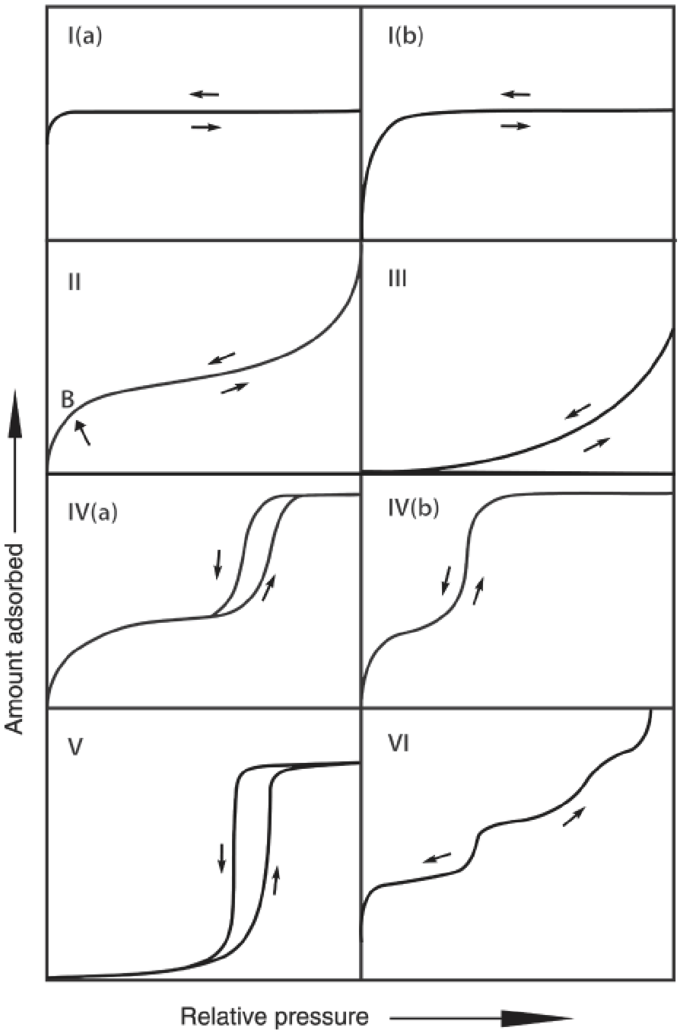

Figure 2.3. Sorption isotherm classification according to IUPAC.[10]

The total surface area of a MOF sample is usually determined with the Brunauer-Emmett-Teller (BET) method.[12] The theory of this method is based on an expansion of the Langmuir adsorption theory. In the Langmuir theory[13], physisorption on an adsorbent is described with the formation of a monolayer that is resulting from an equilibrium of adsorbed and desorbed gas molecules on a surface. The BET theory expands on this model by assuming additional multilayer adsorption where each consecutive layer follows a Langmuir type adsorption. For each adsorbate layer on top of the initial monolayer the theory assumes an adsorption energy equal to the liquefaction energy.

Using the BET method, sorption data are plotted according to Equation 4, where n_m is the material's monolayer capacity, n is the amount of gas adsorbed at the relative pressure $p/p°$ and C is an experimentally determined parameter that is dependent on the monolayer adsorption energy. In this equation experimentally determined data usually exhibit a linear dependency for low relative pressures at $0.05 < p/p° < 0.30$.

Equation 4

$$\frac{\frac{p}{p^{\circ}}}{n(1-\frac{p}{p^{\circ}})} = \frac{1}{n_m C} + \frac{C-1}{n_m C}(\frac{p}{p^{\circ}})$$

The linear form of the BET equation can be used to determine the monolayer capacity n_m in a sorption experiment. It is then possible to calculate a BET area a_s by approximating the molecular cross sectional area σ_m and mass m and the Avogadro Constant L.

Equation 5

$$a_s(BET) = n_m \cdot L \cdot \sigma_m/m$$

Although the BET method is established as a standard procedure for comparing the surface areas of MOFs, the results for these mostly microporous materials have to be treated carefully.[14] The BET method was initially developed for monolayer/multilayer adsorption on open surfaces and does not consider micropore filling. BET surface areas additionally depend on the type of gas-molecules used experimentally and the pressure ranges that are used for evaluation. Quality criteria such as a positive C constant and selecting appropriate $p/p°$ ranges can improve the validity of these results. Nevertheless, the BET area of a MOF has to be rather seen as a characteristic number than an actual accessible surface area.[15]

To evaluate pore size distributions in MOFs, computational methods such as Density Functional Theory (DFT) and Monte Carlo simulations have been established as standard methods in commercially available software. These methods are based on statistical mechanics and can describe the adsorbate distribution in pores. Non-local density functional theory (NLDFT) methods include standardized models that consider the shape and size of pores and different adsorbents. Quenched solid density functional theory (QSDFT) methods further allow the consideration of a heterogeneous surface as it is present in MOFs.[16]

Nitrogen sorption experiments in this thesis have been performed on an Autosorb-1 instrument (*Quantachrome*). Prior to the experiments, all samples were degassed for 24 h at 120 C and $1.3 \cdot 10^{-2}$ mbar.

2.3 Thermogravimetric Analysis

Thermogravimetric analysis (TGA) is a destruction based method that can be used to assess a material's thermal stability and composition.[17] In an experiment, a small amount of sample (~5 mg) is put in a thermobalance and heated in a flow of gas. Depending on the temperature, a sample can exhibit desorption of solvent molecules or undergo phase transitions and chemical reactions. These processes can be examined either by monitoring changes in the sample mass alone or in combination with the energy transfer during heating. For the latter, TGA is combined with differential scanning calorimetry (DSC). In this method, the heat required to increase the sample temperature is compared to an inert reference material, which reveals if a process is endothermic or exothermic.

All thermogravimetric experiments in this work were done on a STA 449 C Jupiter (*Netzsch*) instrument under synthetic air with a flow rate of 25 mL/min. employing a heating rate of 10 °C/min up to 900 °C.

2.4 Electron Microscopy

Electron microscopy is an indispensable tool in MOF nanoparticle characterization that enables morphological analysis of dried samples at the nanoscale.[18,19] In classical light microscopy this is not possible as the limit of spatial resolution *d* is at around 200 nm as given by the Abbe limit (**Equation 6**) with the wavelength λ, the refractive index *n* of the medium between lens and sample and the half aperture angle α.[20]

Equation 6

$$d = 0.5 \frac{\lambda}{n \sin \alpha}$$

In electron microscopy, λ of the electrons is defined by the de Broglie wavelength (**Equation 7**) of the incident electrons with Planck's constant *h*, the electron mass m_e, and electron velocity *v*.

Equation 7 $$\lambda = \frac{h}{\mathrm{m_e} \cdot v}$$

This makes the obtainable resolution dependent on the speed of the electrons (**Equation 8**) that are used during the experiment, which is linked to their acceleration voltage U with q being the electron charge.

Equation 8 $$v = \sqrt{2U\frac{q}{m}}$$

Depending on the mode of operation and on the instrument, electron microscopy allows for resolution that can be even better than the single-nanometer range. One of the typical prerequisites for electron microscopy is operation at high or ultrahigh vacuum, although recent developments in operando microscopy have broken this barrier. Electron microscopy can additionally be coupled with different analysis methods such as energy-dispersive X-ray spectroscopy (EDX) and electron diffraction. In this thesis, both scanning electron microscopy (SEM) and transmission electron microscopy (TEM) were used for nanoparticle characterization.

2.4.1 Scanning Electron Microscopy

SEM relies on electrons that are returning from the sample surface and are recorded by a rastering (scanning) detector. In SEM, electrons that are directed towards a sample feature energies of 0.1 keV to 30 keV.[21]

If electrons are impinging on the surface of a sample they cause various processes to happen. Backscattered electrons are the product of (multiple) elastic scattering events on the sample and feature an energy distribution up to the energy of the impinging electrons. Inelastic scattering leads to the transfer of energy from the electron beam to the sample. If the impinging electron beam pushes out an electron from the inner shell of sample, the leaving electrons are called secondary electrons. They feature energies below 50 eV. When the resulting vacancy is then filled by a higher energy sample electron, the energy surplus is ejected from the sample. This can either be in form of characteristic X-rays that can be analyzed in EDX to determine the elemental composition of a sample. Alternatively, the energy surplus excites another electron that then leaves the sample and is called Auger electron. Auger electrons feature energies of up to about 2 keV and are used in Auger electron spectroscopy. Secondary electrons can be detected up to about 10 nm into the sample surface and can be used for image generation. SEM images in this thesis are generated from backscattered electrons that can penetrate a sample more deeply depending on the energy of the impinging electrons and the atomic number of the elements in the sample.[22]

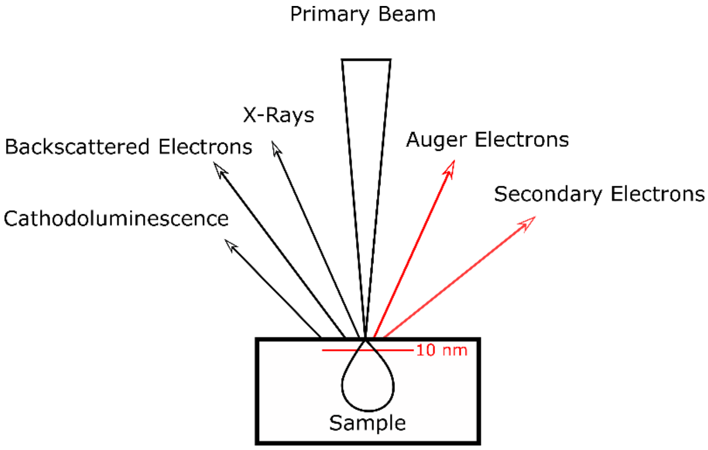

Figure 2.4. Schematic depiction of the different processes that electrons undergo during their interaction with a sample surface.*[23]*

In this thesis electron microscopy was performed on a *Helios G3 UC* (*FEI*). All samples were prepared by drying particle dispersions on carbon pads that are situated on aluminum sample holders. If not stated otherwise the microscope was operated at 3 kV using a through-lens detector.

2.4.2 Transmission Electron Microscopy

In TEM, electrons that are passing through a sample are evaluated. The measurement relies on high energy electrons between 60 keV and 300 keV that are directed onto a thin sample with a thickness of less than a few hundred nanometers.[24] Electrons that pass the sample undergo different processes: If they do not interact with the sample they exit the material in extension of the primary beam. Otherwise they participate in elastic and inelastic scattering processes. In case of inelastic scattering, the energy transfer from beam to sample electrons can be evaluated spectroscopically in electron energy loss spectroscopy (EELS). In case of elastic scattering, a diffraction pattern is resulting that can either be evaluated directly for structural information similar to X-ray diffraction, or be used for further image generation. The contrast in these images depends amongst other things on sample thickness, atomic number, the density of the elements in the sample, and the angle of the diffracted electrons that are used with respect to the optical axis (bright field vs. dark field).

TEM samples were prepared by drying nanoparticle dispersions of on a carbon-coated copper grid. Measurements were performed on a *Titan Themis* (*FEI*) operated at 300 kV.

2.5 Dynamic Light Scattering

Dynamic light scatttering (DLS) is a non-destructive method for size and colloidal-stability determination of nanoparticles. Measurements with this method are performed in dispersions making them closely related to actual, mostly solvent-based, nanoparticle applications. The particle size resulting from DLS measurements is called hydrodynamic diameter. This hydrodynamic diameter is based on the particle size of a hard theoretical sphere that would exhibit the same diffusion properties as the nanoparticle sample in the respective medium. DLS measurements therefore cannot be used to derive exact particle morphologies.

Experimentally, the size of nanoparticles is determined by subjecting a dispersion of particles to a laser beam. The incident beam is scattered by the nanoparticle dispersion and the outgoing light is recorded at a certain angle using a detector. Due to the Brownian motion of the particles, the corresponding pattern is constantly changing.[25] The angular scattering data are evaluated using a time-based autocorrelation fit (**Equation 9**) that compares the signal at a point t to the signal at the points ($t + \tau$) with τ being in the range of nanoseconds.[26] With the drop-off of this function a diffusion-coefficient for all particles can be calculated.

Equation 9

$$g^{(2)}(\tau) = \frac{\langle I(t)I(t+\ \tau\rangle}{\langle I(t)^2\rangle}$$

In more detail, first the intensity-intensity time autocorrelation function is transformed into a field-field time autocorrelation function that decays exponentially. In case of a monodisperse particle dispersion, this drop-off can be described with a single exponential decay function (**Equation 10**) with the delay time τ and the decay rate Γ that is described by the scattering wave vector q and the diffusion coefficient D (**Equation 11**).

Equation 10

$$g^{(1)}(\tau) = e^{-\Gamma\tau}$$

Equation 11

$$\Gamma = Dq^2$$

In polydisperse samples, the exponential decay of the field-field autocorrelation function can be interpreted with the cumulant method. In this method the mean exponential decay of the field-field autocorrelation function is fitted in a Tailor Expansion (**Equation 12**). It also gives the possibility to quantify the polydispersity of the sample in form of the polydispersity index *PDI* (**Equation 13**) that is defined by the second term of this Tailor Expansion.[26]

Equation 12

$$g^{(1)}(\tau) = e^{-\bar{\Gamma}\tau}(1 + \frac{\mu_2}{2!}\tau^2 - \frac{\mu_3}{3!}\tau^2 + \cdots)$$

Equation 13

$$PDI = \frac{\mu_2}{\Gamma^2}$$

The resulting diffusion coefficient can then be assigned to a hydrodynamic particle size using the Stokes-Einstein equation (**Equation 14**) with η being the viscosity of the medium, *D* being the diffusion coefficient of the particles, the Boltzmann constant k_B and the absolute Temperature *T*.[25]

Equation 14

$$D = \frac{k_B \cdot T}{6\pi \cdot \eta \cdot r}$$

In this thesis, DLS measurements were performed on sample dispersions in cuvettes using a Zetasizer Nano Series (Nano-ZS, *Malvern*) that includes a 4 mW He-Ne laser operating at 633 nm and an avalanche photodetector.

2.6 Zeta Potential Measurements

In solutions/dispersions, the behavior of particles is dominated greatly by their surface charge. It influences properties such as particle-protein interactions, colloidal stability and cellular uptake. According to the Debye-Hückel[27] and Stern models[28] a colloid particle in solution that exhibits a negative surface charge is surrounded by a tight layer of oppositely charged ions called Stern layer. Moving further away from the particle surface, a diffuse layer of counter-ions surrounds the particle. The ζ-Potential is the electric potential in the interfacial double layer (DL) at the location of the slipping plane relative to a point in the bulk fluid away from the interface (**Figure 2.5**), and indirectly a measure of the strength at which the counter-ions are bound to the particle.[29]

Experimentally, the ζ-Potential of particles in a sample is determined from their electrophoretic mobility. In these measurements an electric field that is applied to the particle dispersion causes the particles to move towards the electrodes. As the particles move, the tightly bound counter-ion layer in the Stern layer move with the particles as well. At a certain distance in the diffuse counter-ion layer this tied movement breaks off and ions will move to the opposite electrode. This generates a slipping plane at the place of the charge-separation. The particle potential at this slipping plane is called ζ-Potential [29]

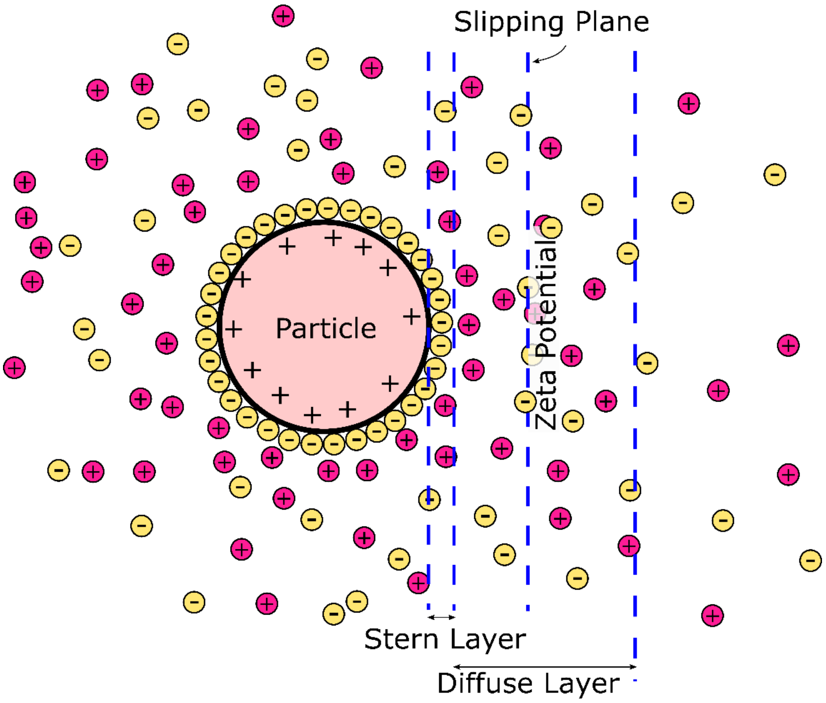

Figure 2.5. Schematic depiction of a positively charged nanoparticle with the ion-arrangement in the surrounding medium

In an experimental setup, the particle velocity, also called electrophoretic mobility can be determined in a variant of Laser Doppler Velocimetry. In this measurement method a laser is directed towards the moving particles. The scattered light of this laser exhibits a phase shift that is proportional to the speed of the nanoparticles. Zeta-potential is determined via the Henry equation (**Equation 15**) from the electrophoretic mobility U_e of the particles, using the dielectric constant ε and dynamic viscosity η of the surrounding medium, and depending on particle size and electrolyte concentrations either the Hückel (*f*(*ka*) = 1) or Smoluchowksi (*f(ka)* = 1.5) approximations are used.[25]

Equation 15

$$U_e = \frac{2\zeta \cdot \varepsilon \cdot f(ka)}{3\eta}$$

Zeta-Potential measurements are usually performed in conjunction with a pH-Titration, as protons and hydroxide ions will attach to the surface of particles and their zeta-potential is therefore strongly pH dependent. Generally, particles need to exhibit a zeta-potential of |30| mV or higher to form colloidally stable suspensions based on electrostatic repulsion.

During this thesis, zeta-potential measurements were performed on diluted samples in cuvettes using a *Zetasizer Nano Series* (Nano-ZS, *Malvern*) that includes a 4 mW He-Ne laser operating at 633 nm and an avalanche photodetector. In case of pH titration, an *MPT-2 Multipurpose Titrator* (Malvern) was additionally connected to the device.

2.7 Vibrational Spectroscopy

Infrared and Raman spectroscopy are label- and destruction-free methods that can be used for the identification of molecules.[30] IR measurements are based on the absorption of mid-infrared light in the range of 4000-400 cm^{-1} (2.5-25 µm wavelength), which causes molecules to be excited into specific vibrational and rotational modes. From 4000 to 1800 cm^{-1}, functional groups such as the CH- or OH-groups can be identified by distinctive absorption bands of their stretching modes. The range of 1800-400 cm^{-1} is called fingerprint region, as it is often characteristic for each molecule and can serve as a molecular fingerprint.

Every IR absorption signal corresponds to either a specific, quantized vibrational or a combined vibrational-rotational transition of the sample. The energy necessary for exciting a vibrational mode depends on the bond strength and the mass of the moving atoms, whereas for the rotation it is depending on the molecule’s moment of inertia and is strongly influenced by its state of matter. These principles allow for the identification of a sample by collecting a spectrum.

The vibrational modes can be subdivided into valence vibrations, where bonds are periodically elongating and contracting and deformation vibrations, where a change in the bond angle occurs. For vibrational modes to be IR active they need to cause a changing dipole moment, which means a vibration cannot be symmetrical to the symmetry center of the molecule (vibrational IR selection rule). Vibrations that are not visible in the IR can often times be seen in Raman spectra.

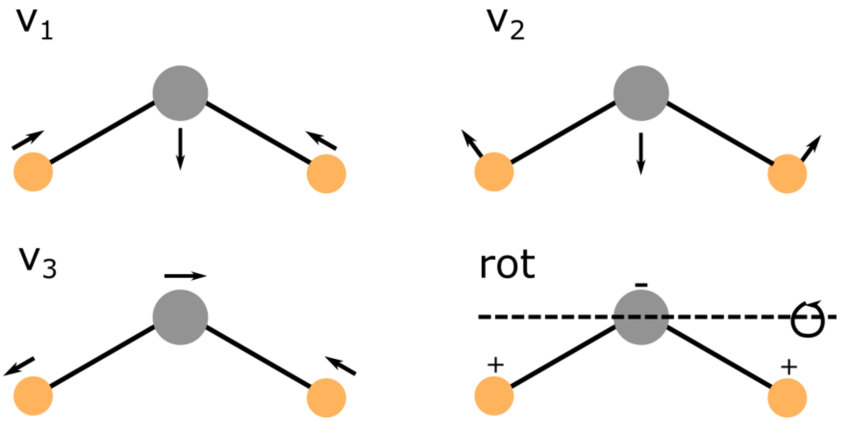

Figure 2.6. In a non-linear molecule consisting of three atoms, such as water, three vibrational modes are possible: vibrational mode v_1 shows symmetrical valence vibrations (IR-active), v_2 depicts the only vibrational deformation mode of the molecule (IR-active), and v_3 depicts valence vibrations that are anti-symmetric (IR-active). In case of a 'deformation vibration' perpendicular to the plane of the molecule, this results in a rotation.[31]

2.7.1 Raman Spectroscopy

Raman spectroscopy is complementary to IR spectroscopy, and relies on monochromatic light that is focused on a sample.[32] While the majority of this light is either passing through the sample or is elastically scattered (*Rayleigh* scattering), a small fraction of the incident light is inelastically scattered. During this scattering process, energy is transferred between the incident photon and the interacting molecule. This scattered light after the interaction is then examined for its shift in frequency.

Similar to IR absorption, Raman scattering excites (or depletes) vibrational and vibrational/rotational modes of a molecule. During the scattering process, a molecule is put into an excited virtual energy state, from which it instantly transits to a vibrational state. In case the molecule was in the vibrational ground state before the inelastic scattering, the emitted photon is shifted to lower energy (red-shift). In analogy to fluorescence, this process (leading to red-shifted inelastically scattered photons) is also called a Stokes process. In case the molecule was in a vibrationally excited state before the inelastic scattering, the process forces the molecule back to the vibrational ground state and photons with higher energy (blue-shift) are emitted. This process is termed an anti-Stokes process.

Analogous to IR spectroscopy, Raman spectroscopy can be employed to characterize and identify unknown substances. Both spectral regions (Stokes and anti-Stokes region) can be used for spectroscopy, although the anti-Stokes scattering shows lower intensity due to a less frequent occupancy of vibrationally excited states in the beginning, which follow a Boltzmann distribution.

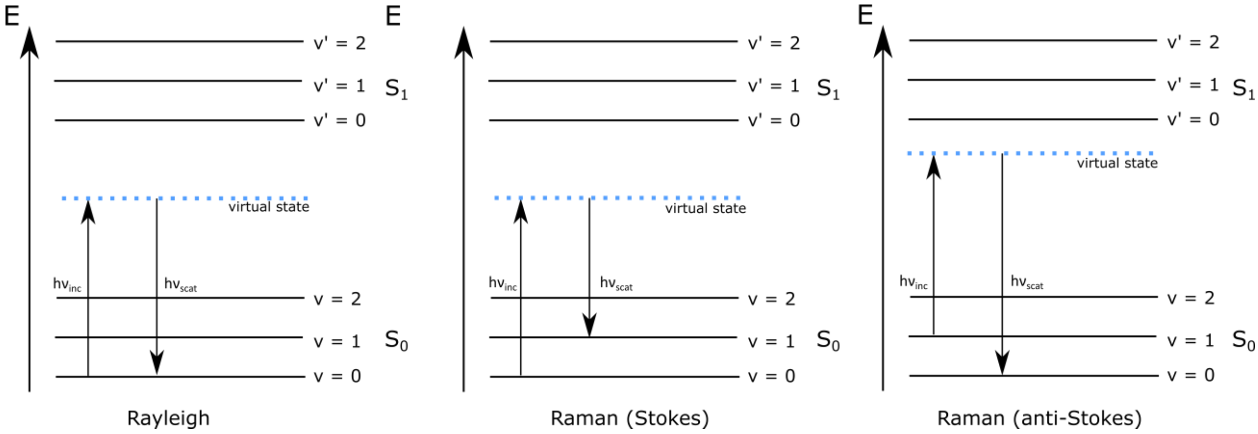

Figure 2.7. Comparison of the energetic transitions during Rayleigh and Raman (Stokes and anti-Stokes) scattering[33]

For a vibration to be visible in a Raman spectrum the vibration needs to induce a change in the molecular polarizability. As this can also happen for vibrations that are symmetrical to the symmetry center of the molecules, Raman spectroscopy is often used complementary to IR spectroscopy. In Raman spectra the wavenumber (1/λ) difference of the emitted light compared to the incident light is plotted versus its intensity.

2.8 Fluorescence Spectroscopy

Fluorescence spectroscopy is a non-destructive analytical method in which the optical emission spectrum from fluorophores is monitored. The fluorescent samples can be molecules such as aromatic hydrocarbons, proteins but also atoms such as the lanthanides.[34]

In a fluorescence experiment, light generated by a broad band source such as a Xenon arc lamp is typically spectrally selected by a monochromator and focused onto a sample. This process causes the sample molecules to transition from their electronic ground state S_0 to an electronic excited state S_1. The relaxation of the electronically excited molecules back to their ground state can lead to the emission of light. The wavelength of this emitted light experiences a red-shift (also called Stokes-shift) due to vibrational relaxation. These processes can schematically be visualized in a Jablonski diagram[35] (**Figure 2.8**).

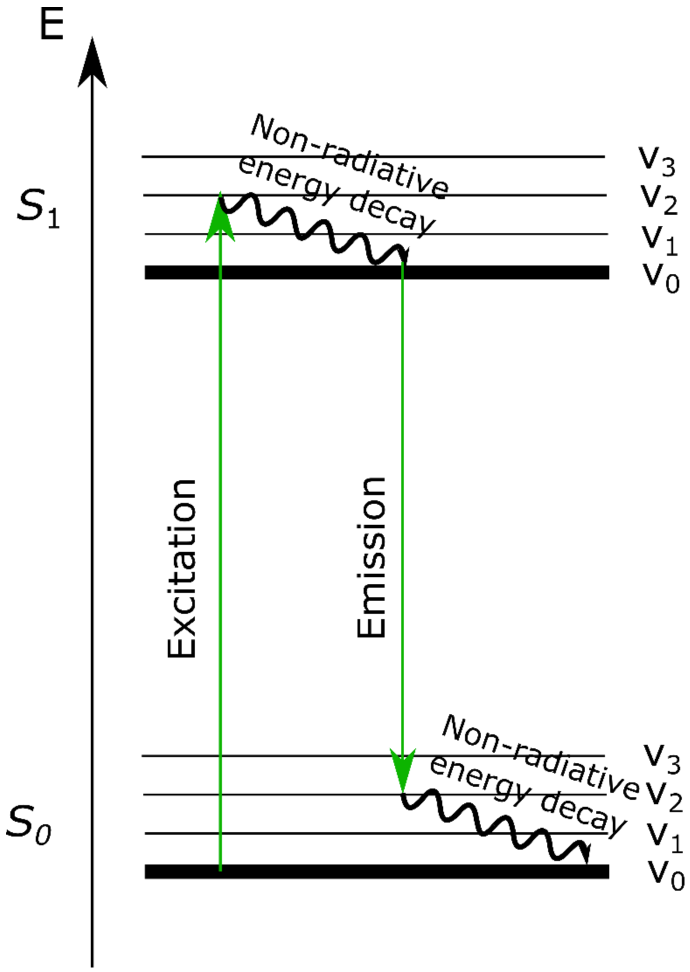

Figure 2.8. Jablonski diagram depicting the processes most important for fluorescence.

In a typical fluoro-spectrometer setup light that is emitted from a sample is recorded perpendicular to the incident light. A monochromator between the sample and a detecting photomultiplier tube allows the recording of specific emission wavelengths.[1]

In this work fluorescence experiments were conducted on a PTI spectrometer that is equipped with a xenon short arc lamp (UXL-75XE USHIO) and a photomultiplier detection system (model 810/814).

2.9 Confocal Microscopy

Confocal microscopy is a non-destructive technique that can be used for imaging and reconstruction of three-dimensional micrometer-sized objects such as microparticles and cells. A detailed description of the microscopy techniques that were performed together with fluorescence and Raman spectroscopy is presented in the respective result chapters. This section is used to describe the basic principles of confocal microscopy.

In a confocal microscope, radiation that is emitted from a light source is passing a pinhole and is then focused via an objective to a small volume in a sample.[36] Light exiting the sample via fluorescence or reflection passes the objective again and, after passing a beamsplitter, is focused on a pinhole aperture that is situated in the intermediate image plane. Only light that is in focus in the sample is also in focus in the intermediate image plane and can therefore pass this aperture. As only light that is in focus on the sample and

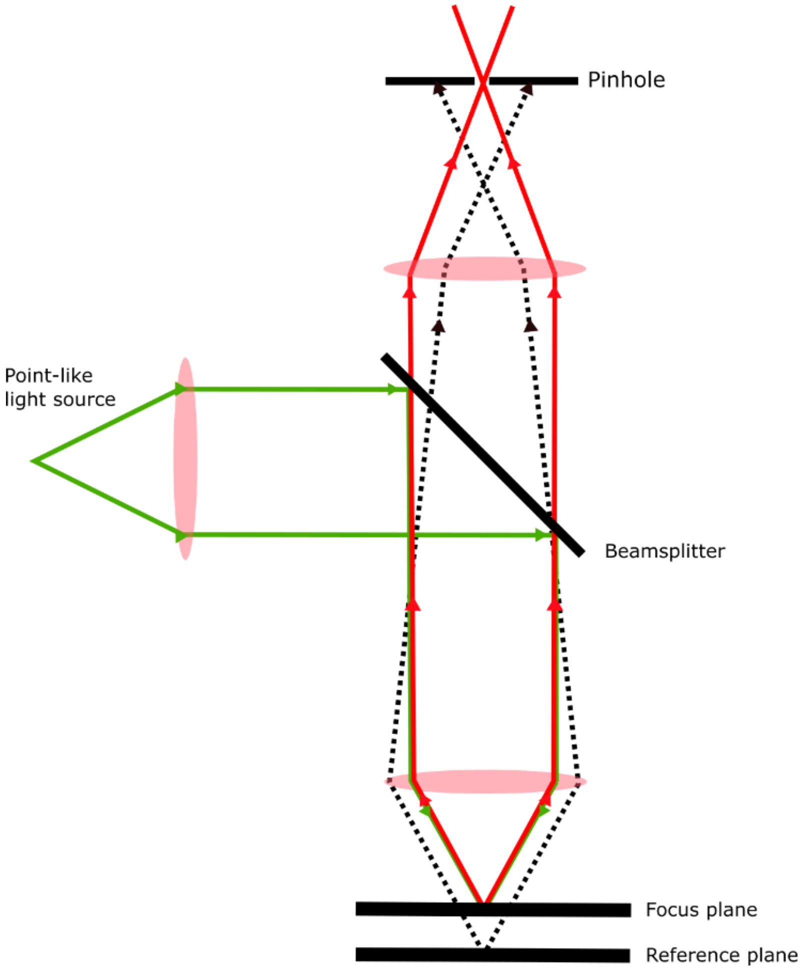

Figure 2.9. Optical pathway of a confocal microscope with incoming light (green), emitted light in focus (red) and emitted light out of focus (black).[37]

that is in focus in the intermediate plane is used for image generation, this allows for selectively imaging small volumes in a sample at high resolution (**Figure 2.9**). Light from other planes that would compromise the resolution of the image is cut off by the pinhole. In a confocal microscope the whole sample is therefore not depicted at once. For image generation, the illumination spot is rastered over the sample and the image is reconstructed via a computer. In a modern version of confocal microscopes, the pinholes selecting the light to and from the sample are replaced with a variant of a Nipkow disc. This spinning disc features multiple concentrically arranged pinholes, allowing to rapidly scan multiple spots on a sample simultaneously and enabling image generation fast enough to view images in real time. Using confocal microscopy, lateral resolution d_R is roughly limited by the Rayleigh criterion (**Equation 16**) with the wavelength λ and the numerical aperture of the objective NA. This corresponds to the product of the refractive index *n* of the medium in which the lense is working and the sinus of the half-angle of thef of its opening angle *Θ (***Equation 17**

Equation 16
$$d_\mathrm{R} = \frac{\lambda}{1.64\ \cdot\ NA}$$

Equation 17
$$NA = n\ \cdot \sin\theta$$

2.10 Magnetic Resonance Imaging

MOF nano and microparticles in this thesis were analyzed for their visibility in Magnetic Resonance Imaging (MRI). MRI is a standard imaging method (free of ionizing radiation) used in medicine for non-destructive analysis of tissue in a patient. In this thesis, the influence of MOF particles on the image contrast was examined.

The contrast in an MRI image strongly depends on the distribution of water in tissue as the water protons are the main source of signal in clinical MRI. The hydrogen nuclei of these water molecules exhibit a nuclear spin $\vec{I}$ of 1/2 and thus concomitantly feature a magnetic dipole moment $\vec{\mu}$ that is proportional to their gyromagnetic ratio γ (**Equation 18**).[1]

Equation 18 $$\vec{\mu} = \gamma \vec{I}$$

The magnetic dipole moment $\vec{\mu}$ is quantized along with its orthogonal components. The component of $\vec{\mu}$ along the z-axis is defined by the magnetic quantum number m and the reduced Planck constant ħ (**Equation 19**).

Equation 19 $$\mu_z = \gamma I_z = \gamma \hbar m$$

The magnetic quantum number can assume two ($2I + 1 = 2$) values for hydrogen nuclei ($I = ½$) resulting in two possible orientations that are energetically degenerate. If a magnetic field B_0 is applied along z, these states are split and feature an energy difference ΔE (**Equation *20***). This can be pictured as the magnetic moments aligning with or against the external magnetic field.

Equation 20 $$\Delta E = \gamma \hbar B_0$$

In a sample, this results in an overall net magnetization of the nuclei corresponding to the lower energy state, in which the magnetic moments precess around the external magnetic field in phase. The frequency υ_L of this precession is called Larmor frequency (**Equation 21**).

Equation 21 $$\omega_L = 2\, \pi\, v_L = \gamma B_0$$

In an MRI system a sample is subjected to a magnetic field leading to the aforementioned energy states and alignment of magnetic moments of the water hydrogen nuclei. Using a short radiofrequency pulse, this equilibrium is then disturbed. The following realignment of the sample magnetization along the external field is called longitudinal relaxation. This exponential process is described by the longitudinal relaxation time T_1). The exponential decay of the phase of the precessing spins is called transverse relaxation (described by relaxation time T_2).[38] Both of these relaxation times of the water molecules' protons are influenced by the chemical environment in particular tissues. Due to this and the varying water content in different types of tissue, different signal intensities are generated depending on tissue type. Transforming these different signal intensities to correspondingly different gray values in an image results in contrast between tissues. It is common practice to use paramagnetic additives, called contrast agents, to further influence the contrast of the generated images. For a clinically used contrast agent in a solution, the inverse of these relaxation times, also called relaxation rates $R_i = 1/T_i$, $i = 1,2$, typically increases linearly with increasing contrast agent concentration. The slope of this linear increase between contrast agent concentration and relaxation rate is called relaxivity r_i ($i = 1,2$) . Relaxivity is commonly used as a measure of the contrast agent effectiveness in MRI. As a rule of thumb MRI contrast agents should exhibit high relaxivities such that small additions of contrast agents or particles can cause large contrast enhancing effects. [39]

MRI experiments in this thesis were performed using a clinical 1.5T MRI system (Siemens MAGNETOM Aera, Siemens Healthineers, Erlangen, Germany). For imaging, samples in 2 mL Eppendorf tubes were submerged in a water bath and positioned in a standard head coil for imaging. During the experiments, saturation-recovery and echo times were varied to determine T_1 and T_2 relaxation times of the samples, respectively. In this process cross-sectional images of the sample that correspond to the respective saturation and echo times were evaluated for their intensity. The squared intensity data were fitted using a squared exponential function to yield T_1 and T_2 relaxation times along with relaxation rates.[40]

2.11 Nanomechanical Mass Correlation Spectroscopy

The density of a macroscopic material is defined as the ratio of its mass and volume. For porous nanoparticles such as MOFs this definition is not as straightforward: The size of a nanoparticle may vary depending on whether the measurement was performed on dried particles or in liquid medium and may be influenced by surface attachment of molecules and ions such as in the stern layer. The porous nature of MOFs additionally poses the question of whether solvent molecules within the pores of the structure should be considered towards particle mass and therefore influence particle density. In the experiments of this thesis, density determination of MOF nanoparticles was solely based on particle mass via nanomechanichal mass correlation spectroscopy.[41]

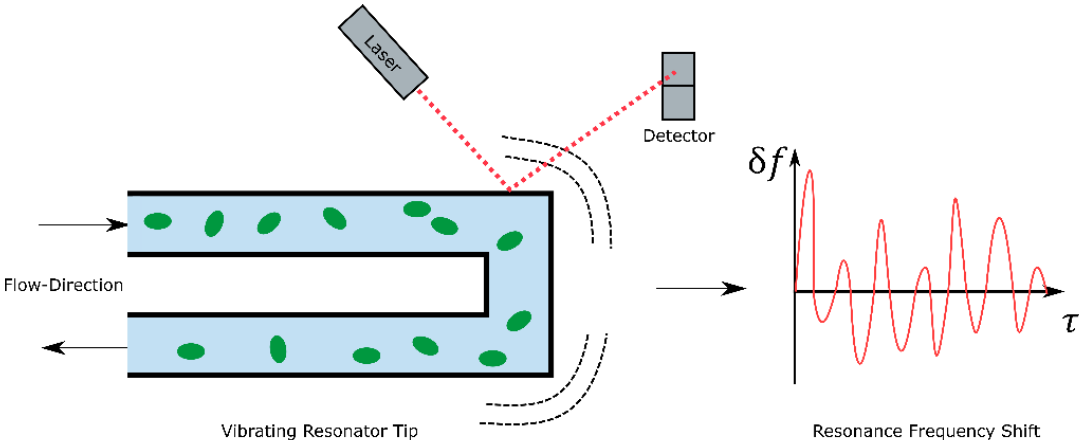

Figure 2.10. Schematic of the measurement principle: A nanoparticle dispersion is flowing through a channel in a hollow vibrating tip. Using a detector, the resonance frequency of this tip is monitored. The buoyant mass of the particles changes this frequency, which is used for further data evaluation.

In such a microfluidic setup (**Figure 2.10**), a nanoparticle suspension moves through the channels of a vibrating hollow tip. The particles traversing this tip cause fluctuations in its resonance frequency that are proportional to the buoyant mass of the particles. For nanoparticle analysis these resonance frequency fluctuations are then evaluated using a time-based autocorrelation function $C(\tau)$ (**Equation 22**), where δf corresponds to a high-pass filtered signal of the frequency change.

Equation 22
$$C(\tau) = \langle \delta f(t) \delta f(t + \tau) \rangle$$

These measurements are then repeated under variation of the solvent-system used for dispersing the particles. Particle density is then determined by plotting the respective autocorrelation amplitudes that are dependent on the mass and concentration of the particles versus the density of the solvents. Subsequent fitting of these data with a parabola results in a zero minimum, where the resonance frequency of the tip does not change. At this point, the particle density is equal to the solvent density.

The setup used in the experiments of this work consisted of two syringe pumps that were varying the composition of solvents flowing through the channel of a microfluidic chip containing a micro-resonator tip containing an embedded channel with a cross-section of 3 x 8 µm^2. Frequency changes were detected with an optical lever consisting of a laser and a split photodiode.

References

1 Atkins, P. W. & de Paula, J. *Physikalische Chemie*. 4. edn, (Wiley-VCH, 2006).

2 Cervantes, G. A. *Technical Fundamentals of Radiology and CT - The basics of x-rays*. 2-1-2-11 (IOP Publishing, 2016).

3 Borchardt-Ott, W. *Kristallographie - Eine Einführung für Naturwissenschaftler*. 8. edn, (2013).

4 Katsaras, J. *et al. Structure and Dynamics of Membranous Interfaces -Neutron and X-Ray Scattering from Isotropic and Aligned Membranes*. (Wiley, 2014).

5 Scherrer, P. Bestimmung der Größe und der inneren Struktur von Kolloidteilchen mittels Röntgenstrahlen. *Nachrichten von der Gesellschaft der Wissenschaften zu Göttingen, Mathematisch-Physikalische Klasse* **1918**, 98-100 (1918).

6 Langford, J. I. & Wilson, A. J. C. Scherrer after sixty years: A survey and some new results in the determination of crystallite size. *J. Appl. Crystallogr.* **11**, 102-113, doi:10.1107/s0021889878012844 (1978).

7 Billinge, S. J. L. The rise of the X-ray atomic pair distribution function method: a series of fortunate events. *Philos Trans A Math Phys Eng Sci* **377**, 20180413, doi:10.1098/rsta.2018.0413 (2019).

8 Batten, S. R. *et al.* Terminology of metal–organic frameworks and coordination polymers (IUPAC Recommendations 2013). *Pure Appl. Chem.* **85**, 1715-1724, doi:10.1351/pac-rec-12-11-20 (2013).

9 Bae, Y. S., Yazaydin, A. O. & Snurr, R. Q. Evaluation of the BET method for determining surface areas of MOFs and zeolites that contain ultra-micropores. *Langmuir* **26**, 5475-5483, doi:10.1021/la100449z (2010).

10 Thommes, M. *et al.* Physisorption of gases, with special reference to the evaluation of surface area and pore size distribution (IUPAC Technical Report). *Pure Appl. Chem.* **87**, 1051-1069, doi:10.1515/pac-2014-1117 (2015).

11 Gatoo, M. A. *et al.* Physicochemical properties of nanomaterials: implication in associated toxic manifestations. *Biomed Res Int* **2014**, 498420, doi:10.1155/2014/498420 (2014).

12 Brunauer, S. E., P. H.; Teller, E. Adsorption of Gases in Multimolecular Layers. *J. Am. Chem. Soc.* **60**, 309-319 (1938).

13 Langmuir, I. The Adsorption of Gases on Plane Surfaces of Glass, Mica and Platinum. *J. Am. Chem. Soc.* **40**, 1361-1403, doi:10.1021/ja02242a004 (1918).

14 Ambroz, F., Macdonald, T. J., Martis, V. & Parkin, I. P. Evaluation of the BET Theory for the Characterization of Meso and Microporous MOFs. *Small Methods* **2**, 1800173, doi:10.1002/smtd.201800173 (2018).

15 Gomez-Gualdron, D. A., Moghadam, P. Z., Hupp, J. T., Farha, O. K. & Snurr, R. Q. Application of Consistency Criteria To Calculate BET Areas of Micro- And Mesoporous Metal-Organic Frameworks. *J. Am. Chem. Soc.* **138**, 215-224, doi:10.1021/jacs.5b10266 (2016).

16 Landers, J., Gor, G. Y. & Neimark, A. V. Density functional theory methods for characterization of porous materials. *Colloids and Surfaces A: Physicochemical and Engineering Aspects* **437**, 3-32, doi:10.1016/j.colsurfa.2013.01.007 (2013).

17 Coats, A. W. & Redfern, J. P. Thermogravimetric analysis. A review. *The Analyst* **88**, 906, doi:10.1039/an9638800906 (1963).

18 Modena, M. M., Ruhle, B., Burg, T. P. & Wuttke, S. Nanoparticle Characterization: What to Measure? *Adv. Mater.* **31**, e1901556, doi:10.1002/adma.201901556 (2019).

19 Wiktor, C., Meledina, M., Turner, S., Lebedev, O. I. & Fischer, R. A. Transmission electron microscopy on metal–organic frameworks – a review. *Journal of Materials Chemistry A* **5**, 14969-14989, doi:10.1039/c7ta00194k (2017).

20 Cremer, C. Lichtmikroskopie unterhalb des Abbe-Limits. Lokalisationsmikroskopie. *Physik in unserer Zeit* **42**, 21-29, doi:10.1002/piuz.201101251 (2011).

21 Burany, S. *et al. Scanning Electron Microscopy and X-Ray Microanalysis*. Vol. 9 (Springer, 2003).

22 Wang, R., Wang, C., Zhang, H., Tao, J. & Bai, X. *Progress in Nanoscale Characterization and Manipulation*. Vol. 272 (Peking University Press and Springer Nature Singapore Pte Ltd, 2018).

23 Wang, R., Wang, C., Zhang, H., Tao, J. & Bai, X. *Progress in Nanoscale Characterization and Manipulation*. Vol. 272 41 (Peking University Press and Springer Nature Singapore Pte Ltd, 2018).

24 Thomas, J. & Gemming, T. *Analytische Transmissionselektronenmikroskopie*. 1st edn, (Springer, 2013).

25 Zetasizer Nano User Manual. (2009).

26 Frisken, B. J. in *Appl. Opt.* Vol. 40 4087-4091 (2001).

27 Debye, P. & E., H. Zur Theorie der Elektrolyte. I. Gefrierpunktserniedrigung und verwandte Erscheinungen. *Physikalische Zeitschrift* **24**, 185-206 (1923).

28 Stern, O. Zur Theorie der Elektrolytischen Doppelschicht. *Zeitschrift für Elektrochemie* **30**, 508, doi:10.1002/bbpc.192400182 (1924).

29 Tay, C. Y., Setyawati, M. I., Xie, J., Parak, W. J. & Leong, D. T. Back to Basics: Exploiting the Innate Physico-chemical Characteristics of Nanomaterials for Biomedical Applications. *Adv. Funct. Mater.* **24**, 5936-5955, doi:10.1002/adfm.201401664 (2014).

30 Günzler, H. & Gremlich, H.-U. *IR-Spektroskopie*. 4. edn, (Wiley-VCH, 2003).

31 Günzler, H. & Gremlich, H.-U. *IR-Spektroskopie*. 2nd edn, 26 (Wiley, 2000).

32 Günzler, H. & Gremlich, H.-U. *IR-Spektroskopie*. 4. edn, (Wiley-VCH, 2003).

33 Günzler, H. & Gremlich, H.-U. *IR-Spektroskopie*. 4. edn, (Wiley-VCH, 2003).

34 Lakowicz, J. R. *Principles of Fluorescence Spectroscopy*. 3. edn, (Springer, 2006).

35 Jablonski, A. Efficiency of Anti-Stokes Fluorescence in Dyes. *Nature* **131**, 839-840, doi:10.1038/131839b0 (1933).

36 Borlinghaus, R. T. *Konfokale Mikroskopie in Weiß - Optische Schnitte in allen Farben*. (Springer, 2016).

37 Toporski, J., Dieing, T. & Hollricher, O. *Confocal Raman Microscopy*. 2nd edn, Vol. 66 27 (Springer, 2011).

38 Böll, K., Zimpel, A., Dietrich, O., Wuttke, S. & Peller, M. Clinically Approved MRI Contrast Agents as Imaging Labels for a Porous Iron-Based MOF Nanocarrier: A Systematic Investigation in a Clinical MRI Setting. *Advanced Therapeutics*, 1900126, doi:10.1002/adtp.201900126 (2019).

39 Haacke, E. M., Brown, R. W., Thompson, M. R. & Venkatesan, R. *Magnetic Resonance Imaging: Physical Principles and Sequence Design*. (Wiley, 1999).

40 Raya, J. G. *et al.* T2 measurement in articular cartilage: impact of the fitting method on accuracy and precision at low SNR. *Magn Reson Med* **63**, 181-193, doi:10.1002/mrm.22178 (2010).

41 Modena, M. M., Wang, Y., Riedel, D. & Burg, T. P. Resolution enhancement of suspended microchannel resonators for weighing of biomolecular complexes in solution. *Lab Chip* **14**, 342-350, doi:10.1039/c3lc51058a (2014).

3 Mass Measurements reveal Preferential Sorption of Mixed Solvent Components in Porous Nanoparticles

This chapter is based on the following publication:

Modena MM, **Hirschle P**, Wuttke S, Burg TP. Small. **2018**;14(27):e1800826. (DOI: 10.1002/smll.201800826)

3.1 Introduction

Porous nanoparticles are a unique class of materials that open many new opportunities in fields ranging from drug delivery and sensing to catalysis, green chemistry, and energy conversion. [1-8] Their physicochemical properties, in particular their morphology, surface charge, composition, porosity, and extremely high surface-to-volume ratio, are of paramount importance in defining their potential applications. Therefore, it is necessary to precisely control and measure these parameters. [4,9-17] Several characterization methods can be used to probe nanoparticles:[18,19] Nanometer-scale resolution on particle morphology and crystallinity can be obtained using solid-state approaches (e.g., electron microscopy and X-ray diffraction).[20] However, these methods can only be used on dry samples, and thus they cannot account for interactions between the nanoparticles and the suspending solution. Mobility-based methods (e.g., dynamic light scattering) are commonly used to measure the hydrodynamic radius and zeta-potential of nanoparticles in liquids. [19] Mobility, however, does not vary significantly with the internal state of nanoparticles, such as the filling of the pores. Therefore, pore volume, pore accessibility, and the internal affinity to specific gases are currently only probed in the dry state (e.g., nitrogen adsorption and helium pycnometry), or by the indirect measurement of the adsorption of probe molecules dissolved in solvents of different polarity. [21]

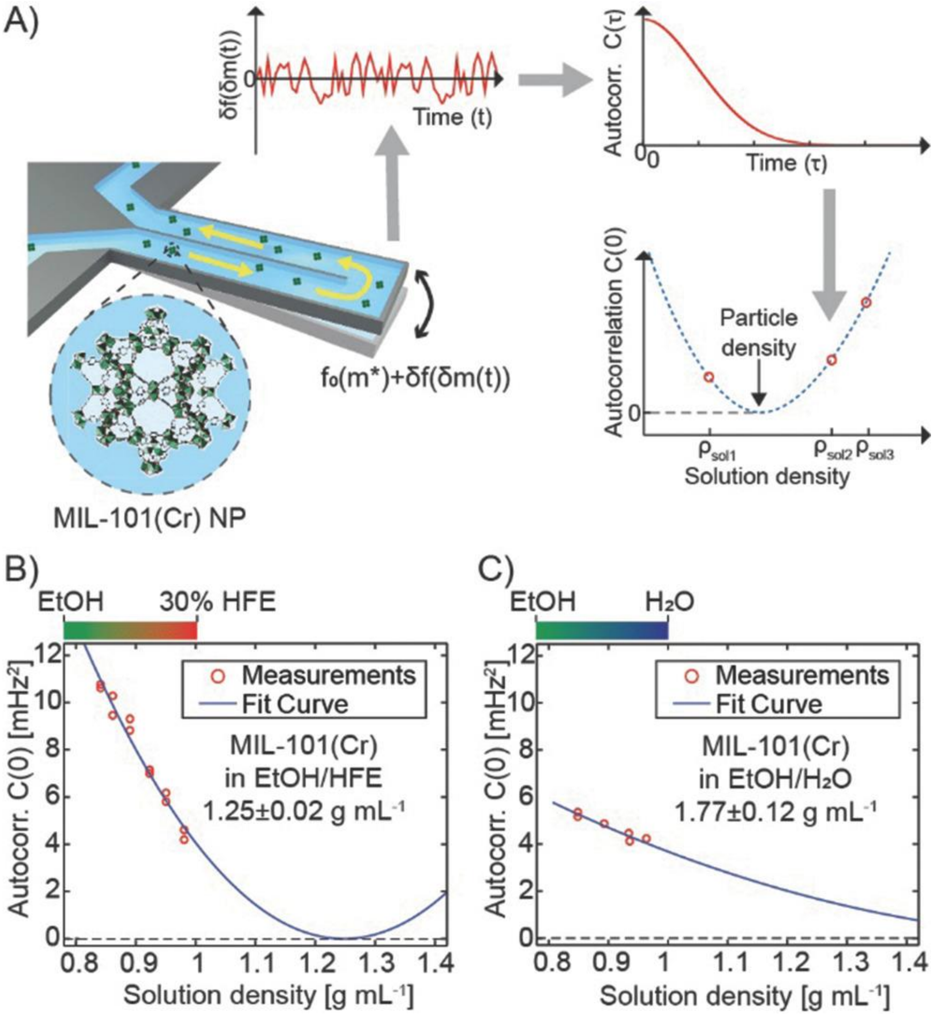

Figure 3.1. Density characterization of MIL-101(Cr) nanoparticles. **A**) Direct mass measurements with suspended microchannel resonators reveal the mass density of porous nanoparticles in different mixed solvents. Particles flowing through a microfluidic channel embedded into a nanomechanical resonator cause resonance-frequency variations proportional to the induced mass fluctuations. These mass fluctuations are measured with high precision by correlation analysis. **B**) Variation of the magnitude *C*(0) of the autocorrelation for the MIL-101(Cr) nanoparticle signal in mixtures of HFE-7100/EtOH with a solution density ranging from 0.84 g mL^{-1} (≈8% HFE-7100) to 0.98 g mL^{-1} (≈30% HFE-7100). The measured density of the particles is 1.25 ± 0.02 g mL^{-1}; **C**) The density of MIL-101(Cr) nanoparticles in polar solvents was measured by using a mixture of 50 × 10^{-3} M Glycine-HCl (pH 2.5)/EtOH, with density ranging from 0.85 g mL^{-1} (≈76% EtOH) to 0.96 g mL^{-1} (≈2% EtOH). A buffer solution with low pH was selected as the MIL-101(Cr) nanoparticles present higher stability and low aggregation when suspended in acid conditions (**Figure S3.20**).

To circumvent this limitation, we used nanomechanical mass correlation spectroscopy (MCS)[22] to measure the effective mass density of metal–organic framework (MOF) nanoparticles in different solvent systems. In this approach, the MOF nanoparticles are dispersed in a range of binary solvent systems and the mass fluctuations resulting from the flow of this suspension through a suspended microchannel resonator (SMR) mass sensor of 10 pL volume are measured (1 pL = 10^{-12} L; **Figure 3.1**). We used materials institute lavoisier (MIL)-101(Cr) MOF nanoparticles[23] with different inner pore functionalizations and suspended them in binary mixtures of ethanol and water, and methoxyperfluorobutane (HFE-7100) and ethanol (EtOH). Based on geometry alone, these modifications of the solvent systems and of the functionalization of the pores are not expected to change the mass of the nanoparticles. The observed differences therefore provide new information about the specific interaction between the different solvent components and the internal surface.

3.2 Results

MIL-101(Cr) nanoparticles are mesoporous MOF nanoparticles featuring two types of cages with respective diameters of 2.9 and 3.4 nm, and an accessible window of 1.2 and 1.4 nm. [23] Here, we have examined the effective density of three different MIL-101(Cr) species: MIL-101(Cr) nanoparticles and MIL-101(Cr) derivatives functionalized at the coordinatively unsaturated metal sites with pyridine or pyrazine using post-synthetic modification. [24] The crystallinity, porosity, and morphology of the MIL-101(Cr) nanoparticle species were investigated with powder X-ray diffraction (PXRD) (**Figure S3.6**), nitrogen adsorption/desorption isotherms (**Table S3.7**), transmission and scanning electron microscopy, (TEM, **Figure S3.7**-**Figure S3.9**; SEM, **Figure S3.11**-**Figure S3.16**), respectively. We characterized the nanoparticles using both SEM of dried ethanolic suspensions, resulting in a size distribution of d^{SEM} = 41 ± 10 nm (**Figure S3.17**-**Figure S3.19**), and dynamic light scattering (DLS) in ethanol yielding in a hydrodynamic diameter of d^{DLS} = 105 ± 31 nm (**Figure S3.21**).

The density of MIL-101(Cr) nanoparticles was measured using both apolar and polar solvents to probe the behavior of particles when exposed to different solvent mixtures (**Figure 3.1**). Surprisingly, the effective mass density of the particles depends significantly on the solvent system. In the relatively apolar mixture of HFE-7100 with EtOH, MIL-101(Cr) nanoparticles present a density $\rho_{\mathrm{eff}}^{\mathrm{HFE/EtOH}} = 1.25 \pm 0.02$ g cm^{-3} (**Figure 3.1b**), while their density increases to $\rho_{\mathrm{eff}}^{\mathrm{EtOH/Water}} = 1.77 \pm 0.12$ g cm^{-3} (**Figure 3.1c**) in the more polar mixture of ethanol with an aqueous buffer (50 × 10^{-3} M Glycine-HCl, pH 2.5). Both values are much larger than the mass density of the empty framework, which can be calculated from the crystal structure as $\rho_{\mathrm{eff}}^{\mathrm{HFE/EtOH}} = 0.66$ g cm^{-3} (**Figure S3.24**).

Next, we modified MIL-101(Cr) nanoparticles using a post-synthetic grafting approach. The coordinatively unsaturated chromium sites (Lewis acid sites) are used to coordinate Lewis bases,[24] pyrazine or pyridine, to render the particles more hydrophilic or hydrophobic, respectively (**Figure 3.2**). As for the unfunctionalized MIL-101(Cr) nanoparticles, the measurements were carried out in mixtures of HFE-7100/EtOH and of 50 × 10^{-3} M Glycine–HCl (pH 2.5)/EtOH to detect both the particle densities and their permeability to the solvents in solution. Measurements in the HFE-7100/EtOH mixtures return an effective density of $\rho_{\mathrm{eff}}^{\mathrm{HFE/EtOH}} = 1.31 \pm 0.03$ g cm^{-3} for the pyrazine-functionalized particles and $\rho_{\mathrm{eff}}^{\mathrm{HFE/EtOH}} = 1.30 \pm 0.05$ g cm^{-3} for the pyridine-functionalized particles.

These results are in line with the values found for the unfunctionalized MOF nanoparticles. More pronounced differences are detected when measuring the density of the functionalized nanoparticles in the polar mixture. For the pyrazine-functionalized nanoparticles, we find a surprisingly high effective density of $\rho_{\mathrm{eff}}^{\mathrm{EtOH/Water}} = 1.42 \pm 0.06$ g cm^{-3} in the mixture of ethanol and water (**Figure 3.2b**). As for the measurements of the unfunctionalized MIL-101(Cr) nanoparticles, the uncertainty on the effective density increases with the value of the estimated density. In contrast, the pyridine-functionalized nanoparticles show a drastic decrease in effective density to $\rho_{\mathrm{eff}}^{\mathrm{EtOH/Water}} = 1.12 \pm 0.02$ g cm^{-3} when suspended in the same mixture (**Figure 3.2d**). The lower effective density may be due to an increased ethanol content within the particles. This could occur due to particle aggregation with concomitant inclusion of ethanol in the interstitial volume and/or due to the formation of an ethanol solvation layer surrounding the nanoparticles. In both cases, the ethanol fraction may be locally increased in the aqueous mixture because of the hydrophobic functional groups presented both on the inner and outer surface of the nanoparticles. This hypothesis is supported by DLS measurements of the nanoparticles suspended in the two mixtures: the nanoparticles in ethanol have a hydrodynamic diameter of 96 nm (polydispersivity 18%), while their size increases to 149 nm (polydispersivity 40%) in a 95% 50 × 10^{-3} m Glycine-HCl/5% ethanol mixture.

The density estimations obtained for the different cases of MIL-101(Cr) nanoparticles when suspended in the different solvent mixtures are summarized in **Table 3.1**. The observed dependence of mass density on the chemical identity of the solvent in MOF nanoparticles can be understood by considering the possible interactions of the solvent components with the pore volume. Our measured correlation signal $C(0)$ represents the variance of the resonance frequency fluctuations of the SMR. This is directly proportional to the variance of mass fluctuations arising from Poisson statistics, i.e., $C(0) \sim c_0 V \cdot \left.\frac{\partial \rho}{\partial c}\right|_{\mu}^{2}$, where c_0 denotes the solid concentration, V = 10 pL is the volume, and $\left.\frac{\partial \rho}{\partial c}\right|_{\mu}$ is the density increment of the solution at constant chemical potential. In the simplest case, when particles are described as hard spheres, the density increment follows Archimedes' law

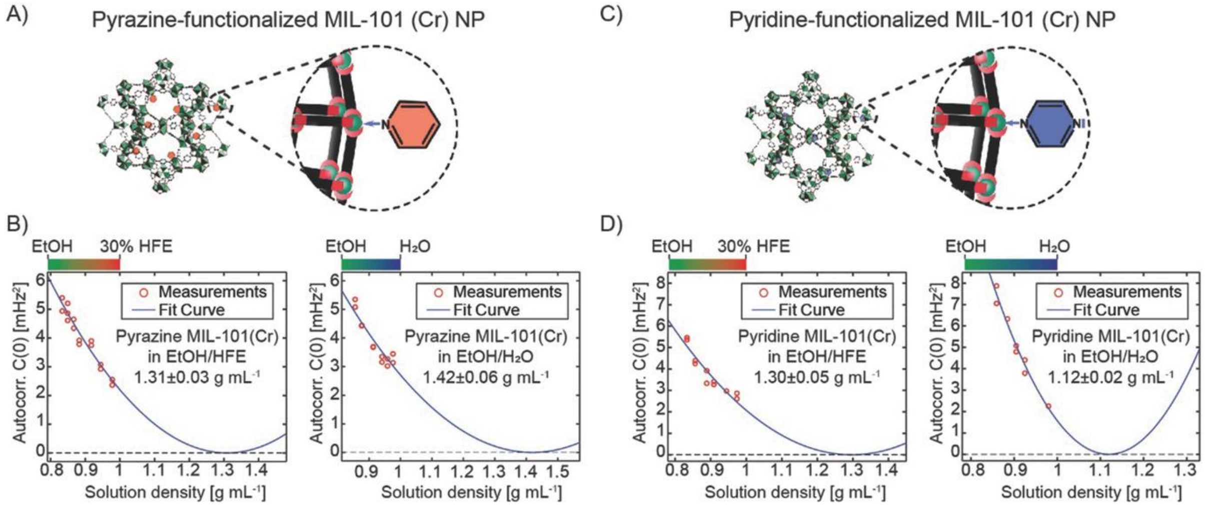

Figure 3.2. Density measurements of functionalized MIL-101(Cr) nanoparticles. **A**) MIL-101(Cr) nanoparticles were functionalized with pyrazine at the coordinatively unsaturated metal sites. **B**) Density measurements of pyrazine-functionalized MIL-101(Cr) particles suspended in mixtures of HFE-7100/EtOH (left) and 50 × 10^{-3} M Glycine-HCl/EtOH (right). The particles present an unexpected higher effective density in the polar mixture; **C**) The hydrophobicity of MIL-101(Cr) nanoparticles was increased by functionalization of the inner and outer-surface area with pyridine. **D**) Density characterization of the pyridine-functionalized MIL-101(Cr) particles in mixtures of HFE-7100/EtOH (left) and 50 × 10^{-3} M Glycine-HCl/EtOH (right).

Equation 23

$$\left.\frac{\partial \rho}{\partial c}\right|_{\mu} = 1 - \frac{\rho_s}{\rho_{\mathrm{eff}}}$$

where ρ_s is the mass density of the solvent and ρ_{eff} denotes the mass density of the solid, which is equal to the inverse partial specific volume of the particles. In this case, the autocorrelation curve presents zero amplitude when the density of the suspending solution matches the density of the particles.

Table 3.1. Summary of density estimations for the functionalized and unfunctionalized MIL-101(Cr) MOF nanoparticles in the different solvent mixtures

MIL-101(Cr) functionalization	**Solvent mixture**	
	EtOH/HFE [g cm^{-3}]	**EtOH/50 x 10^{-3} M Glycine-HCl [g cm^{-3}]**
Unfunctionalized	1.25 ± 0.02	1.77 ± 0.12
Pyrazine-functionalized	1.31 ± 0.03	1.42 ± 0.06
Pyridine-functionalized	1.30 ± 0.02	1.12 ± 0.02

Porous nanoparticles present a fundamentally different behavior. In solution, their effective density depends not only on their dry mass and volume but also on the ability of the solvent to access the pore volume. There can be significant differences in pore accessibility for different solvent components due to size exclusion and more complex interactions, such as solvation effects and gating. All of these phenomena may alter the effective mass density of the particles and necessitate an extension of the pure physical/geometric description, which is inherent to Archimedes' principle.

3.3 Discussion

To explain the range of the observed differences, we represent the pore volume by two compartments, as shown in **Figure 3.3**. Note that this is done only for modeling purposes; in reality, there need not be a defined physical boundary. In the first compartment (light blue) the solvent composition tracks the composition outside the pore exactly. In contrast, the composition in the second compartment (blue/yellow in **Figure 3.3**) is fixed and given by specific adsorption or exclusion of individual solvent components. The dry mass of the particle is increased by the fixed mass of adsorbed solvent molecules. This leads to the following expression for the density increment

Equation 24
$$\left.\frac{\partial\rho}{\partial c}\right|_{\mu} = (1 + B_{\mathrm{A}} + B_{\mathrm{B}})\left(1 - \frac{\rho_{\mathrm{s}}}{\rho'_{\mathrm{eff}}}\right)$$

where the adsorption coefficients B_{A} and B_{B} denote the mass fractions of the solvent components A and B, respectively, that are bound to the particles. [25,26] The total adsorbed mass fraction is ($B_A + B_B$) and the effective mass density of the particles is given by

Equation 25
$$\rho'_{\mathrm{eff}} = \frac{1 + B_{\mathrm{A}} + B_{\mathrm{B}}}{\rho_{\mathrm{f}}^{-1} + B_{\mathrm{A}}\rho_{\mathrm{A}}^{-1} + B_{\mathrm{B}}\rho_{\mathrm{B}}^{-1}}$$

Note that ρ_{f} represents the density of the nanoparticle framework and depends on the accessibility of the pores to the solvent. To illustrate different scenarios, we consider three special cases. First, if the particles are fully permeable (case I), $B_{\mathrm{A,B}} = 0$ and ρ'_{eff} is given by Equation 25 and $\rho_{\mathrm{f}} = \frac{M_{\mathrm{f}}}{V_{\mathrm{f}}}$ (**Figure 3.3,I**), where M_{f} is the dry mass of one particle and V_{f} is the volume occupied by the framework. In our experiments with MIL-101(Cr) nanoparticles, this yields a value of $\rho'_{eff} = 3.1$ g cm^{-3} based on a pore volume fraction of 79% calculated from the crystal structure (**Figure S3.24**). Second, if the particles are impermeable (case II), the solid particle model applies with $\rho_{\mathrm{efff}} = \frac{M_{\mathrm{f}}}{V_p}$ (**Figure 3.3,II**), where V_{p} is the hard-sphere volume of one particle. In this case, the crystal structure reveals a value $\rho_{eff} = 0.66$ g cm^{-3}. Finally, if one solvent component, e.g., component A, permeates selectively (case III), then $B_B = 0$ and $B_A > 0$ (**Figure 3.3,III**).

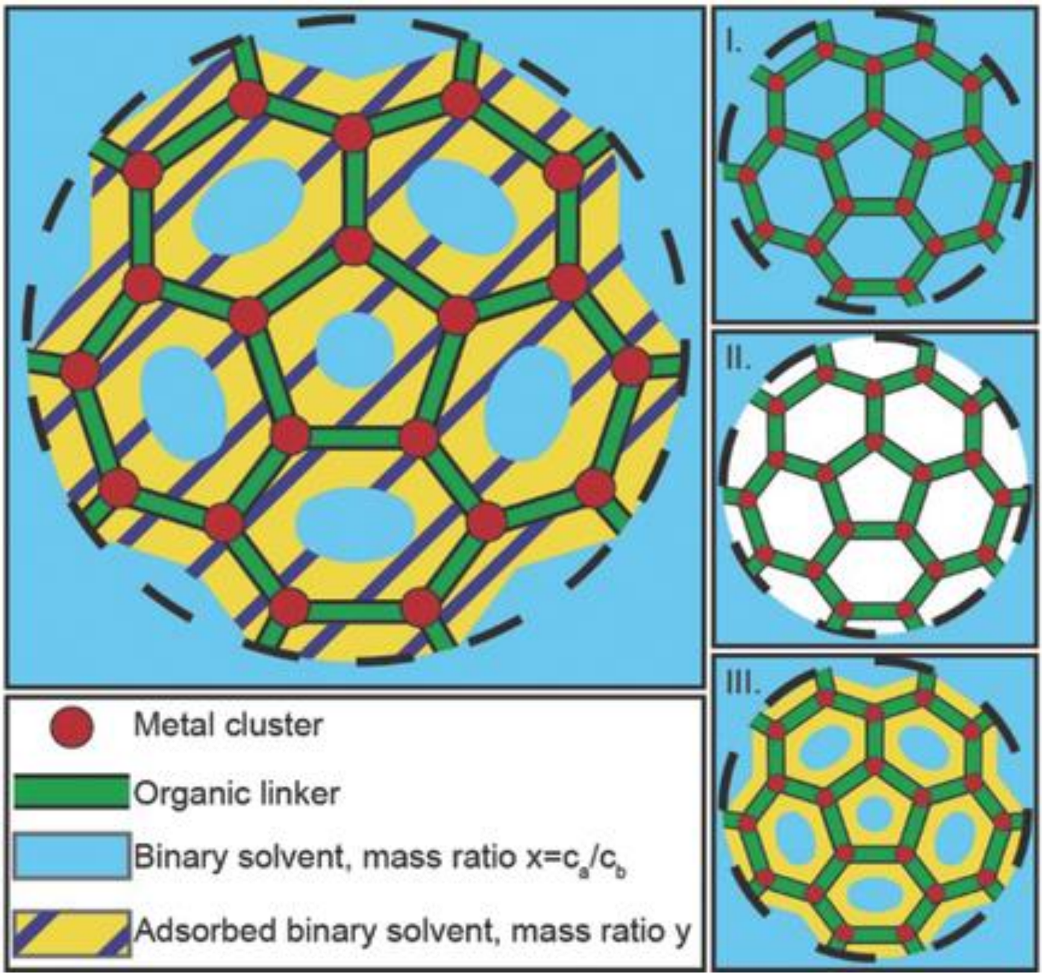

Figure 3.3. Schematic representation of the selective sorption of mixed solvents into porous MOF nanoparticles. The dashed line symbolizes the outer perimeter of the nanoparticle with dry mass M_f and total volume V_p. In the most general case, different solvent components can freely access only a fraction of the pore volume (shown in light blue). Here the mass ratio x of solvent components matches that of the surrounding fluid. In another part of the internal volume, the composition is altered by specific interactions between the different solvent components and the solid framework (yellow/blue hatched region). The mass ratio *y* of solvent components in this region can differ significantly from the surrounding fluid. Three special cases of this model are of particular interest: **I**) All solvent components can freely access the entire pore volume. **II**) Nonsolvent molecules can access the internal volume. **III**) One of the solvent components (light yellow) can access a larger portion of the internal volume than the other.

The wide range of effective density values corresponding to these cases explains the differences we observe in the different experiments. Although the measurements do not provide sufficient information to extract each of the parameters (ρ_f, B_A, and B_B) individually for the different solvent systems and particle functionalizations, the observed variation in density establishes that their combination differs significantly in each of the measured cases, with case I and II not being supported by our experimental findings.

Our results show that tuning the inner functionalization of porous MOF nanoparticles can produce considerably different local compositions of the solvent mixtures within and/or around the nanoparticles. This capability opens interesting new opportunities for the use of MOF nanoparticles, such as separation of solvent mixture based on selective enhancement of a solvent component in the pores.

Finally, the novel density method presented here can be applied to any other porous nanoparticle system, which will greatly advance our understanding of one key physicochemical parameter of porous nanoparticles and open up a broad spectrum of applications of this class of materials, from separation to biomedical science.

3.4 Experimental Methods

Density Measurements

Density of particles in solution is measured by detecting the variation of buoyant mass when the particles are suspended in mixtures of different concentrations of ethanol and 50×10^{-3} M Glycine-HCl (pH = 2.5) or ethanol and HFE-7100. The test solutions are injected into a suspended microchannel resonator featuring an embedded channel with a cross-section of $3 \times 8\ \mu m^2$. The resonance frequency of the resonator is measured by using an optical-lever detection scheme (see **Figure S3.4** and section 3.5 for more information on the experimental setup). During the measurement, particle concentration is kept constant to simplify the subsequent data analysis process. As the buoyant mass of the particles is proportional to the induced frequency fluctuations, the time-domain mass signal is first high-pass filtered (cutoff frequency = 1 Hz) to remove slow-term-noise fluctuations, caused by temperature and/or mechanical variations. Frequency fluctuations are then analyzed by use of an autocorrelation analysis of the high frequency domain to minimize the effect of the uncorrelated readout noise background. The effective density of the particles is calculated after fitting the autocorrelation amplitude as a function of solution density, with the estimated particle density corresponding to the minimum of the fitting parabola. Therefore, the uncertainty on density estimation depends on the range of solution densities accessed during the measurement. More information on and validation measurements of the density characterization method are reported in the Supporting Information.

References

1 Meng, X., Gui, B., Yuan, D., Zeller, M. & Wang, C. Mechanized azobenzene-functionalized zirconium metal-organic framework for on-command cargo release. *Sci Adv* **2**, e1600480, doi:10.1126/sciadv.1600480 (2016).

2 Zhao, M. *et al.* Core-shell palladium nanoparticle@metal-organic frameworks as multifunctional catalysts for cascade reactions. *J. Am. Chem. Soc.* **136**, 1738-1741, doi:10.1021/ja411468e (2014).

3 Ghalei, B. *et al.* Enhanced selectivity in mixed matrix membranes for CO2 capture through efficient dispersion of amine-functionalized MOF nanoparticles. *Nature Energy* **2**, 17086, doi:10.1038/nenergy.2017.86 (2017).

4 Lu, G. *et al.* Imparting functionality to a metal–organic framework material by controlled nanoparticle encapsulation. *Nature Chemistry* **4**, 310-316, doi:10.1038/nchem.1272 (2012).

5 Wuttke, S., Lismont, M., Escudero, A., Rungtaweevoranit, B. & Parak, W. J. Positioning metal-organic framework nanoparticles within the context of drug delivery - A comparison with mesoporous silica nanoparticles and dendrimers. *Biomaterials* **123**, 172-183, doi:10.1016/j.biomaterials.2017.01.025 (2017).

6 Furukawa, H., Müller, U. & Yaghi, O. M. “Heterogeneity within Order” in Metal-Organic Frameworks. *Angew. Chem. Int. Ed.* **54**, 3417-3430, doi:10.1002/anie.201410252 (2015).

7 Li, Z., Barnes, J. C., Bosoy, A., Stoddart, J. F. & Zink, J. I. Mesoporous silica nanoparticles in biomedical applications. *Chem. Soc. Rev.* **41**, 2590-2605, doi:10.1039/c1cs15246g (2012).

8 Tibbitt, M. W., Dahlman, J. E. & Langer, R. Emerging Frontiers in Drug Delivery. *J. Am. Chem. Soc.* **138**, 704-717, doi:10.1021/jacs.5b09974 (2016).

9 Walkey, C. D., Olsen, J. B., Guo, H., Emili, A. & Chan, W. C. Nanoparticle size and surface chemistry determine serum protein adsorption and macrophage uptake. *J. Am. Chem. Soc.* **134**, 2139-2147, doi:10.1021/ja2084338 (2012).

10 Furukawa, H. *et al.* Ultrahigh porosity in metal-organic frameworks. *Science* **329**, 424-428, doi:10.1126/science.1192160 (2010).

11 Wuttke, S. *et al.* Validating Metal-Organic Framework Nanoparticles for Their Nanosafety in Diverse Biomedical Applications. *Adv Healthc Mater* **6**, doi:10.1002/adhm.201600818 (2017).

12 MacParland, S. A. *et al.* Phenotype Determines Nanoparticle Uptake by Human Macrophages from Liver and Blood. *ACS Nano* **11**, 2428-2443, doi:10.1021/acsnano.6b06245 (2017).

13 Sakata, Y. *et al.* Shape-Memory Nanopores Induced in Coordination Frameworks by Crystal Downsizing. *Science* **339**, 193-196, doi:10.1126/science.1231451 (2013).

14 Goesmann, H. & Feldmann, C. Nanoparticulate Functional Materials. *Angew. Chem. Int. Ed.* **49**, 1362-1395, doi:10.1002/anie.200903053 (2010).

15 Rungtaweevoranit, B., Zhao, Y., Choi, K. M. & Yaghi, O. M. Cooperative effects at the interface of nanocrystalline metal–organic frameworks. *Nano Research* **9**, 47-58, doi:10.1007/s12274-015-0970-0 (2016).

16 Xu, S. *et al.* Generation of monodisperse particles by using microfluidics: control over size, shape, and composition. *Angew. Chem. Int. Ed. Engl.* **44**, 724-728, doi:10.1002/anie.200462226 (2005).

17 Ma, J., Kalenak, A. P., Wong-Foy, A. G. & Matzger, A. J. Rapid Guest Exchange and Ultra-Low Surface Tension Solvents Optimize Metal-Organic Framework Activation. *Angew. Chem. Int. Ed. Engl.* **56**, 14618-14621, doi:10.1002/anie.201709187 (2017).

18 Hirschle, P. *et al.* Exploration of MOF nanoparticle sizes using various physical characterization methods – is what you measure what you get? *CrystEngComm* **18**, 4359-4368, doi:10.1039/c6ce00198j (2016).

19 Tay, C. Y., Setyawati, M. I., Xie, J., Parak, W. J. & Leong, D. T. Back to Basics: Exploiting the Innate Physico-chemical Characteristics of Nanomaterials for Biomedical Applications. *Adv. Funct. Mater.* **24**, 5936-5955, doi:10.1002/adfm.201401664 (2014).

20 Sin, M. *et al.* Surface polarity estimation of metal-organic frameworks using liquid-phase mixture adsorption. *Microporous Mesoporous Mater.* **251**, 129-134, doi:10.1016/j.micromeso.2017.06.001 (2017).

21 Modena, M. M., Wang, Y., Riedel, D. & Burg, T. P. Resolution enhancement of suspended microchannel resonators for weighing of biomolecular complexes in solution. *Lab Chip* **14**, 342-350, doi:10.1039/c3lc51058a (2014).

22 Férey, G. M.-D., C.; Serre, C.; Millange, F.; Dutour, J.; Surblé, S.; Margiolaki, I. A Chromium terephthalate-Based Solid with Unusually Large Pore Volumes and Surface Area. *Science* **309**, 2040-2042 (2005).

23 Wuttke, S. *et al.* Turn-on fluorescence triggered by selective internal dye replacement in MOFs. *Chem. Commun.* **50**, 3599, doi:10.1039/c3cc46591h (2014).

24 Brown, P. H., Balbo, A., Zhao, H., Ebel, C. & Schuck, P. Density contrast sedimentation velocity for the determination of protein partial-specific volumes. *PLoS One* **6**, e26221, doi:10.1371/journal.pone.0026221 (2011).

25 Eisenberg, H. Analytical ultracentrifugation in a Gibbsian perspective. *Biophys. Chem.* **88**, 1-9, doi:10.1016/s0301-4622(00)00205-2 (2000).

26 Wuttke, S. *et al.* MOF nanoparticles coated by lipid bilayers and their uptake by cancer cells. *Chem Commun (Camb)* **51**, 15752-15755, doi:10.1039/c5cc06767g (2015).

3.5 Supplementary Information

3.5.1 Density Measurements

Detection method

Figure S3.4 shows a schematic of the experimental setup and of the subsequent data analysis. The buoyant mass of the particles is measured in mixtures of two solvents with different densities and mixed at different concentrations, therefore obtaining solutions of different densities. The test solutions are prepared with equal particle concentration to avoid variations during the measurement and simplify the data analysis. The sample is then drawn into the SMR device by means of syringe pumps, while the flow velocity in the detection channel is controlled by pressurizing the chip inlets. The combination of pressure control and syringe pumps enables smooth pulse-free flow during measurement and precise estimation of the mixture composition throughout the measurement. The density of the solution at any time is estimated by measuring the frequency shifts induced by added reference particles of known volume and density, and by pre-calibration of the mass/frequency responsivity of the SMR. After high-pass filtering of the time-domain mass trace and the removal of the reference particle signatures, the frequency fluctuations can be analyzed by means of the autocorrelation function. As white noise is largely confined to in the autocorrelation function, where is the sampling frequency, the estimation of is obtained by fitting of the autocorrelation curve using an approximated fit function of the curve.[1] Finally, the magnitudes of the autocorrelation curves are plotted against as functions of the density of the solutions and fitted with a parabola with zero minimum to estimate the intercept of the curve with the x-axis, which corresponds to the effective density of the particles in solution. Although only two measurements at different densities would be needed to fit the parabola, the resulting fit curve would present an ambiguity on the position of the curve minimum. The measurement scheme presented here enables the rapid acquisition of measurements at several solution densities, increasing the accuracy and reliability of the density estimation, and returning a unique solution of the fit parabola.

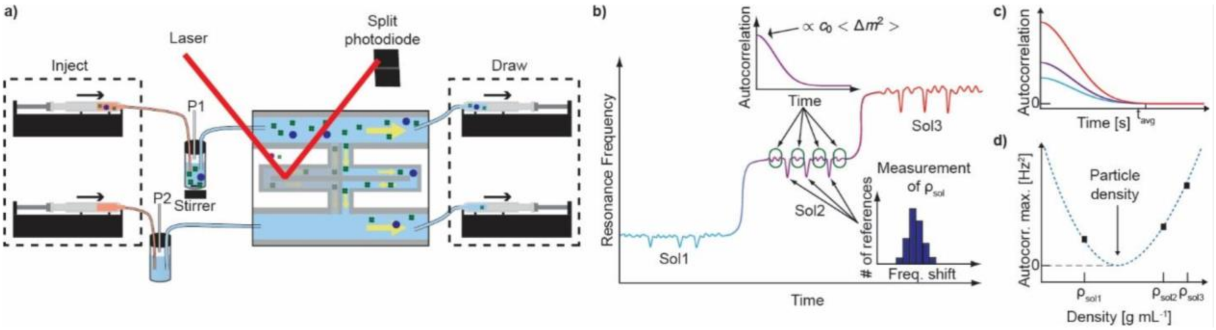

Figure S3.4. Measurement of particle density with SMRs. **a**) Schematic of the experimental setup, which includes (from the left): two syringe pumps for varying the solution density, pressurized inlets (P1 and P2) to control the flow in the microfluidic chip, an optical lever composed of a laser beam focused on the resonator and a split photodiode, two syringe pumps for drawing out the solution and precisely controlling the volume of solution flown in the chip; **b**) time-domain mass signal. The insets show the autocorrelation of small fluctuations of resonance frequency caused by the random number fluctuations of the nanoparticles in the channel (top) and the frequency shifts of the large calibration particles used for the detection of the solution density (bottom); **c**) the amplitude of the autocorrelation of the time-domain mass signal depends on the difference in density between the nanoparticles and the suspending solution; **d**) the amplitude of the autocorrelation as a function of solution density. The minimum of the fit parabola corresponds to the effective density of the particles in solution.

Experimental Procedure

The SMR presents two large bypass channels for the rapid exchange of the solutions, and a torsional resonating structure with embedded microfluidic channels of 3x8 μm^2 cross-section (HeightxWidth). First, the sample and wash solutions are drawn into the SMR. Then, the direction and velocity of the flow inside the embedded microfluidic channel are controlled by pressurizing the vials containing the solutions. The density of the solutions is varied during the measurement by mixing them with known volumes of solutions with different density at specific times. Preparing the sample and the diluting solution with the same concentration of particles ensures constant sample concentration throughout the measurement. The resonance frequency of the resonator is detected by using an optical lever readout scheme. The average resonance frequency varies with the density of the solution flowing in the embedded microfluidic channels. Particles of known size and density are added to the solution to estimate the density of the fluid at any moment from their induced transient shifts in resonance frequency.

Method validation

Characterization of polystyrene nanoparticles. As validation of the density characterization method, we measured the density of 210 nm (nominal size) polystyrene nanoparticles suspended in mixtures of pure water and ethanol by gradually increasing the ethanol fraction to 50% v/v. The variation of the autocorrelation amplitude with solution density is shown in **Figure S3.5**. The autocorrelation amplitude strongly increases with the ethanol concentration, clearly indicating that the particles have a density higher than that of pure water. Fitting of the experimental points with a parabola finds an effective mass density for the polystyrene nanoparticles of $\rho_{\mathrm{eff}}^{\mathrm{EtOH/Water}} = 1.056 \pm 0.001\ \mathrm{g \cdot cm^{-3}}$, which agrees with the manufacturer specifications[2]. As expected, the polystyrene particles behave as hard spheres, which are impermeable to the solvent. From the known total solid content and the measurement of $\rho_{\mathrm{eff}}^{\mathrm{EtOH/Water}}$ we can calculate the mean mass $M_f = 4.03 \pm 0.36\ \mathrm{fg}$ and the mean diameter $d_{\mathrm{p}} = 194 \pm 6\ nm$ of the nanoparticles

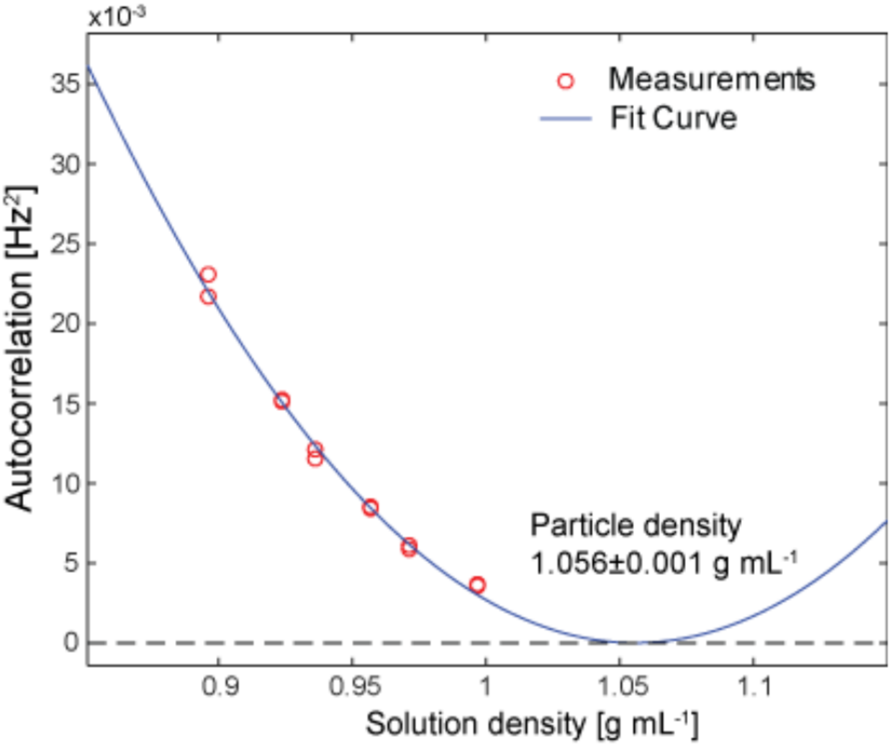

Figure S3.5. Density characterization of 210 nm (nominal size) polystyrene beads in mixtures of ethanol and water.

3.5.2 Methods and Characterization of MIL-101(Cr) Nanoparticles

Dynamic Light Scattering and Zeta-Potential:

Dynamic light scattering experiments and measurements of Zeta-Potential were conducted with a *Zetasizer Nano Series* (Nano-ZS, *Malvern*) featuring a laser with the wavelength λ = 633 nm. All DLS measurements were performed on the freshly synthesized samples in ethanol. Zeta-Potential measurements were performed in aqueous solution of the nanoparticles (c = 0.1 mg ml^{-1}). During the measurement, the pH was adjusted from pH = 2 to pH = 9 with a *MPT-2 Multi Purpose Titrator* (*Malvern*) using aqueous hydrochloric acid and sodium hydroxide solutions.

Scanning Electron Microscopy

The three MOF samples were examined on a *Helios NanoLab G3UC* (*FEI*) operating with 3 eV. The three samples were dried from ethanolic dispersions of the respective MOF species. Prior to the SEM measurements they were additionally sputtered with carbon. The resulting micrographs from the SEM measurements were evaluated manually using the software *ImageJ v1.49*.

Transmission Electron Microscopy

All three MOF samples were examined using a *Titan Themis* (*Fei*) operated with an acceleration voltage of 300 kV. Sample preparation was performed via drying an ethanolic NP dispersion on a carbon-coated copper grid.

Thermogravimetry

Dried samples of MIL-101(Cr) (5.90 mg), pyridine functionalized MIL-101(Cr) (6.20mg) and pyrazine functionalized MIL-101(Cr) (2.68mg) were examined on a *TASC 414/4* (*Netzsch*) under synthetic air. The results of the experiments, which were performed employing a heating rate of 10 °C/min up to 900 °C, were evaluated with the included software *Proteus v4.3*.

X-Ray Diffraction

In order to confirm a successful synthesis of MIL-101(Cr) MOF and to check the intactness of the crystal structure after functionalization, X-ray diffraction was performed. The instrument used was a *STOE Transmissions-Diffraktometer System STADI P.* The experiments were performed in transmission setup derived from Debye-Scherrer geometry. All experiments were performed with CuK$_{\alpha1}$-radiation. For data analysis the included software package

WinXPOW RawDat v3.0.2.5 and *WinXPOW PowDat_n v3.0.2.7* was used. The simulation of unfunctionalized MIL-101(Cr) bulk material was based on the structural data from the group of Férey[3] using the software *Materials Studio v7.0* (*BIOVIA*).

Nitrogen sorption

Ethanolic dispersions of the respective samples were dried in an oven at 70 °C for 3 days. The dried powders of each of the samples were outgassed in high vacuum (see **Table S3.2**). Nitrogen sorption experiments were performed with a *Autosorb-1* (*Quantachrome*). The results were evaluated using the software *ASiQwin v3.0*. The linearized form of the BET equation was used to calculate BET surface areas. For the calculation of the pore size distribution a QSDFT adsorption based model was used assuming slit, cylindrical, and spherical pores.

Table S3.2. Conditions employed during the outgassing of the samples.

MIL-101(Cr)	Pyridine-Functionalization	Pyrazine-Functionalization
38 h, 120 °C	72 h, 120 °C	38h, 70°C

3.5.3 Synthesis of the Nanoparticle Samples

Synthesis of MIL-101(Cr) NP

The synthesis of MIL-101(Cr) was conducted using microwave (MW) assisted synthesis. A mixture of $Cr(NO_3)_3 \cdot 9\ H_2O$ (1.48 g, 3.70 mmol) and terephthalic acid (0.615 g, 3.70 mmol) was given to water (20 ml, Milli-Q) and stirred until all $Cu(NO_3)_3 \cdot 9\ H_2O$ was dissolved. Subsequently, the reaction mixture was placed in a Teflon tube (80 ml) and sealed. The tube was placed in a microwave oven (*Synthos 3000*, *Anton-Paar*) along with 3 other vessels, two of them being filled with water (20ml) and one of them being a control vessel filled with an aqueous $Cu(NO_3)_3 \cdot 9\ H_2O$ (1.48 g, 3.70 mmol) solution. The heating sequence shown in **Table S3.3** was applied:

Table S3.3: MW Heating program for the MIL-101(Cr) synthesis

Heating	Dwelling	Cooling
4 min	2 min	1.5 h
To 210 °C	210 °C	To RT

The resulting nanoparticles were washed via centrifuging (20500 rpm, 45 min), removal of supernatant, and redispersing them under sonication in ethanol (30 ml). Subsequently the MOF NP dispersion was filtered in order to remove excess terephthalic acid. Afterwards, the nanoparticles were centrifuged (20500 rpm, 45 min), followed by removal of the supernatant and redispersing of the pellet under sonication for 3 additional times.

Post-synthetic functionalization with pyridine and pyrazine

For the pyrazine functionalization an ethanolic MIL-101(Cr) NP dispersion (7.2 ml, c = 12.4 mg ml^{-1}) was given to an ethanolic pyrazine solution (7.2 ml, c = 320 mg/ml, 4 mM). The reaction mixture was kept stirring for 24h. The resulting modified nanoparticles were washed in 4 cycles consisting of centrifuging (14000 rpm, 30 min), removal of supernatant and redispersing in ethanol under sonication.

For the pyridine functionalization, pyridine (12.2 ml, 154 mmol) was given to an ethanolic MIL-101(Cr) NP dispersion (7.2 ml, c = 12.4 mg ml^{-1}) in addition to ethanol (2.2 ml). The reaction mixture was kept stirring for 24 h. The resulting modified nanoparticles were washed in 4 cycles consisting of centrifuging (14000 rpm, 30 min), removal of supernatant and redispersing in ethanol under sonication.

3.5.4 Characterization of the MOF species

X-ray Diffraction

The results of the X-ray diffraction experiments are shown in **Figure S3.6**. The PXRD data of all three MIL-101(Cr) species is in agreement with literature results.[3] The reflex broadening in the MIL-101(Cr) NPs samples is not caused by lack of crystallinity as can be seen in the TEM results, but are caused by the nanosized crystalline domains.

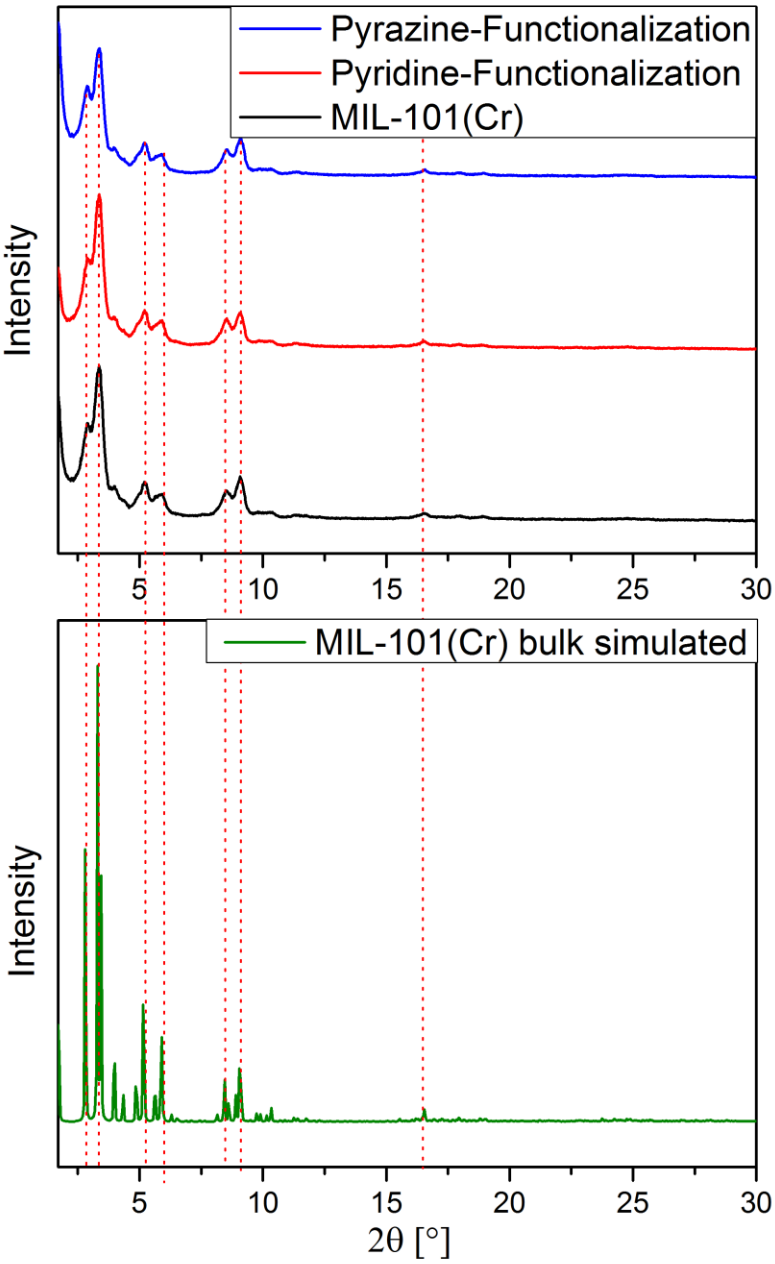

Figure S3.6. Powder X-ray diffraction patterns of the initial MIL-101(Cr) sample as well as the functionalized species.

3.5.5 Transmission Electron Microscopy

Overview pictures gained from TEM measurements are shown in **Figure S3.7**, **Figure S3.8**, **Figure S3.9** and for the respective samples. Generally, the micrographs prove the crystallinity of the MOF samples prior and after functionalization with pyridine/pyrazine. For better comparison small agglomerates for each of the respective species are shown in **Figure S3.10**.

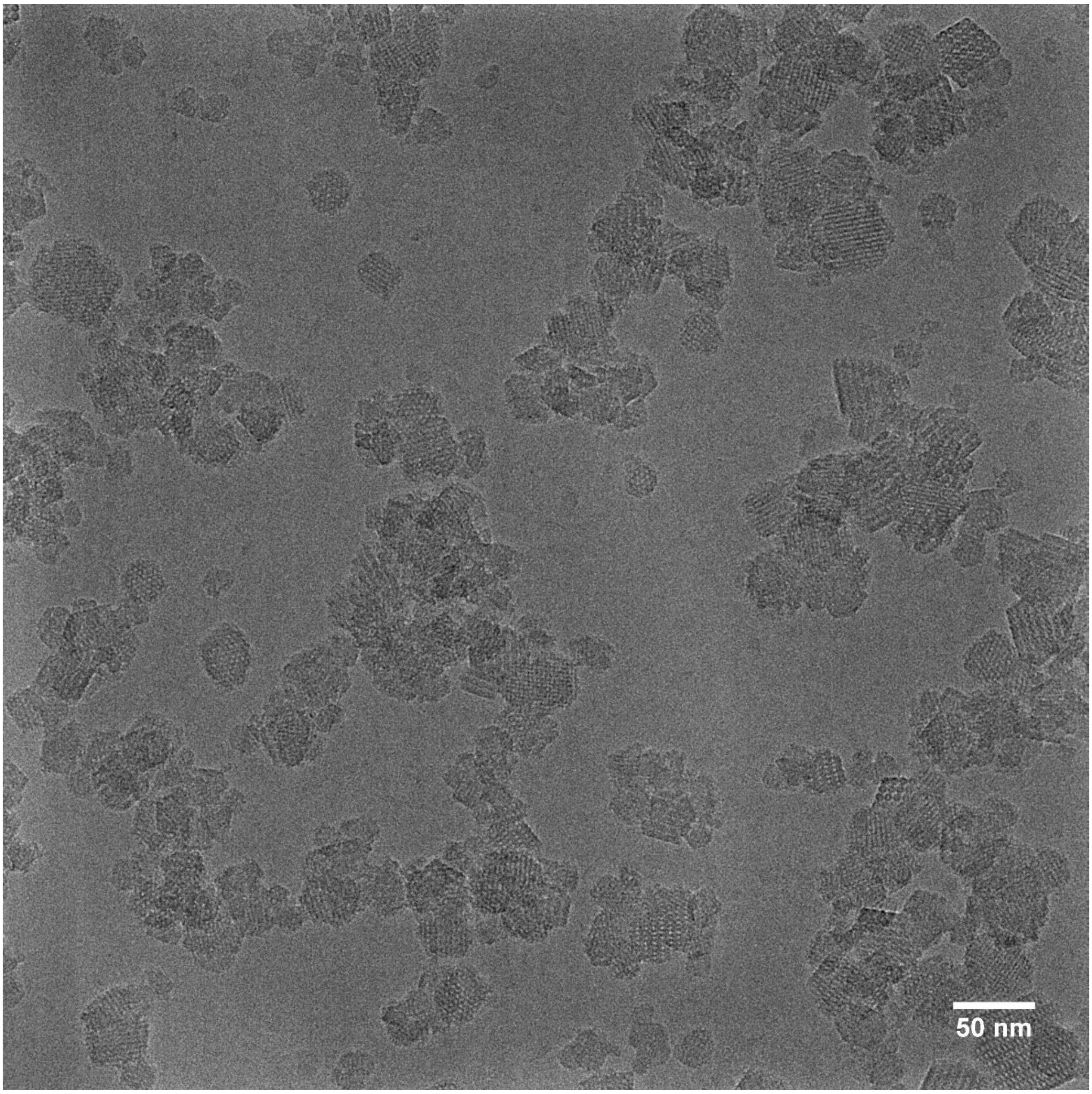

Figure S3.7. TEM micrograph of MIL-101(Cr).

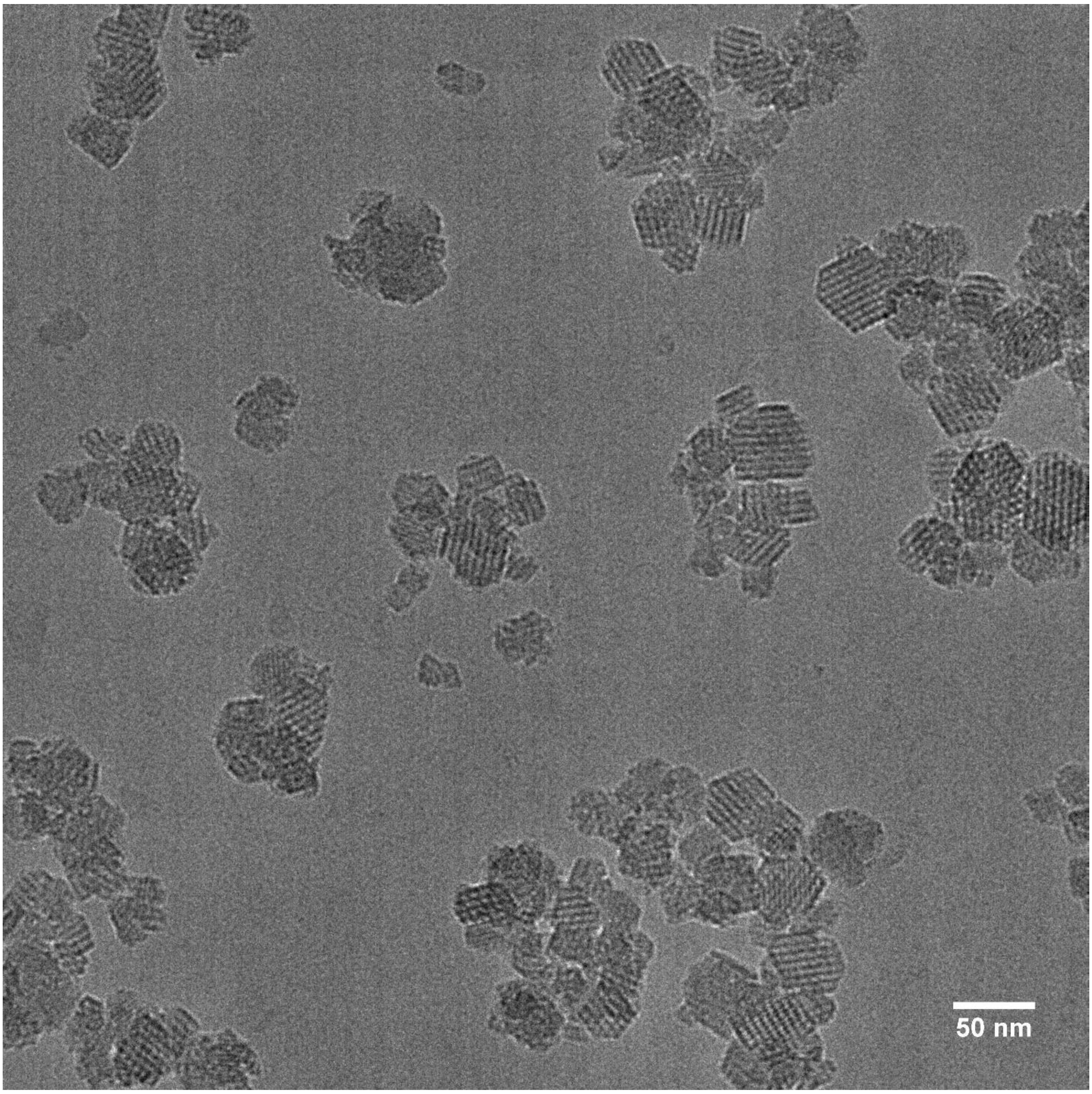

Figure S3.8. TEM micrograph of pyridine-functionalized MIL-101(Cr).

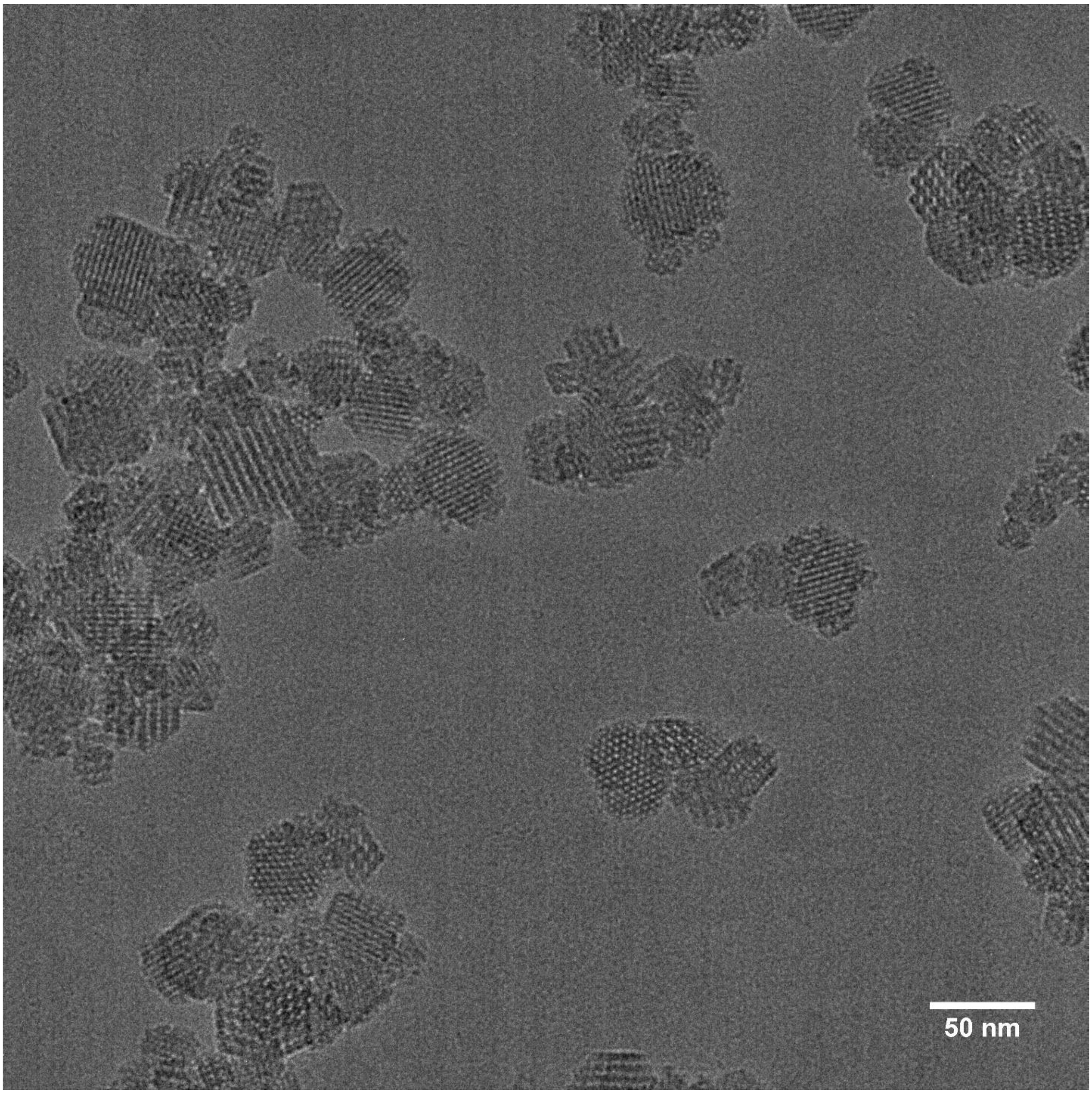

Figure S3.9. TEM micrograph of pyrazine-functionalized MIL-101(Cr).

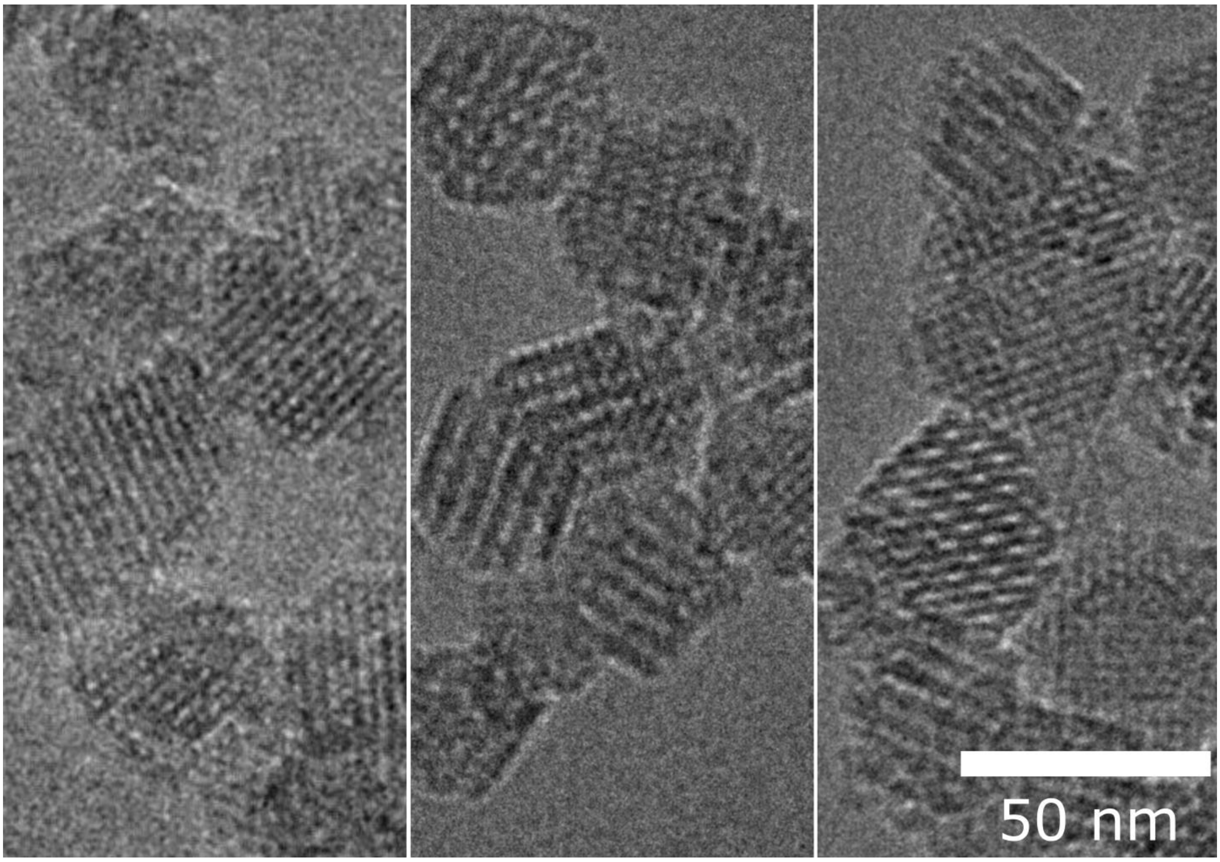

Figure S3.10. Zoomed-in micrographs of MIL-101(Cr) (left) and its pyridine-functionalized (middle) and pyrazine-functionalized (right) derivatives.

3.5.6 Scanning Electron Microscopy

Figure S3.11, **Figure S3.13** and **Figure S3.15** give an overview of the initial MIL-101(Cr) sample and the pyridine and pyrazine functionalized derivatives. Additionally in the top right corner of each of the micrographs, the nanoparticles, which have been used for particle size determination, are marked with yellow lines. All three samples look homogeneous. A more detailed view on the particles is shown in **Figure S3.12**, **Figure S3.14** and **Figure S3.16**. Again, the samples look very similarly. The resulting particle size distributions for the dried species have been determined manually by measuring the diameter of ~100 particles of the respective species and are shown in **Figure S3.17**, **Figure S3.19** and **Figure S3.18** and are additionally summarized in **Table S3.4**.

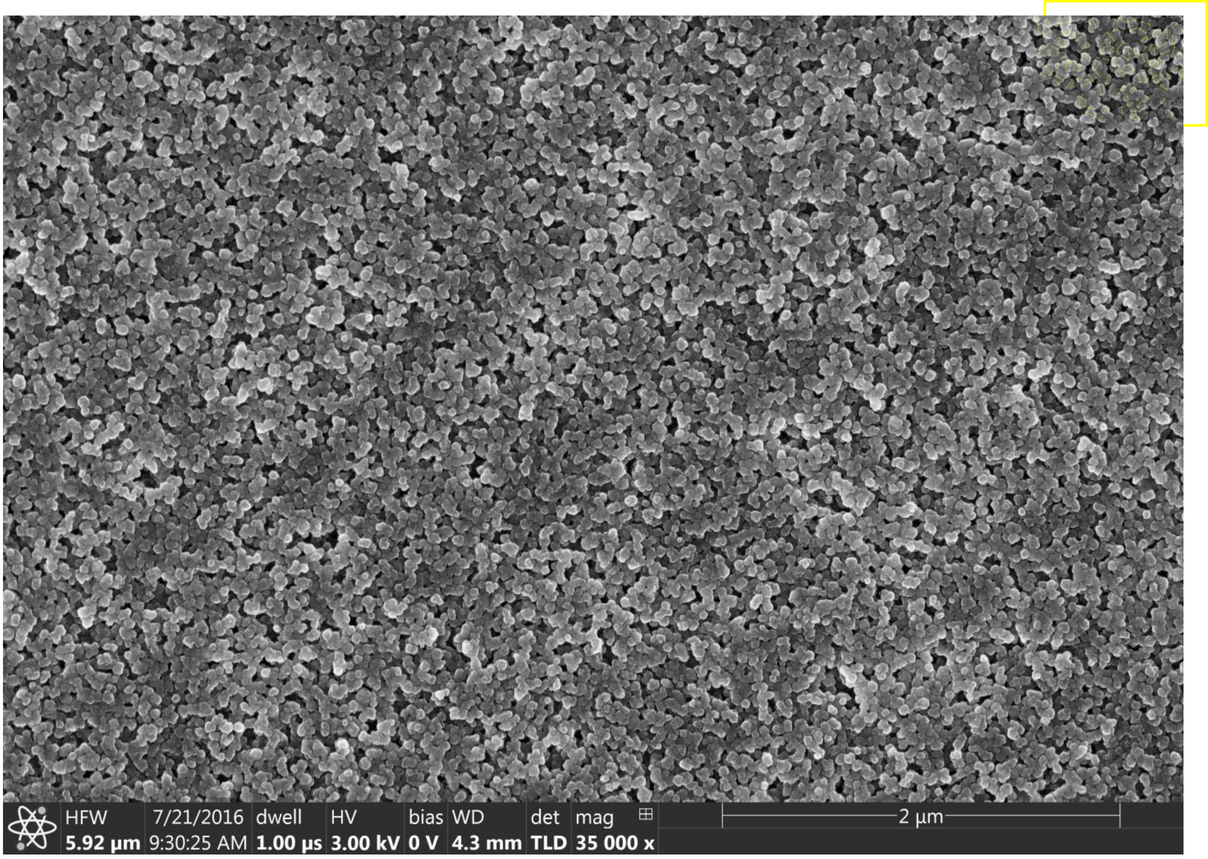

Figure S3.11. SEM micrograph of MIL-101(Cr). In the top right corner: Particles which have been measured for the size determination.

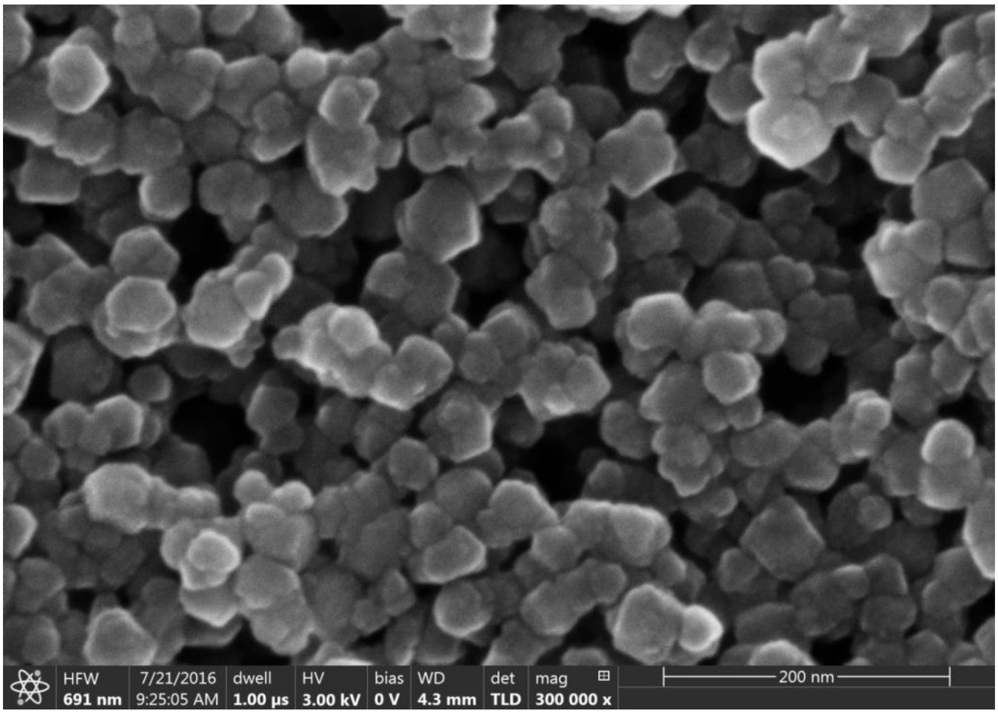

Figure S3.12. SEM micrograph of MIL-101(Cr).

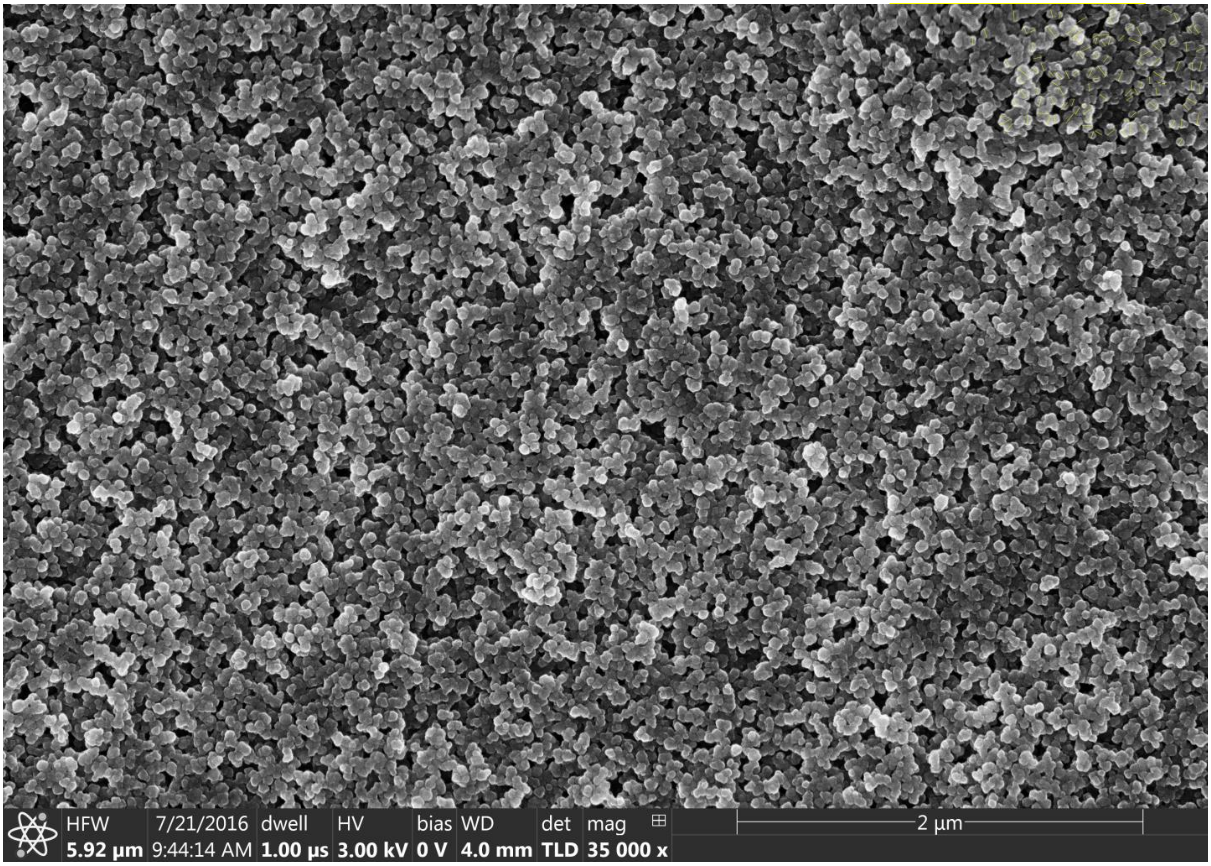

Figure S3.13. SEM micrograph of pyridine-functionalized MIL-101(Cr). In the top right corner: Particles which have been measured for the size determination.

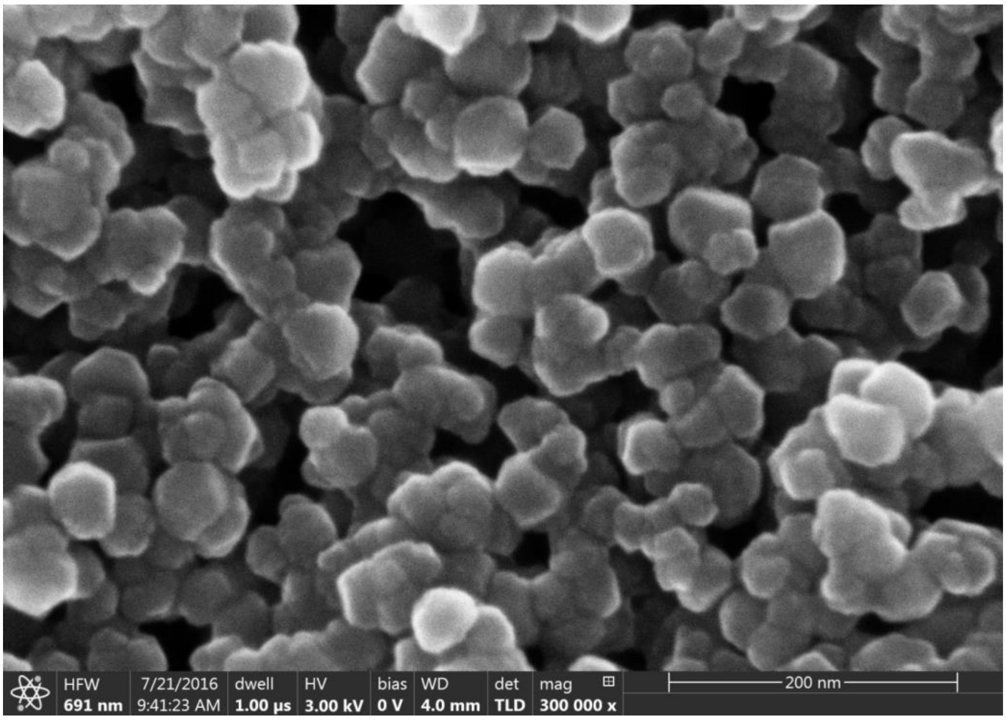

Figure S3.14. SEM micrograph of pyridine-functionalized MIL-101(Cr)

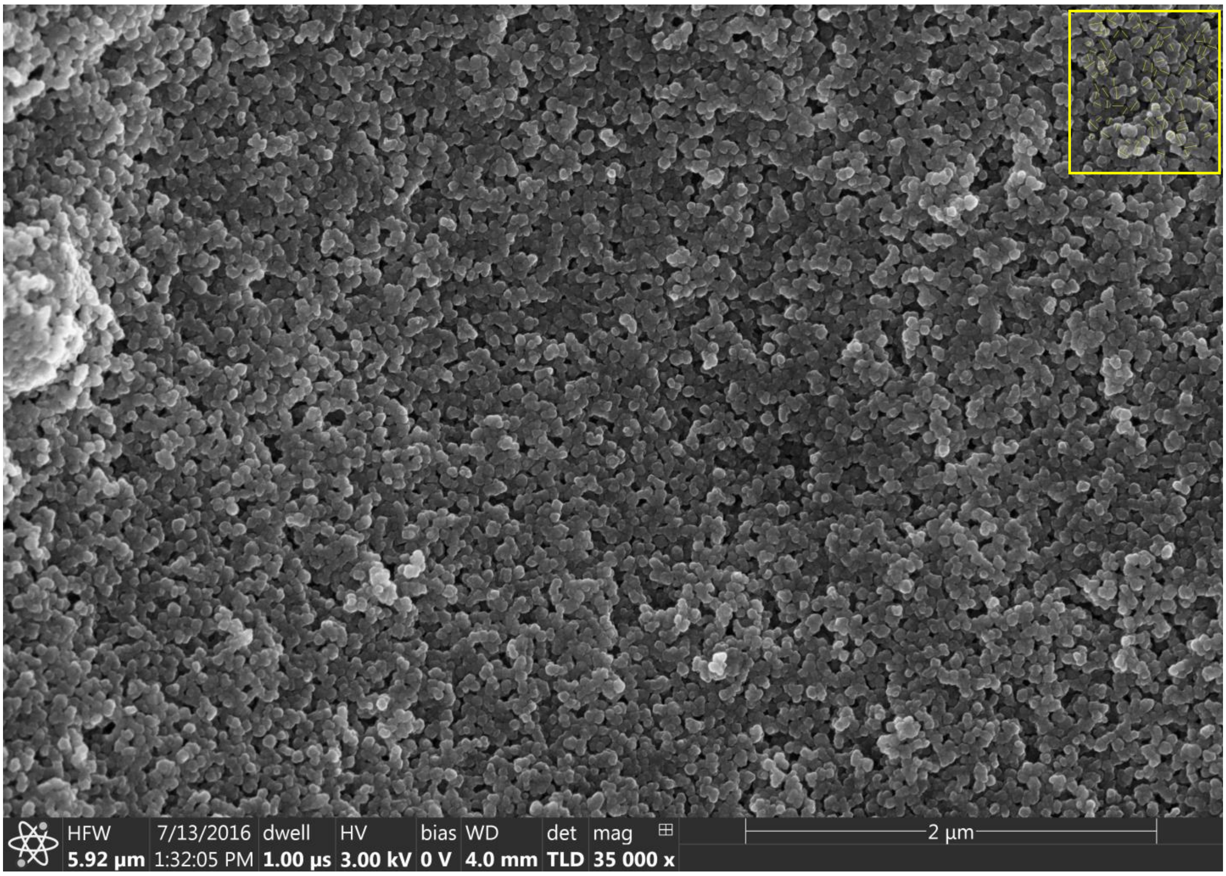

Figure S3.15. SEM Micrograph of pyrazine-functionalized MIL-101(Cr). In the top right corner: Particles which have been measured for the size determination.

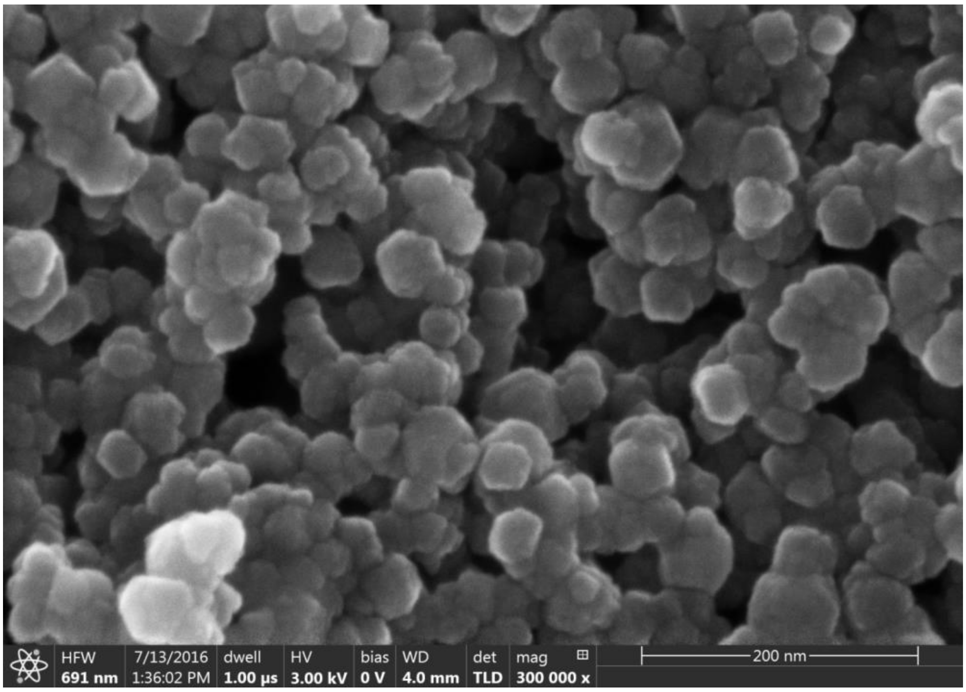

Figure S3.16. SEM micrograph of pyrazine-functionalized MIL-101(Cr).

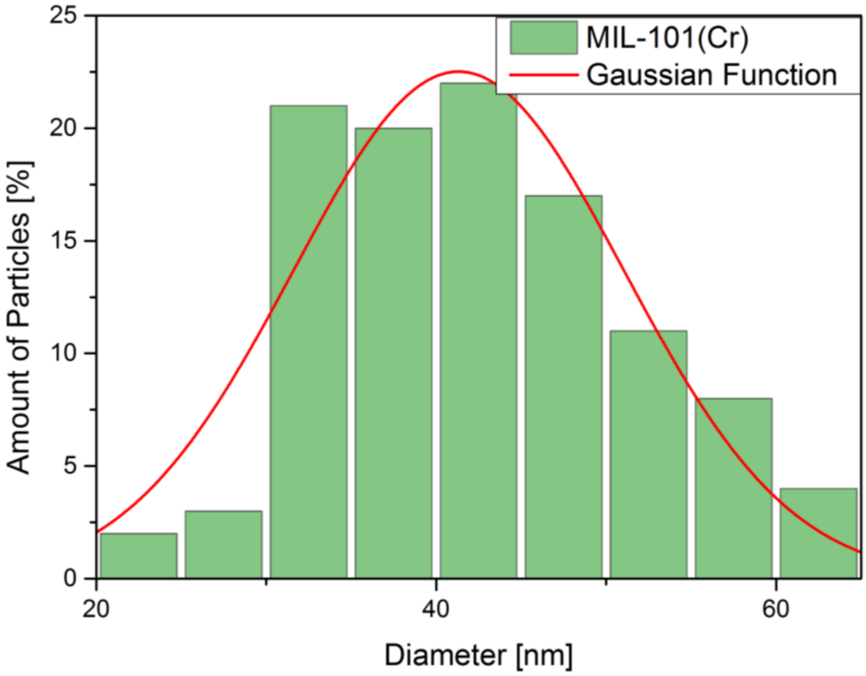

Figure S3.17. Particle size distribution of MIL-101(Cr) determined from the SEM micrograph in **Figure S3.11**.

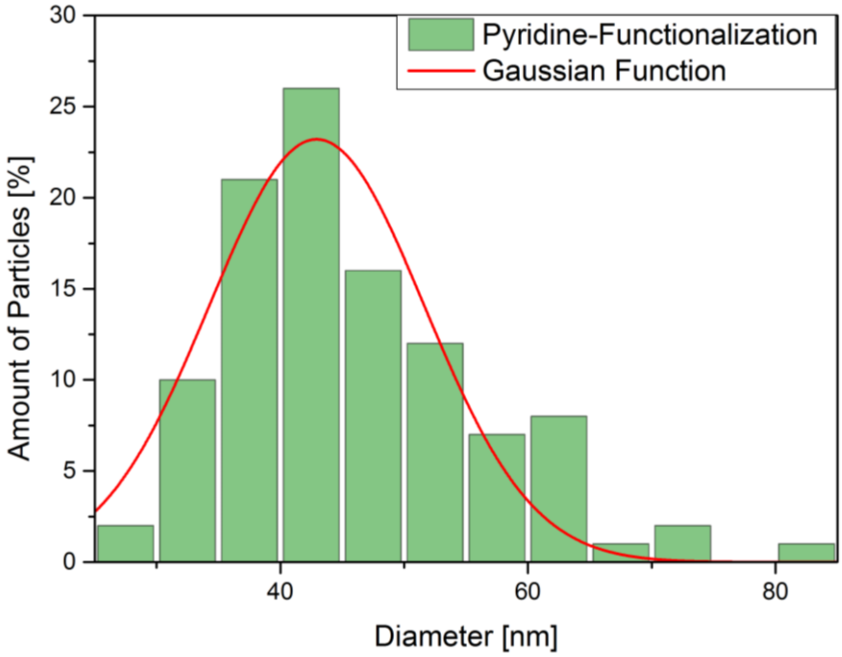

Figure S3.18. Particle size distribution of pyridine-functionalized MIL-101(Cr) determined from the SEM micrograph in **Figure S3.13**.

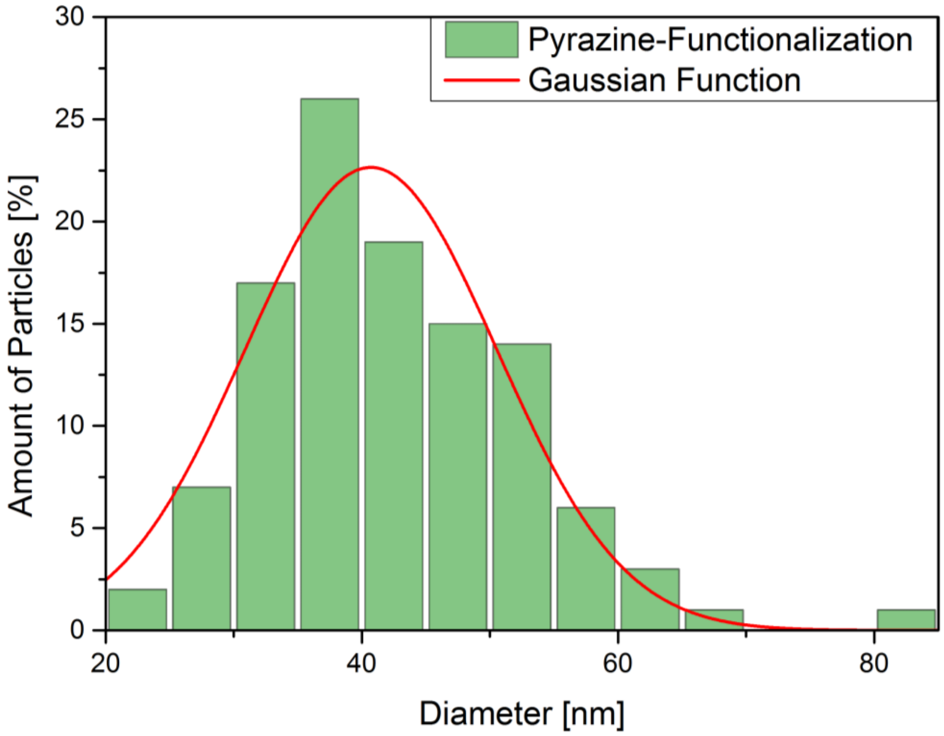

Figure S3.19. Particle size distribution of pyrazine-functionalized MIL-101(Cr) determined from the SEM micrograph in **Figure S3.15**.

Table S3.4. Results of particle size distribution analysis from the SEM images

Sample	**MIL-101(Cr)**	**Pyridine-Functionalization**	**Pyrazine-Functionalization**
Particle Diameter [nm]	41	43	41
Standard Deviation [nm]	10	9	10

3.5.7 Dynamic Light Scattering and Zeta-Potential measurements

Figure S3.20 depicts the pH dependent Zeta-Potential of MIL-101(Cr) NPs in aqueous solution. At pH = 2 starting from around 30 mV, the potential drops for increasing pH. In the initial acidic conditions, the particles are stable and not agglomerated. When reaching pH = 7 upwards, the Zeta-Potential passes through 0 mV, which causes the particles to agglomerate.

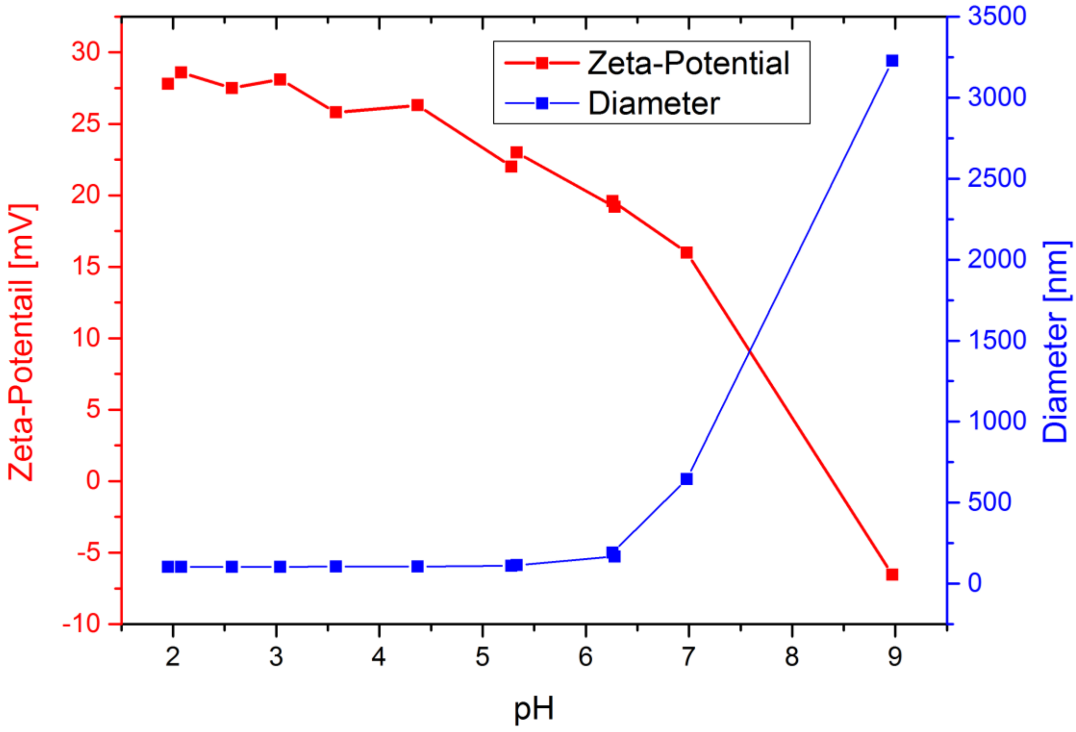

Figure S3.20. Zeta-Potential of an aqueous solution of MIL-101(Cr) NPs, when titrating from pH = 2 to pH = 7.

The results of the DLS-measurements for the functionalized and unfunctionalized MIL-101(Cr) NPs in ethanol are given in **Figure S3.21**. **Table S3.5** gives the average intensity-based diameter of the nanoparticles along with their polydispersity index. Overall, the DLS based hydrodynamic diameter of the particles was nearly not influenced during their functionalization. In all three cases, the particles show similar a similar size around 105 nm and a very monodisperse particle size distribution.

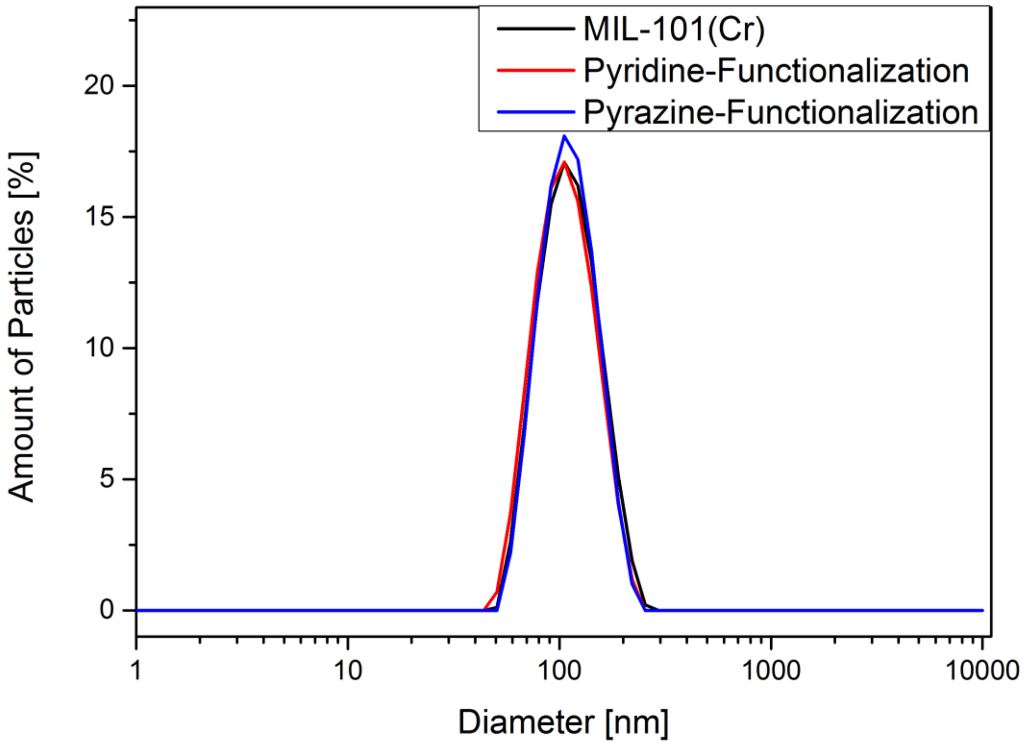

Figure S3.21. Intensity based particle size distribution of functionalized and non-functionalized MIL-101 (Cr) NPs in ethanol.

Table S3.5. Summarized results of the DLS measurements

Sample	Diameter [nm]	Polydispersity Index
MIL-101(Cr)	105	0.088
Pyridine-Functionalized	105	0.174
Pyrazine-Functionalized	106	0.066

3.5.8 Thermogravimetric Analysis

The thermogravimetric analysis for the MIL-101(Cr) NPs sample and its functionalized derivatives is shown in **Figure S3.22**. All three samples show similar stability. The samples feature a degradation range between 327 – 374 °C. The values of the residual masses of the nanoparticle species are slightly shifted. This may be caused for several reasons: Due to the pyridine/pyrazine functionalization the overall ratio of the solvent/framework masses is altered due to the additional mass of the introduced molecules and the varying capability of the nanoparticle species to incorporate solvent molecules. The functionalization approach overall however has not influenced the framework stability.

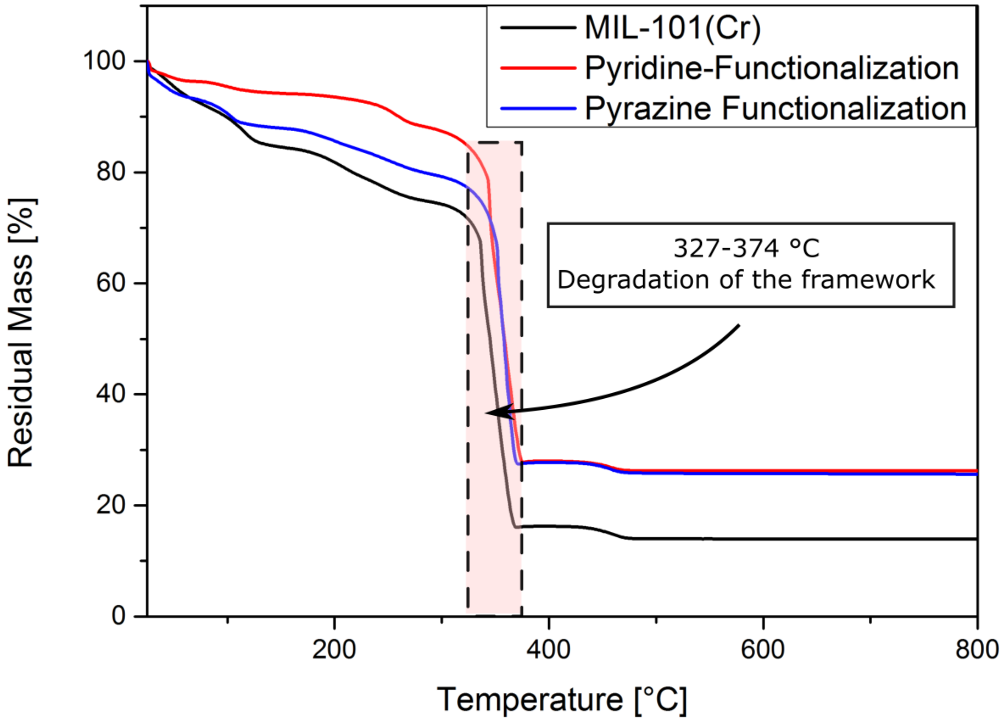

Figure S3.22. Thermogravimetric analysis of MIL-101(Cr) NPs, pyridine-functionalized MIL-101(Cr) NPs and pyrazine-functionalized MIL-101(Cr) NPs.

3.5.9 Elemental Analysis

In order to estimate the degree of functionalization of the MIL-101(Cr) species elementary analysis (CHNS) was performed. Weight-in masses of the respective samples and their results are summarized in **Table S3.6**.

Table S3.6. Elementary analysis results

Sample	Mass [mg]	wt% N	wt% C	wt% H
MIL-101(Cr)	4.882	0.87	18.50	6.85
Pyridine-Functionalization	4.905	2.11	23.69	6.56
Pyrazine Functionalization	4.595	1.37	20.20	6.67

This data has been interpreted the following way: In the pure MIl-101(Cr) MOF sample, there is still a small amount of residual nitrogen trapped within the framework, which is caused due to the synthesis route having $Cu(NO_3)_3 \cdot 9\ H_2O$ as a substrate. The difference in wt% for nitrogen after subtracting the amount of initial nitrogen was assumed to be caused by pyridine and pyrazine respectively the functionalized samples. Based on the crystallographic data from the group of Férey[3] the theoretical wt% of nitrogen in pyridine and pyrazine-functionalized MIL-101(Cr) was calculated and compared with the experimental results. This resulted in a functionalization of (26.8 ± 9.2)% for the pyridine functionalized sample and (5.4 ± 4.6)% for the pyrazine-functionalized sample.

3.5.10 Nitrogen Sorption

The results of the BET calculation of the nitrogen sorption experiments are summarized in **Table S3.7**. The corresponding Isotherms are shown in **Figure S3.23**. The BET-surface was reduced both for the pyridine and the pyrazine-functionalization. This is expected, since aromatic use up space within the framework. The greater reduction in case of pyrazine is expected as well, since the functionalization degree for pyridine was higher than for the pyrazine-functionalized sample. The pyrazine-functionalization had no notable effect on the pore size distribution on the sample. The pyridine-functionalization did reduce the amount of pores in the 3 nm range, however they are still present. This might be attributed to the greater functionalization degree of the pyridine-functionalized sample. As shown in the XRD experiments, this had no influence on the structure of the MOF.

Table S3.7. Results of the BET analysis

Sample	MIL-101(Cr)	Pyridine-Functionalization	Pyrazine-Functionalization
BET-surface area [m²/g]	4789	3194	3506
Relative pressure range used for calculation	0.11-0.23	0.07 - 0.18	0.07-0.21
Correlation coefficient	0.999	0.999	0.999
C-constant	positive	positive	positive

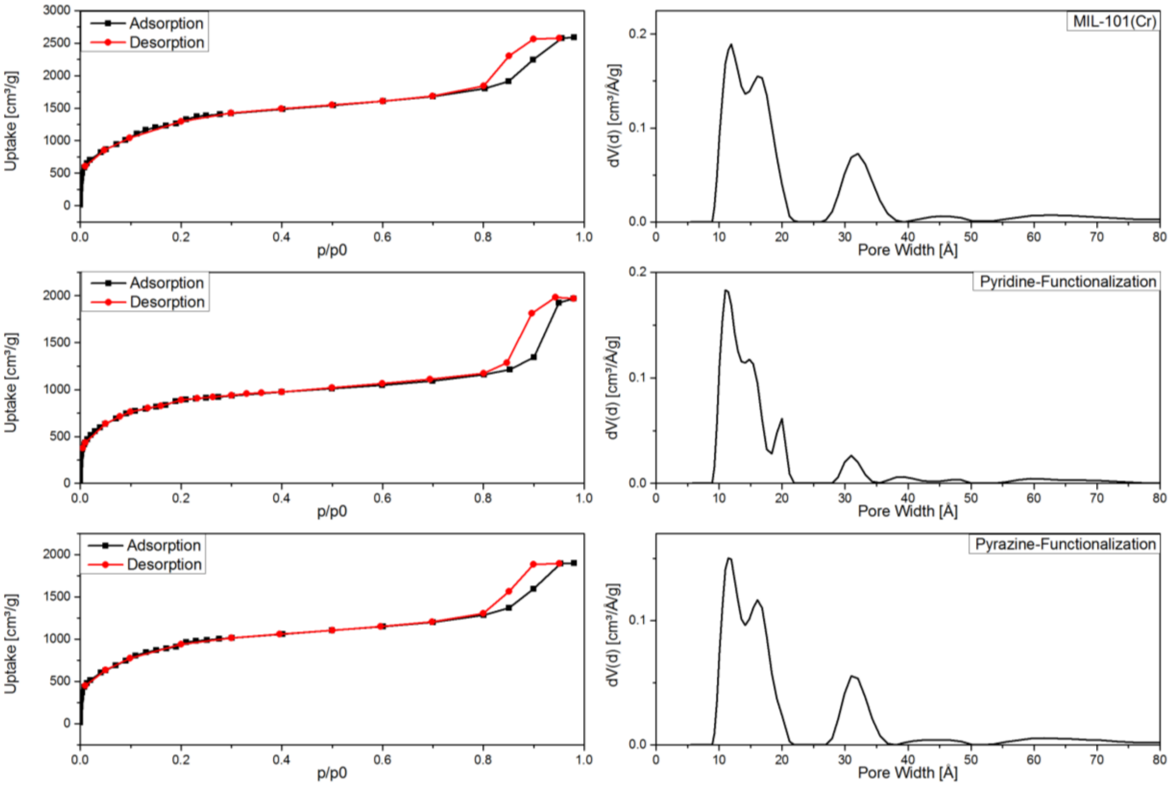

Figure S3.23. Results Nitrogen Sorption Experiments of MIL-101(Cr) (Top) and the pyridine (middle) and pyrazine-functionalized (bottom) species

3.5.11 Porosity Estimation and Calculation

The density of dry MIL-101(Cr) at 0.66 g/cm³was calculated using literature crystallographic data[4] from which all free solvent molecules were removed, and by dividing the mass of the remaining atoms in the elementary cell of the structure by the cell volume. This modified crystal structure was then used for an estimation of the porosity of MIL-101(Cr). The data were evaluated using the “Atom Volumes & Surfaces” tool of the software package Materials Studio v7.0 (*Accelrys Software Inc*.). The program was used to calculate a probe-molecule dependent Connolly surface with a grid interval of 0.75 Å. The program also provides an occupied and free volume within the elementary cell. This free volume and the total volume of the elementary cell were then used to calculate the porosity of the crystal structure. With the probe radius set to 0 Å the porosity equals 84.5%. The corresponding Connolly surface is shown in **Figure S3.24**. Using a probe radius of 1.4 Å to simulate water, the porosity of the framework equaled 82.1%. In case of ethanol, a probe radius of 2.2 Å was assumed resulting in a porosity of 79.1%.

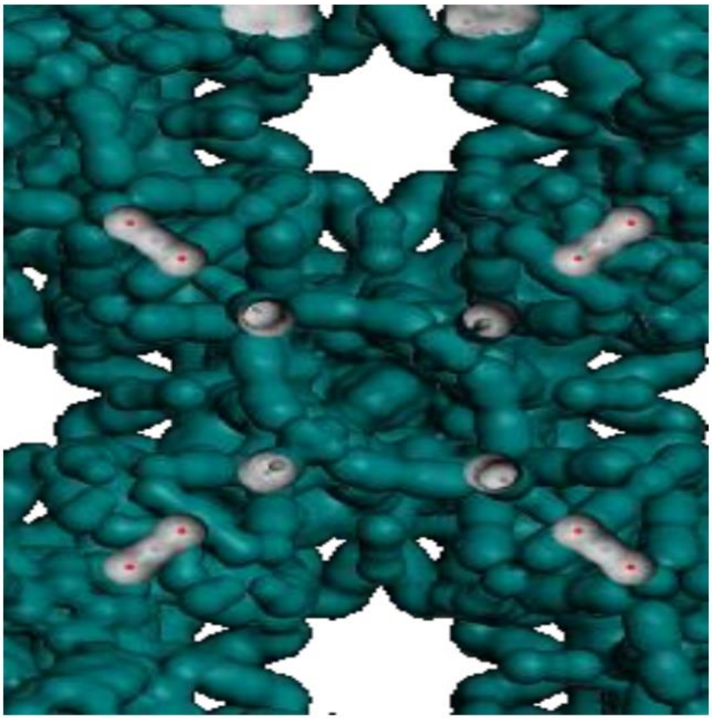

Figure S3.24. Connolly surface of MIL-101(Cr).

References

1 Modena, M. M., Wang, Y., Riedel, D. & Burg, T. P. Resolution enhancement of suspended microchannel resonators for weighing of biomolecular complexes in solution. *Lab Chip* **14**, 342-350, doi:10.1039/c3lc51058a (2014).

2 “Useful Latex Bead Formulae, c. b. f. u. w. t. c. c. e. h. l.-s. c.-a. q.-m.-n. i.-s.-f.-l.-b. l.-b.-t.-o.

3 Lebedev, O. I., Millange, F., Serre, C., Van Tendeloo, G. & Férey, G. First Direct Imaging of Giant Pores of the Metal−Organic Framework MIL-101. *Chem. Mater.* **17**, 6525-6527, doi:10.1021/cm051870o (2005).

4 Férey, G. M.-D., C.; Serre, C.; Millange, F.; Dutour, J.; Surblé, S.; Margiolaki, I. A Chromium terephthalate-Based Solid with Unusually Large Pore Volumes and Surface Area. *Science* **309**, 2040-2042 (2005).

4 The Need for Material Optimization of Nanoparticles in Biomedicine: The Example of Iron(III) fumarate

This chapter is based on the following article:

Hirschle P, Hirschle C, Böll K, Döblinger M, Höhn M, Tuffnell JM, Ashling CW, Keen DA, Bennett TD, Rädler JO, Wagner E, Peller M, Lächelt U, Wuttke S. *The need for material optimization of nanoparticles in biomedicine: the example of iron(III) fumarate.* Chem Mater. **Currently in Revision**

4.1 Introduction

There is a perpetual need for new colloidal nano and microparticles in biomedical applications such as drug delivery, imaging, cell labeling and cancer therapy.[1-10] The last two decades have witnessed the development of many new material classes that can be used in these applications, but these advances have also identified a new range of problems to tackle.[11-13] One such problem is the feasibility of synthesis; biomedical applications desire particles that are simple to synthesize, ideally under aqueous conditions. Any synthesis must also reliably produce particles with specific characteristics. Products should be of high purity, and monodisperse size and shape to ensure reproducible *in vitro* and *in vivo* results.[9] These particles should be functionalizable in order to equip them with imaging capabilities and/or to improve their colloidal stability and/or control their biodistribution with cell-targeting receptors. In general, particles destined for drug delivery should be highly porous and have a functionalizable inner surface to control loading and release of drugs. And as always, biomedical applications require intense study and control over the potential toxicity of new materials – a problem that can be mitigated by using biocompatible building blocks and ensuring biodegradability.[8,9]

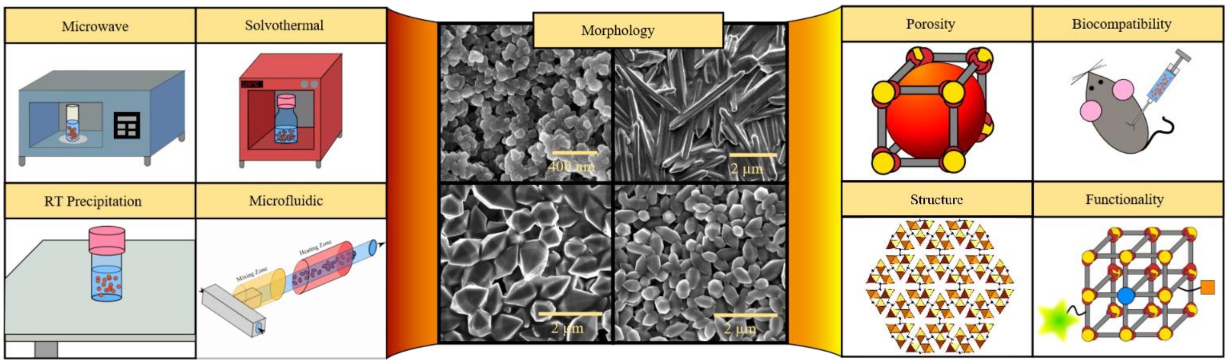

Figure 4.1. Schematic idea of this work, from left to right: The synthesis of iron(III) fumarate particles was optimized using four different synthesis approaches. By controlling reaction parameters four different iron(III) fumarate variants depicted here in scanning electron micrographs have been isolated. These particles were then further characterized with biological and physicochemical techniques to understand the connection between morphology, size, porosity, functionality and biocompatibility.

Iron(III) fumarate excels in all of these categories and is therefore a promising candidate for biomedical use. This material features a mixed organic and inorganic architecture and has been used to produce crystalline solids of various particle sizes (**Table 4.1**). In its crystalline form, iron(III) fumarate exhibits the metal-organic framework (MOF) structure of MIL-88A.[14] The hexagonal crystal structure of this coordination framework consists of Fe^{3+} ions arranged into Fe_3O_{16} iron-oxo trimers that are in turn connected by the bridging ligand fumaric acid (**Figure S4.8**). The resulting material is a microporous and flexible hybrid structure. Solvent and other guest molecules can penetrate into the pores resulting in a shifting of the lattice parameters that allows for pore volume increase, so-called “breathing”.[15-18] Iron(III) fumarate is highly biocompatible since its components are ubiquitous in the human body; fumaric acid is a critical component of the citric acid cycle, and iron is a trace element in our body and part of many enzymes and proteins such as hemoglobin. Iron(III) fumarate particles offer remarkable functionality due to their hybrid nature. Coordinatively unsaturated metal-centers on the particle surface are available for Lewis bases to bond, enabling post-synthetic modification.[19] These molecules can be used to either modify the finished material by selectively changing its outer surface to feature hydrophilic properties[20] or adding functionalities such as fluorescent centers[21]. Other functionalization approaches can be applied during particle synthesis to introduce monovalent capping agents that carry functional groups at the particle surface.[22]

In addition to this functionalizability, iron(III) fumarate offers important intrinsic functionality that makes it well-suited for clinical imaging: crystalline iron(III) fumarate is built to a large part from paramagnetic Fe^{3+} ions, which qualifies the framework material for potential use as a contrast agent in magnetic resonance imaging (MRI).[23,24] Furthermore, gold functionalized iron(III) fumarate particles have done well as contrast agents in other clinical imaging methods such as computer tomography and photoacoustic imaging.[24] Iron(III) fumarate nanoparticles have shown great compatibility with biological coatings such as exosomes[25,26] and liposomes[26]. Being both a biocompatible and functionalizable material, numerous reports concerning iron(III) fumarate nano and microparticles as potential drug carriers have been published. [19,21,23,25-28] Functionalized iron(III) fumarate has also been discussed as a platform for sensing large bio-molecules such as DNA[22] and for small molecule detection[29]. The large internal surface area of the material and its heterogeneous organic and inorganic architecture make it also an ideal candidate for non-biomedical applications such as storage of small molecules, catalysis and electrochemistry. Catalytic and electrochemical studies may make use of the active iron(III) centers of the framework itself [30-33] , use the material in combination with other active components[34,35], or use it as a precursor for porous carbon-based catalysts with methods such as calcination.[36-43] The storage and capturing of small molecules relies on host-guest interactions such as physisorption or chemisorption with the iron(III) centers and linker molecules of the framework. Iron(III) fumarate has been examined for the uptake of nitrogen(II) monoxide[19], fluoride,[44] alkanes[45], ethylene[46] and hydrogen[47]. A summary of all applications along with their respective iron(III) fumarate variants is shown in **Table 4.1**. All of these applications are based on iron(III) fumarate, however their material properties such as particle size and shape do not appear to be standardized.

To date the monodisperse synthesis of particles in this system is contradictory and not well established.[48] Advances that were made to characterize the crystallization of this structure either rely on the usage of modulating additives or fail to characterize the particles' functionality and biocompatibility.[27,39,49-51] Mastering the synthesis of iron(III) fumarate particles and understanding the connection of their morphology and structure with their material and biological properties is imperative for unlocking their potential for biomedical purposes. The study presented here therefore serves multiple purposes: (i) to systematically study the relationship between synthesis conditions (e.g. heating method, reaction parameters, solvent, reactant concentration), morphology and crystallinity of iron(III) fumarate; (ii) to investigate the impact of morphology upon the particles' intrinsic material properties (e.g. MRT activity and porosity); and (iii) to explore their biocompatibility to finally connect those data with their physicochemical parameters (e.g. morphology and size).

Table 4.1. Applications of iron(III) fumarate in the literature

Iron(III) fumarate type	Application	Publication
Nanoparticles	Drug delivery	21,23,25-28
	Imaging	23,24
	Sensing	22,29,39
	Catalysis	38,42
Microparticles	Water purification	44
	Catalysis	31-37
	Electrochemistry	38, 41, 43
	Gas storage	46
Not specified	Gas storage	45,52
	Catalysis	30
	Drug Delivery	19

Having all these points in mind, we investigated the influence of different synthesis approaches including solvothermal, microwave assisted and microfluidic heating as well as room temperature precipitation on the iron(III) fumarate system. By optimizing the reaction conditions such as time, temperature, reactant concentration, and solvents we were able to control the morphology of the emerging particles, resulting in four isolated distinct iron(III) fumarate variants. These particles were then further characterized to address the three aforementioned targets. To reach our first goal, the iron(III) fumarate types generated under different synthesis conditions were characterized with a combination of electron microscopy, electron diffraction and X-ray diffraction. To address our second point we were examining the iron(III) fumarate types with nitrogen sorption, *in-situ* X-ray diffraction and by determining magnetic resonance relaxivities. Lastly, we were testing the particles for cytotoxicity and interactions with cells.

4.2 Results: Morphological Control of Iron(III) Fumarate

Biomedical applications rely on high-quality nano and microparticles generated with reproducible synthesis protocols that are up-scalable and yield a product with monodisperse morphology and size. The growth of nanocrystalline MOFs is typically controlled by using modulating capping agents such as surfactants and short monocarboxylic acids.[53] In our study we avoid this chemical approach as it comes with adverse side effects. The modulating agents complicate an otherwise simple reaction by introducing another component to the reaction mixture that accumulates on the outer particle surface.[54] Additionally, these modulating agents are typically toxic. Therefore, in this section we study the formation of iron(III) fumarate particles using a variety of heating methods and devices including conventional and microwave ovens in addition to a microfluidic reactor, a synthesis technique that has recently captured the attention of the MOF community.[28,55-58] We compare the particle formation in the most commonly used solvent for iron(III) fumarate synthesis, namely *N*,*N*-dimethylformamide (DMF), and water which is the solvent of choice for any kind of biomedical applications.

Iron(III) fumarate synthesis in DMF was performed by first dissolving iron(III) chloride hexahydrate in fresh DMF under sonication and subsequently adding a corresponding amount of fumaric acid to the reaction mixture. The resulting solution (0.2 M iron(III) chloride hexahydrate, 0.2 M fumaric acid) was used as a basis for the different synthesis approaches. This reaction solution was incubated for several weeks at room temperature (RT) to check for any crystallites forming. No particle formation was observed, which suggests that the synthesis of iron(III) fumarate under these conditions requires heating. For solvothermal experiments, this stock solution was used in its concentrated (0.2 M) form and additionally in a tenfold diluted concentration (0.02 M). The morphology and homogeneity of the resulting iron(III) fumarate particles shown in this section depends, amongst other factors, on heating time. In order to provide the steep heating ramps and fast heat transfer throughout the reaction vessel that is necessary for a well-defined nucleation and growth period of the iron(III) fumarate crystallites, solvothermal experiments with reaction times of less than 2 h were performed in reaction volumes limited to 1 mL (for more reaction details see section 4.7). For high reactant concentrations, solvothermal heating triggered the first formation of iron(III) fumarate over the course of 6 h at 60 °C. Increasing the temperature to 120 °C shortened the reaction time to 30 min. These particles are micrometer-sized and exhibit homogeneous pyramidal shape when first formed, however with further increase of reaction time this homogeneity is lost (**Figure S4.9**). We attribute this to the formation of new nucleation centers during the longer heating period. To study the influence of reactant concentration on iron(III) fumarate particles in DMF the reactant concentration was lowered by a factor of 10. This led to improved homogeneity as well as to an elongated morphology of the particles (**Figure S4.10**). A tenfold reduction of the reaction time improved particle homogeneity under these low concentration conditions even further (**Figure S4.11**). Additional decrease of temperature did not influence the resulting particle morphology but slowed down the time for particle formation (**Figure S4.11**). Microfluidic particle growth in DMF was conducted using a single syringe setup that was fed with a premixed high concentration solution of all precursors into PTFE tubing. Upon traversing this tubing, the reaction mixture was subjected to a heating zone with a defined length. Therefore, reaction times in these experiments were determined by the speed of the reaction solution within the tubing (**Figure S4.12**). Due to the improved heat transfer and reaction times in this setup the particles crystallization time was shortened by a factor of two to 15 min, as well as a decrease in the particle size to below 1 µm. Using lower flow rates and therefore longer reaction times led to an increase in particle size (**Figure S4.13**). Prolonged use (2 h) of this setup lead to a clogging of the microfluidic tubing due to particle growth on the tubing walls. The challenge of implementing fast heating and cooling rates in DMF could be overcome by microwave-assisted heating. In these experiments reaction temperatures were adjusted in less than a minute while providing 20 times the reaction volume of the solvothermal approaches and were stopped by fast quenching in cold DMF. Compared to microfluidic synthesis, microwave assisted heating at 120 °C in a 5 minute synthesis protocol decreased particle size by 50% (**Figure S4.14**). Further decrease of reaction time resulted in polydisperse particles and very low yields.

Iron(III) fumarate synthesis in water was conducted by preparing an aqueous solution of iron(III) chloride hexahydrate and adding a stoichiometric amount of fumaric acid (0.2 M iron(III) chloride hexahydrate, 0.2 M fumaric acid). The resulting suspension was used as a basis for further experiments. Within the first two minutes after preparing this reaction mixture, precipitation of spherical iron(III) fumarate nanoparticles can be observed (**Figure**

S4.15). Over time, there was additional formation of crystalline iron(III) fumarate needles embedded in a matrix of interconnected spherical nanoparticles. With longer reaction time these needles grew larger until after 4 days the matrix had completely vanished leading to micrometer sized particles (**Figure S4.16**). During this time, the crystallinity of the overall sample increased drastically (**Figure S4.17**). Elevated temperatures such as in solvothermal and microwave assisted growth (**Figure S4.18** and **Figure S4.19**) enhanced the rate at which this crystallization transformation was completed. Further reaction time did not change the resulting crystal product noticeably (**Figure S4.19**). Similar to the solvothermal growth experiments in DMF, these experiments were limited to reaction volumes of 1 mL for reaction times below 1 h to ensure a sufficiently fast heating rate. For faster heat transfer and better control over reaction time the microfluidic setup shown schematically in Figure S5 was used. The setup consisted of syringe pumps that feed both aqueous iron(III) chloride and fumaric acid precursor solutions via a T-junction into heated PTFE tubing at a 1 : 1 ratio. These experiments require fully soluble precursors, and thus reactant concentrations were lowered twentyfold. The onset time of the needle formation in this microfluidic reactor was in the same range as for solvothermal growth despite the low reactant concentrations (**Figure S4.20**). During this growth, iron(III) fumarate however precipitates on the walls of the microfluidic tubing, rendering the approach unfeasible for reaction times longer than 10 min. Similar to the other aqueous approaches, under these conditions of fully dissolved precursors the growth of the needle morphology was still preceded by the precipitation of spherical nanoparticles. In order to relate these microfluidic experiments to solvothermal and room temperature experiments, additional experiments were performed. For this, a tenfold diluted iron(III) fumarate solution was mixed with a stoichiometric amount of fumaric acid in a 1:1 ratio. These experiments also initially resulted in the precipitation of spherical nanoparticles of iron(III) fumarate that transformed over time into crystalline micro-needles (**Figure S4.21**). At room temperature, needle crystallization growth was considerably slowed while the microparticles grew in a more bulky shape (**Figure S4.22**).

4.3 Results: Material Characterization

Through optimization of the aforementioned synthesis conditions we isolated 4 variants of iron(III) fumarate particles based on their distinct monodispersity, upscalability and morphology to further compare to each other (**Figure 4.2**). The smallest of these particles referred to as “spherical nanoparticles” were synthesized via RT precipitation from water and feature a diameter of (49 ± 12) nm. The iron(III) fumarate “dipyramidal nanoparticles” feature a length of (400 ± 95) nm and a width of (184 ± 30) nm and were synthesized in a microwave reactor in DMF. “Dipyramidal microparticles” with a diameter of (1.2 ± 0.2) µm were synthesized solvothermally from DMF and needle-shaped microparticles featuring a length of (10 ± 2) µm and a width of (975 ± 420) nm were synthesized solvothermally in water (**Figure S4.23**). The detailed synthesis conditions of these particles are described in the Supporting Information. Chemical stability measurements showed that all iron(III) fumarate particles show resistance towards aqueous cell medium (**Figure S4.24**) and feature excellent long-term

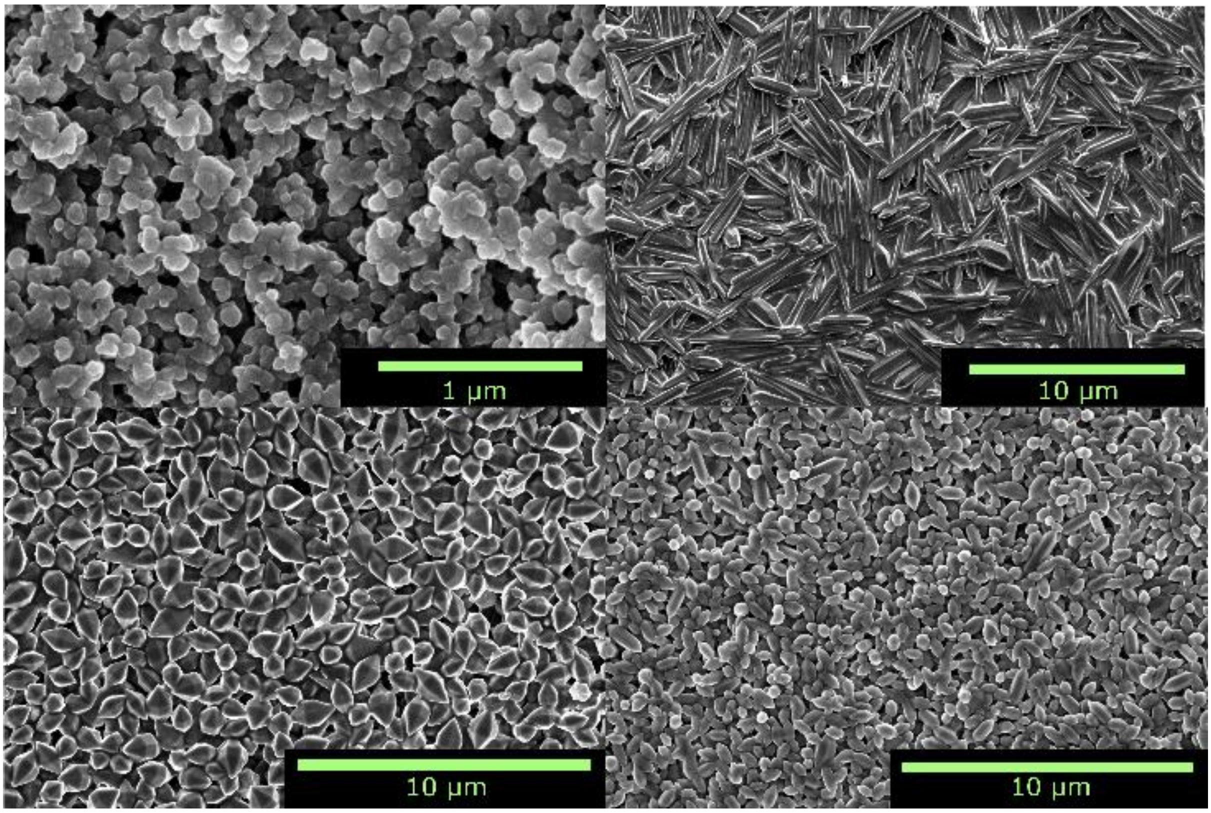

Figure 4.2. SEM micrographs depicting the morphology of the four variants of iron(III) fumarate that were used for further characterization. Top left: spherical nanoparticles, top right: needle-shaped microparticles, bottom left: dipyramidal microparticles, bottom right: dipyramidal nanoparticles.

storage capabilities as all particles can be stored at RT for many months in ethanol (**Figure S4.25**- **Figure S4.28**).

4.3.1 X-Ray Diffraction

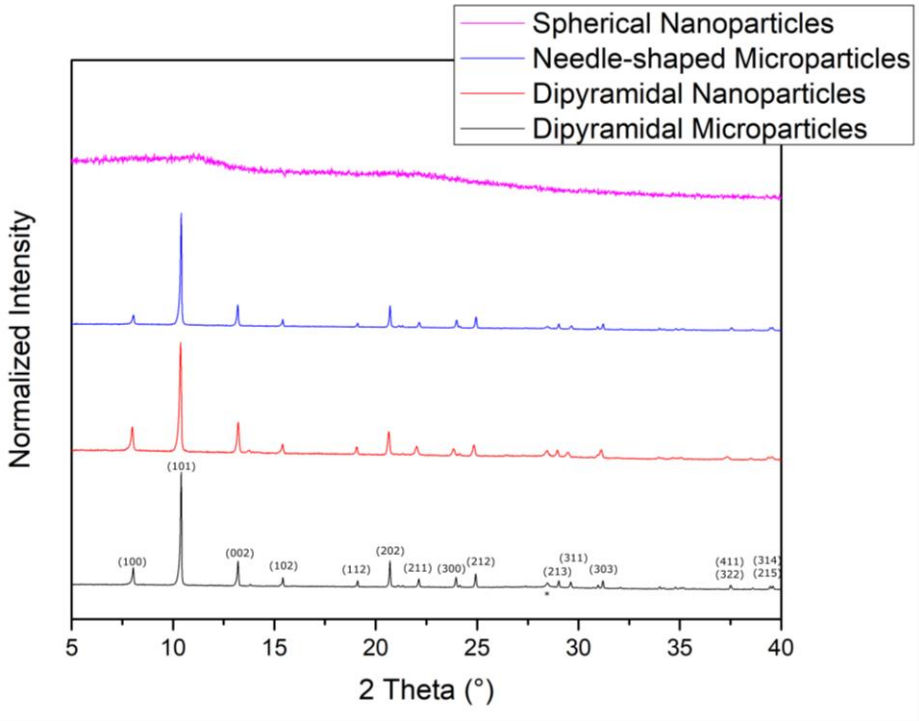

Figure 4.3. X-ray diffraction patterns of the morphologically distinct iron(III) fumarate samples.

X-ray diffraction experiments of all 4 morphologies were performed on powdered samples generated via RT vacuum drying of ethanolic particle dispersions (**Figure 4.3**). Three of the four iron(III) fumarate variants depict crystallinity with X-ray diffraction patterns corresponding to MIL-88A[16] (**Figure S4.8**). The corresponding nano and microparticles exhibit dipyramidal or needle-shaped morphologies (**Figure 4.2**).

Lattice parameter refinements of these 3 samples showing sharp reflections resulted in very similar values (**Table 4.2**). The small deviations can be attributed to the drying process of the flexible MIL-88A structure and distortion of the lattice due to the nanosize of the particles. The spherical nanoparticles on the other hand appear amorphous in these X-ray diffraction experiments. However, we stress that this, as demonstrated later in this work, is only an effect of the small particle domain size. This highlights a key misconception in current MOF literature – i.e. confusion between nanocrystalline and amorphous samples.

Table 4.2. Lattice parameters of the three crystalline iron(III) fumarate samples.

Iron fumarate variant	**a** (Å)	**c (Å)**
Needle-Shaped Microparticles	12.8678(09)	13.5139(14)
Dipyramidal Nanoparticles	12.9307(15)	13.4325(27)
Dipyramidal Microparticles	12.8701(12)	13.4870(17)

4.3.2 Thermogravimetric Analysis

To more closely identify the chemical relationship between the crystalline and the spherical iron(III) fumarate nanoparticle samples, we performed thermogravimetric measurements. The thermogravimetric data for all 4 samples are shown in **Figure S4.29** and **Table S4.8**. The degradation behavior of the samples matches literature data for the MOF MIL-88A.[59] All four samples show a similar two-step degradation upon heating and indicate a similar chemical composition. Due to initial drying of the samples only a low amount (around 5-8 wt%) of residual solvent is physisorbed to the surface. The onset of the degradation at 259 °C- 285 °C agrees well with literature data for the MOF and is caused by the degradation of fumaric acid.[39] After decomposition of the organic component in a two-step process that constitutes 52-57% of the total sample mass, the residual mass of the samples lies at 37-41%, pointing towards a final composition of an iron(III) oxide than can be identified as hematite by XRD (**Figure S4.29**).

4.3.3 Electron Diffraction

For further structural and morphological characterization of the less crystalline spherical nanoparticles, transmission electron microscopy (TEM) was performed. TEM images depict particles featuring a uniform size distribution between 20-30 nm (**Figure 4.4**). Several particles exhibited lattice fringes that quickly vanish during illumination. More gentle electron diffraction (ED) of larger areas resulted in broadened Bragg-rings confirming that a substantial percentage of the particles exhibit crystalline domains (**Figure 4.4**). ED patterns match the lattice distances as well as the expected intensity distribution for MIL-88A.[16] **Figure 4.4** shows a comparison of an experimental ED pattern after azimuthal integration and background subtraction and an ED simulation of iron(III) fumarate with MIL-88A structure. The best fit with respect to reflection broadening was obtained by the Scherrer equation for 3.5 nm along the *a*- and *b*-axes and around 1 nm along the *c*-axis of the hexagonal unit cell.

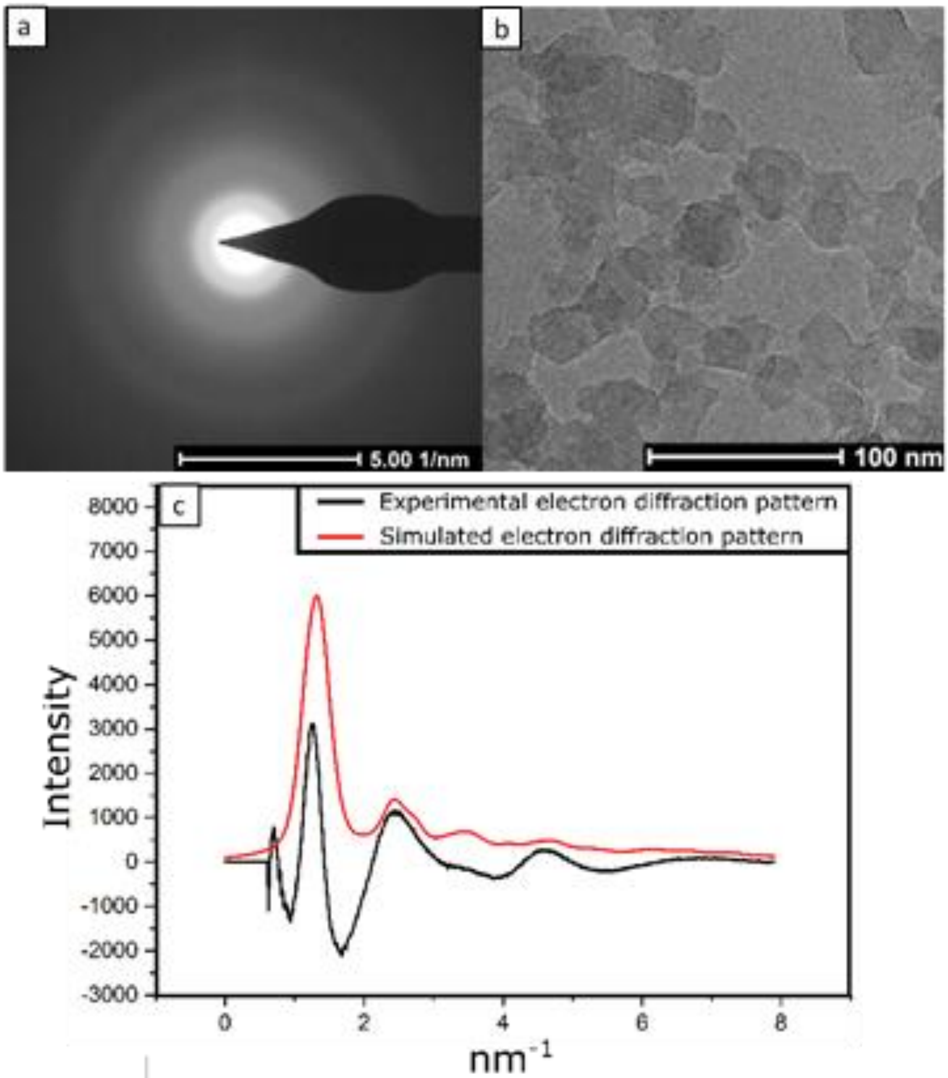

Figure 4.4. a) Electron diffraction pattern and **b**) TEM micrograph of spherical iron(III) fumarate nanoparticles. **c**) Shows the azimuthally integrated electron diffraction pattern after subtraction of the mean scattering intensity (black) compared to the theoretical diffraction pattern of MIL-88A nanoparticles (red).

4.3.4 Pair Distribution Function Analysis

To complement the data acquired from electron diffraction, X-ray total scattering experiments were performed at the I15-1 beamline at the Diamond Light Source, UK (λ = 0.161669 $Å^{-1}$), on all four samples. The total scattering structure factors *S*(*Q*)s (**Figure S4.31**) were extracted after appropriate data corrections.[60] The sharp Bragg features still visible in the *S*(*Q*) for the spherical nanoparticles clearly identify the sample as crystalline, and therefore different from amorphous solid or metal-organic framework glasses, where only smooth features in the structure factors are observed.[61,62] The pair distribution functions, *D*(*r*) for all four samples were obtained upon Fourier Transform (**Figure 4.5**). Identical atom-atom correlations are evident up to ca. 12 Å. The PDFgui software[63] was used to identify the atom-atom correlations responsible for peaks in the 0 – 12 Å region (**Figure S4.32**). These assignments are labelled in the *PDFs* (**Figure 4.5**), and show that the correlations appear due to near identical links between Fe_3O clusters. Above 12 Å, i.e. the medium range order, correlations within the spherical nanoparticles reduce drastically, which is broadly consistent with the electron microscopy data and the nanoparticulate nature of the sample. It is also interesting to note that the sample of dipyramidal microparticle morphology is dissimilar at this lengthscale to either the needle or dipyramidal nanoparticle sample, though continues to display crystallinity to ca. 40 Å (**Figure S4.33).**

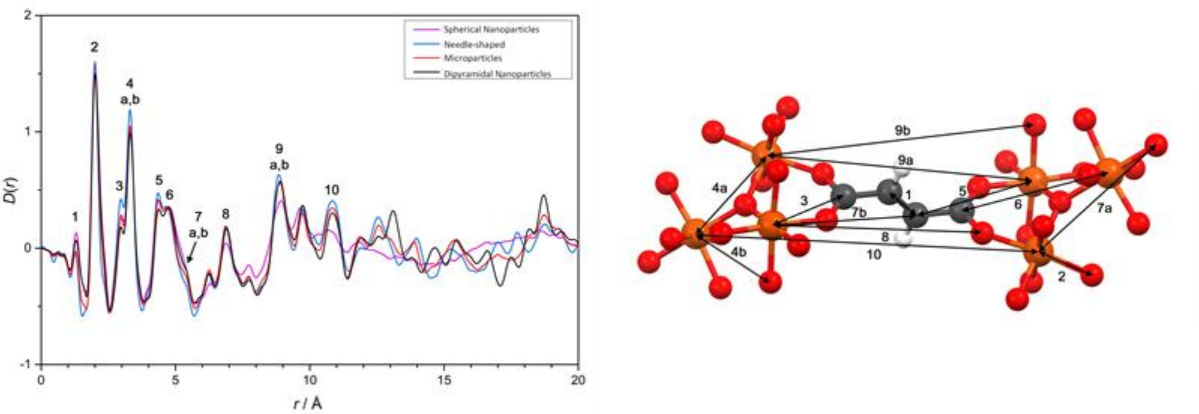

Figure 4.5. Pair distribution functions *D*(*r*) (left) and corresponding labelled partial structure of MIL-88A showing two iron oxide metal clusters linked by a fumarate ligand (right) (red – oxygen, orange – iron, dark grey – carbon, white – hydrogen).

4.3.5 Nitrogen Sorption

Porous materials are favorable for drug delivery systems as they allow for higher drug loading capacities due to their internal surface area that is accessible via pores. To determine the surface area of the iron(III) fumarate samples nitrogen sorption experiments were performed and analyzed with the BET method. All samples show BET surface areas of 120 to 450 m^2/g (**Table S4.10**) which is in agreement with literature where surface areas for iron(III) fumarate are reported ranging from 15 to 580 m^2/g depending on reaction conditions and sample perparation.[21,34,46] With decreasing particle size, the experimentally determined BET surface areas of the particles increase. This effect can partially (30 %) be explained by the increased surface to volume ratio due to the nano dimensions of the particles (see supporting

Information "Calculation of the theoretical surface depending on particle size"**).** Additionally we attribute the increased surface area to a texturing during the drying of the particles that results in an increasing slope in the sorption isotherms for the smaller particle types after their micropores are filled (**Figure 4.6**). The pore size distributions of all iron(III) fumarate variants (**Figure S4.34**) show a similar pore size at a diameter of 11-13 Å for all iron fumarate variants. The aforementioned texturing effect can also be monitored in the pore size distributions with decreasing particle size where it leads to mesopores for the smaller spherical nanoparticles and dipyramidal nanoparticles.

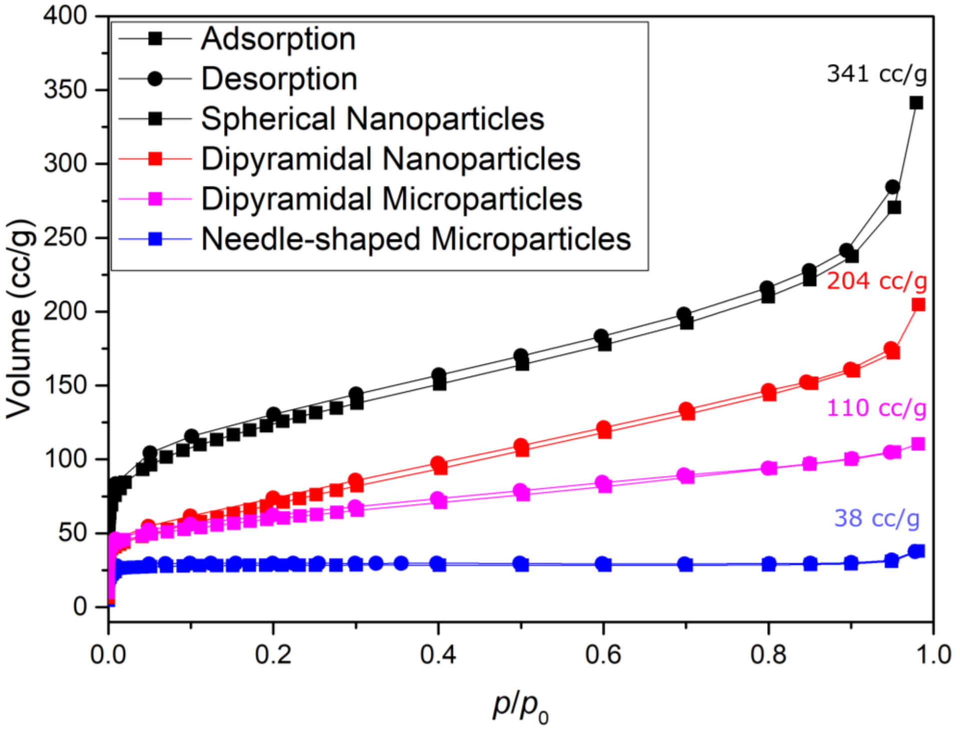

Figure 4.6. Nitrogen sorption isotherms of the four iron(III) fumarate types.

4.3.6 Breathing Behavior

While nitrogen sorption experiments can give hints about the surface area and porosity of a material, the actual loading and release of potential drugs is conducted in solvent systems. As the MIL-88A structure of crystalline iron(III) fumarate is known for its flexible pores that expand upon solvent incorporation[16] we analyzed the influence of the solvents on the lattice parameters. The data shown in **Figure S4.35**-**Figure S4.37** were generated from *in-situ* X-ray diffraction on each of the higher crystallinity iron(III) fumarate variants using various solvents that would typically be encountered in biological applications. During these experiments the particles retained their crystallinity in all of the tested solvents for multiple hours showing the stability of the particles. Powder XRD patterns were used for refinement of the lattice parameters of the different iron(III) fumarate variants with their respective solvent combinations. As shown in **Table 4.3**, the lattice dimensions for the respective iron(III) fumarate/solvent systems varied with a volume change of up to 12% upon depending on the solvent chosen, regardless of morphology.

Table 4.3. Lattice parameter evolution upon exposure of the higher crystalline iron(III) fumarate variants to various solvents.

Solvent	a [Å]	c [Å]	Volume [Å^3]
Needle-shaped Microparticles			
DMSO	14.506(21)	11.828(15)	2155.4(38)
H_2O	13.830(8)	12.702(6)	2103.9(14)
EtOH	13.636(5)	12.812(4)	2063.2(9)
MeOH	12.863(6)	13.584(6)	1946.4(11)
DMF	12.92(3)	13.385(19)	1933.7(37)
Dipyramidal Nanoparticles			
DMSO	14.620(4)	11.722(4)	2169.9(8)
H_2O	13.880(21)	12.711(4)	2120.7(39)
EtOH	13.616(8)	12.844(7)	2062.1(15)
MeOH	12.90(6)	13.60(3)	1961.3(113)
DMF	12.820(7)	13.638(12)	1941.0(19)
Dipyramidal Microparticles			
DMSO	14.647(13)	11.728(9)	2178.9(27)
H_2O	13.873(14)	12.659(10)	2109.9(25)
EtOH	13.629(10)	12.835(8)	2064.8(17)
MeOH	12.86(10)	13.585(11)	1945.8(20)
DMF	12.829(9)	13.625(8)	1942.1(16)

4.4 MRI measurements

MIL-88A NPs may be used as future MRI contrast agent as demonstrated impressively in recent *in vivo* experiments.[64] In this clinical method, contrast generation is based on different longitudinal and transverse relaxation times that the protons of water molecules in portrayed tissues exhibit in a magnetic field. MRI contrast agents enhance these differences further by decreasing the longitudinal (T_1) or transverse (T_2) relaxation times of the tissue they are situated in. The MOF MIL-88A is believed to influence this behavior as a result of its paramagnetic iron(III) centers that can be easily accessed by water molecules due to its porous MOF structure.[64,65] The inverse of these relaxation times, i.e. $R_i = 1/T_i$ ($i = 1,2$), are determined to measure the strength of a potential contrast agent at a certain concentration. Typically, the R_i values display a linear dependency on the concentration of the contrast agent. In such cases, the slope is called the relaxivity and indicates the effectiveness of the contrast agent to shorten relaxation times of water protons. In the experiments presented here we determined the relaxivity of the four iron(III) fumarate variants in a clinical MRI setting at 1.5 T. These measurements were performed either in Xanthan gel in the case of the microparticle variants or in water for the spherical nanoparticles.

The mass-based relaxivities of the dipyramidal and needle-shaped iron(III) fumarate variants increase inversely to the particle size (**Table 4.4**). The spherical nanoparticle sample on the other hand breaks with this trend and features comparably low r_2 values. In literature, other factors such as agglomeration behavior, crystallinity and particle shape have shown to influence the relaxivities of nanoparticles[66-69]. The experimentally determined mass-based relaxivities are additionally depicted as particle-based relaxivities (**Figure S4.40**). Here, both the r_1 and r_2 relaxivities of a single particle are shown to increase with its size. This may be explained by an accordingly increasing number of paramagnetic iron centers in a particle. For comparison with commercially used contrast agents, the experimentally determined mass-based relaxivities were converted to molar relaxivities (**Figure S4.40**). In this depiction the amount of iron(III) ions in the sample is considered. Overall the iron(III) fumarate particles in this study achieve 3-8% of the molar relaxivities of iron-based R_2 contrast agents such as Feridex (41 L $mmol^{-1}$ s^{-1})[70]. However, the dipyramidal nanoparticles are in the same magnitude as commercially used R_1 contrast agents featuring ~40% of the strength of gadoteric acid

(2.9 L $mmol^{-1}$ s^{-1}).[70] These results confirm the overall potential of iron(III) fumarate as MRI agents, especially since the particles can simultaneously be used in drug delivery.

Table 4.4. Mass-based relaxivities of iron(III) fumarate particles as determined in xanthan and in water (spherical nanoparticles).

Morphology	r_1 [s^{-1} (mg/mL)$^{-1}$]	r_2 [s^{-1} (mg/mL)$^{-1}$]
Needle-shaped Microparticles	1.46 ± 0.03	8.6 ± 0.5
Dipyramidal Microparticles	2.16 ± 0.02	15.7 ± 0.2
Dipyramidal Nanoparticles	6.094 ± 0.004	18.8 ± 0.4
Spherical Nanoparticles	4.23 ± 0.02	5.93 ± 0.03

4.5 Results: Biological Characterization

After establishing the synthesis of monodisperse iron(III) fumarate nano and microparticles and their physicial and functional characterization, we wanted to understand the impact of the different morphologies on cellular interactions and biological criteria that are important for biomedical applications. For this purpose, we conducted toxicity assessments and cell association experiments.

4.5.1 Cellular interaction

Since iron(III) fumarate particles are hard to label and detect by fluorescence based techniques due to fluorescence quenching effects,[71] the cellular interaction and association was investigated by inductively coupled plasma optical emission spectroscopy (ICP-OES). In these experiments, the iron content in HeLa cells before and after incubation with the respective particles was monitored. For that purpose, aqueous dispersions of the different iron(III) fumarate variants were incubated with HeLa cells for 24 h at a final concentration of 100 µg/mL. Afterwards the medium was separated from the cells, both fractions were dried and the individual iron-content was determined via ICP-OES. The detected iron content in the separate fractions depends on the amount of iron(III) fumarate particles associated with HeLa cells (membrane bound and internalized) and the remaining dispersed fraction in the supernatant respectively. The relative amount of nanoparticles associated with the cells in percent was then determined by relating the mass of iron(III) ions detected in the cell to the overall mass of iron(III) ions in the experiment (cells and supernatant). As a control experiment for nanoparticle-independent iron(III) uptake, an iron(III) chloride-solution containing the same iron(III) amount was used in the same experimental setup.

Table 4.5. Fraction of iron(III) fumarate associated with HeLa cells after 24 h incubation as determined by ICP.

Sample	Uptake
Spherical Nanoparticles	(14 ± 0.3)%
Dipyramidal Microparticles	(56 ± 2)%
Dipyramidal Nanoparticles	(29 ± 1)%
Needle-shaped Microparticles	(66 ± 3)%
Free Fe^{3+}	(3 ± 0.5)%

The data from these experiments suggest association of all four iron(III) fumarate variants with HeLa cells to different extents from 14 to 66% (**Table 4.5**). Unspecific uptake of free Fe^{3+} caused by particle degradation can be excluded due to the negligible increase of Fe^{3+} ions in the cells in the control experiment (3 %), as well as stability measurements of the particles in cell culture medium that showed all particle types to retain their morphology. The micrometer sized particles mediated the highest cellular iron increase and a general correlation of particle size with cellular association could be observed. A possible explanation are the higher sedimentation rate and cellular uptake of bigger particles in static cell culture conditions, which has also been described in the context of other nanomaterials.[72]

4.5.2 Cytotoxicity

Despite the chemical composition of all 4 iron(III) fumarate variants being equal, the effect of their varying synthesis routes and morphology on cellular tolerance and potential cytotoxicity was investigated. In these experiments human cervix carcinoma HeLa cells were incubated with aqueous dispersions of each of the particle variants at different doses. After 24 h the metabolic activity was determined by MTT assay in comparison to buffer treated control cells. As shown in **Figure 4.7** all iron(III) fumarate variants exhibited similar behavior and did not mediate distinct effects on cell viability (metabolic activity >80%) over a concentration range from 10 to 100 µg/mL. Notably, the iron(III) fumarate variants synthesized in DMF did exhibit similar toxicity compared to the variants synthesized in water.

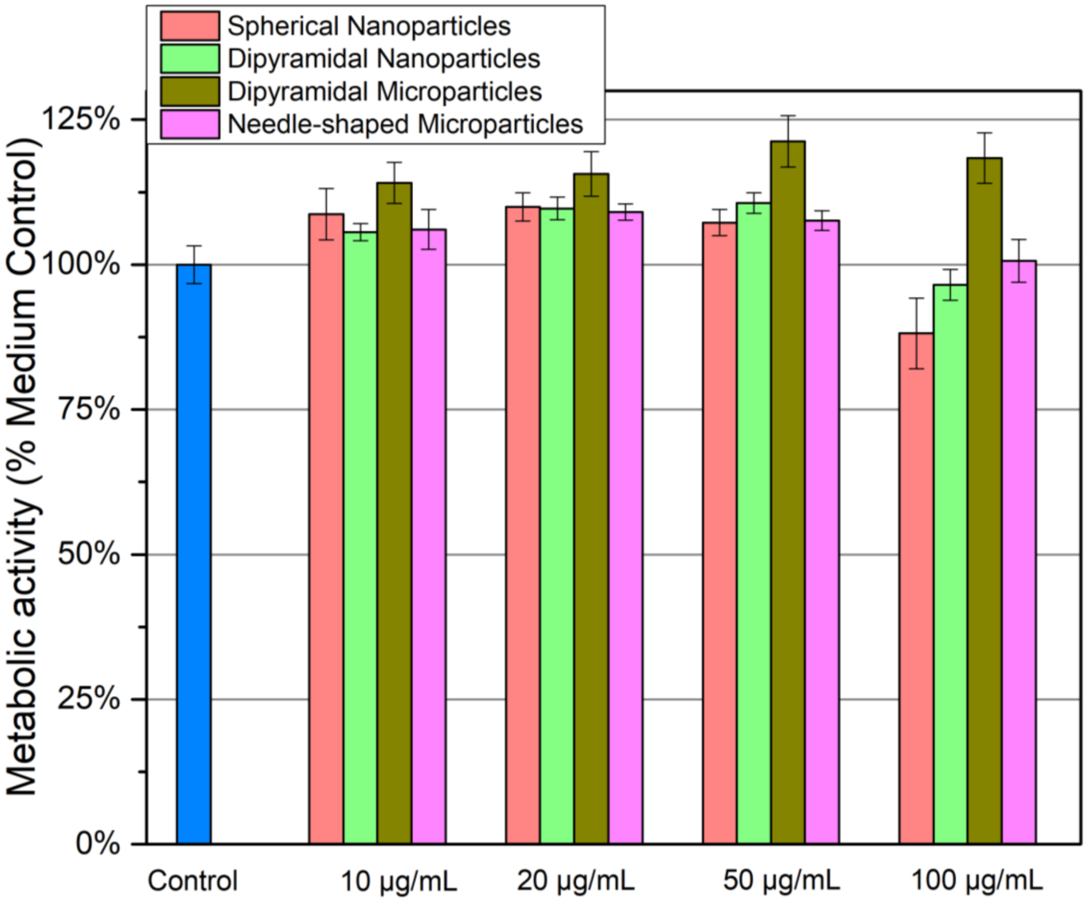

Figure 4.7. MTT assay of iron(III) fumarate particles on HeLa cells

4.6 Conclusion

At first glance, iron(III) fumarate particles seem to fulfill the strict requirements towards nano- and microparticles that can be used in biomedicine. However, this system features a great morphological and structural variety (**Table 4.1**) whose effect on biomedical functionality and biocompatibility is insufficiently explored. In this work, the influence of different reaction methods and parameters on the surfactant-free generation of iron(III) fumarate has therefore been examined and the resulting particles have been characterized with a combination of X-ray diffraction, nitrogen sorption, thermogravimetry, spectroscopy, electron microscopy, MRI and biological assays.

Synthesis-optimization in water and DMF was performed with 4 different approaches that are based on RT precipitation and solvothermal, microwave and microfluidic heating while considering reaction times, temperatures, and reactant concentrations. While the microfluidic approach has addressed the fundamental challenges of controlled heat distribution and precise reaction times, solvothermal and microwave-based techniques were overall more feasible for upscaling. In the synthesis approaches using water as solvent, the synthesis of iron(III) fumarate turned out to be a two-step process consisting initially of the formation of spherical iron(III) fumarate nanoparticles followed by the crystallization of needles. For iron(III) fumarate growth in DMF, conventional heating in an oven and in a microfluidic reactor yielded micrometer sized particles. For the synthesis of dipyramidal nanoparticles, microwave synthesis turned out to be the most efficient technique as we were able to produce homogeneous particles in large quantities in a fast and experimentally easy way. Overall this optimization resulted in 4 variants of iron(III) fumarate that were chosen for further characterization due to their distinct morphology, monodispersity and upscalability while spanning a particle size range from nano- to microparticles.

Although all four materials are iron(III) fumarate based on their chemical composition, they differ in their porosity and functionality. All particle types crystallize in the MOF structure MIL-88A. The extension of the crystalline domains in the smallest nanoparticles is however limited to a few nanometers. *In-situ* X-ray diffraction confirmed the typical breathing behavior of MIL-88A for all higher crystalline iron(III) fumarate variants. Lattice parameters and cell volume of the crystal structure were changed up to 12% via solvent exchange. This behavior is favorable for drug delivery as in the future it may enable gated trapping of biologically active molecules. Regardless of the synthesis method, all iron(III) fumarate variants were shown to be non-toxic even at high concentrations and to exhibit cell association. Iron(III) fumarate additionally features intrinsic functionality in form of paramagnetic iron(III) centers, rendering it suitable for MRI experiments. In these experiments the importance of optimization of particle size becomes apparent: by reducing the particle size of the more highly crystalline iron(III) fumarate variants r_2 relaxivities have been doubled or in case of r_1 relaxivities even have been quadrupled.

Overall, we have demonstrated the influence of morphological and structural optimization of nano and microparticles with the example of iron(III) fumarate. Synthesis and characterization of the resulting four particle variants were conducted with special emphasis regarding the field of biomedicine where high standards on monodispersity and biocompatibiltiy are required. Our study demonstrates the importance of precise synthesis control for improving the performance of such materials and ultimately enabling their clinical use.

References

1 Giner-Casares, J. J., Henriksen-Lacey, M., Coronado-Puchau, M. & Liz-Marzán, L. M. Inorganic nanoparticles for biomedicine: where materials scientists meet medical research. *Mater. Today* **19**, 19-28, doi:10.1016/j.mattod.2015.07.004 (2016).

2 Mitragotri, S., Burke, P. A. & Langer, R. Overcoming the challenges in administering biopharmaceuticals: formulation and delivery strategies. *Nat Rev Drug Discov* **13**, 655-672, doi:10.1038/nrd4363 (2014).

3 Dawidczyk, C. M. *et al.* State-of-the-art in design rules for drug delivery platforms: lessons learned from FDA-approved nanomedicines. *J Control Release* **187**, 133-144, doi:10.1016/j.jconrel.2014.05.036 (2014).

4 Yun, Y. H., Lee, B. K. & Park, K. Controlled Drug Delivery: Historical perspective for the next generation. *J Control Release* **219**, 2-7, doi:10.1016/j.jconrel.2015.10.005 (2015).

5 Lammers, T., Kiessling, F., Hennink, W. E. & Storm, G. Drug targeting to tumors: principles, pitfalls and (pre-) clinical progress. *J Control Release* **161**, 175-187, doi:10.1016/j.jconrel.2011.09.063 (2012).

6 Faria, M. *et al.* Minimum information reporting in bio-nano experimental literature. *Nat Nanotechnol* **13**, 777-785, doi:10.1038/s41565-018-0246-4 (2018).

7 Hare, J. I. *et al.* Challenges and strategies in anti-cancer nanomedicine development: An industry perspective. *Adv Drug Deliv Rev* **108**, 25-38, doi:10.1016/j.addr.2016.04.025 (2017).

8 Krug, H. F. Nanosafety research--are we on the right track? *Angew. Chem. Int. Ed. Engl.* **53**, 12304-12319, doi:10.1002/anie.201403367 (2014).

9 Freund, R., Lachelt, U., Gruber, T., Ruhle, B. & Wuttke, S. Multifunctional Efficiency: Extending the Concept of Atom Economy to Functional Nanomaterials. *ACS Nano* **12**, 2094-2105, doi:10.1021/acsnano.8b00932 (2018).

10 Modena, M. M., Ruhle, B., Burg, T. P. & Wuttke, S. Nanoparticle Characterization: What to Measure? *Adv. Mater.*, e1901556, doi:10.1002/adma.201901556 (2019).

11 Raliya, R., Singh Chadha, T., Haddad, K. & Biswas, P. Perspective on Nanoparticle Technology for Biomedical Use. *Current Pharmaceutical Design* **22**, 2481-2490, doi:10.2174/1381612822666160307151409 (2016).

12 Pelaz, B. *et al.* Diverse Applications of Nanomedicine. *ACS Nano* **11**, 2313-2381, doi:10.1021/acsnano.6b06040 (2017).

13 Tibbitt, M. W., Dahlman, J. E. & Langer, R. Emerging Frontiers in Drug Delivery. *J. Am. Chem. Soc.* **138**, 704-717, doi:10.1021/jacs.5b09974 (2016).

14 Surble, S., Serre, C., Mellot-Draznieks, C., Millange, F. & Ferey, G. A new isoreticular class of metal-organic-frameworks with the MIL-88 topology. *Chem Commun (Camb)*, 284-286, doi:10.1039/b512169h (2006).

15 Mellot-Draznieks, C. Role of computer simulations in structure prediction and structure determination: from molecular compounds to hybrid frameworks. *J. Mater. Chem.* **17**, 4348, doi:10.1039/b702516p (2007).

16 Serre, C. *et al.* Role of solvent-host interactions that lead to very large swelling of hybrid frameworks. *Science* **315**, 1828-1831, doi:10.1126/science.1137975 (2007).

17 Mellot-Draznieks, C., Serre, C., Surble, S., Audebrand, N. & Ferey, G. Very large swelling in hybrid frameworks: a combined computational and powder diffraction study. *J. Am. Chem. Soc.* **127**, 16273-16278, doi:10.1021/ja054900x (2005).

18 Serre, C., Surble, S., Mellot-Draznieks, C., Filinchuk, Y. & Ferey, G. Evidence of flexibility in the nanoporous iron(iii) carboxylate MIL-89. *Dalton Trans*, 5462-5464, doi:10.1039/b805408h (2008).

19 McKinlay, A. C. *et al.* Nitric Oxide Adsorption and Delivery in Flexible MIL-88(Fe) Metal–Organic Frameworks. *Chem. Mater.* **25**, 1592-1599, doi:10.1021/cm304037x (2013).

20 Zhu, W. *et al.* Versatile Surface Functionalization of Metal-Organic Frameworks through Direct Metal Coordination with a Phenolic Lipid Enables Diverse Applications. *Adv. Funct. Mater.* **28**, 1705274, doi:10.1002/adfm.201705274 (2018).

21 Roder, R. *et al.* Multifunctional Nanoparticles by Coordinative Self-Assembly of His-Tagged Units with Metal-Organic Frameworks. *J. Am. Chem. Soc.* **139**, 2359-2368, doi:10.1021/jacs.6b11934 (2017).

22 Mejia-Ariza, R. *et al.* DNA Detection by Flow Cytometry using PNA-Modified Metal-Organic Framework Particles. *Chemistry* **23**, 4180-4186, doi:10.1002/chem.201605803 (2017).

23 Horcajada, P. *et al.* Porous metal-organic-framework nanoscale carriers as a potential platform for drug delivery and imaging. *Nat Mater* **9**, 172-178, doi:10.1038/nmat2608 (2010).

24 Shang, W. *et al.* Core-Shell Gold Nanorod@Metal-Organic Framework Nanoprobes for Multimodality Diagnosis of Glioma. *Adv. Mater.* **29**, doi:10.1002/adma.201604381 (2017).

25 Illes, B. *et al.* Exosome-Coated Metal–Organic Framework Nanoparticles: An Efficient Drug Delivery Platform. *Chem. Mater.* **29**, 8042-8046, doi:10.1021/acs.chemmater.7b02358 (2017).

26 Illes, B., Wuttke, S. & Engelke, H. Liposome-Coated Iron Fumarate Metal-Organic Framework Nanoparticles for Combination Therapy. *Nanomaterials (Basel)* **7**, doi:10.3390/nano7110351 (2017).

27 Mejia-Ariza, R. & Huskens, J. The effect of PEG length on the size and guest uptake of PEG-capped MIL-88A particles. *Journal of Materials Chemistry B* **4**, 1108-1115, doi:10.1039/c5tb01949d (2016).

28 Jeong, G.-Y. *et al.* Bioactive MIL-88A Framework Hollow Spheres via Interfacial Reaction In-Droplet Microfluidics for Enzyme and Nanoparticle Encapsulation. *Chem. Mater.* **27**, 7903-7909, doi:10.1021/acs.chemmater.5b02847 (2015).

29 Gao, C., Zhu, H., Chen, J. & Qiu, H. Facile synthesis of enzyme functional metal-organic framework for colorimetric detecting H 2 O 2 and ascorbic acid. *Chin. Chem. Lett.* **28**, 1006-1012, doi:10.1016/j.cclet.2017.02.011 (2017).

30 Guan, Z.-Y., Wang, Y., Ma, Y.-W., Wan, J.-Q. & Wang, J.-M. Influence of Preparation Conditions of MIL-88A on Catalytic Degradation of Orange G and Dibutyl Phthalate. doi:10.2991/icsd-17.2017.3 (2017).

31 Xu, W. T. *et al.* Metal-organic frameworks MIL-88A hexagonal microrods as a new photocatalyst for efficient decolorization of methylene blue dye. *Dalton Trans* **43**, 3792-3798, doi:10.1039/c3dt52574k (2014).

32 Wang, J. *et al.* Metal–organic frameworks MIL-88A with suitable synthesis conditions and optimal dosage for effective catalytic degradation of Orange G through persulfate activation. *RSC Advances* **6**, 112502-112511, doi:10.1039/c6ra24429g (2016).

33 Zhang, Y., Zhou, J., Chen, X., Wang, L. & Cai, W. Coupling of heterogeneous advanced oxidation processes and photocatalysis in efficient degradation of tetracycline hydrochloride by Fe-based MOFs: Synergistic effect and degradation pathway. *Chem. Eng. J.* **369**, 745-757, doi:10.1016/j.cej.2019.03.108 (2019).

34 Liu, N. *et al.* Ultrathin graphene oxide encapsulated in uniform MIL-88A(Fe) for enhanced visible light-driven photodegradation of RhB. *Applied Catalysis B: Environmental* **221**, 119-128, doi:10.1016/j.apcatb.2017.09.020 (2018).

35 Shao, Z. *et al.* Fabrication of MIL-88A/g-C3N4 direct Z-scheme heterojunction with enhanced visible-light photocatalytic activity. *Sep. Purif. Technol.* **220**, 16-24, doi:10.1016/j.seppur.2019.03.040 (2019).

36 Park, S.-K., Kim, J. K. & Kang, Y. C. Electrochemical properties of uniquely structured Fe2O3 and FeSe2/graphitic-carbon microrods synthesized by applying a metal-organic framework. *Chem. Eng. J.* **334**, 2440-2449, doi:10.1016/j.cej.2017.12.014 (2018).

37 Li, Y., Zhou, Y. X., Ma, X. & Jiang, H. L. A metal-organic framework-templated synthesis of gamma-Fe2O3 nanoparticles encapsulated in porous carbon for efficient and chemoselective hydrogenation of nitro compounds. *Chem Commun (Camb)* **52**, 4199-4202, doi:10.1039/c6cc00011h (2016).

38 Dong, Z., Le, X., Liu, Y., Dong, C. & Ma, J. Metal organic framework derived magnetic porous carbon composite supported gold and palladium nanoparticles as highly efficient and recyclable catalysts for reduction of 4-nitrophenol and hydrodechlorination of 4-chlorophenol. *J. Mater. Chem. A* **2**, 18775-18785, doi:10.1039/c4ta04010d (2014).

39 Wang, L. *et al.* The MIL-88A-Derived Fe3O4-Carbon Hierarchical Nanocomposites for Electrochemical Sensing. *Sci Rep* **5**, 14341, doi:10.1038/srep14341 (2015).

40 Wang, Y. *et al.* Controlled pyrolysis of MIL-88A to Fe2O3@C nanocomposites with varied morphologies and phases for advanced lithium storage. *Journal of Materials Chemistry A* **5**, 25562-25573, doi:10.1039/c7ta08314a (2017).

41 Wang, Z. *et al.* Fe2O3@C core@shell nanotubes: Porous Fe2O3 nanotubes derived from MIL-88A as cores and carbon as shells for high power lithium ion batteries. *J. Alloys Compd.* **769**, 969-976, doi:10.1016/j.jallcom.2018.08.081 (2018).

42 Andrew Lin, K.-Y. & Hsu, F.-K. Magnetic iron/carbon nanorods derived from a metal organic framework as an efficient heterogeneous catalyst for the chemical oxidation process in water. *RSC Advances* **5**, 50790-50800, doi:10.1039/c5ra06043e (2015).

43 Hu, X. *et al.* Low-temperature pseudomorphic transformation of polyhedral MIL-88A to lithium ferrite (LiFe3O5) in aqueous LiOH medium toward high Li storage. *Nanoscale* **11**, 11892-11901, doi:10.1039/c9nr03006a (2019).

44 Ke, F. *et al.* Porous metal–organic frameworks adsorbents as a potential platform for defluoridation of water. *J. Porous Mater.* **23**, 1065-1073, doi:10.1007/s10934-016-0164-5 (2016).

45 Ramsahye, N. A. *et al.* Impact of the Flexible Character of MIL-88 Iron(III) Dicarboxylates on the Adsorption of n-Alkanes. *Chem. Mater.* **25**, 479-488, doi:10.1021/cm303830b (2013).

46 Amaro-Gahete, J. *et al.* Fast ultrasound-assisted synthesis of highly crystalline MIL-88A particles and their application as ethylene adsorbents. *Ultrason. Sonochem.* **50**, 59-66, doi:10.1016/j.ultsonch.2018.08.027 (2019).

47 Gomez, D. A. & Sastre, G. From microscopic insights of H2 adsorption to uptake estimations in MOFs. *Phys Chem Chem Phys* **13**, 16558-16568, doi:10.1039/c1cp21865d (2011).

48 Chalati, T., Horcajada, P., Gref, R., Couvreur, P. & Serre, C. Optimisation of the synthesis of MOF nanoparticles made of flexible porous iron fumarate MIL-88A. *J. Mater. Chem.* **21**, 2220-2227, doi:10.1039/c0jm03563g (2011).

49 Bagherzadeh, E., Zebarjad, S. M., Madaah Hosseini, H. R. & Chagnon, P. Preparation, optimization and evolution of the kinetic mechanism of an Fe-MIL-88A metal–organic framework. *CrystEngComm* **21**, 544-553, doi:10.1039/c8ce01876f (2019).

50 Bagherzadeh, E., Zebarjad, S. M. & Hosseini, H. R. M. Morphology Modification of the Iron Fumarate MIL-88A Metal-Organic Framework Using Formic Acid and Acetic Acid as Modulators. *Eur. J. Inorg. Chem.* **2018**, 1909-1915, doi:10.1002/ejic.201800056 (2018).

51 Medvedev, P. V. *et al.* Analysis of the Local Atomic Structure of the MIL-88a Metal–Organic Framework by Computer Simulation Using XANES Data. *JETP Letters* **108**, 318-325, doi:10.1134/s0021364018170083 (2018).

52 Diego, A. G. & Sastre, G. From microscopic insights of H2 adsorption to uptake estimations in MOFs. *Phys. Chem. Cheml. Phys.* **13**, 16558-16568, doi:10.1039/c1p21865d (2011).

53 Tsuruoka, T. *et al.* Nanoporous nanorods fabricated by coordination modulation and oriented attachment growth. *Angew. Chem. Int. Ed. Engl.* **48**, 4739-4743, doi:10.1002/anie.200901177 (2009).

54 McGuire, C. V. & Forgan, R. S. The surface chemistry of metal-organic frameworks. *Chem Commun (Camb)* **51**, 5199-5217, doi:10.1039/c4cc04458d (2015).

55 Paseta, L. *et al.* Accelerating the controlled synthesis of metal-organic frameworks by a microfluidic approach: a nanoliter continuous reactor. *ACS Appl Mater Interfaces* **5**, 9405-9410, doi:10.1021/am4029872 (2013).

56 Jambovane, S. R. *et al.* Continuous, One-pot Synthesis and Post-Synthetic Modification of NanoMOFs Using Droplet Nanoreactors. *Sci Rep* **6**, 36657, doi:10.1038/srep36657 (2016).

57 Rubio-Martinez, M. *et al.* Versatile, high quality and scalable continuous flow production of metal-organic frameworks. *Sci Rep* **4**, 5443, doi:10.1038/srep05443 (2014).

58 Faustini, M. *et al.* Microfluidic approach toward continuous and ultrafast synthesis of metal-organic framework crystals and hetero structures in confined microdroplets. *J. Am. Chem. Soc.* **135**, 14619-14626, doi:10.1021/ja4039642 (2013).

59 Pinna, A. *et al.* A MOF-based carrier for in situ dopamine delivery. *RSC Advances* **8**, 25664-25672, doi:10.1039/c8ra04969f (2018).

60 Soper, A. K. GudrunN and GudrunX: Programs for Correcting Raw Neutron and X-ray Diffraction Data to Differential Scattering Cross Section. Report No. RAL-TR-2011-013, (Rutherford Appleton Laboratory Technical Report, Oxfordshire, 2011).

61 Bennett, T. D. *et al.* Connecting defects and amorphization in UiO-66 and MIL-140 metal–organic frameworks: a combined experimental and computational study. *PCCP* **18**, 2192-2201, doi:10.1039/c5cp06798g (2016).

62 Zhou, C. *et al.* Metal-organic framework glasses with permanent accessible porosity. *Nat Commun* **9**, 5042, doi:10.1038/s41467-018-07532-z (2018).

63 Farrow, C. L. *et al.* PDFfit2 and PDFgui: computer programs for studying nanostructure in crystals. *J Phys Condens Matter* **19**, 335219, doi:10.1088/0953-8984/19/33/335219 (2007).

64 Horcajada, P. *et al.* Metal-organic frameworks in biomedicine. *Chem. Rev.* **112**, 1232-1268, doi:10.1021/cr200256v (2012).

65 Peller, M., Böll, K., Zimpel, A. & Wuttke, S. Metal–organic framework nanoparticles for magnetic resonance imaging. *Inorganic Chemistry Frontiers* **5**, 1760-1779, doi:10.1039/c8qi00149a (2018).

66 Vuong, Q. L., Gillis, P. & Gossuin, Y. Monte Carlo simulation and theory of proton NMR transverse relaxation induced by aggregation of magnetic particles used as MRI contrast agents. *J Magn Reson* **212**, 139-148, doi:10.1016/j.jmr.2011.06.024 (2011).

67 Vuong, Q. L., Berret, J. F., Fresnais, J., Gossuin, Y. & Sandre, O. A universal scaling law to predict the efficiency of magnetic nanoparticles as MRI T(2)-contrast agents. *Adv Healthc Mater* **1**, 502-512, doi:10.1002/adhm.201200078 (2012).

68 Merbach, A., Helm, L. & Tóth, É. *The Chemistry of Contrast Agents in Medical Magnetic Resonance Imaging*. (John Wiley & Sons, Ltd, 2013).

69 Zhou, Z., Yang, L., Gao, J. & Chen, X. Structure-Relaxivity Relationships of Magnetic Nanoparticles for Magnetic Resonance Imaging. *Adv. Mater.* **31**, 1804567, doi:10.1002/adma.201804567 (2019).

70 Rohrer, M., Bauer, H., Mintorovitch, J., Requard, M. & Weinmann, H.-J. Comparison of magnetic properties of MRI contrast media solutions at different magnetic field strengths. *Investigative Radiology* **40**, 715-724 (2005).

71 Wuttke, S. *et al.* MOF nanoparticles coated by lipid bilayers and their uptake by cancer cells. *Chem Commun (Camb)* **51**, 15752-15755, doi:10.1039/c5cc06767g (2015).

72 Cui, J. *et al.* A Framework to Account for Sedimentation and Diffusion in Particle-Cell Interactions. *Langmuir* **32**, 12394-12402, doi:10.1021/acs.langmuir.6b01634 (2016).

4.7 Supplementary Information

4.7.1 Methods and Characterization

Powder X-ray diffraction

X-ray diffraction experiments were performed on a *STOE Transmissions-Diffraktometer System STADI P* with Ge(111) primary monochromator using CuK$_{\alpha 1}$-radiation. The device operates in a transmission setup derived from Debye-Scherrer geometry were dried sample is fixated between two polymer foils. Analysis was conducted with the included software package *WinXPOW RawDat v3.0.2.5* and *WinXPOW PowDat_n v3.0.2.7.* Lattice parameter refinement was done in UnitCell using 11-19 reflections per sample. Peak positions were corrected based on an internal silicon standard. All diffraction patterns depict an additional low intensity reflection at 24.12 – 24.14 ° that cannot be explained completely by the published structure of MIL-88A. This reflection could be indexed (113), which should not be present in the space group P-62c. It might be caused by an impurity, which formed during the synthesis as the dried samples have proven stable in air over the course of the measurement.

Transmission electron microscopy

TEM samples were prepared by drying an ethanolic dispersion of the X-ray amorphous spherical nanoparticles on a carbon-coated copper grid. Electron microscopy and electron diffraction was performed with a *Titan Themis* (*FEI*) operated at 300 kV.

Scanning electron microscopy

Sample preparation was performed by drying ethanolic dispersions of the respective samples on a carbon film fixed on an aluminum sample holder under air. After subsequent carbon sputtering the samples were measured using a *Helios G3 UC* (*FEI*) scanning electron microscope. If not stated otherwise the microscope was operated at 3 kV using a trough-lens detector. To visualize particles below the sample surface the setup was operated at 15 kV using a mirror detector which is also mentioned in the respective pictures.

Pair distribution function analysis

Data were obtained at the I15-1 beamline, Diamond Light Source, UK (λ = 0.161669 Å, 72 keV). All samples were vacuum dried for 2 h at room temperature and finely ground before packing into sealed 1.17 mm (inner) diameter borosilicate capillaries. Data were taken of the background, empty capillary, and of all four samples to a $Q_{\max}$ of 24 Å^{-1}. A 50% beam absorber was required for the acquisition of the data for the dipyramidal nanoparticles and dipyramidal microparticles samples to prevent oversaturation of the detector. Normalised total scattering data were corrected individually using the GudrunX program[1,2] to obtain PDFs of each sample (Figure S24). Predicted $G(r)$ patterns of the samples were generated using crystallographic information files available online[3] and the PDFGUI software[4].

Nitrogen sorption

Nitrogen sorption experiments were performed on dried powders (9-56 mg) of the respective samples. Prior to the measurements the samples were outgassed at 120 °C in vacuum for 24 h. All nitrogen sorption experiments were conducted on an *Autosorb-1* (*Quantachrome*) using the software *ASiQwin v3.0* for data evaluation. The linearized form of the BET equation was used to calculate BET surface areas. For the calculation of the pore size distribution of the microparticles a QSDFT adsorption based model was used assuming cylindrical pores. Due to the mesotexturing of the spherical nanoparticle sample the pore size distribution of these particles was calculated with a QSDFT adsorption based model assuming cylindrical and slit pores.

Magnet resonance imaging

MRI experiments were performed either on dispersions of larger iron(III) fumarate variants while they were embedded in 0.2 wt% Xanthan Gel (2 mL) or of the spherical nanoparticles when suspended in water (2 mL). The Xanthan gels were prepared by generating aqueous dispersion of the respective particle concentrations and subsequent addition of dry Xanthan. After vortexing the particle dispersion were sonicated for 20 min followed by additional pipetting and repeated sonication for 30 min.

In-situ X-ray diffraction

In-situ X-ray diffraction experiments were performed on dispersions the samples with sharp reflections in **Figure 4.3**. The experiments were performed on a *STOE Transmissions-Diffraktometer System STADI P* with Ge(111) primary monochromator using CuK$_{\alpha1}$-radiation operating in transmission geometry. The particle dispersions were placed in sealed glass capillary tubes. Analysis was conducted with the included software package *WinXPOW RawDat v3.0.2.5*, *WinXPOW PowDat_n v3.0.2.7* and *WinXPOW Index v3.0.2.1*. For refinement of the lattice parameters 5-11 reflections were considered. Additionally the X-ray diffraction pattern of an empty glass capillary was recorded (**Figure S4.38**). The capillary corresponds to a reflection at the angle of 8.495 ° which can be visible in a few of the *in-situ* diffraction patterns.

Inductively coupled optical emission spectroscopy

ICP-OES measurements were performed in on dried samples that were digested using 10% HNO_3 (*Aristar VWR*). The setup consisted of an *ICP AES Vista RL* with a *CCD simultaneous ICP AES* detector (*Agilent*). Measurements were performed with Argon plasma at 1.2 kW in 3 x 8 s periods with 45 s stabilization time. Wavelengths used were at 238 nm and 259 nm.

Thermogravimetric Analysis

For gravimetric measurements all dried samples of the respective iron(III) fumarate variants (**Figure S4.29**) were measured on a *TASC 414/4* (*Netzsch*) under synthetic air at a flow rate of 25 mL/min. The experiments were performed with a heating rate of 10 °C/min up to 900 °C. The resulting data was evaluated using the software *Proteus v4.3*.

Cell culture

HeLa cells (ATCC CCL-2) were grown in RPMI-1640 medium (L-alanyl-glutamine and sodium bicarbonate) supplemented with 10 % FBS, 100 U/mL penicillin, 100 µg/mL streptomycin. The cells were cultured in ventilated flasks in the cell incubator at 37 °C and 5 % CO_2 in a humidified atmosphere. Cells were passaged at approx. 80 % confluency.

4.7.2 Chemicals

Ethanol (VWR, 99.9%), Iron(III) chloride hexahydrate (*Grüssing*, 99%), Fumaric acid (*Sigma*, ≥99.0%), *N*,*N* Dimethylformamide (DMF, *VWR*, 99.9%), Xanthan gum from Xanthoma campestris (*Sigma*).

4.7.3 Synthesis of the 4 different iron(III) fumarate variants

In this section the synthesis protocols used to generate the four iron(III) fumarate variants that were later characterized for functionality and biocompatibility are shown.

Spherical Nanoparticles

A solution of $FeCl_3 \cdot 6\ H_2O$ (2168 mg, 8.02 mmol) in water (40 mL, *Merck, Milli-Q*) was prepared. Fumaric acid (970 mg, 8.36 mmol) was added under stirring. After incubation at room temperature (2 min) the reaction was stopped and washed three times by centrifuging (7197 rcf, 20 min) and redispersing in ethanol.

Needle-shaped Microparticles

A reaction mixture of fumaric acid (485 mg, 4.18 mmol) and $FeCl_3 \cdot 6\ H_2O$ (1084 mg, 4.01 mmol) in water (20 mL, *Merck, Milli-Q*) was prepared. The reaction mixture was placed in a 50 mL Schott glass vial and put into an oven for 24 h at 80 °C. The resulting particles were washed three times by centrifuging (7197 rcf, 20 min) and redispersing in ethanol.

Dipyramidal Nanoparticles

Fumaric acid (485 mg, 4.18 mmol) and $FeCl_3 \cdot 6\ H_2O$ (1084 mg, 4.01 mmol) were dissolved in DMF (20 mL). This reaction mixture was placed in a 80 mL Teflon tubes and put in a microwave reactor (*Synthos 3000*, *Anton Paar*) along with a reference solution containing $FeCl_3 \cdot 6\ H_2O$ (1084 mg, 4.01 mmol) in DMF (20 mL) and two additional vessels containing tap water (20 mL). A reaction program consisting of first heating the sample for 30 s up to 120 °C and subsequent holding of this temperature for 5 min was used. At the end of this program the reaction was quenched by pouring the hot reaction mixture in DMF (room temperature, 50 mL). The resulting product was washed with DMF (40 mL) washed three times by centrifuging (7197 rcf, 20 min) and redispersing in DMF.

Dipyramidal Microparticles

A stock solution of fumaric acid (194 mg, 1.67 mmol) and $FeCl_3 \cdot 6\ H_2O$ (433 mg, 1.604 mmol) in DMF (8 mL) was prepared and divided equally into 8 1.5 mL Eppendorf tubes. The reaction mixtures were placed in an oven for 30 min at 120 °C. The resulting particles were washed three times by centrifuging (16873 rcf, 10 min) and redispersing in DMF.

4.7.4 Optimization of the aqueous and DMF based iron(III) fumarate synthesis

In this section reaction parameters for the morphological optimization of iron(III) fumarate in water and DMF are shown.

Microfluidic synthesis of iron(III) fumarate in DMF

This microfluidic approach was based on a continuous flow reactor (**Figure S4.12**) heating a premixed a solution of fumaric acid (485 mg, 4.18 mmol) and $FeCl_3 \cdot 6\ H_2O$ (1084 mg, 4.01 mmol) in DMF (20 mL). Using a syringe pump, the solution was then pressed through a microfluidic channel consisting of a Teflon tube (120 cm, 1/16” outer diameter). The larger segment of this tubing (1 m) tubing was immersed in an oil bath (120 °C) in order to heat the traversing reaction solution. By varying the speed of the syringe pumps, different incubation times (1 min, 2min, 4 min, 5 min, 8 min, 16 min, and 30 min) for the particle synthesis were preset. The respective fractions (**Figure S4.13**) were collected in an Eppendorf Tube and washed three times by centrifuging (16873 rcf, 10 min) and redispersing in DMF.

Microfluidic synthesis of iron(III) fumarate in water

This microfluidic setup was based on the continuous flow reactor shown in **Figure S4.12 (left).** A solution of fumaric acid (485 mg, 4.18 mmol) and FeCl3 · 6 H2O (1084 mg, 4.01 mmol) in DMF (20 mL) was incubated at room temperature for three weeks. No particle formation could be monitored. Using two syringe pumps precursor aqueous (*Merck*, *Milli-Q*) solutions of fumaric acid (40 mg, 0.34 mmol, 20 mL) and $FeCl_3 \cdot 6\ H_2O$ (90 mg, 0.33 mmol, 20 mL) were then pressed through a microfluidic channel consisting of a Teflon tube (15 cm, 1/16” Outer diameter) into a T-junction (*Elveflow*) serving as a mixing zone. Following this junction the reaction mixture traversed a heating zone (1 m) in which the Teflon tube was immersed in a water bath (80 °C). By varying the speed of the syringe pumps, different incubation times (1 min, 2 min, 3 min, and 10 min) for the particles were preset. The respective fractions (**Figure S4.20**) were collected in an Eppendorf Tube and washed three times by centrifuging (16873 rcf, 10 min) and redispersing in ethanol.

Solvothermal synthesis of iron(III) fumarate in DMF

A stock solution of fumaric acid (485 mg, 4.18 mmol) and $FeCl_3 \cdot 6\ H_2O$ (1084 mg, 4.01 mmol) in DMF (20 mL) was prepared. For low concentration experiments this sock solution was further diluted with DMF in a 1:10 ratio. To test the temperature necessary for iron(III) fumarate formation under these conditions small fractions of the concentrated stock solution (1.0 mL) were put into 1.5 mL Eppendorf tubes and incubated in an Thermoshaker (*TS-100, PeqLab*) at RT, 30 °C, 40 °C 50 °C and 60 °C and heated for 18 h under monitoring. Due to slower particle formation in case of the lower concentrated solution this process was repeated at 70 °C, 80 °C, 100 °C and 120 °C in an oven. In these experiments precipitation of iron(III) fumarate could only be observed for heating at temperatures above 100 °C (**Figure S4.11**). Additional optimization was done at 120 °C using the concentrated iron(III) fumarate stock solution in DMF in volumes of 1 mL. At specific times (1 min, 2 min, 5 min, 10 min, 20 min, 30 min, 60 min, 6 h and 24 h) aliquots were removed. Formation of iron(III) fumarate could be observed from 30 min onwards. In case of product formation (**Figure S4.9**) the solution washed three times by centrifuging and redispersing in DMF.

Solvothermal synthesis of iron(III) fumarate in water

A reaction mixture of fumaric acid (485 mg, 4.18 mmol) and $FeCl_3 \cdot 6\ H_2O$ (1084 mg, 4.01 mmol) in water (20 mL, *Merck, Milli-Q*) was produced. Aliquots of the dispersion (1.0 mL) were put into 1.5 mL Eppendorf tubes and incubated at 80 °C in a thermoshaker (*TS-100, PeqLab*). At specific times (1 min, 5 min, 20 min, 24 h and 7 d) these samples were removed from the thermoshaker. The samples (**Figure S4.19**) were washed three times by centrifuging and redispersing in ethanol.

Lower concentration experiments were performed by dissolving fumaric acid (16 mg, 138 µmol) and $FeCl_3 \cdot 6\ H_2O$ (36.6 mg, 136 µmol) each in water (10 mL, *Merck, Milli-Q*). These solutions were mixed and the resulting reaction mixture heated in 1.5 mL Eppendorf tubes (80 °C, 1.0 mL reaction volume) using a thermoshaker (TS-100, *PeqLab*). At specific times (5 min and 20 min) heating was stopped and the samples (**Figure S4.21**) were washed three times by centrifuging (16873 rcf, 10 min) and redispersing in ethanol.

Microwave synthesis of iron(III) fumarate in DMF

Fumaric acid (485 mg, 4.18 mmol) and $FeCl_3 \cdot 6\ H_2O$ (1084 mg, 4.01 mmol) were dissolved in DMF (20 mL) under stirring. The clear yellow solution was placed in 80 mL Teflon tubes and put in a microwave reactor (*Synthos 3000, Anton Paar*) along with a reference solution containing $FeCl_3 \cdot 6\ H_2O$ (1084 mg, 4.01 mmol) in DMF (20 mL) and two additional vessels containing tap water (20 mL). The microwave programs shown in **Table S4.6** were applied. After finishing the program, the crystal growth was stopped by pouring the hot reaction solution into DMF (RT, 50 mL). The product (**Figure S4.14**) was washed three times by centrifuging (7197 rcf, 20 min) and redispersing in DMF.

Table S4.6. Microwave parameters of the synthesis of iron(III) fumarate in DMF.

Heating to 120 °C	Incubation at 120 °C
30 s	2 min
30 s	3 min
30 s	5 min

Microwave synthesis of iron(III) fumarate in water

Fumaric acid (485 mg, 4.18 mmol) and $FeCl_3 \cdot 6\ H_2O$ (1084 mg, 4.01 mmol) were dissolved in Millipore water (20 mL, *Merck, Milli-Q*). The orange dispersion was placed in a Teflon tube (80 mL) and put in a microwave reactor (*Synthos 3000*, *Anton Paar*) along with a reference solution containing $FeCl_3 \cdot 6\ H_2O$ (1084 mg, 4.01 mmol) in water (20 mL, *Merck, Milli-Q*) and two additional vessels containing tap water (20 mL). The microwave programs shown in **Table S4.7** were applied. After finishing the program, reaction was quenched by pouring the hot reaction solution into water (RT, 50 mL). The product (**Figure S4.18**) was washed three times by centrifuging (7197 rcf, 20 min) and redispersing in ethanol.

Table S4.7. Microwave parameters of the synthesis of iron(III) fumarate in water.

Heating to 80 °C	**Incubation at 80 °C**
30 s	1 min
30 s	2 min
30 s	5 min

Room temperature precipitation of iron(III) fumarate in DMF

A solution of fumaric acid (485 mg, 4.18 mmol) and $FeCl_3 \cdot 6\,H_2O$ (1084 mg, 4.01 mmol) in DMF (20 mL) was incubated at room temperature for three weeks. No particle formation could be monitored.

Room temperature precipitation of iron(III) fumarate in water

A reaction mixture of fumaric acid (485 mg, 4.18 mmol) and $FeCl_3 \cdot 6\,H_2O$ (1084 mg, 4.01 mmol) in water (20 mL, *Merck, Milli-Q*) was incubated at room temperature. Aliquots were taken after a certain reaction time (2 min, 2 h, 8 h, 24 h, 4 d and 7 d). The samples (**Figure S4.16**) were washed three times by centrifuging (16873 rcf, 10 min) and redispersing in ethanol.

A lower concentration experiment was performed by dissolving fumaric acid (16 mg, 138 µmol) and $FeCl_3 \cdot 6\,H_2O$ (36.66 mg, 136 µmol) each in 10 mL water (*Merck, Milli-Q)*. The solutions were unified and the resulting reaction mixture incubated for 7 d at room temperature. The final product (**Figure S4.22**) was washed three times by centrifuging (7197 rcf, 20 min) and redispersing in ethanol

4.7.5 MTT Assay

One day prior to the experiment HeLa cells were seeded at a density of 5.000 cells per well in 96-well plates (Corning ® Costar, Sigma-Aldrich, Germany). 24 h after cell seeding, the medium was replaced by 80 µL fresh medium. The different iron(III) fumarate particle suspensions were diluted in HBG (20 mM HEPES, 5 % glucose w/v, pH 7.4) to 50, 100, 250 and 500 µg/mL and 20 µL of the dilutions was added per well. The cells were incubated for 24 hours at 37 °C and 5% CO_2. 10 µL MTT (3-(4,5-dimethylthiazol-2-yl)-2,5-diphenyltetrazolium bromide) (5 mg/mL) resulting in a final concentration of 0.5 mg/mL was added to each well. The plates were incubated for 1 h at 37 °C. Unreacted dye and medium were removed and the 96-well plates frozen at −80 °C for 60 min. After thawing, 100 µL DMSO was added to each well and the plates were incubated for 30 minutes at 37 °C under shaking to dissolve the purple formazan product. Absorbance was quantified at 590 nm with a background correction at 630 nm using a microplate reader (TecanSpectrafluor Plus, Tecan, Switzerland). All treatments were performed in quintuplicates. The relative cell viability (%) normalized to HBG treated control cells was calculated as ([A] test/[A] control) × 100%. Mean values +/- standard deviation are reported.

4.7.6 Supplementary Figures and Tables

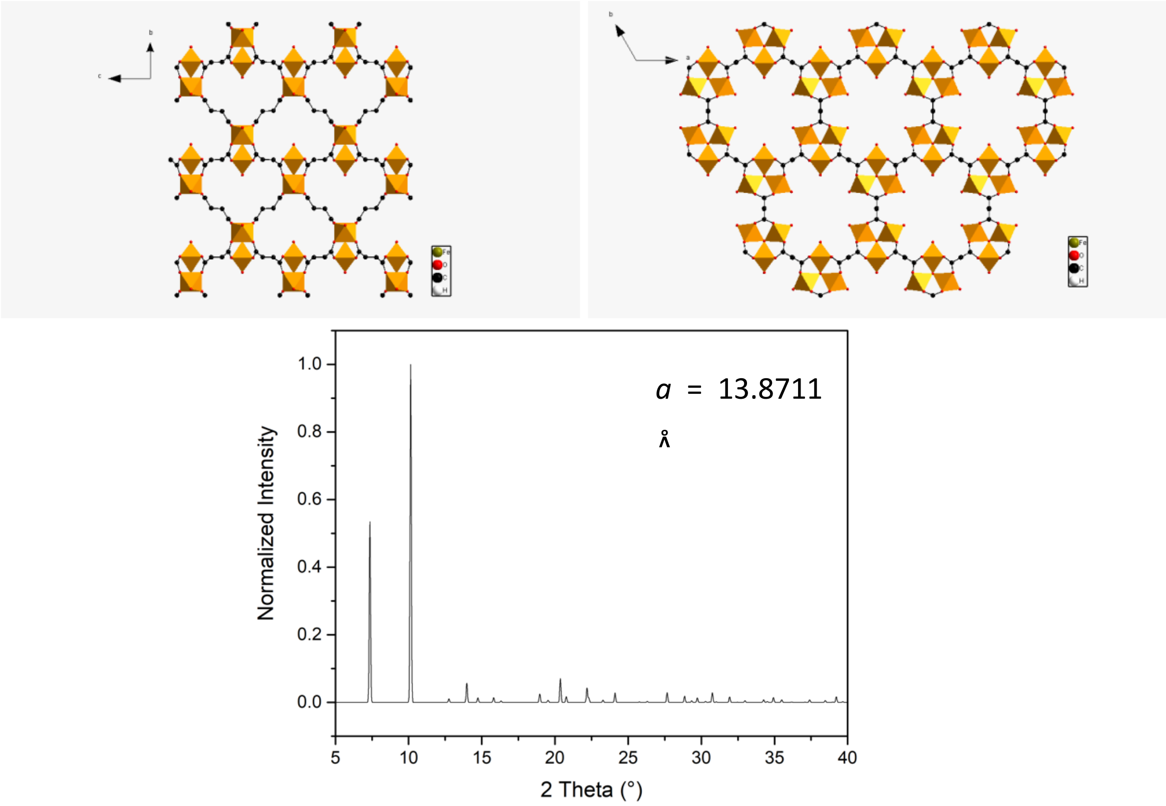

Figure S4.8. Depiction of the crystal structure of open-pore MIL-88A simulated (Software: *Diamond v3.0, Crystal Impact*) according to data published by Serre.[5] Top left: Depiction of the crystal structure along the *a*-axis. Top right: Depiction of the crystal structure along the *c*-axis. Bottom: Simulated diffraction pattern of open-pore MIL-88(A) along with lattice parameters.

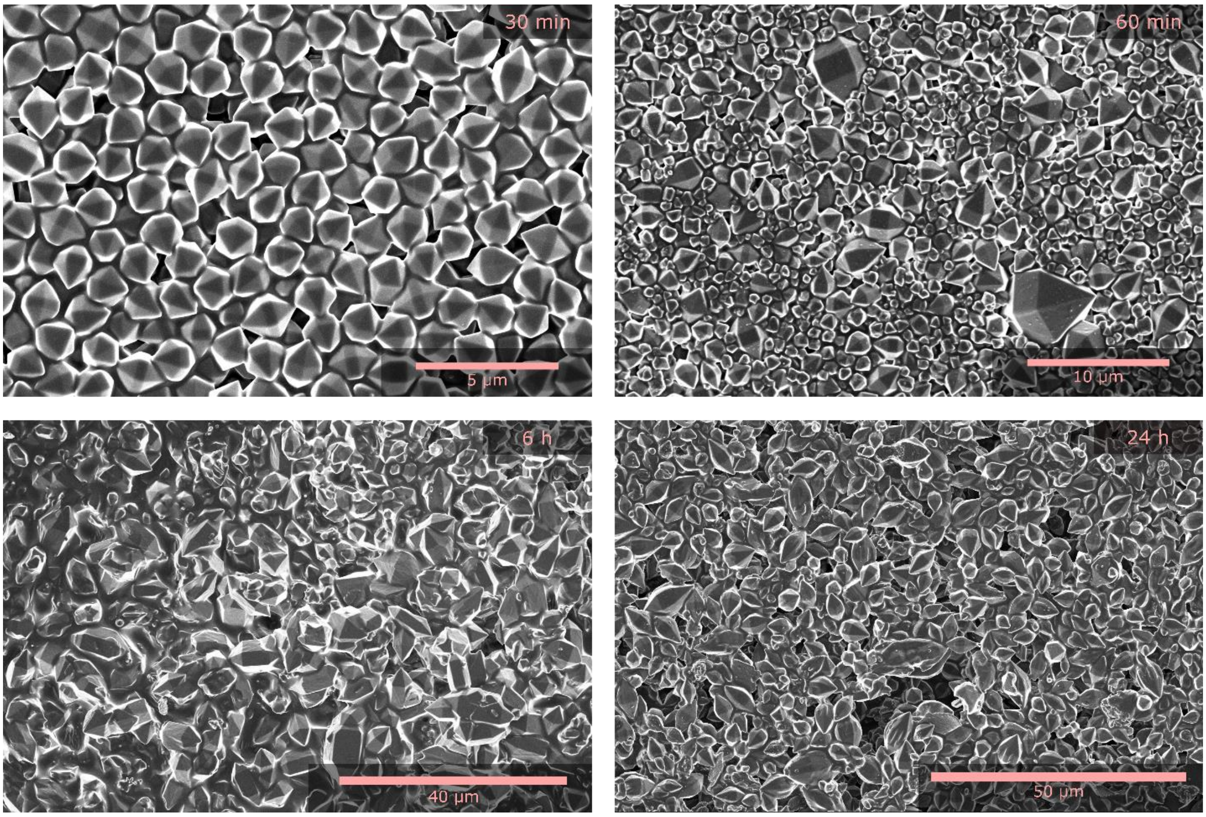

Figure S4.9. SEM micrographs of iron(III) fumarate microparticles grown in a solvothermally at 120 °C in DMF for reaction times of 30 min, 60 min, 6 h and 24 h.

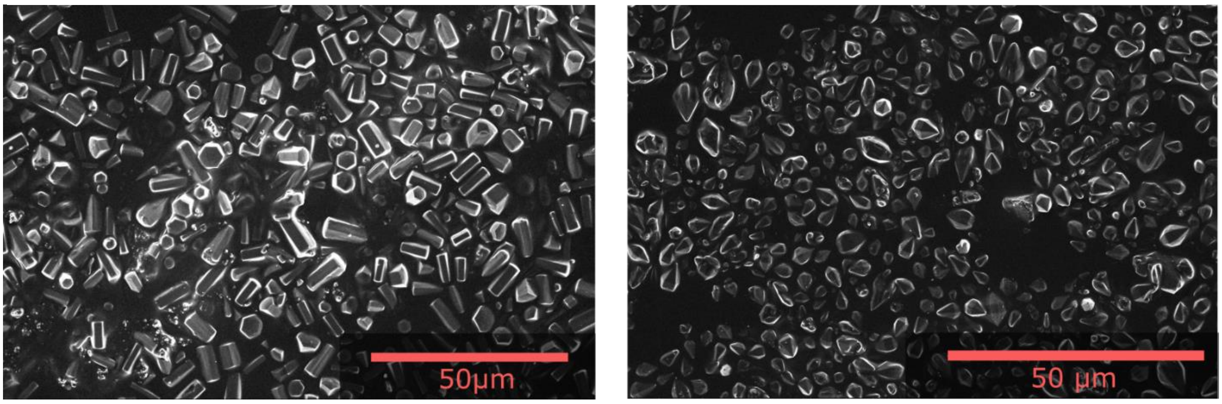

Figure S4.10. SEM micrographs of iron(III) fumarate microparticles grown solvothermally 120 °C in DMF with 24 h incubation time. Right: Growth from high-concentration stock solution, Left: Growth from low-concentration stock solution.

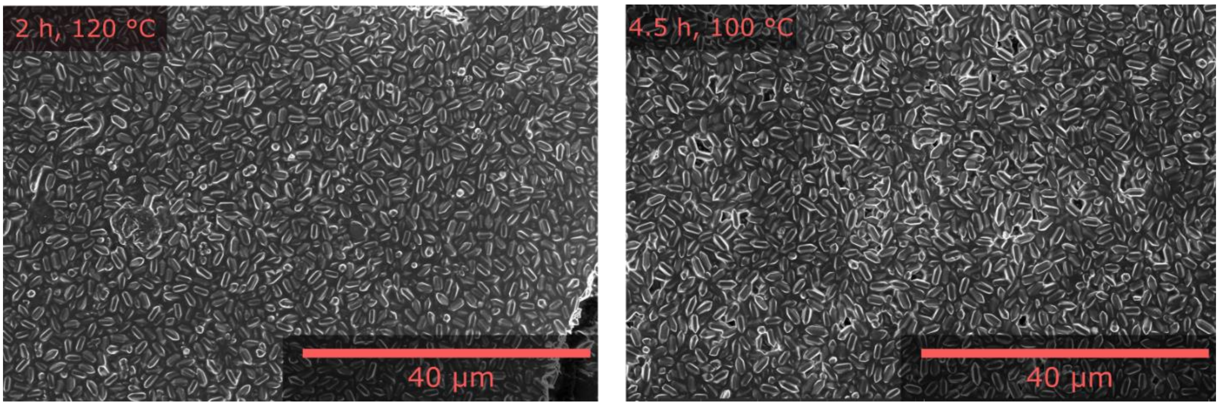

Figure S4.11. SEM micrographs of iron(III) fumarate microparticles grown solvothermally from a low concentration stock solution at 100 °C and 120 °C in DMF in dependency of reaction time.

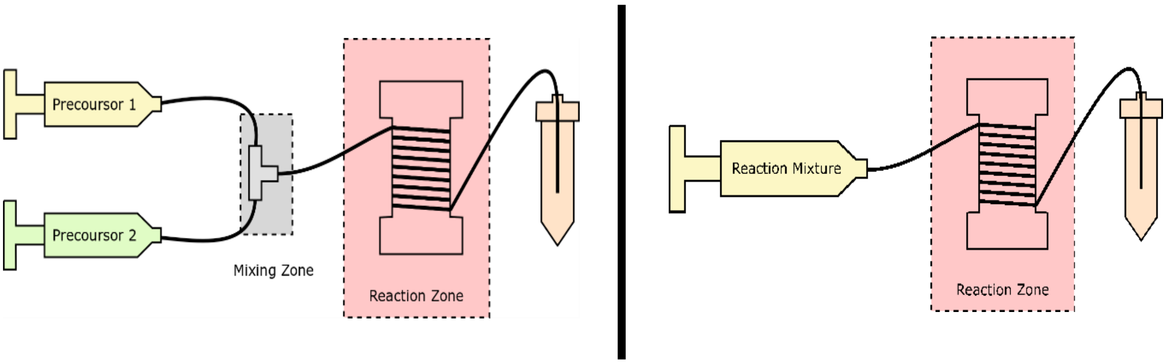

Figure S4.12. Left: Schematic of the microfluidic setup used for optimization of iron(III) fumarate particles in water: Aqueous precursor solutions of iron(III) chloride (Precursor 1) and fumaric acid (Precursor 2) were pressed into a microfluidic tubing (*PTFE*, *Elveflow*, OD 1/16”, ID 1/32”, length 1.2 m) and mixed in a T-junction. Part of the tubing then traversed a heating zone (water bath, 1 m, 80 °C) before being collected in an Eppendorf tube. Right: Schematic illustration of the microfluidic setup used for iron(III) fumarate synthesis in DMF. A premixed reaction mixture containing fumaric acid and iron(III) chloride was pressed into a microfluidic tubing (*PTFE*, *Elveflow*, OD 1/16”, ID 1/32”, length 1.2 m) via a syringe pump. Part of this tubing (1 m) was traversing a heating zone (oil bath, 120 °C) before being collected in an Eppendorf tube.

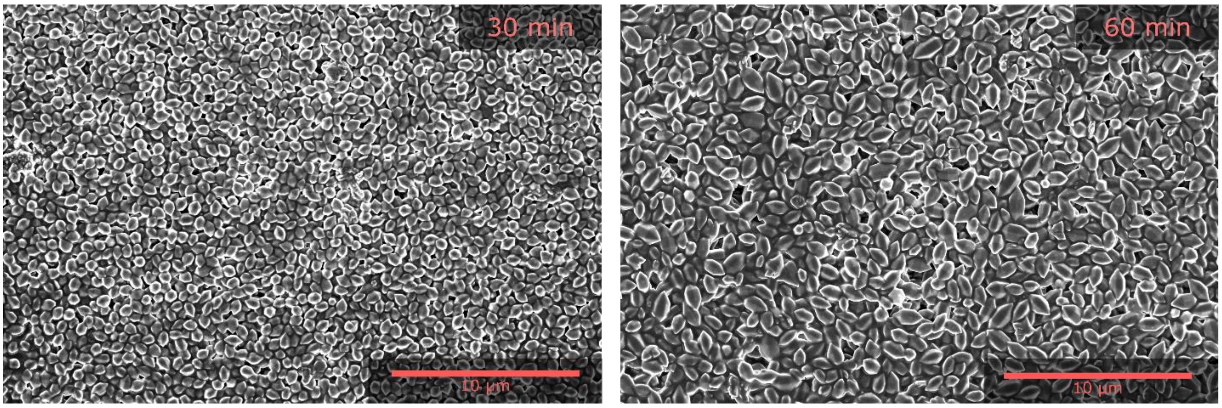

Figure S4.13. SEM micrographs of iron(III) fumarate microparticles grown in a microfluidic reactor at 120 °C in DMF for reaction times of 30 min and 60 min.

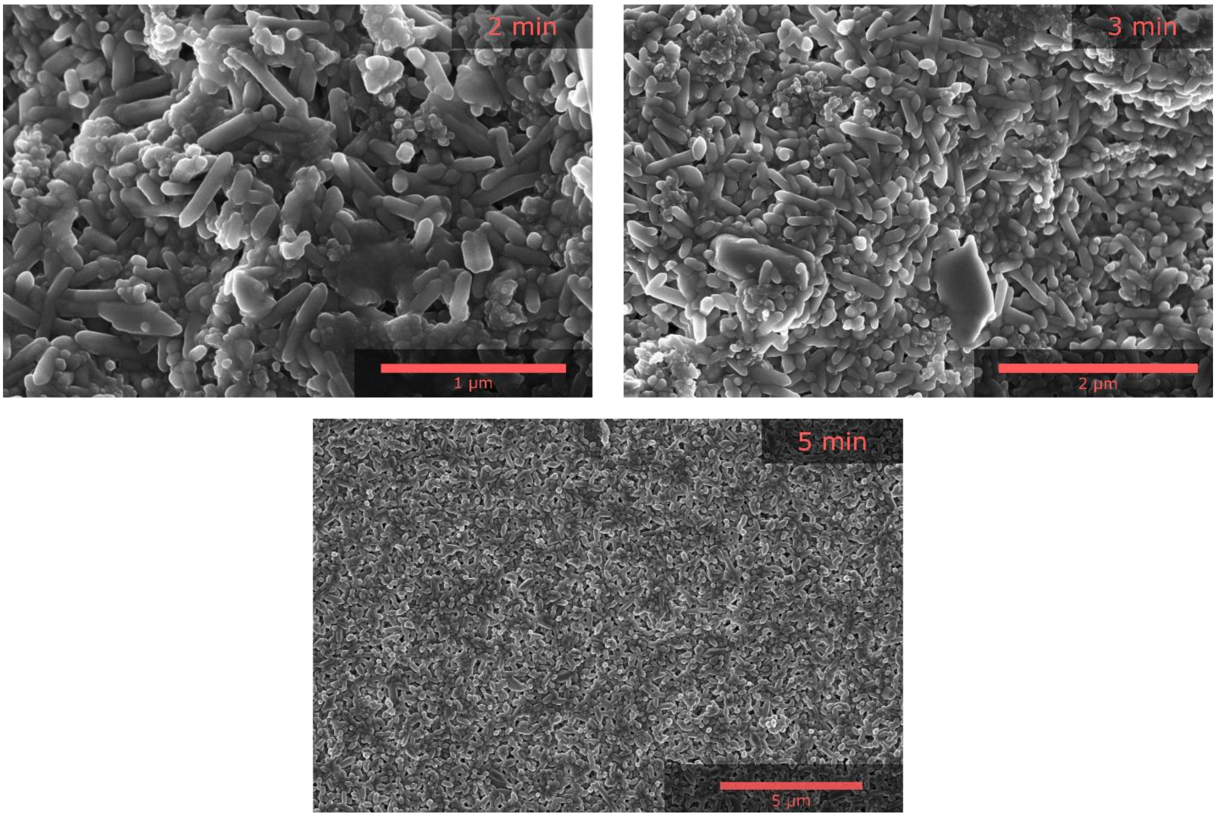

Figure S4.14. SEM micrographs of iron(III) fumarate nanoparticles grown in a microwave reactor at 120 °C in DMF in dependency of reaction time.

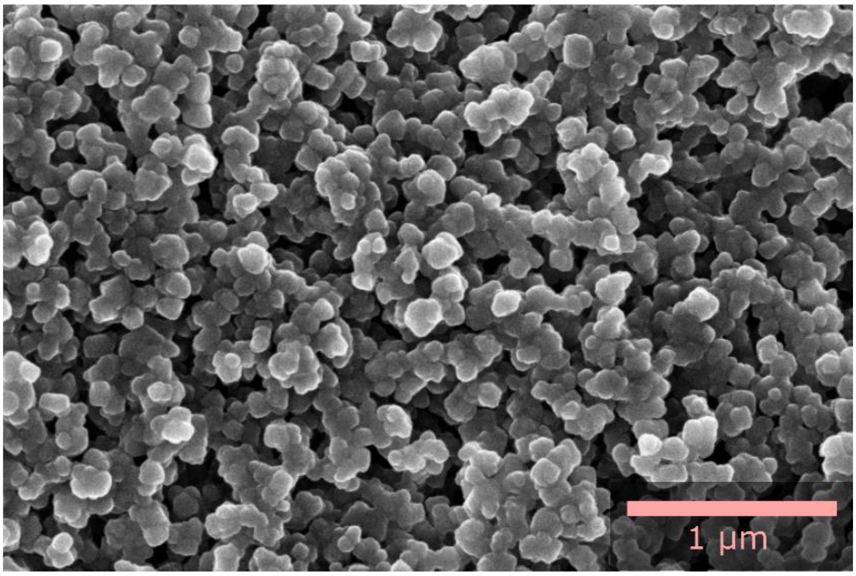

Figure S4.15. SEM micrograph of spherical iron(III) fumarate particles precipitated immediately after mixing iron(III) chloride and fumaric acid.

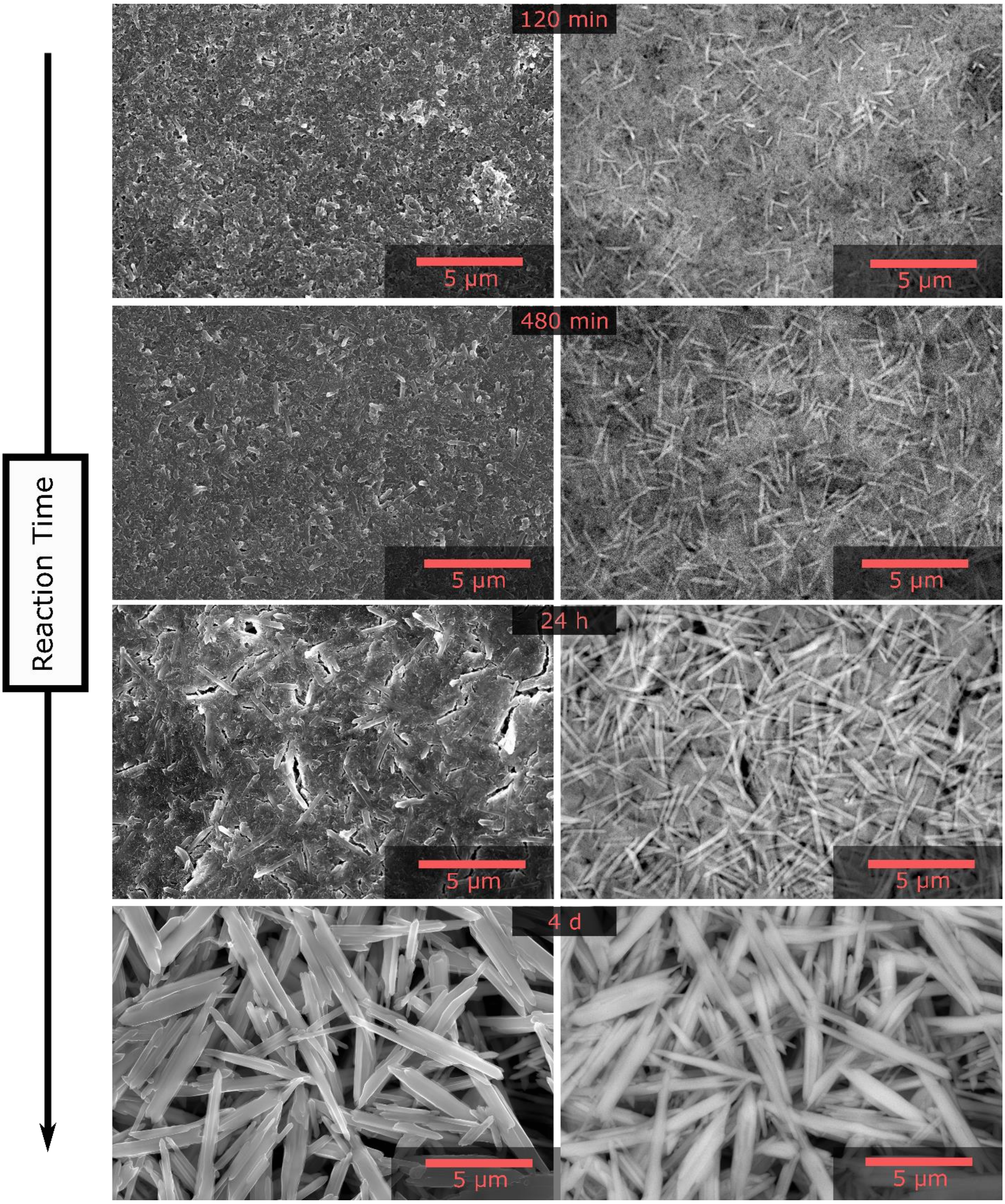

Figure S4.16. SEM micrographs of iron(III) fumarate nano and microparticles grown at RT in water for reaction times of 2 h, 8 h, 24 h and 4 d. On the left and right side the same spot in each sample is depicted. The micrographs on the right side were recorded at 15 kV using a mirror detector, the micrographs on the left side were recorded at 3 kV using a secondary electron detector.

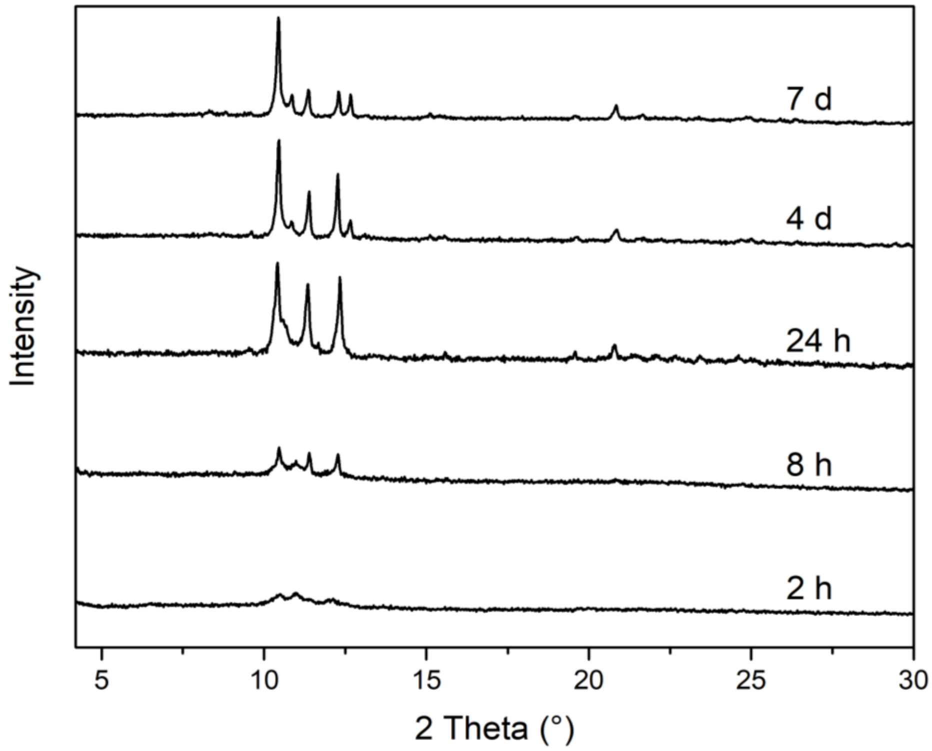

Figure S4.17. X-ray diffraction patterns of dried aqueous iron(III) fumarate reaction mixtures that were incubated at RT with different reaction times. The reaction was stopped by centrifuging and redispersion in ethanol. With time, the samples become increasingly crystalline. As reported in literature, these reflections during the aqueous synthesis of the MOF do not fully correspond to the final crystal structure of MIL-88A but have similarly been reported elsewhere.[6,7,]

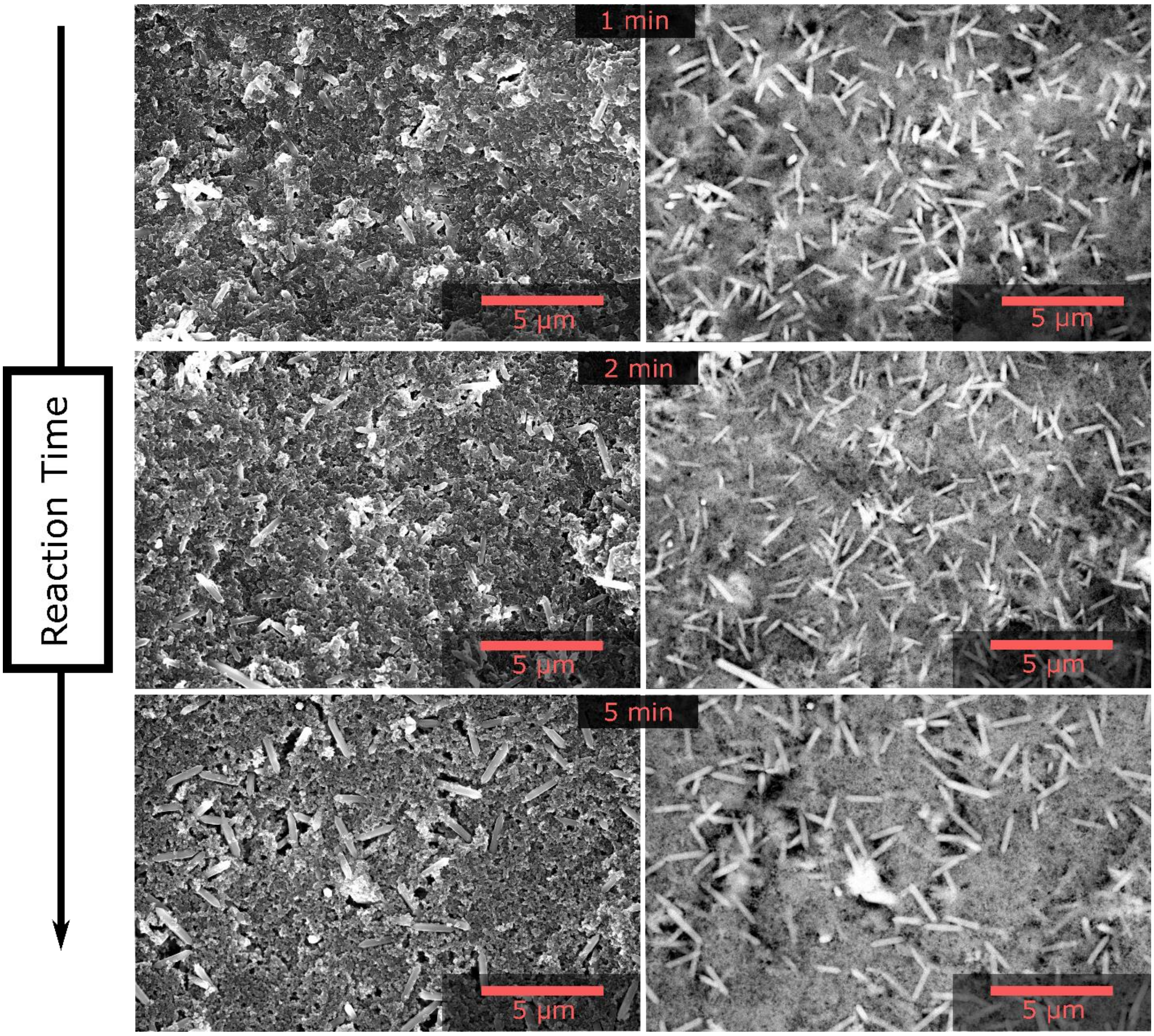

Figure S4.18. SEM micrographs of iron(III) fumarate nano and microparticles grown in a microwave reactor at 80 °C in water for reaction times of 1 min, 2 min, and 5 min. On the left and right side the same spot in each sample is depicted. The micrographs on the right side were recorded at 15 kV using a mirror detector, the micrographs on the left side were recorded at 3 kV using a secondary electron detector.

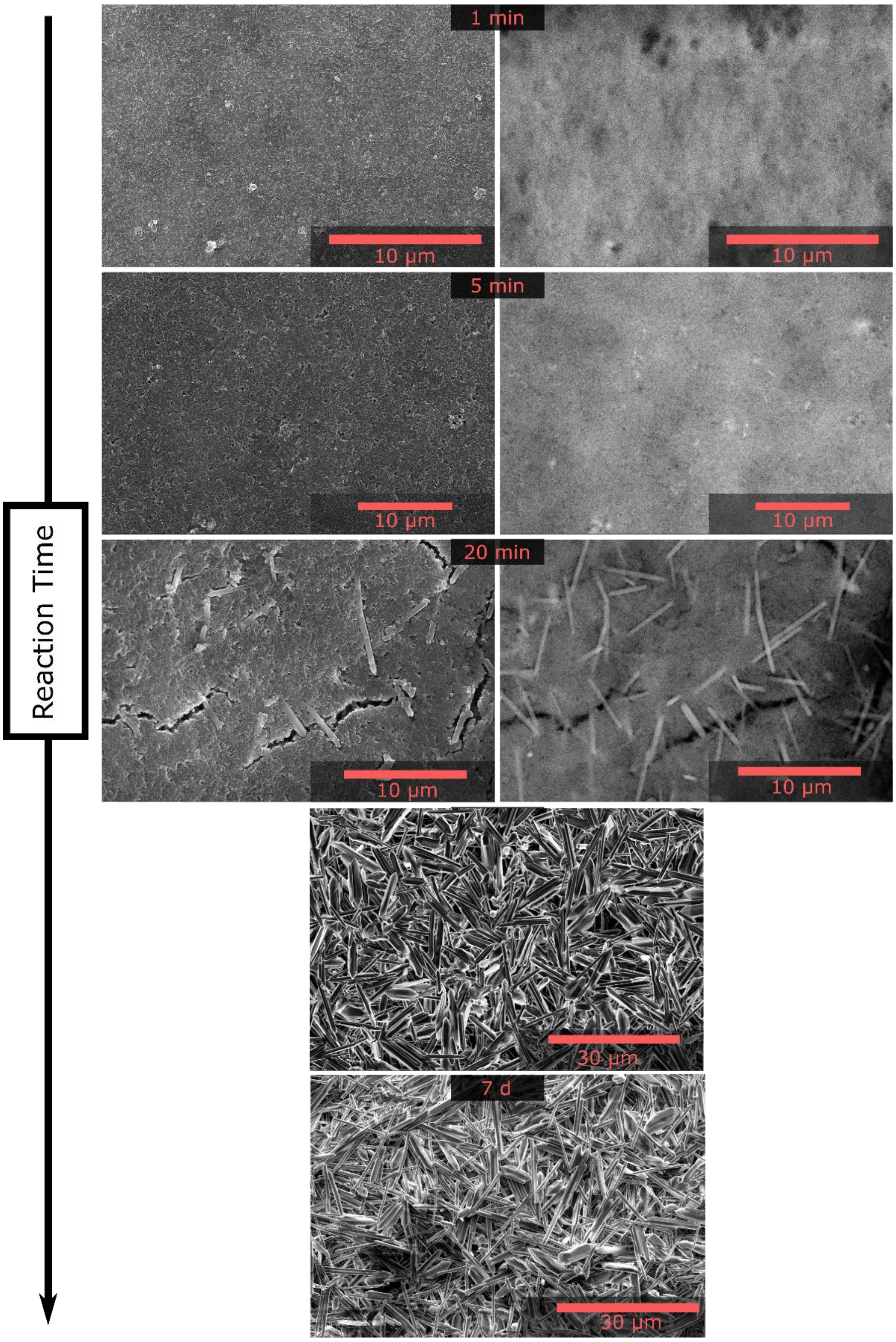

Figure S4.19. SEM micrographs of iron(III) fumarate nano and microparticles grown solvothermally at 80 °C in water for reaction times of 1 min, 5 min, 20 min, 24 h and 7 d. On the left and right side the same spot in each sample is depicted. The micrographs on the right side were recorded at 15 kV using a mirror detector, the micrographs on the left side were recorded at 3 kV using a secondary electron detector.

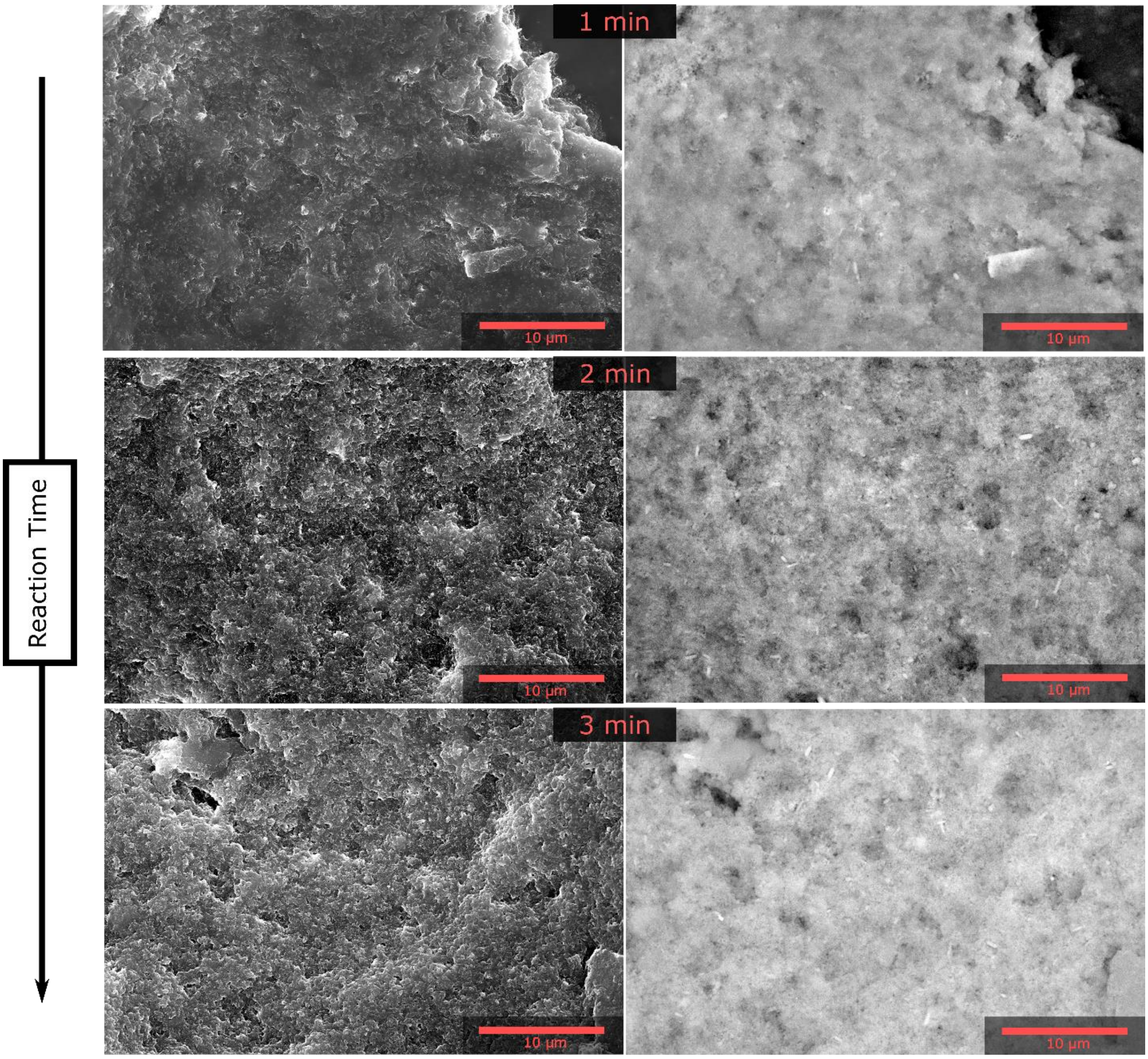

Figure S4.20. SEM micrographs of iron(III) fumarate nano and microparticles grown in a microfluidic reactor at 80 °C in water for low reaction times (1-3 min). On the left and right side the same spot in each sample is depicted. The micrographs on the right side were recorded at 15 kV using a mirror detector, the micrographs on the left side were recorded at 3 kV using a secondary electron detector.

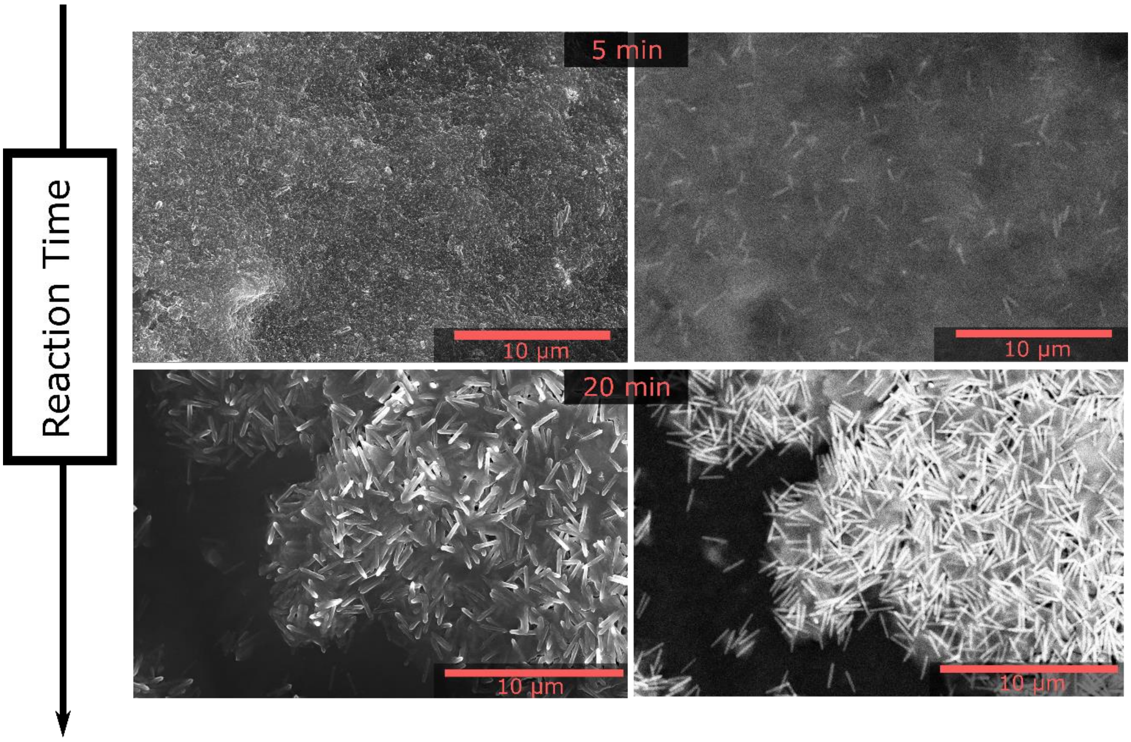

Figure S4.21. SEM micrographs of iron(III) fumarate nano and microparticles grown solvothermally at 80 °C in water at low concentration for reaction times of 5 min and 20 min. On the left and right side the same spot in each sample is depicted. The micrographs on the right side were recorded at 15 kV using a mirror detector, the micrographs on the left side were recorded at 3 kV using a secondary electron detector.

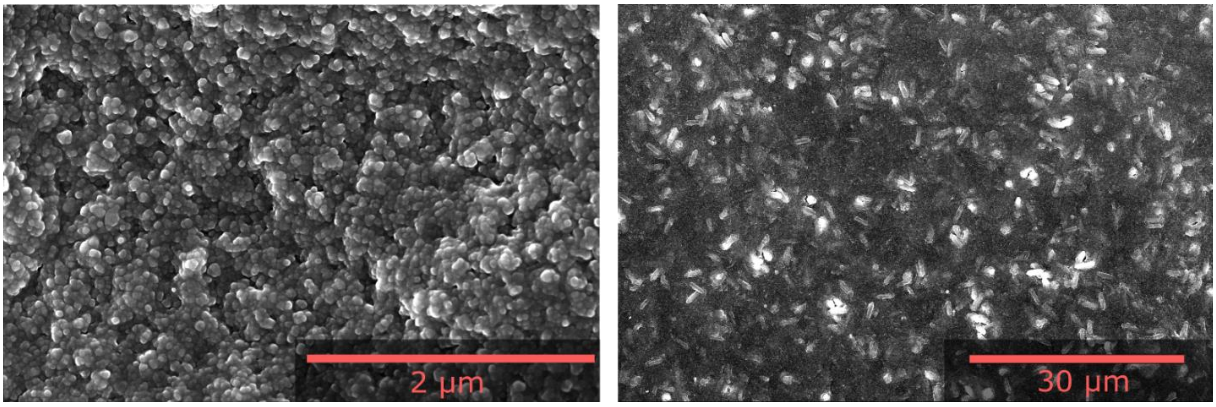

Figure S4.22. SEM micrographs of iron(III) fumarate nano and microparticles grown at RT in water for seven days at low concentration. The micrographs on the right side were recorded at 15 kV using a mirror detector, the micrographs on the left side were recorded at 3 kV using a secondary electron detector.

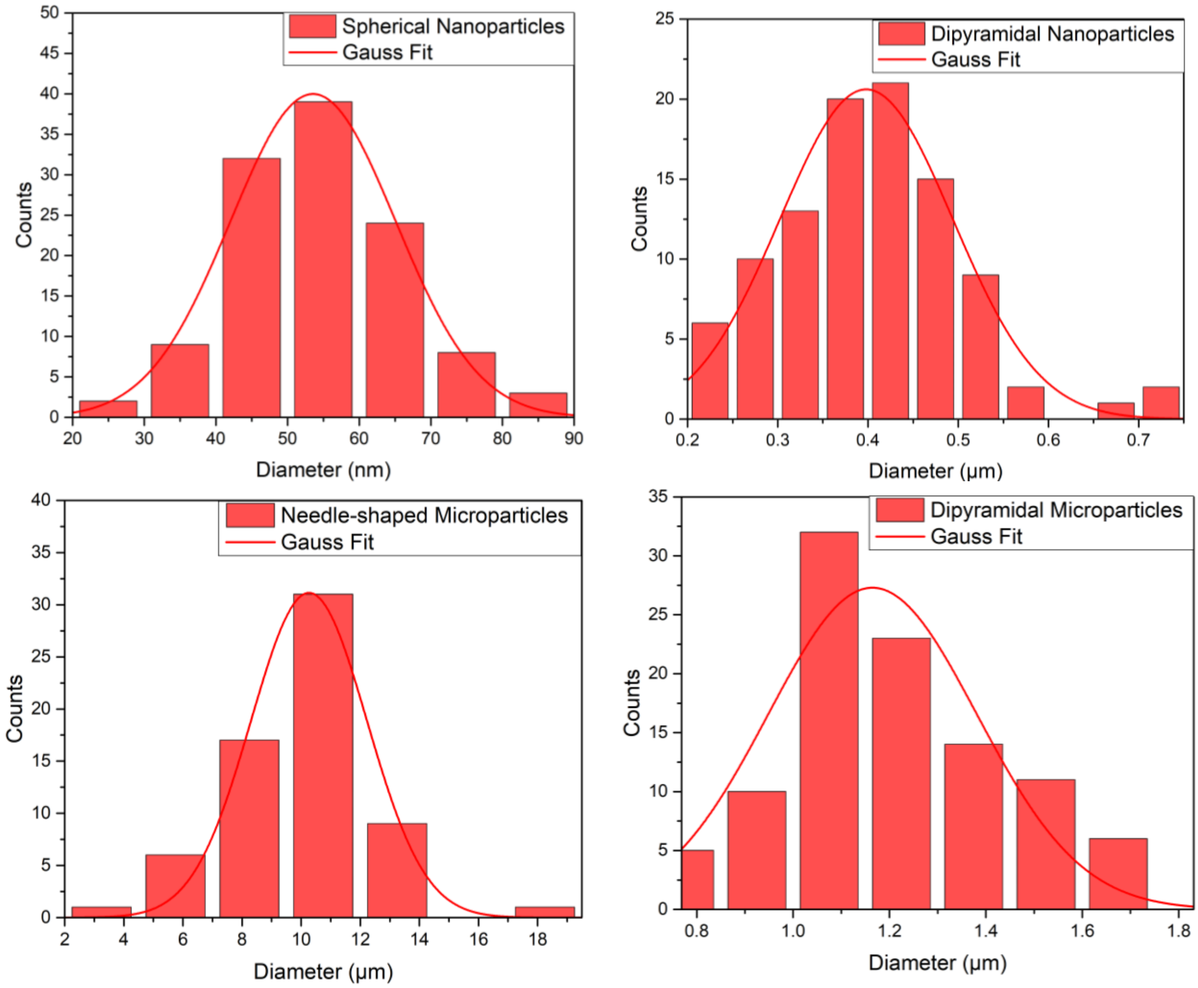

Figure S4.23. Particle size distributions of the four iron(III) fumarate variants determined from SEM micrographs in Figure 2. Depending on the iron(III) fumarate variant 60-120 particles were measured by hand with the software Imagej v1.52e. Using the software Origin Pro v9.1.0., these data were then plotted in histograms and fitted with a Gaussian fit.

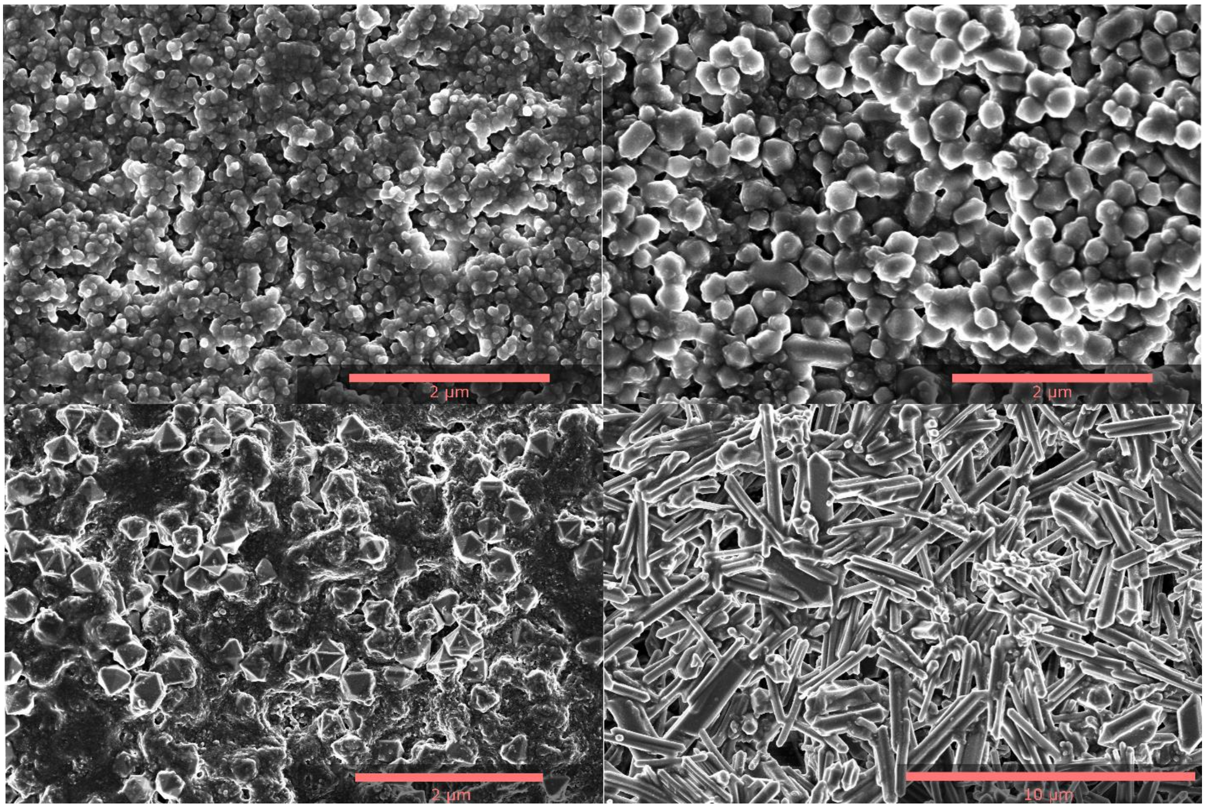

Figure S4.24. SEM micrographs of iron (III) fumarate particles after 24 h in 20% cell medium. Top left (spherical nanoparticles), top right (top right dipyramidal nanoparticles), bottom left (dipyramidal microparticles), bottom right (needle-shaped microparticles).

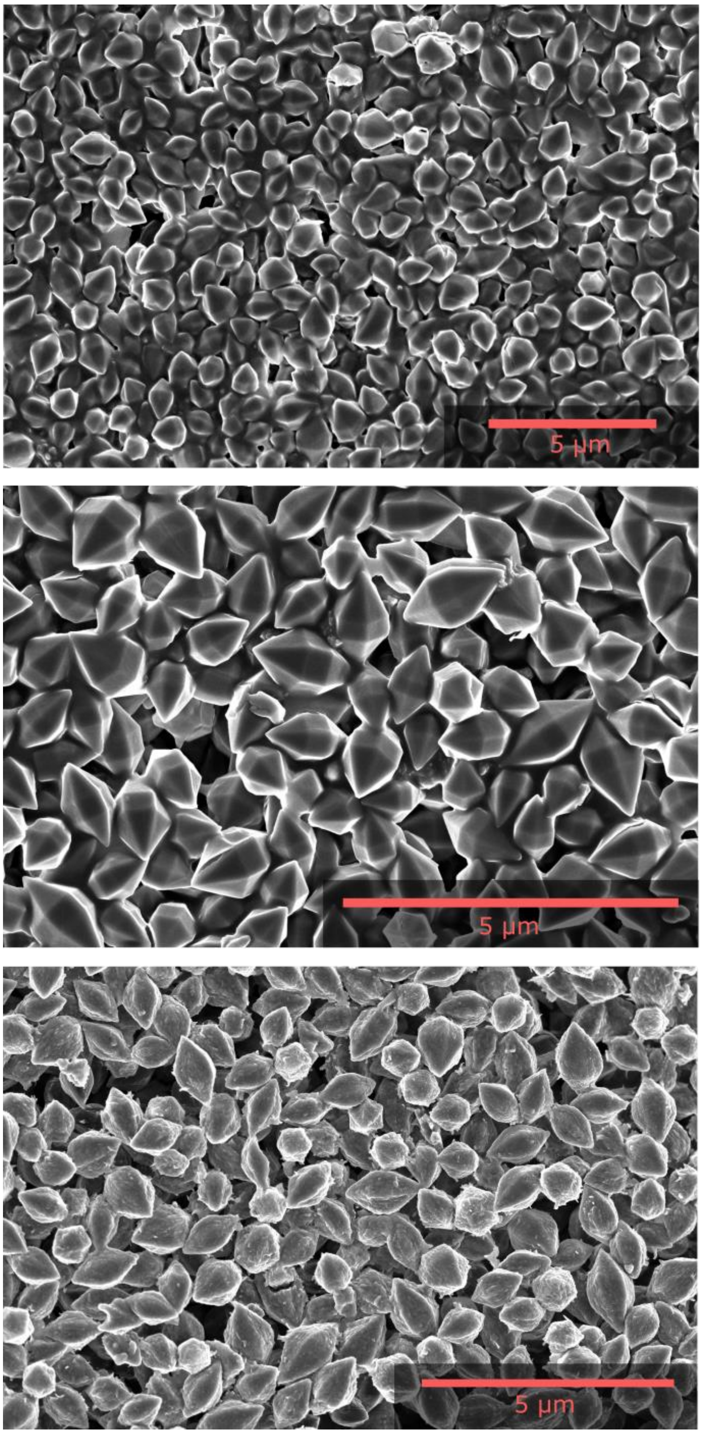

Figure S4.25. SEM micrographs of iron(III) fumarate microparticles solvothermally synthesized in DMF (top), stored for 6 months in ethanol (middle) and stored for 2 weeks in water (bottom).

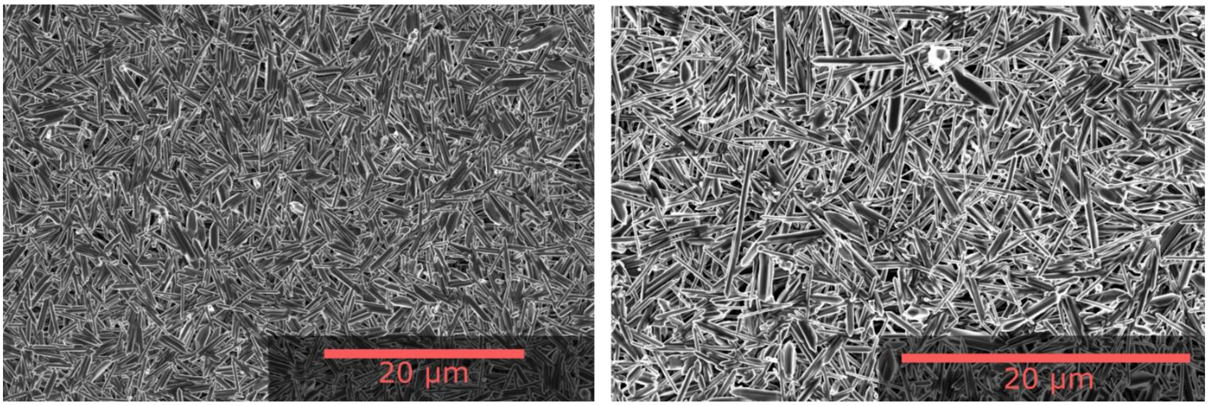

Figure S4.26. SEM micrographs of needle-shaped iron(III) fumarate microparticles freshly prepared from water (left) and stored for 2 months in ethanol (right).

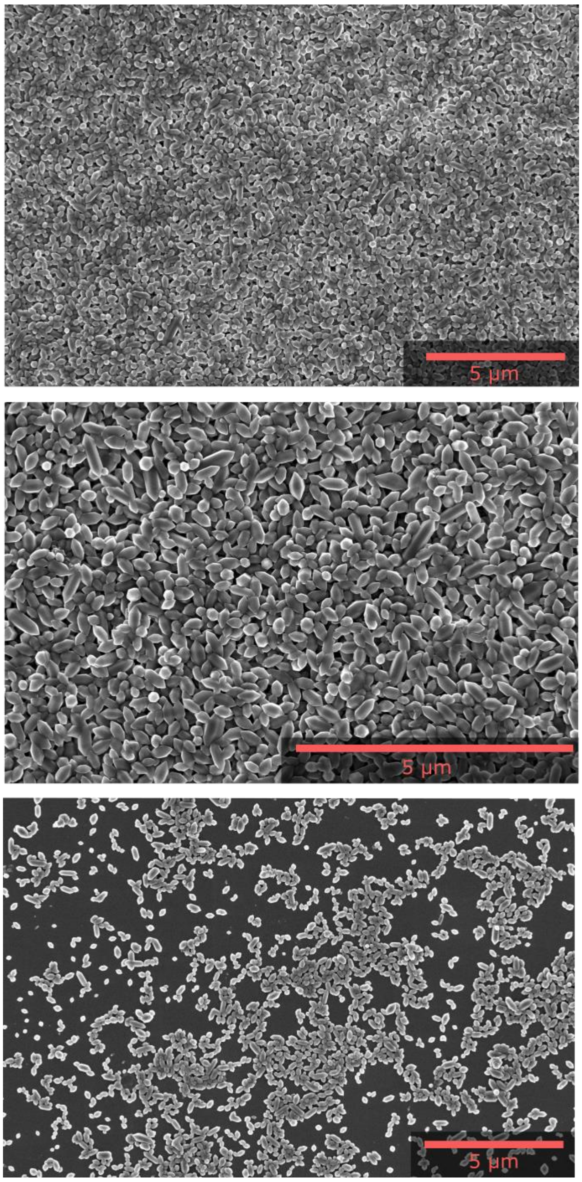

Figure S4.27. Dipyramidal iron(III) fumarate nanoparticles microwave-synthesized in DMF (top), stored for 3 months in ethanol (middle) and stored for 1 day in water (bottom).

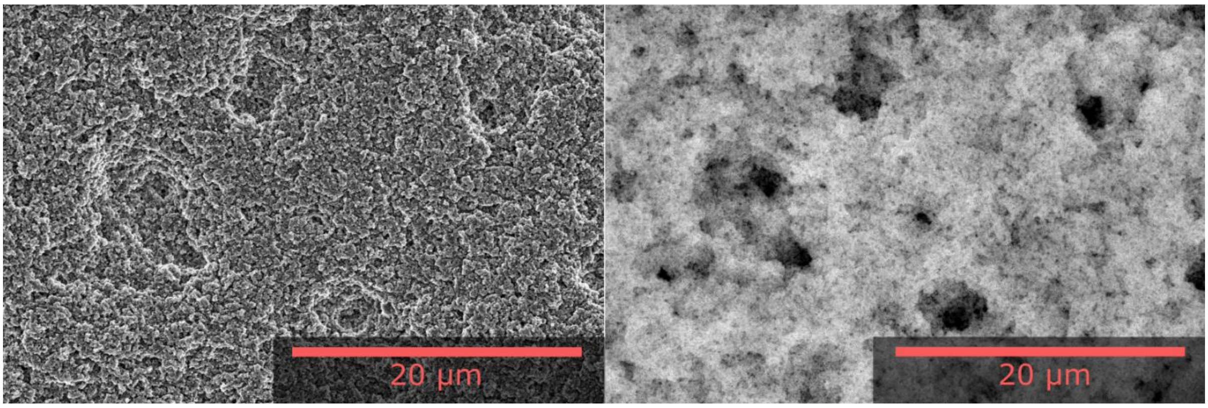

Figure S4.28. SEM micrographs of spherical iron(III) fumarate nanoparticles that were stored for 6 months in ethanol. On the left and right side the same spot in each sample is depicted. The micrographs on the left side were recorded at 3 kV using a secondary electron detector, the micrographs on the right side were recorded at 15 kV using a mirror detector. No formation of needle morphology can be seen in this picture showing the stability of the spherical phase.

Table S4.8. Analysis data on the thermogravimetric degradation of the iron(III) fumarate variants.

	Spherical Nanoparticles	**Needle-shaped Microparticles**	**Dipyramidal Microparticles**	**Dipyramidal Nanoparticles**
Residual mass dried framework	93.7%	97.2%	92.0%	94.8%
Onset of framework degradation	267.4 °C	273.5 °C	259.2 °C	285.0 °C
Residual mass	38.5%	40.2%	40.7%	37.2%

Figure S4.29. Left: Degradation curves of the different iron(III) fumarate variants. Right: X-ray diffraction pattern of the resulting degradation product.

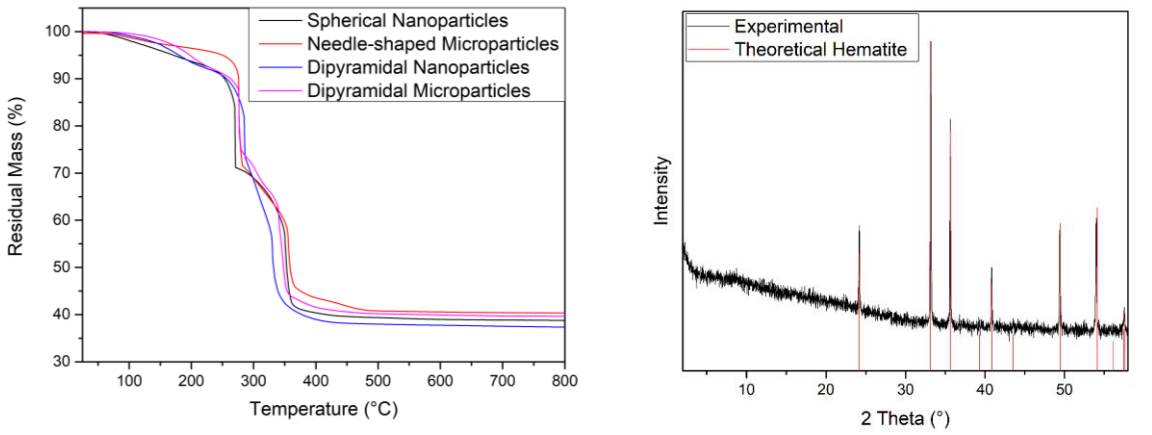

Table S4.9. The lattice parameters of the X-ray amorphous spherical iron(III) fumarate nanoparticles were determined with electron diffraction on the basis on the theoretical fully dry-pore (*a* = 9.78, *c* = 14.83) and fully open-pore (*a* = 13.87 , *c* = 12.66) MIL-88A crystal structures published by Serre.[5] For the spherical nanoparticle sample, our experimentally observed d-values are between these two extreme cases but closer to the open pore structure.

Laue indices	011	020	$\bar{1}32$	$\bar{1}35$	$\bar{2}57$
Theoretical lattice distances of closed-pore MIL-88A[Å] [5]	7.35	4.2	2.93	2.17	1.43
Theoretical lattice distances of open-pore MIL-88A[Å] [5]	8.72	6.01	3.69	2.21	1.51
Experimental lattice distances [Å]	7.8	4.1	2.92	2.17	1.47

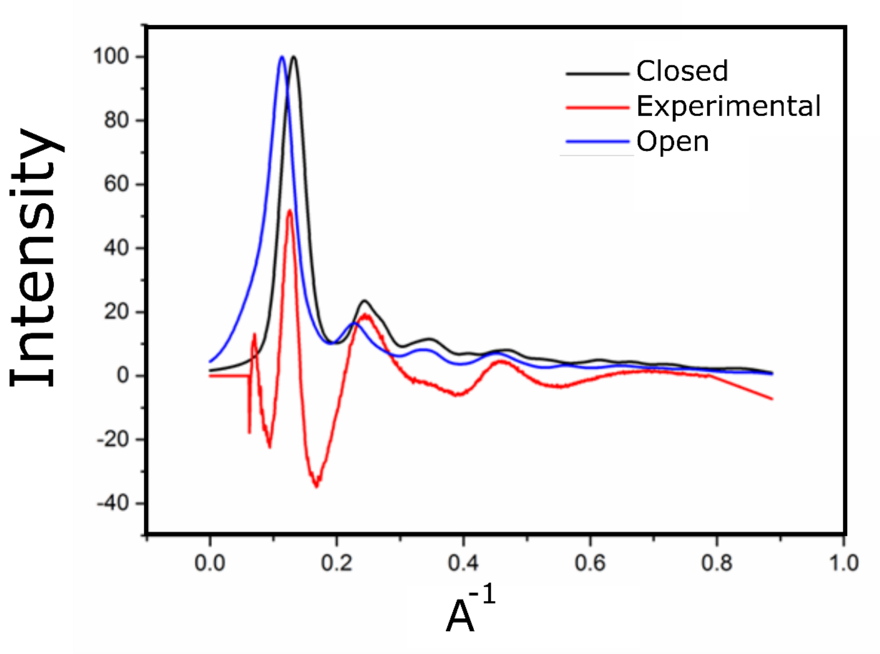

Figure S4.30. Simulated electron diffraction patterns of closed pore and open pore MIL-88A compared experimental azimuthally integrated and background subtracted Electron diffraction pattern of X-ray amorphous iron(III) fumarate nanoparticles.

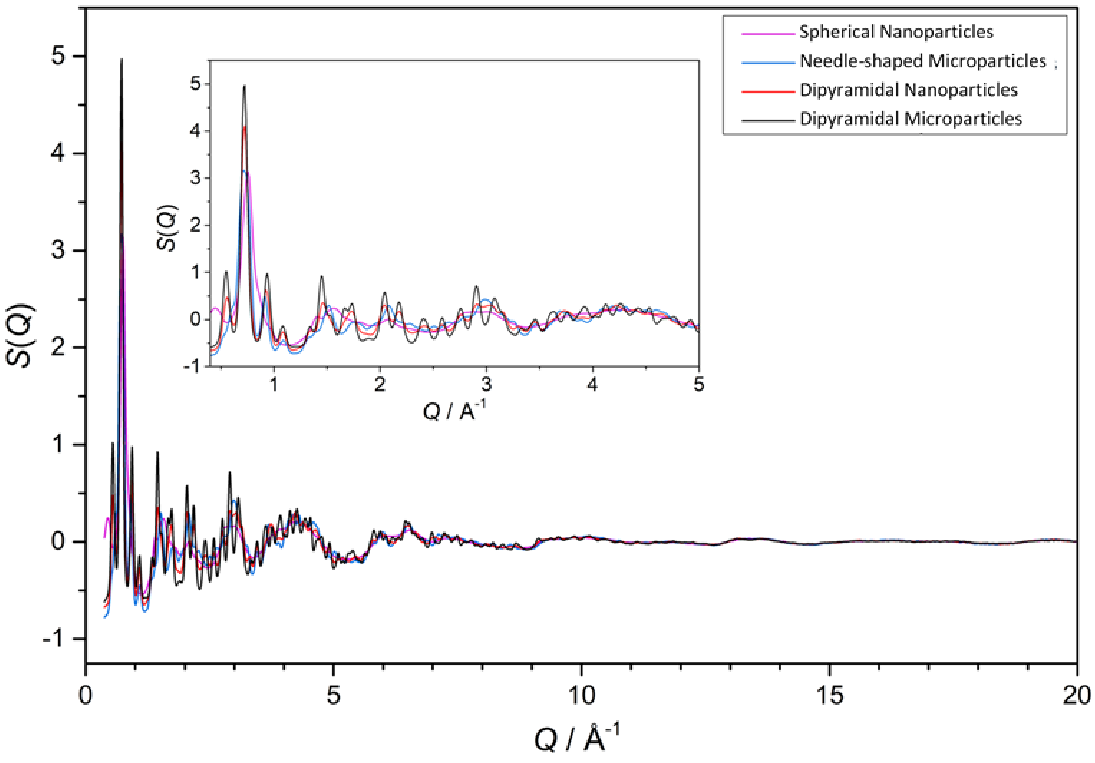

Figure S4.31. X-ray structure factors S(Q)s of the four samples.

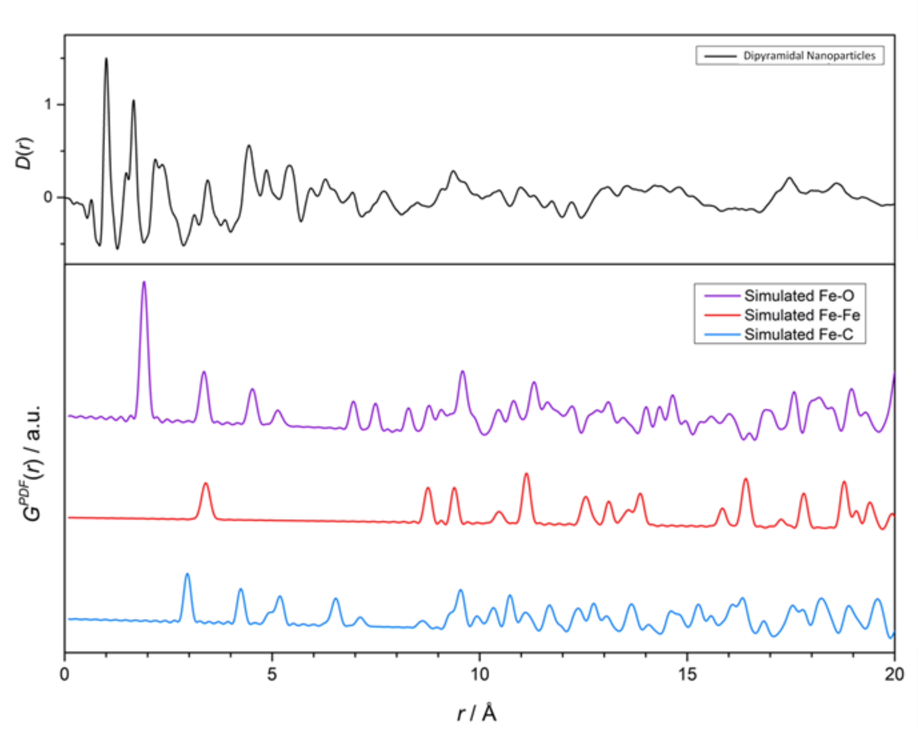

Figure S4.32. *D*(*r*) of MIL-88A Dipyramidal nanoparticles (upper) and simulated partial PDFs of Fe-O (purple), Fe-Fe (red), and Fe-C (blue) atom-atom correlations using PDFGUI and the corresponding MIL-88A Open CIF file[5] (lower).

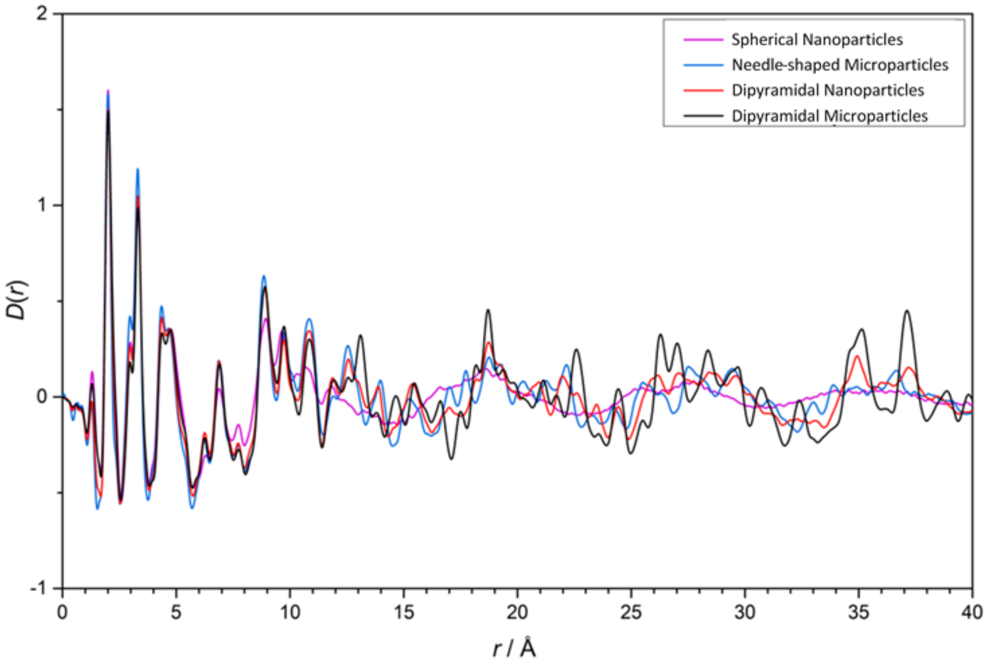

Figure S4.33. Pair distribution functions *D*(*r*) of the four samples.

Table S4.10. BET-analysis data of iron(III)-fumarate.

Sample	**BET surface area**	**Relative pressure range**	**c**	**Correlation coefficient**
Spherical Nanoparticles	446 m² g^{-1}	0.05-0.17	154	0.999
Dipyramidal Nanoparticles	264 m² g^{-1}	0.15-0.27	43	0.999
Dipyramidal Microparticles	212 m² g^{-1}	0.04-0.15	428	0.999
Needle-shaped Microparticles	119 m² g^{-1}	0.002-0.02	1131	0.999

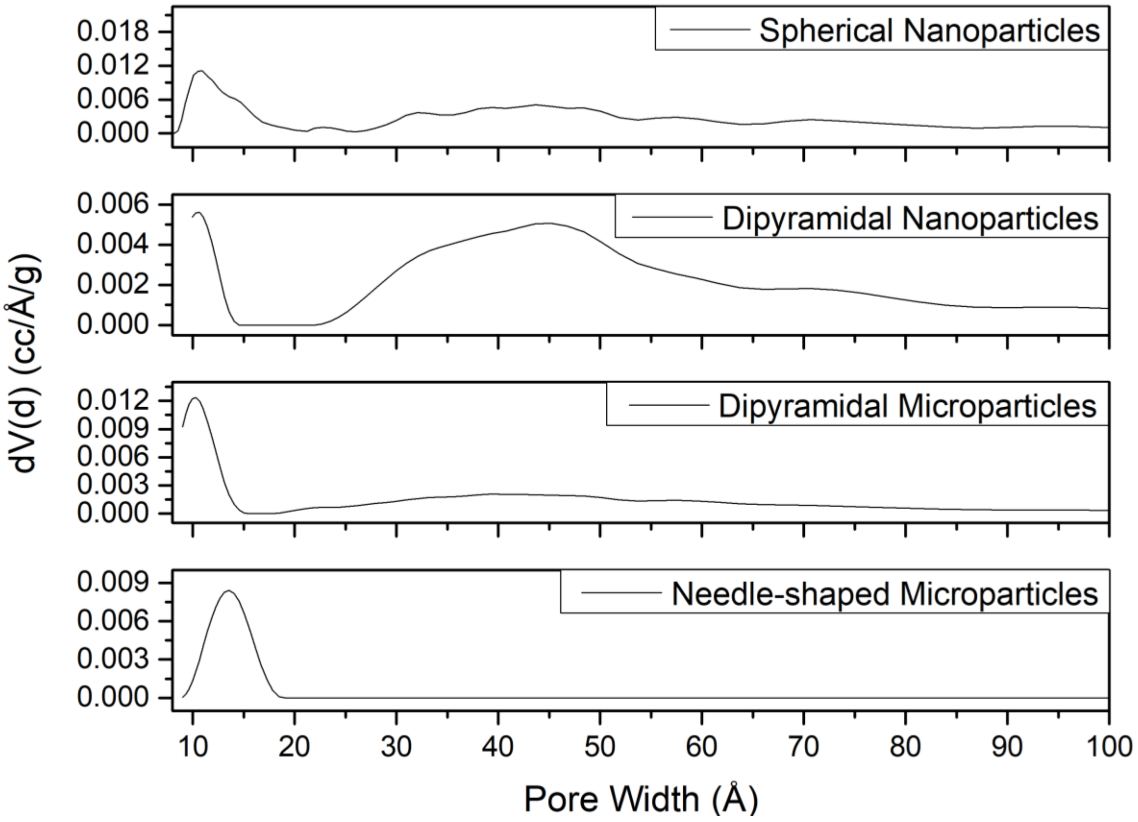

Figure S4.34. Pore size distribution of the 4 iron(III) fumarate variants as determined with nitrogen sorption.

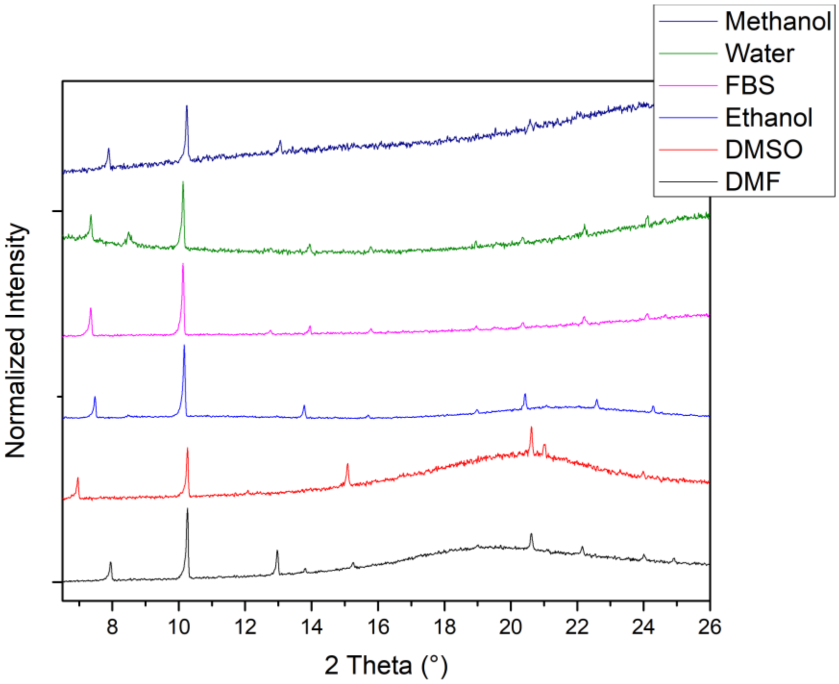

Figure S4.35. *In-situ* X-ray diffraction patterns of dipyramidal iron(III) fumarate microparticles.

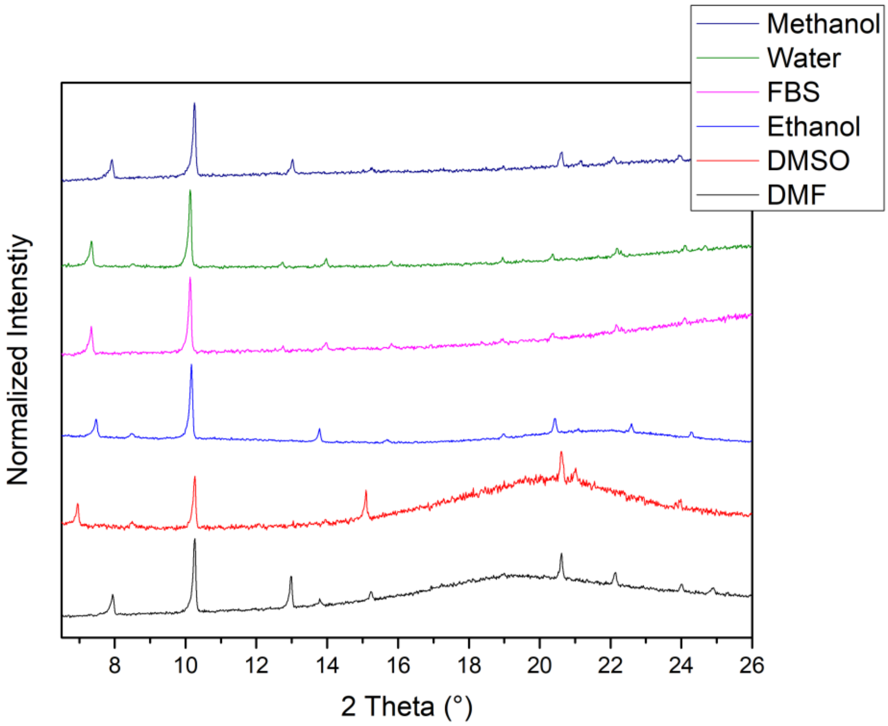

Figure S4.36. *In-situ* X-ray diffraction patterns of dipyramidal iron(III) fumarate nanoparticles.

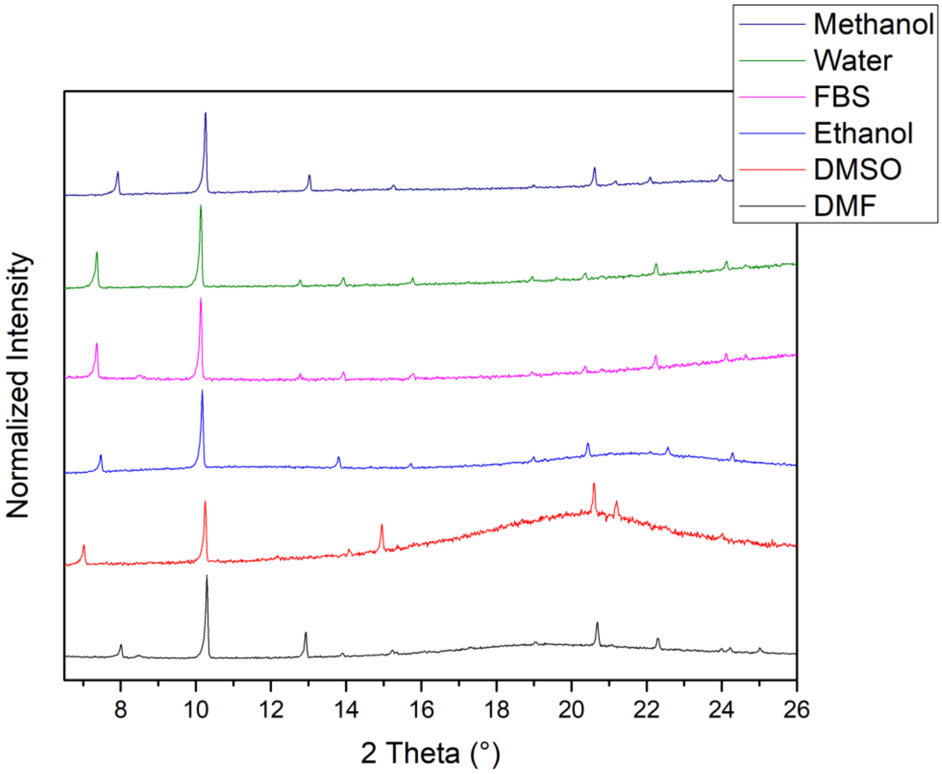

Figure S4.37. *In-situ* X-ray diffraction patterns of needle-shaped iron(III) fumarate microparticles.

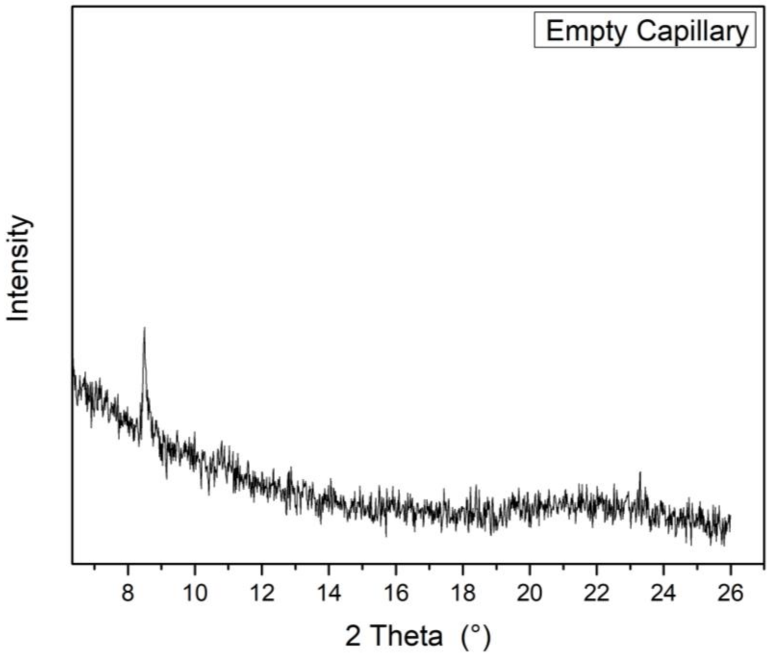

Figure S4.38. X-ray diffraction data of an empty glass used during *in-situ* X-ray diffraction experiments.

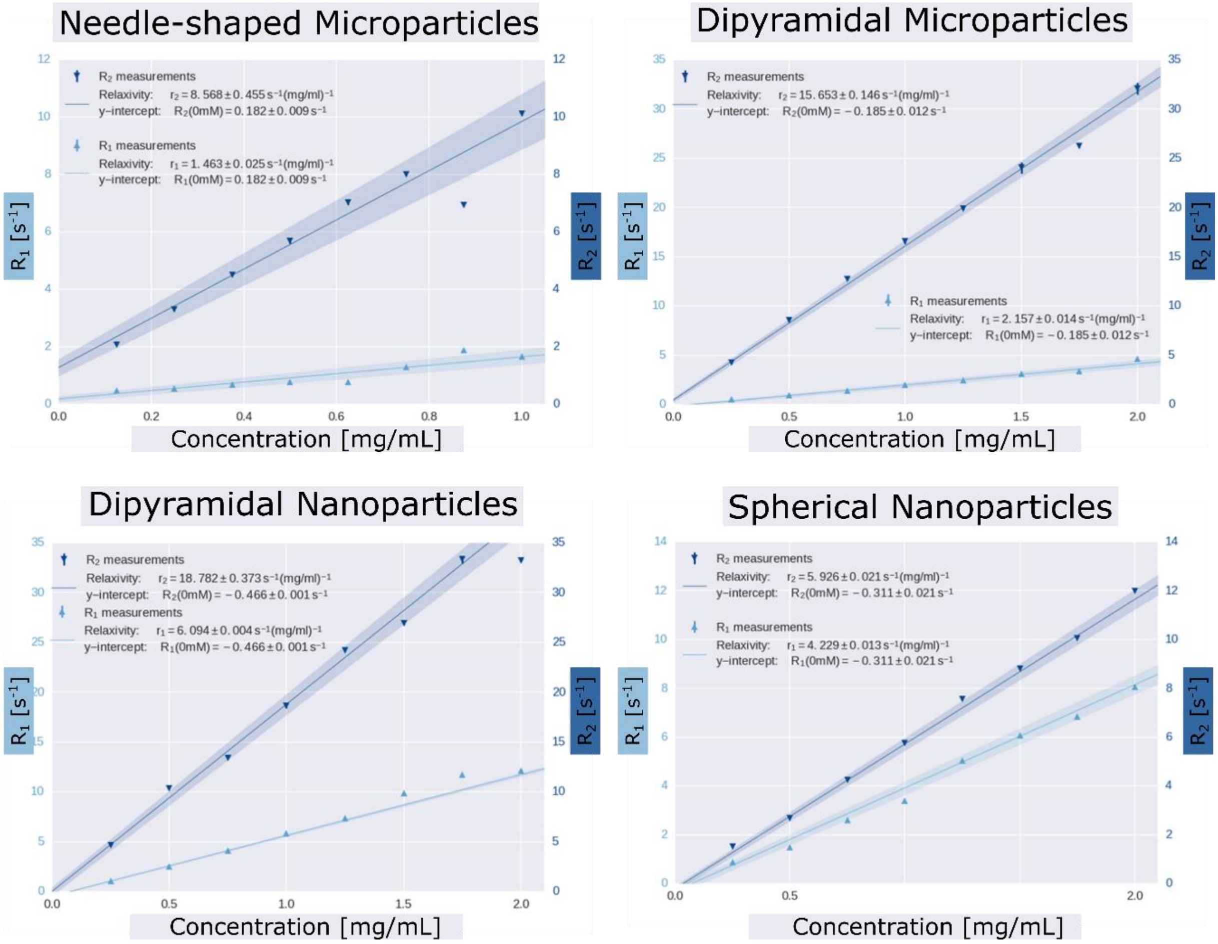

Figure S4.39. Determination of the mass-based relaxivities in accordance to Table 4 for the respective iron(III) fumarate variants. Experimentally determined inverse relaxation times are plotted vs iron(III) fumarate concentration. Relaxivity values can be determined from the slope of the linear plot.

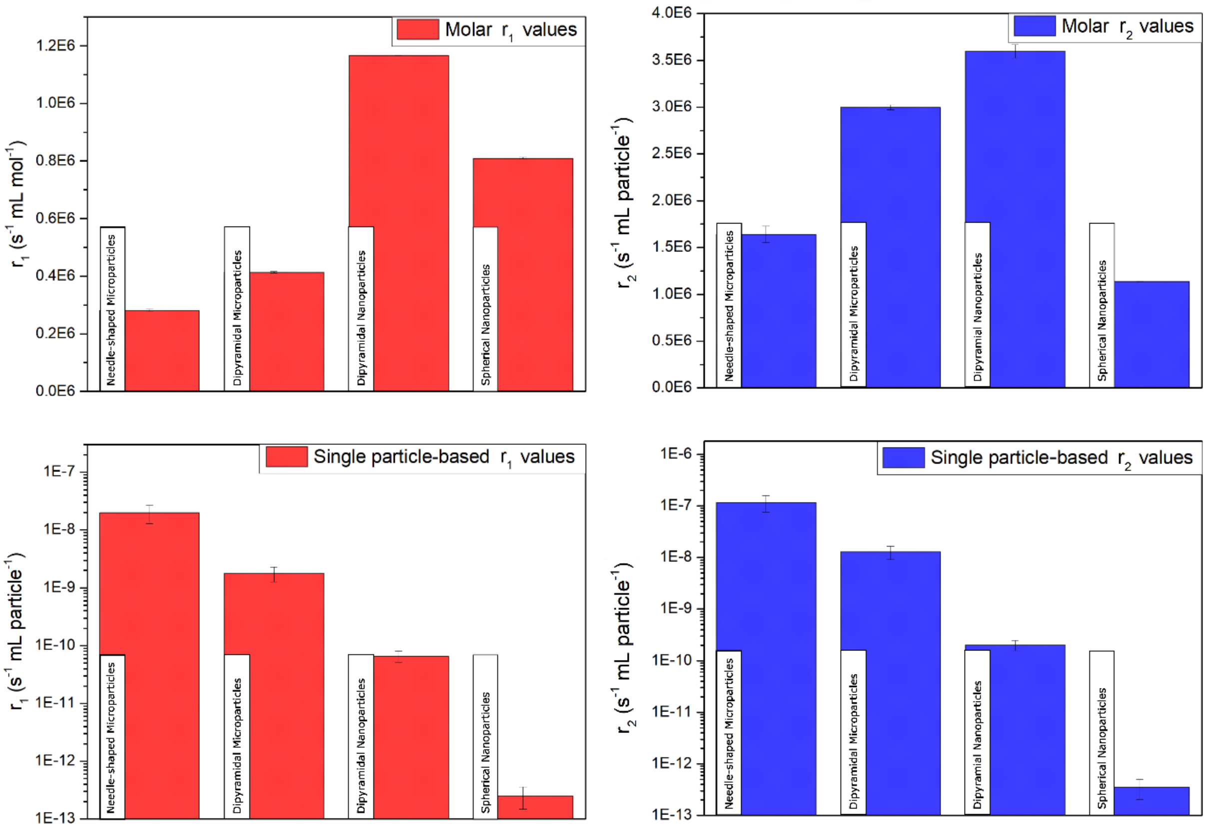

Figure S4.40. MRI relaxivities of the four iron(III) fumarate particles with different focus. The data that are presented as mass-based relaxivities in Table 4 and Figure S4.39 can be converted to other relaxivity values for better comparison. For evaluating the relaxivities per single particle we were approximating the particle size of the respective iron(III) fumarate variants from SEM measurements. In our estimate, we treated the dipyramidal microparticles (diameter 1200 ± 200 nm) and the spherical nanoparticles (diameter 50 ± 12 nm) as spheres calculating their volume from their particle size distribution (**Figure S4.23**). The morphology of the needle-shaped microparticles was approximated as a cylindrical shape and their particle volume calculated from their mean diameter (975 ± 420 nm) and length (10 ± 2 µm). The volume of the dipyramidal nanoparticles (length 400 ± 95 nm, diameter 185 ± 30 nm) was approximated as a cylinder with 2 cone shaped tips, featuring a ratio of 1/3 : 1/3 : 1/3. With these approximations and assuming an open porous MIL-88A structure with a crystallographic density of 0.902 g/cm[35,8] the mass based relaxivities were transformed to single particle-based relaxivities. Similarly, these values can be transformed into relaxivities that are normalized towards single iron(III)-ions in the structure assuming a 29.2 wt% iron in the crystal structure[5]. For better comparison with commercially available MRI contrast coordination complexes these values were additionally normalized towards the molar quantity of iron(III) ions.

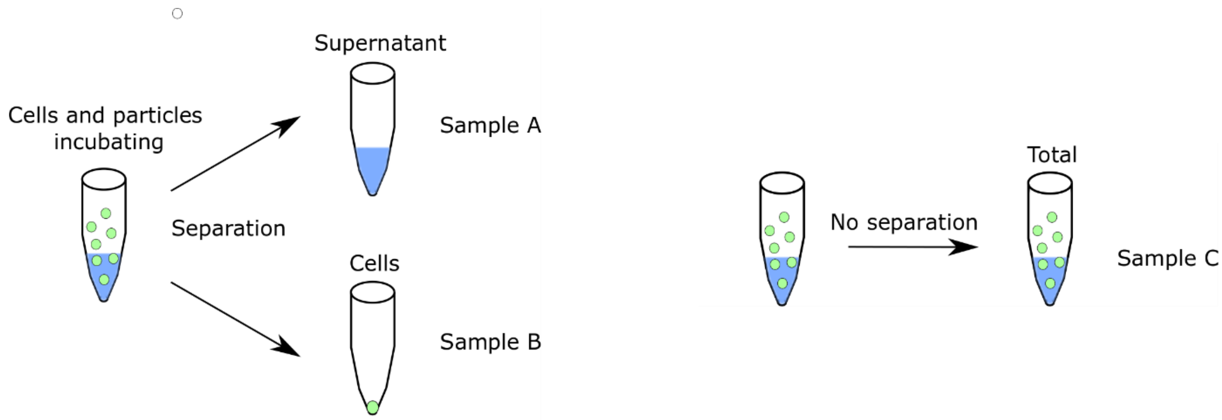

Figure S4.41. To measure the cell association of the respective iron(III) fumarate variants ICP-OES measurements were performed. For sample preparation HeLa-Cells (500 µL) were incubated for 24 h at 37 °C with aqueous solutions of iron(III) fumarate particles (100 µg/mL) in a 24 well plate. After this incubation period cells and supernatant were separated. The cells were washed twice with phosphate buffered saline (500 µL), these washing solutions were then unified with the incubation-supernatant (Samples A). The cells were recovered separately by adding 500 mL of aqueous triton solution (1%) with an additional washing step afterwards (500 µL H2O) Samples B). To quantify the iron content in the extracellular medium and associated with cells (100 %), control samples in which incubation solution and cells were not separated were additionally prepared (Samples C). As a background control of physiological iron content, cells were treated in the same fashion without addition of iron(III) fumarate particles (Cells A-C). This incubation was additionally repeated with using an iron(III) chloride solution (29.2 µg/mL) ($FeCl_3$ A-C). All samples labelled with A and B were prepared in triplicate. Prior to the measurements the samples were dried in an oven (100 °C, 48 h). The residuals were dissolved in HNO_3 (10%) and the respective iron content of the solutions analyzed with ICP-OES. The measured iron contents can be found in **Table S4.11.**

Table S4.11. Iron Content in cell association experiments determined from ICP-OES measurements.

Sample	Iron content (µg/mL)
Spherical Nanoparticles A	22.63 ± 0.25
Dipyramidal Microparticles A	10.49 ± 0.24
Needle-shaped Microparticles A	8.61 ± 0.33
Dipyramidal Nanoparticles A	20.44 ± 0.49
$FeCl_3$ A	31.66 ± 0.08
Spherical Nanoparticles B	4.28 ± 0.18
Dipyramidal Microparticles B	18.00 ± 0.55
Needle-shaped Microparticles B	20.12 ± 0.41
Dipyramidal Nanoparticles B	8.71 ± 0.20
$FeCl_3$ B	0.82 ± 0.14
Cells A	Below threshold
Cells B	Below threshold
Spherical Nanoparticles C	28.60
Dipyramidal Microparticles C	30.42
Needle-shaped Microparticles C	30.54
Dipyramidal Nanoparticles C	30.30
$FeCl_3$ C	31.69
Cells C	1.06

4.7.7 Calculations on the Theoretical Particle Surface Area

Equation 26
$$S = 4\,\pi\,r^2$$

Equation 27
$$V = \frac{4}{3}\,\pi\,r^3$$

The change in BET surface area of the iron(III) fumarate microparticles variants (**Table S4.10**) cannot only be explained with just the varying particle sizes. Using the equations above and approximating a spherical morphology for the dipyramidal microparticle iron(III) fumarate variant, the outer surface area of a single such particle with a diameter of 1600 nm can be calculated at $8.4\,x\,10^{-8}$ cm². The corresponding particle volume is at $2.4\,x\,10^{-12}$ cm³. Assuming a density of 1.55138 g/cm³ (crystallographic density of dry MIL-88A[5]) this results in an outer surface area of 2.4 m²/g for the entire sample. The same calculations result in outer surface area of 13 m²/g for when approximating the dipyramidal nanoparticle iron(III) fumarate variant. The respective increase of surface area in these samples however exceeds this approximation. As all samples exhibit the same crystal structure this effect either stems from pore clogging and/or from texturing. We assume that both of these effects are present. On the one hand the pore size distributions of the dipyramidal microparticles and dipyramidal nanoparticles exhibit mesopores. On the other hand thermogravimetric analysis shows a ~ 3 fold increase of residual solvent molecules in the pores that was not removable even under heating in high-vacuum.

When comparing spherical iron(III) fumarate to the other iron(III) fumarate microparticles crystallinity might play an effect as well: Using the equations above, a single spherical particle with a diameter of 60 nm exhibits a volume of $1.13\,x\,10^{-16}$ cm³ and an outer surface area of $1.13\,x\,10^{-10}$ cm². Assuming crystallinity and a density of 1.55138 g/cm³ (crystallographic density of dry MIL-88A[5]) this results in a theoretical surface area of 64 m²/g. If the same calculations are done for a spherical particle (as this is roughly the shape of the dipyramidal microparticles) with a diameter of 1600 nm the theoretical surface area stemming from the outer surface of the particles can be calculated at 2.4 m²/g. The actual increase of the surface area of the spherical nanoparticles to the dipyramidal microparticles is at 244 m²/g and must originate from a different reason. In case of the spherical nanoparticles this can be explained due to texturing during drying or due to effects from their decreased crystallinity.

References

1 Soper, A. K. GudrunN and GudrunX: Programs for Correcting Raw Neutron and X-ray Diffraction Data to Differential Scattering Cross Section. Report No. RAL-TR-2011-013, (Rutherford Appleton Laboratory Technical Report, Oxfordshire, 2011).

2 Soper, A. K. & Barney, E. R. Extracting the pair distribution function from white-beam X-ray total scattering data. *J. Appl. Crystallogr.* **44**, 714-726, doi:10.1107/s0021889811021455 (2011).

3 Mellot-Draznieks, C. Role of computer simulations in structure prediction and structure determination: from molecular compounds to hybrid frameworks. *J. Mater. Chem.* **17**, 4348, doi:10.1039/b702516p (2007).

4 Farrow, C. L. *et al.* PDFfit2 and PDFgui: computer programs for studying nanostructure in crystals. *J Phys Condens Matter* **19**, 335219, doi:10.1088/0953-8984/19/33/335219 (2007).

5 Serre, C. *et al.* Role of solvent-host interactions that lead to very large swelling of hybrid frameworks. *Science* **315**, 1828-1831, doi:10.1126/science.1137975 (2007).

6 Wang, J. *et al.* Metal–organic frameworks MIL-88A with suitable synthesis conditions and optimal dosage for effective catalytic degradation of Orange G through persulfate activation. *RSC Advances* **6**, 112502-112511, doi:10.1039/c6ra24429g (2016).

7 Liu, N. *et al.* Ultrathin graphene oxide encapsulated in uniform MIL-88A(Fe) for enhanced visible light-driven photodegradation of RhB. *Applied Catalysis B: Environmental* **221**, 119-128, doi:10.1016/j.apcatb.2017.09.020 (2018).

8 Chalati, T., Horcajada, P., Gref, R., Couvreur, P. & Serre, C. Optimisation of the synthesis of MOF nanoparticles made of flexible porous iron fumarate MIL-88A. *J. Mater. Chem.* **21**, 2220-2227, doi:10.1039/c0jm03563g (2011).

5 Exosome-coated Metal-Organic Framework Nanoparticles: An Efficient Drug Delivery Platform

This chapter is based on the following publication:

Illes B, **Hirschle P**, Barnert S, Cauda V, Wuttke S, Engelke H. Chem Mater. **2017**;29(19):8042-6. (DOI: 10.1021/acs.chemmater.7b02358)

5.1 Introduction

Drug delivery systems aim at a reduction of side effects in chemotherapy. This is achieved by encapsulation of drugs in nanocarriers followed by controlled release of these drugs at the site of the diseased tissue. While inorganic or polymeric nanoparticles (NPs) are often used as nanocarriers[1,2], hybrid nanomaterials such as metal-organic framework (MOF) NPs have recently emerged as a valuable alternative.[3-6] They are synthesized from inorganic and organic building block units to create porous three-dimensional frameworks. Due to this building principle, the composition and structure of these materials are highly tunable.[7-10] Furthermore, both external and internal surfaces can be functionalized independently. With these properties, MOF NPs can be designed to fit the specific requirements of the desired application.[6,11] For drug delivery purposes these so called “design materials” have been synthesized with high porosity allowing for high drug loading capacities. They also have been designed to be biodegradable. Specifically, iron-based MOF NPs have attracted great attention. In addition to the above-mentioned properties, they can be detected via magnetic resonance imaging (MRI), rendering them an ideal platform for theranostics.[12-14] In our study we focus on one of these iron-based MOFs, namely MIL-88A NPs, which are composed of iron(III) and fumaric acid.[15,16] Both compounds can be found in the body and the NPs are reported to be non-toxic.[14] Additionally, MIL-88A NPs have been shown to efficiently host chemotherapeutic drugs.[14] Thus, they represent a promising nanocarrier.

To complete the drug delivery system, nanocarriers need a capping system that prevents leakage of the drug, protects both drug and NP from degrading enzymes, and hides them from the immune system to avoid premature clearance from the circulatory and rethiculoendothelial systems. Out of many potential capping systems, such as proteins or polymers, lipid bilayers are especially advantageous: they prevent enhanced NP aggregation in biological environments (e.g. human blood), they provide an efficient sealing, and they can be easily equipped with targeting ligands.[17-22] Up to now, release from lipid coated NPs after endosomal uptake has been achieved using toxic photosensitizers that need to be protected from sunlight[23-26], membrane-permeable drugs[18], or cationic lipids[27,28], all of which need to be optimized regarding their interaction with NPs to avoid premature leakage of the drug. Recently, a lipid coating has been applied to MOF NPs as a capping system, yielding a nanocarrier that efficiently encapsulates dye molecules and is taken up by cells.[21] However, no intracellular release was shown – possibly due to lack of an opening mechanism.

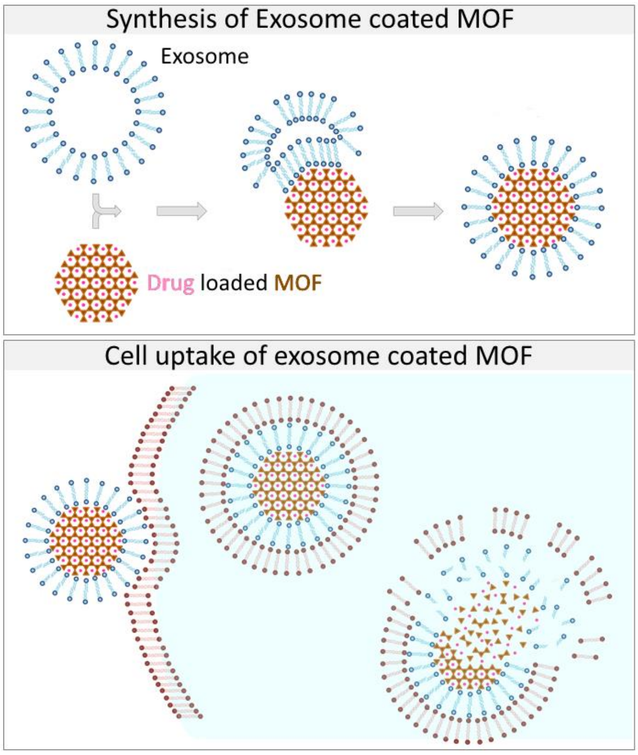

Figure 5.1. Schematic illustration of the synthesis of the exosome coated MOF and the subsequent cell uptake and proposed release mechanism of the cargo.

Exosomes might provide additional important advantages as compared to artificial lipid layers as a capping system. They are endogenous liposomes present in many body liquids. They supposedly are non-immunogenic and are used by cells for communication purposes.[29,30] Hence, they combine the advantages of a lipid bilayer with a potential shielding from the immune system and – unlike artificial lipid bilayers – they have a not yet understood endogenous mechanism that supports release from the endosomal entrapment.**[31]** With these properties they overcome the main challenges of drug delivery: leakage-free delivery, release as well as endosomal escape of the drug, shielding from the immune system for long circulation times, and full biocompatibility.[32] However, loading exosomes with biologically active molecules (e.g. drugs) is a major challenge. No technique has been reported yet that achieves efficient loading of exosomes. Here, we overcome this challenge and facilitate simple drug loading, leakage-free delivery and efficient release by a synergistic combination of the advantages of MOF NPs, specifically MIL-88A, as chemically tunable nanocarriers with those of exosomes as a capping system.

5.2 Results

MIL-88A NPs were synthesized via microwave synthesis,[15] loaded with cargo, and subsequently coated with exosomes derived from HeLa cell culture (characterization in section 5.4, **Figure S5.8**-**Figure S5.19**). The coating was achieved using the fusion method, which we employ here for the first time for MOF NPs (**Figure 5.1**).[33] Up to now MOF NPs have been coated with lipids using a solvent exchange method that would involve total disassembly of the exosomal bilayer.[21,34] The fusion method allows for leaving the bilayer of the exosomes mainly intact during the coating process and thus does not obstruct the advantageous properties of the exosome as much.

To investigate the uptake and possible release behavior of the newly synthesized NPs, we used membrane-impermeable calcein as a model cargo and incubated the exosome coated MOF NPs on HeLa-cells. After two days of incubation the cells showed uptake of particles, but no release of calcein into the cell was visible yet (**Figure.5.2a** and **Figure S5.22**). Strikingly, after three days of incubation the exosome coated particles showed release in several cells resulting in a spread of calcein over the entire cell (**Figure S5.17** and **Figure S5.19**). The number of cells exhibiting release increased slightly after 4 days of incubation (**Figure.5.2b**). This release of a membrane-impermeable dye without the use of toxic photosensitizers, renders the exosome-coated MIL-88A NPs a promising drug delivery system.

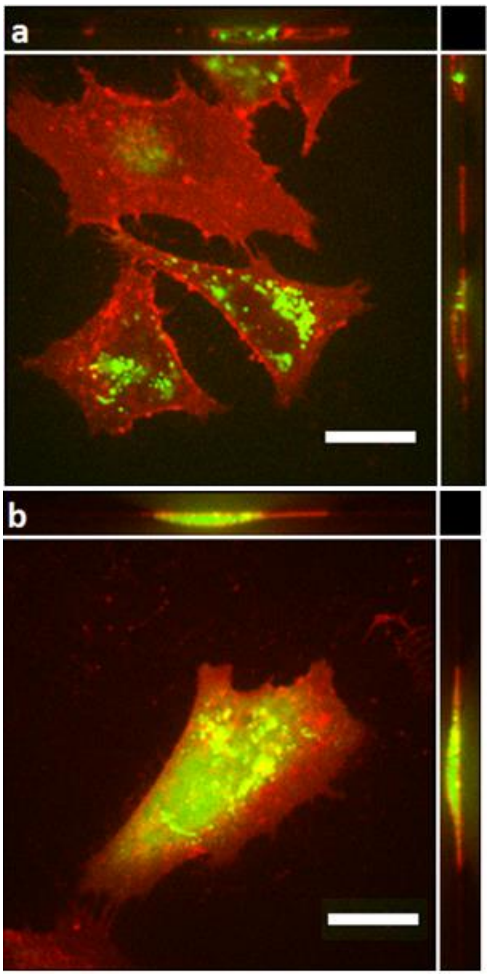

Figure.5.2. a) HeLa-Cells (red) with exosome coated calcein loaded particles (green) after 2 days of incubation. The particles have arrived inside the cell, but there is no sign of release. **b)** HeLa-Cells (red) with exosome coated calcein loaded particles (green) after 4 days of incubation. The particles have arrived inside the cell, and release of calcein from the particles is clearly visible. The side view on top and on the right side of the images shows that the particles reside inside of the cell and the release of the calcein is also confined to the cell. The white scale bar represents 20 µm.

To further understand and validate the promise of this system, fluorescence release experiments in a custom-built setup were conducted with the coated NPs (**Figure 5.3**).[18] To confirm the successful coating and to investigate the sealing properties of the exosomal bilayer, calcein-loaded MIL-88A NPs were coated with exosomes and fluorescence release was measured in water. Even over long times (**Figure 5.3** and **Figure S5.25**), no release was detected indicating a very tight coating without premature leakage, while uncoated particles leaked steadily. Next, we disassembled the exosome coating by addition of the nonionic surfactant Triton X-100. As expected, this lead to an instant release of calcein resulting in an increase of fluorescence intensity that reaches saturation over time. The release is even stronger than from uncoated particles, possibly due to the sudden release upon addition of Triton and/or release-promoting interaction of Triton and particle or due to premature leakage of the uncoated particles during the preparation process. To simulate the environment that particles encounter inside cells during endocytosis, the experiment was repeated in artificial lysosomal fluid (ALF) instead of water. Even in the absence of Triton, this lead to a strong intensity increase over the course of a few hours. The observed release is even stronger than that in water with Triton X-100. Stability measurements of the coated MOF NPs reveal their rapid decomposition in ALF (**Figure S5.18**-**Figure S5.19**) and might deliver a possible explanation for this efficient release: the particles completely decompose in ALF leading to an enhanced osmotic pressure in the exosome coating, which might lead to a burst of the exosome followed by a complete release of all loaded calcein molecules (**Figure 5.1**). Such a release following complete disintegration is more efficient than that triggered by Triton

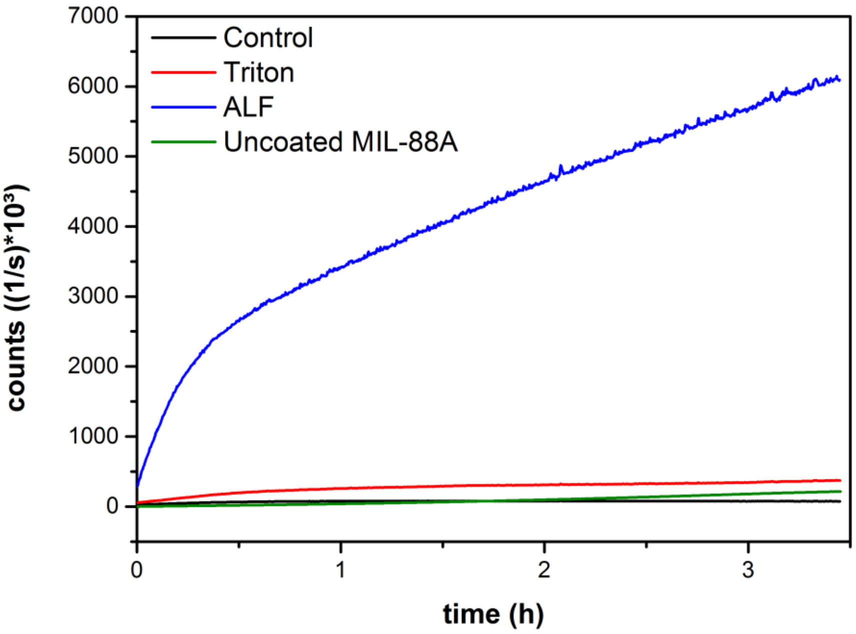

Figure 5.3. Fluorescence release experiments of encapsulated calcein in exosome coated MIL-88A(Fe) nanoparticles (the data points correspond to the intensities at the peak maxima at 512 nm of the spectrum for calcein). A solution of the coated particles in water was used as a negative control, while a Triton-X100 solution was used as a positive control. Uncoated MIL-88A NPs were used to test the effectiveness of the exosome coating in preventing leakage. The higher release in the ALF solution is caused by the decomposition of the MIL-88A NPs in this media and as a consequence a strong calcein release is observed. At the bottom a schematic of the measurement can be seen. 1) The cap is filled with loaded NPs. 2) The cap is sealed with a dialysis membrane. 3) The released calcein permeates through the membrane, while the particles stay in the cap.

X-100. The latter only destroys the coating, which does not necessarily lead to the release of all cargo molecules due to interactions with the MOF-lattice.[35] Since ALF simulates the lysosomal environment in the cell at advanced stages of endocytosis, the release observed in cells might be mediated by the decomposition of the MOF similarly to the release experiments here, in addition to possible endogenous release mechanisms of exosomes. The molecules of the dissolved NPs (i.e. fumaric acid and iron(III) ions) in combination with the protons pumped into the lysosome by the cell might enhance the osmotic pressure in the exosome coating and the lysosome and thus create cracks in both membranes that enable the release. All in all, the release experiments confirm the successful coating of MIL-88A NPs as well as the efficient storage and release (quantification see section 5.4) of dye molecules inside the MOF core without premature leakage. They also deliver a possible explanation for the observed efficient

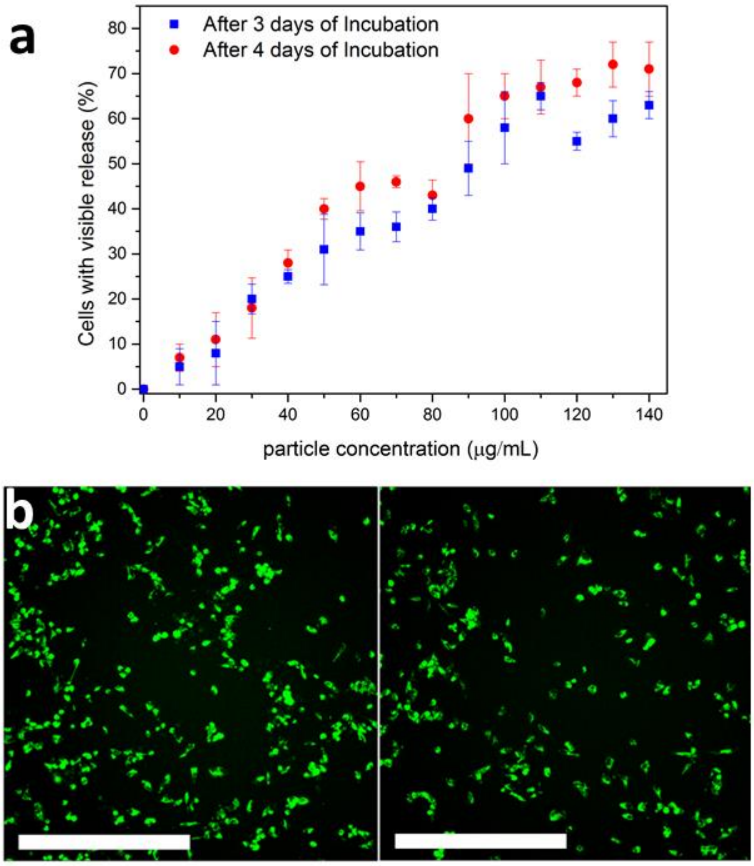

Figure 5.4. a) Release measured in cells after 3 (blue) and 4 (red) days of incubation with exosome coated, calcein loaded MIL-88A NPs. Each data point and its error bar have been compiled from 12 measurements and are based on a total number of at least 1000 investigated cells. The error bars mark the SD. b) Fluorescence microscopy images of cells incubated with calcein loaded exosome coated MIL-88A nanoparticles. (Left: three days, right: four days; 12 µg/ml). The scale bars represent 500 µm.

release inside cells with the decomposition of the MOF in the lysosome acting as an "onboard-trigger".

Next, we assessed the efficiency of our novel drug delivery system further and quantified intracellular release in high-content experiments. HeLa cells were incubated with different concentrations (10-140 µg/ml) of exosome-coated MIL-88A NPs loaded with calcein (**Figure 5.4**). Release of calcein was evaluated in at least 1000 cells per concentration after three and four days of incubation using a high-content fluorescence microscope. The percentage of cells with clear calcein release was measured relative to the total number of cells. With increasing NP concentration we found an increasing percentage of cells that showed release, culminating in about 70 % at the highest concentration used. The percentage of cells with calcein release is not much higher after 4 days of incubation as compared to 3 days. The widely spread release measured here further establishes the promise of the exosome coated NPs as an efficient drug delivery system.

To test the therapeutic potential of our drug delivery system, we finally replaced the cargo calcein with a chemotherapeutic drug and studied its effect on cell viability. We chose SBHA, a histone inhibitor and anti-cancer drug,[36] as active cargo and measured the cell viability at different concentrations of NPs with MTT-tests. While the exosome coated particles without cargo showed no significant impact on cell viability, they efficiently caused cell death even at very low concentrations when loaded with SBHA as shown in **Figure 5.5**. The IC50 value after

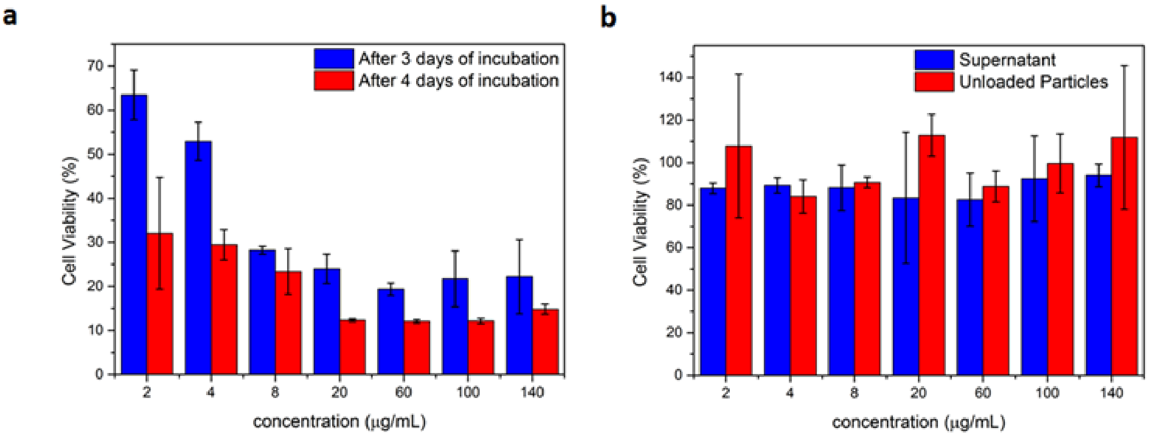

Figure 5.5. MTT-Assay results of HeLa-cells that were exposed to different concentrations of SBHA loaded MIL-88A NPs coated with exosomes. a) Cell viability after incubation for 3 and 4 days. b) Cell viability for the supernatant and unloaded coated particles. The error bars in both images signify the SD

3 days of incubation was calculated to be 4.78 µg/mL. This is 3 times higher than the IC50 of free SBHA (see SI). The supernatant of the NP solution did not affect cell viability – a proof of the encapsulation efficiency of the exosome coating. These results demonstrate that exosome coated MIL-88A NPs can store, deliver and release therapeutic molecules efficiently to cancer cells with minimal premature leakage. Hence, they show great potential to serve as smart drug delivery system.

5.3 Conclusion

In conclusion, we report for the first time on exosome coated MOF NPs as a smart and efficient drug delivery system with "onboard-trigger". It synergistically combines the features of MOF NPs and exosomes yielding a promising system that facilitates easy and efficient loading and sealing. Furthermore, it shows high therapeutic efficiency, yet no premature leakage. Intracellular cargo release is possibly mediated by a combination of the endogenous exosomal release mechanism and degradation of the nanocarrier, which decomposes into substances that are naturally present in the body. In the future, further advantages of the system will be exploited and analyzed: the MOF NP core will facilitate loading of several different drugs at the same time and monitoring of the NPs via MRI, targeting can be readily achieved by insertion of targeting ligands into the exosomal bilayer, and the use of autologous exosomes will ensure that they are not susceptible to responses from the immune system, allowing for longer circulation times.

References

1 Li, Z., Barnes, J. C., Bosoy, A., Stoddart, J. F. & Zink, J. I. Mesoporous silica nanoparticles in biomedical applications. *Chemical Society Reviews* **41**, 2590-2605, doi:10.1039/C1CS15246G (2012).

2 Cabral, H. & Kataoka, K. Progress of drug-loaded polymeric micelles into clinical studies. *J Control Release* **190**, 465-476, doi:10.1016/j.jconrel.2014.06.042 (2014).

3 Horcajada, P. *et al.* Metal–Organic Frameworks in Biomedicine. *Chem. Rev.* **112**, 1232-1268, doi:10.1021/cr200256v (2012).

4 He, C., Liu, D. & Lin, W. Nanomedicine Applications of Hybrid Nanomaterials Built from Metal–Ligand Coordination Bonds: Nanoscale Metal–Organic Frameworks and Nanoscale Coordination Polymers. *Chem. Rev.* **115**, 11079-11108, doi:10.1021/acs.chemrev.5b00125 (2015).

5 Falcaro, P. *et al.* Application of metal and metal oxide nanoparticles@MOFs. *Coord. Chem. Rev.* **307**, 237-254, doi:10.1016/j.ccr.2015.08.002 (2016).

6 Wuttke, S., Lismont, M., Escudero, A., Rungtaweevoranit, B. & Parak, W. J. Positioning metal-organic framework nanoparticles within the context of drug delivery - A comparison with mesoporous silica nanoparticles and dendrimers. *Biomaterials* **123**, 172-183, doi:10.1016/j.biomaterials.2017.01.025 (2017).

7 Furukawa, H., Cordova, K. E., O'Keeffe, M. & Yaghi, O. M. The Chemistry and Applications of Metal-Organic Frameworks. *Science* **341**, doi:10.1126/science.1230444 (2013).

8 Ferey, G. Hybrid porous solids: past, present, future. *Chemical Society Reviews* **37**, 191-214, doi:10.1039/B618320B (2008).

9 Zhou, H.-C., Long, J. R. & Yaghi, O. M. Introduction to Metal–Organic Frameworks. *Chemical Reviews* **112**, 673-674, doi:10.1021/cr300014x (2012).

10 H. C. Zhou, S. K. *Chem. Soc. Rev.* **43**, 5415 (2014).

11 Anna G. Slater, A. I. C. *Science* **348** (2015).

12 P. Horcajada, R. G., T. Baati, P. K. Allan, G. Maurin, P. Couvreur,. *Chem. Sci.*, 1597 (2013).

13 Zimpel, A. *et al.* Imparting Functionality to MOF Nanoparticles by External Surface Selective Covalent Attachment of Polymers. *Chem. Mater.* **28**, 3318-3326, doi:10.1021/acs.chemmater.6b00180 (2016).

14 Horcajada, P. *et al.* Porous metal-organic-framework nanoscale carriers as a potential platform for drug delivery and imaging. *Nat Mater* **9**, 172-178, doi:10.1038/nmat2608 (2010).

15 Chalati, T., Horcajada, P., Gref, R., Couvreur, P. & Serre, C. Optimisation of the synthesis of MOF nanoparticles made of flexible porous iron fumarate MIL-88A. *Journal of Materials Chemistry* **21**, 2220-2227, doi:10.1039/C0JM03563G (2011).

16 Serre, C. *et al.* Role of solvent-host interactions that lead to very large swelling of hybrid frameworks. *Science* **315**, 1828-1831, doi:10.1126/science.1137975 (2007).

17 van Meer, G., Voelker, D. R. & Feigenson, G. W. Membrane lipids: where they are and how they behave. *Nat Rev Mol Cell Biol* **9**, 112-124 (2008).

18 Cauda, V. *et al.* Colchicine-Loaded Lipid Bilayer-Coated 50 nm Mesoporous Nanoparticles Efficiently Induce Microtubule Depolymerization upon Cell Uptake. *Nano Letters* **10**, 2484-2492, doi:10.1021/nl100991w (2010).

19 Mackowiak, S. A. *et al.* Targeted Drug Delivery in Cancer Cells with Red-Light Photoactivated Mesoporous Silica Nanoparticles. *Nano Letters* **13**, 2576-2583, doi:10.1021/nl400681f (2013).

20 Ashley, C. E. *et al.* Delivery of Small Interfering RNA by Peptide-Targeted Mesoporous Silica Nanoparticle-Supported Lipid Bilayers. *ACS Nano* **6**, 2174-2188, doi:10.1021/nn204102q (2012).

21 Wuttke, S. *et al.* MOF nanoparticles coated by lipid bilayers and their uptake by cancer cells. *Chemical Communications* **51**, 15752-15755, doi:10.1039/C5CC06767G (2015).

22 Allen, T. M. & Cullis, P. R. Liposomal drug delivery systems: from concept to clinical applications. *Adv Drug Deliv Rev* **65**, 36-48, doi:10.1016/j.addr.2012.09.037 (2013).

23 Schloßbauer, A. *et al.* Cascaded Photoinduced Drug Delivery to Cells from Multifunctional Core–Shell Mesoporous Silica. *Advanced Healthcare Materials* **1**, 316-320, doi:10.1002/adhm.201100033 (2012).

24 Yang, Y. *et al.* Lipid coated mesoporous silica nanoparticles as photosensitive drug carriers. *Physical Chemistry Chemical Physics* **12**, 4418-4422, doi:10.1039/B924370D (2010).

25 Febvay, S., Marini, D. M., Belcher, A. M. & Clapham, D. E. Targeted Cytosolic Delivery of Cell-Impermeable Compounds by Nanoparticle-Mediated, Light-Triggered Endosome Disruption. *Nano Letters* **10**, 2211-2219, doi:10.1021/nl101157z (2010).

26 de Bruin, K. G. *et al.* Dynamics of photoinduced endosomal release of polyplexes. *J Control Release* **130**, 175-182, doi:10.1016/j.jconrel.2008.06.001 (2008).

27 Moller, K. *et al.* Highly efficient siRNA delivery from core-shell mesoporous silica nanoparticles with multifunctional polymer caps. *Nanoscale* **8**, 4007-4019, doi:10.1039/C5NR06246B (2016).

28 Wan, C., Allen, T. M. & Cullis, P. R. Lipid nanoparticle delivery systems for siRNA-based therapeutics. *Drug Delivery and Translational Research* **4**, 74-83, doi:10.1007/s13346-013-0161-z (2014).

29 Bang, C. & Thum, T. Exosomes: new players in cell-cell communication. *Int. J. Biochem. Cell Biol.* **44**, 2060-2064, doi:10.1016/j.biocel.2012.08.007 (2012).

30 Ludwig, A. K. & Giebel, B. Exosomes: small vesicles participating in intercellular communication. *Int. J. Biochem. Cell Biol.* **44**, 11-15, doi:10.1016/j.biocel.2011.10.005 (2012).

31 Ha, D., Yang, N. & Nadithe, V. Exosomes as therapeutic drug carriers and delivery vehicles across biological membranes: current perspectives and future challenges. *Acta Pharm Sin B* **6**, 287-296, doi:10.1016/j.apsb.2016.02.001 (2016).

32 Tibbitt, M. W., Dahlman, J. E. & Langer, R. Emerging Frontiers in Drug Delivery. *Journal of the American Chemical Society* **138**, 704-717, doi:10.1021/jacs.5b09974 (2016).

33 Liu, J., Jiang, X., Ashley, C. & Brinker, C. J. Electrostatically Mediated Liposome Fusion and Lipid Exchange with a Nanoparticle-Supported Bilayer for Control of Surface Charge, Drug Containment, and Delivery. *Journal of the American Chemical Society* **131**, 7567-7569, doi:10.1021/ja902039y (2009).

34 Hohner, A. O., David, M. P. C. & Rädler, J. O. Controlled solvent-exchange deposition of phospholipid membranes onto solid surfaces. *Biointerphases* **5**, 1-8, doi:10.1116/1.3319326 (2010).

35 T. Preiß , A. Z., S. Wuttke and J. O. Rädler. *Materials*, accepted (2017).

36 Marks, P. A., Richon, V. M. & Rifkind, R. A. Histone Deacetylase Inhibitors: Inducers of Differentiation or Apoptosis of Transformed Cells. *Journal of the National Cancer Institute* **92**, 1210-1216, doi:10.1093/jnci/92.15.1210 (2000).

5.4 Supporting Information

5.4.1 Experimental Methods

Dynamic Light Scattering (DLS): DLS was performed on a *Zetasizer Nano Series* (Nano-ZS, *Malvern*) equipped with a laser with the wavelength λ = 633 nm. For sample preparation the freshly prepared nanoparticles (NPs) were dispersed in ethanol or phosphate-buffered saline (PBS) in the case of the capped NPs.

Scanning Electron Microscopy (SEM): All SEM micrographs were recorded with a *Helios NanoLab G3UC* (*FEI*) operating at 5 kV. During sample preparation an ethanolic NP dispersion was dried on a carbon film placed on an aluminum sample holder. The sample was stored overnight to evaporate the solvent followed by carbon sputtering prior to the measurement. For evaluation of the SEM micrographs the software *ImageJ v1.49.* was used.

Transmission Electron Microscopy (TEM): The TEM micrographs of the sample particles were taken on a *Titan Themis* (*Fei*) that was operated at an acceleration voltage of 300 kV. For sample preparation, an ethanolic NP solution was dried overnight on a carbon-coated copper grid.

Cryogenic Transmission Electron Microscopy (CryoTEM): The CryoTEM images were measured on a *Leo 912 Ω-mega* that was operated at 120 keV. The sample was applied to a carbon-coated copper grid and flash frozen with Kryogen (90 k) for the measurements.

Thermogravimetric Analysis (TGA): A dried sample of MIL-88A NPs (3.125 mg) was heated using a *TASC 414/4* (*Netzsch*). The sample was heated under synthetic air at 10 °C/min up to 900 °C. The resulting data was evaluated using the software *Proteus v4.3*.

Nitrogen sorption: Nitrogen sorption experiments were conducted with an *Autosorb-1* (*Quantachrome*). Prior to the measurement the sample (27.9 mg) was outgassed under high vacuum at 120 °C for 38 h. The resulting data was evaluated with the software *ASiQwin v3.0*. The linearized form of the BET equation was used to calculate BET surface areas. For the calculation of the pore size distribution a QSDFT equilibrium based model was used assuming slit and cylindrical pores.

X-Ray Diffraction: X-ray diffraction experiments were performed on the initial MIL-88A NPs. The samples were measured on a *STOE Transmissions-Diffraktometer System STADI P* operating in transmission mode. The setup is using $CuK_{\alpha 1}$-radiation with a wavelength λ = 015418 nm. The resulting diffraction pattern was evaluated using the software package *WinXPOW RawDat v3.0.2.5* and *WinXPOW PowDat_n v3.0.2.7.*

Fluorescence Microscopy: The fluorescence microscope images were recorded with a *Zeiss Observer SD* spinning disk confocal microscope using a Yokogawa CSU-X1 spinning disc unit and an oil objective with 63x magnification and BP 525/50 and LP 690/50 filters. The setup was heated to 37 °C and a CO_2 source was provided to keep the atmosphere at 5% CO_2. For both excitation of the calcein and the cell marker a laser with a wavelength λ = 488 nm was used. The images were processed with the *Zen* software by *Zeiss* to optimize contrast and provide the orthogonal views.

Fluorescence Spectroscopy: The fluorescence spectroscopy experiments were recorded with a MD-5020 setup from *PTI Photon Technology International*. The software *Felix32* was used for recording and evaluating the measured data.

UV/Vis Measurements: The UV/Vis measurements were performed on a Lambda 1050 UV/Vis/NIR spectrometer form *Perkin Elmer*. The software used to record the measured spectra was *Perkin Elmer UVWinLab*.

High-Content Quantification: The release quantification measurements were performed with a *ImageXpress Micro XLS* from *Molecular Devices* using an objective with 10x magnification with a GFP filter and the resulting images were evaluated with the *MetaXpress* software.

Cell culture: All cell experiments were prepared in a *Hera-Safe* cell culture unit from *Heraus*. The cells were incubated in *Hera Cell incubators* also from *Heraus*.

MTT Assays: The MTT-Assays were performed with a *Spectra Fluor Plus* from *Tecan* and were then evaluated with *Excel 2010*

5.4.2 Synthesis of the Uncoated and Coated MIL-88A Nanoparticles

Synthesis of MIL-88A NPs

MIL-88A NPs were synthesized in a microwave assisted approach based on the results of Chalati et al.[1] In this synthesis route an aqueous solution of $FeCl_3 \cdot 6\ H_2O$ (1.084 g, 4.01 mmol) and fumaric acid (485 mg, 4.18 mmol) are given to water (20 ml, Milli-Q). The reaction mixture was stirred until the metal salt was completely dissolved. The reaction mixture was then given into a Teflon tube (80 ml) and placed into a microwave oven (*Synthos 3000*, *Anton-Paar*) along with 3 additional vessels. Two of these vessels are filled with water (20 ml), the third vessel is filled with an aqueous $FeCl_3$ (20 ml, 1.084 g, 4.01 mmol) and is used to monitor the reaction progress. The vessels were heated under stirring with the sequence shown in **Table S5.1**:

Table S5.1: MW Heating program for the MIL-88(A) NPs synthesis

Heating	Dwelling	Cooling
30 s	5 min	45 min
To 80 °C	80 °C	To RT

To remove residual reactants the sample was subsequently washed via centrifugation (7840 rpm, 20 min) and redispersion of the pellet in ethanol (20 ml). This washing cycle was repeated 3 additional times. To remove also bulk material formed during the reaction, the dispersion was then centrifuged 3 times (3 min, 3000 rpm) and the pellet fraction of the product discarded.

Preparation of the exosome coating solution

Approximately 100000 HeLa cells were transferred to a 75 cm culture flask and incubated in 10 mL fetal bovine serum (FBS)-free Dulbecco's modified Eagle Medium (DMEM) for three days. The exosomes were then extracted from the medium using the *Exospin* kit from *Cell Guidance Systems* following the protocol from the kit.

Preparation of the loaded and coated particles

1 mg of MIL-88A NPs were solved in 1 mL of a 1 mM solution of calcein or suberohydroxamic acid (SBHA) and incubated overnight for loading. Next they were centrifuged for 5 min at 14000 rpm, to discard the supernatant and the pellet was dissolved in 0.2 mL of the exosome coating solution and 0.2 mL water and incubated for 2 h. The particles were then centrifuged (5 min at 14000 rpm) and redispersed in 1 mL PBS after washing several times.

5.4.3 Characterization of MIL-88A NPs

Scanning Electron Microscopy

An overview picture of the MIL-88A NPs used in this work is presented in **Figure S5.6**.

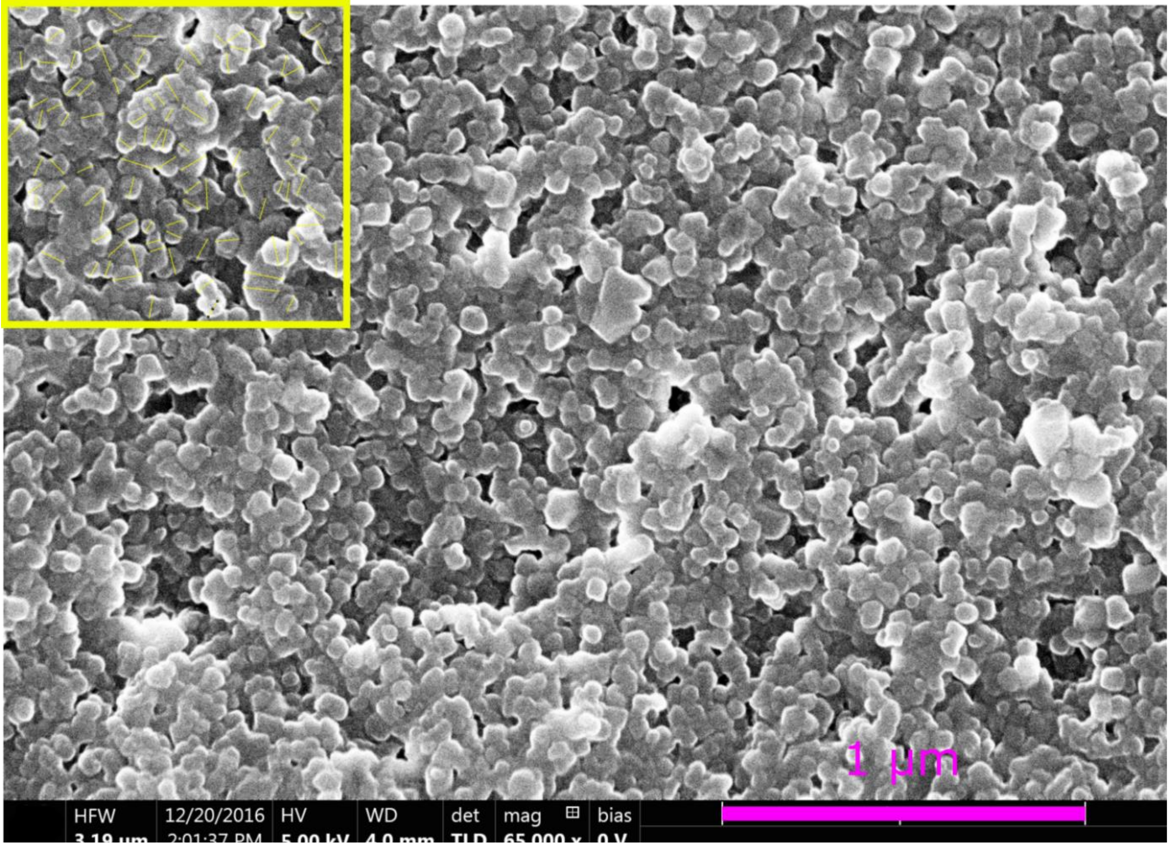

Figure S5.6. Scanning Electron micrograph of MIL-88A nanoparticles.

The particles look uniform and feature a roundish morphology. For further characterization, the particles marked in the yellow box were used to determine a particle size distribution of the sample.[2]

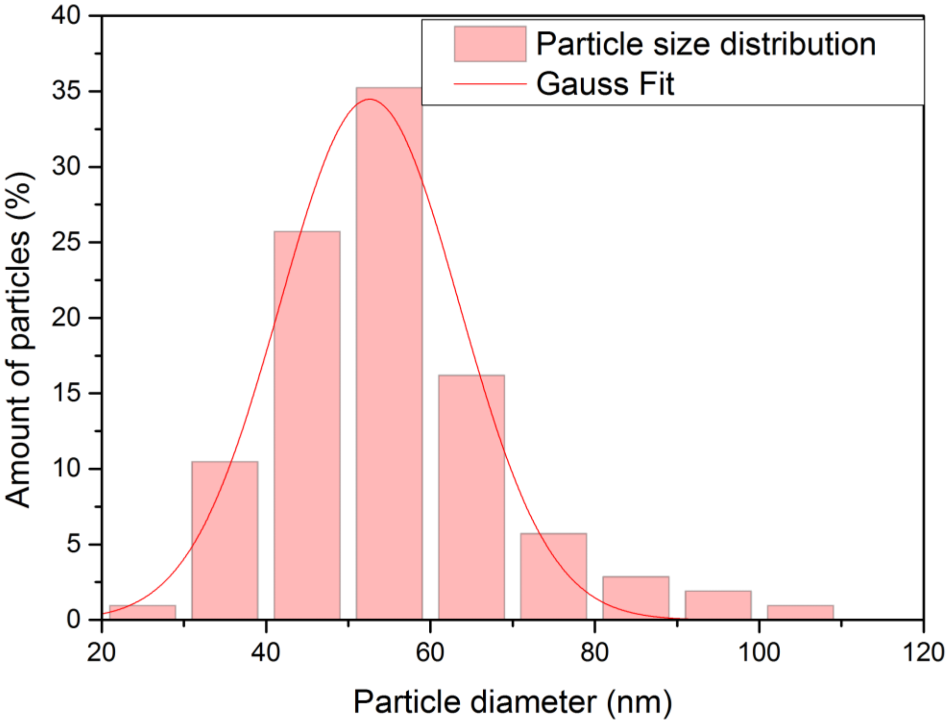

Figure S5.7. Particle size distribution determined from the SEM micrograph shown in **Figure S5.6**(yellow box).

The particle size distribution was determined by manually measuring the diameter of ~ 150 particles (Figure S1 yellow box) and fitting the data with a Gaussian function using the software Origin v9.0.0.[2] This results in an average particle diameter of 52 nm with a standard deviation of 11 nm.

Transmission Electron microscopy

Figure S5.8 and **Figure S5.9** depict TEM micrographs of the MIL-88A NP sample. The particles feature a round morphology and are connected via thin necks. The MIL-88A sample is fairly homogenous, which is also shown in a particle size distribution given in **Figure S5.10**.

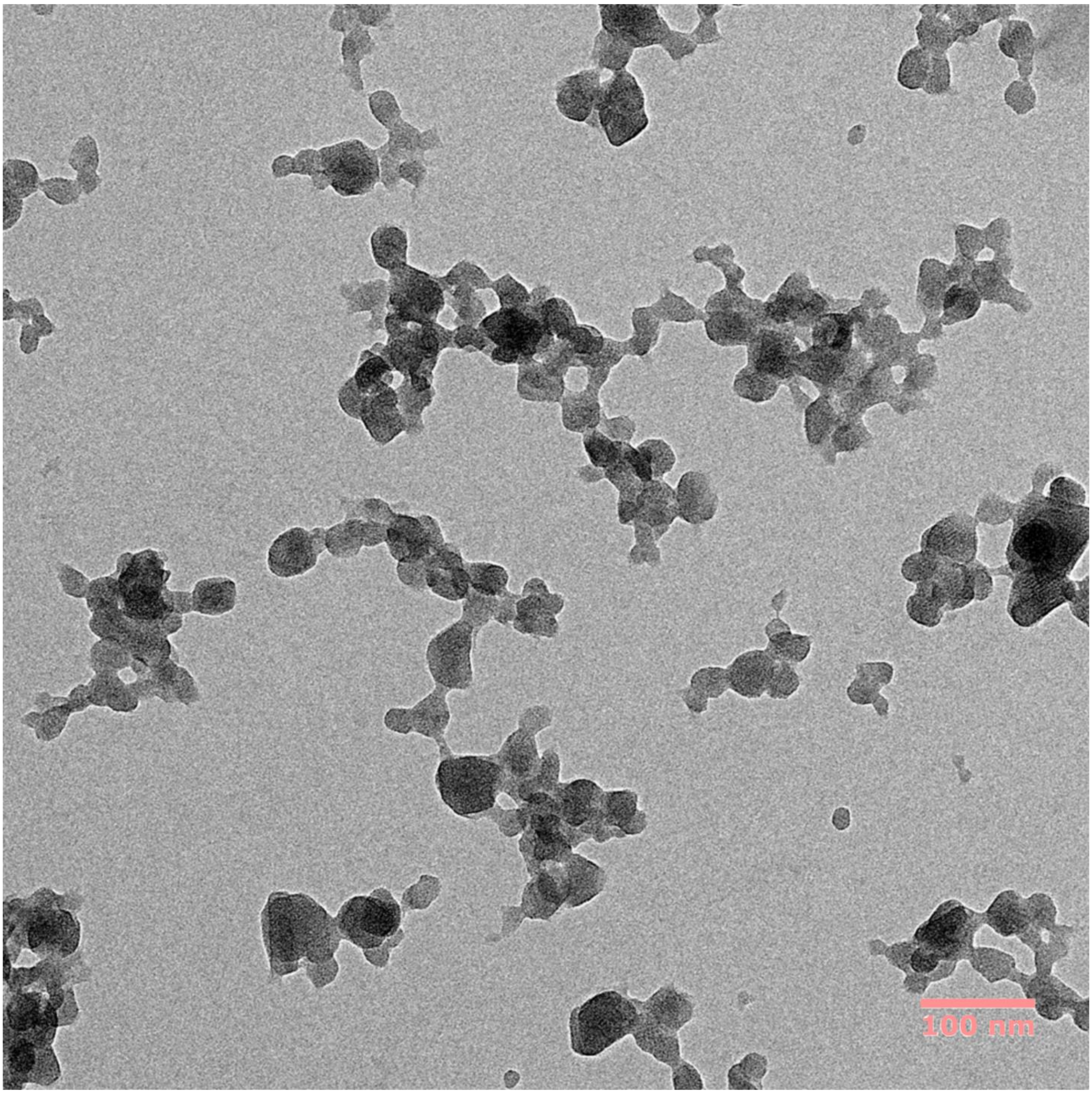

Figure S5.8. Transmission electron micrograph of MIL-88A NPs – detailed image.

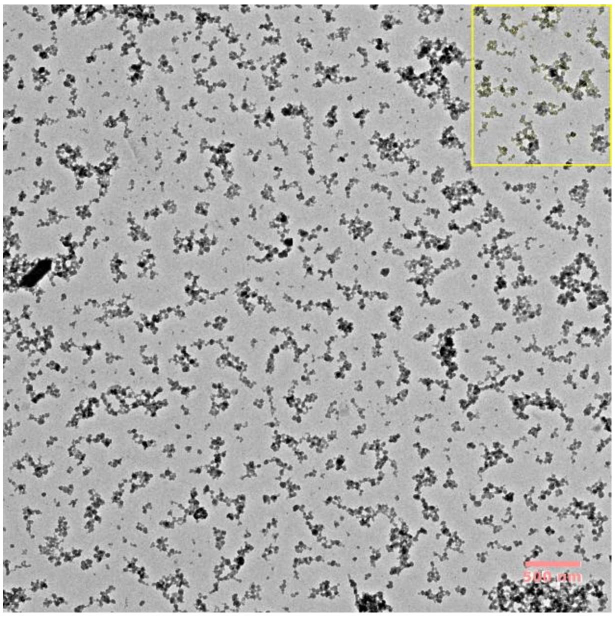

Figure S5.9. Transmission electron micrograph of MIL-88A NPs.

The particle size distribution was determined by manually measuring the diameter of ~ 200 particles and fitting the data with a Gaussian function using the software Origin v9.0.0.[2] The average diameter was determined at 36 nm with a standard deviation of 9 nm.

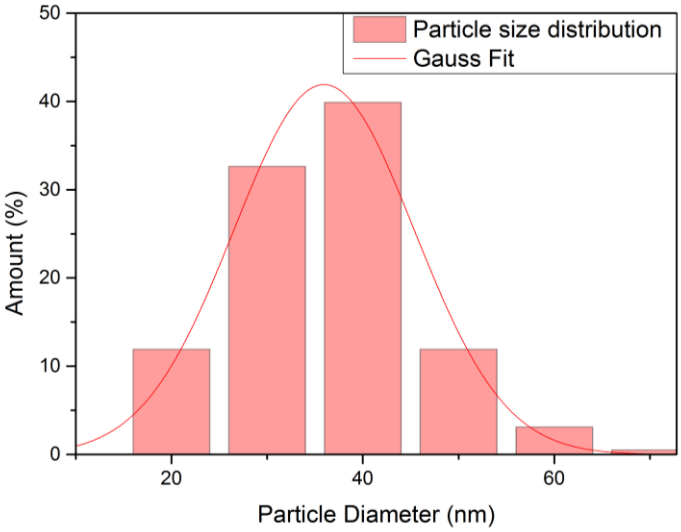

Figure S5.10. Particle Size distribution determined from the TEM micrograph shown in **Figure S5.9**(yellow box).

This diameter differs from the results shown in the SEM measurements. This behavior however is not unusual in size determination of MOFs with SEM and TEM. Beam damage of a sample is a known problem in TEM mostly with high-energy electron beams (E > 100 keV).[2]

Dynamic Light Scattering

The results of the DLS measurements of the unfunctionalized MIL-88A NPs are shown **Figure S5.7**. In water, the particles have an intensity based hydrodynamic average diameter of 99 nm with a polydispersity index (PDI) of 0.131, which translates to a good monodisperse particle size distribution.

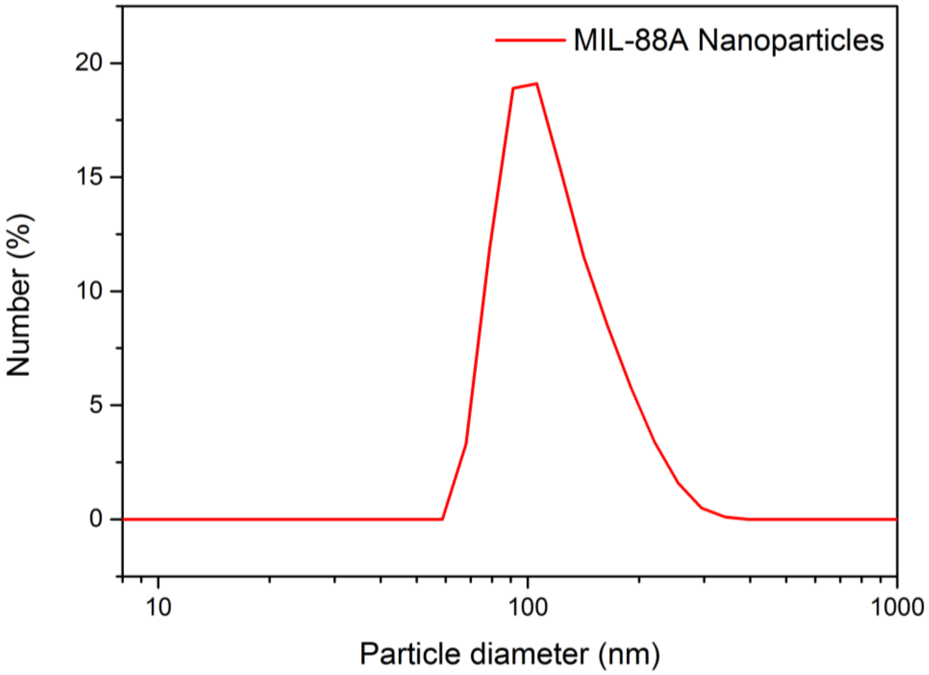

Figure S5.11. DLS size distribution of MIL-88A NPs showing the percentage of particles for each size.

DLS measurements of the exosome coated MIL-88A NPs can be seen in. In PBS the exosome coated particles possess an average diameter of 101 nm (**Figure S5.12**). The measured PDI is 0.143 meaning that sample possesses a good monodispersity.

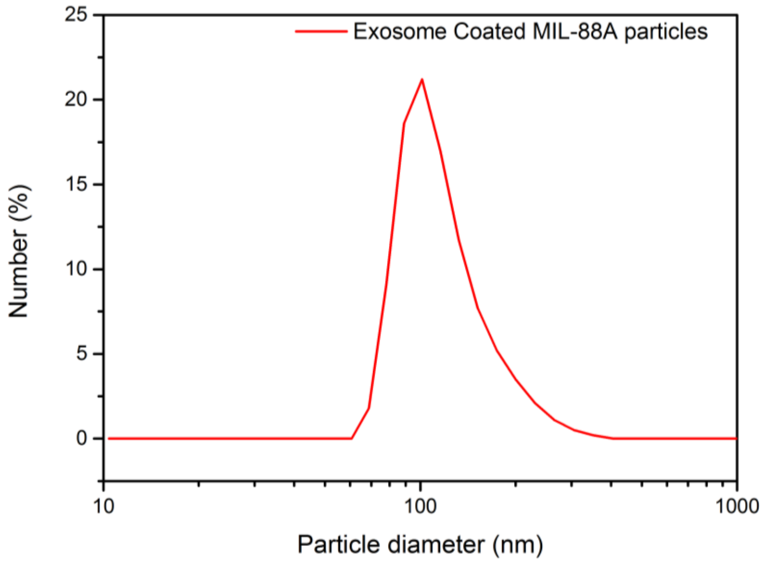

Figure S5.12. DLS size distribution of exosome coated MIL-88A NPs showing the percentage of particles for each size.

DLS measurements of the exosomes can be seen in **Figure S5.13**Error! Reference source not found.. In PBS the exosomes possess an average diameter of 100 nm. The measured PDI is 0.157 meaning that sample possesses a good monodispersity.

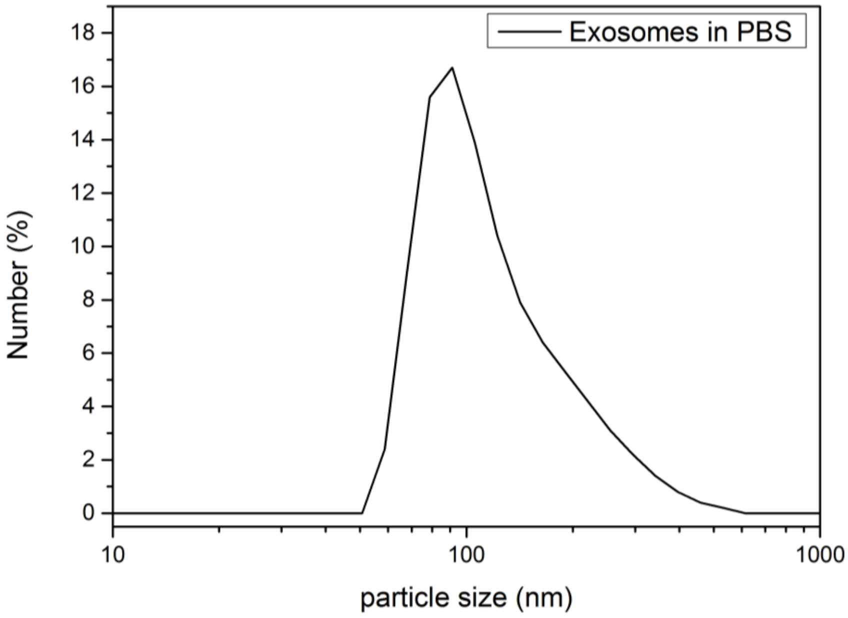

Figure S5.13. DLS size distribution of exosomes recovered with the Exospin kit showing the percentage of exosomes and extracellular vesicles for each size.

X-Ray Diffraction

Figure S5.14 shows the X-ray diffraction pattern of the initial MIL-88A NPs. The peak at 2θ = 10° is fairly weak suggesting an overall rather amorphous nature of the particles and less pronounced crystallinity than in other MOF structures. The diffractogram however is in good agreement with the data reported in literature for MIL-88A NPs.[1,3]

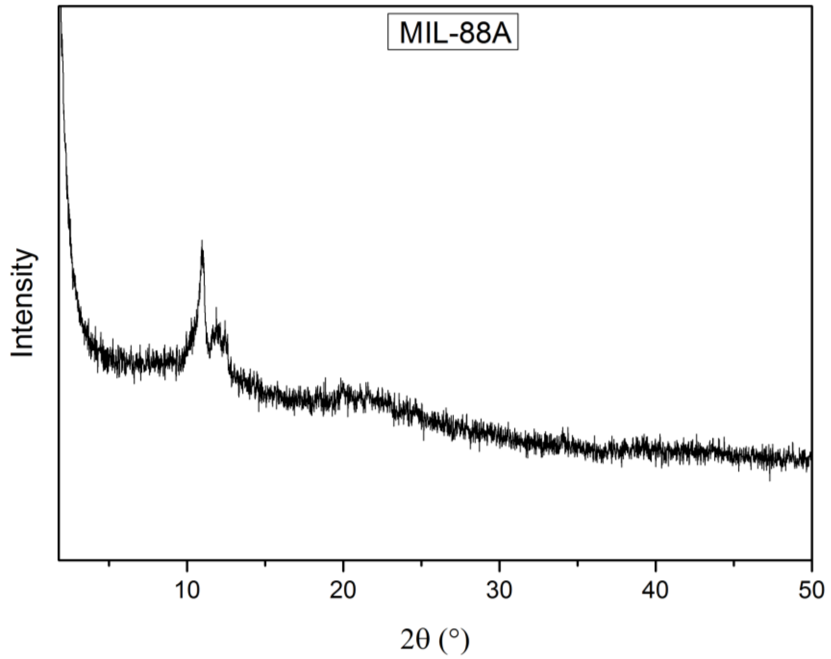

Figure S5.14. X-ray diffraction patter of dried MIL-88A NPs.

Thermogravimetric Analysis

The results of the thermogravimetric analysis of the initial MIL-88A NPs are shown in **Figure S5.15**. Up to 204 °C the residual solvent in the sample is desorbed resulting in a mass loss of 6 %. Subsequently, in a range between 204 – 433 °C the framework decomposes. The residual mass left of the sample remains at 42%. This data is in agreement with literature data for MIL-88A NPs and shows the successful synthesis of the MOF.[3]

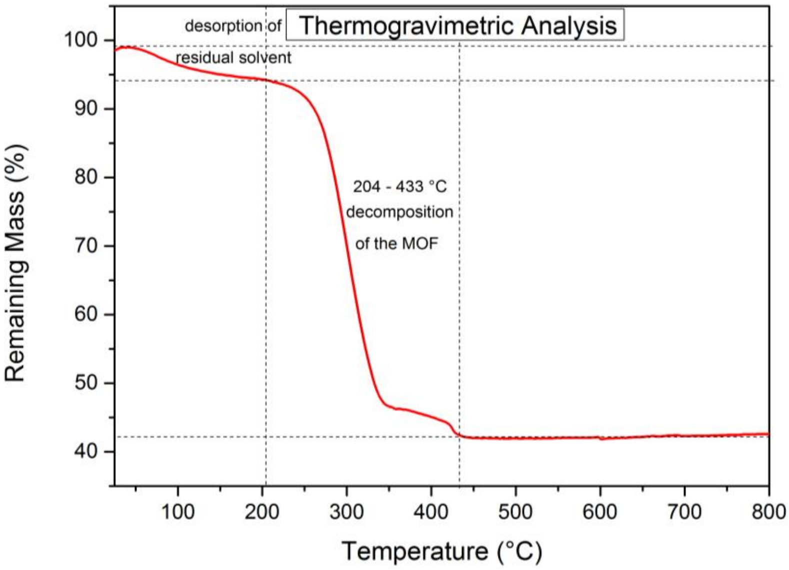

Figure S5.15. Thermogravimetric analysis of MIL-88A NPs.

Nitrogen Sorption

The results of the nitrogen sorption experiments are shown in **Figure S5.16** which depicts the sorption isotherm and the corresponding pore size distribution. The results are summarized in **Table S5.2** as well. The nitrogen uptake is in good agreement with reported data of MIL-88A NPs.[4]

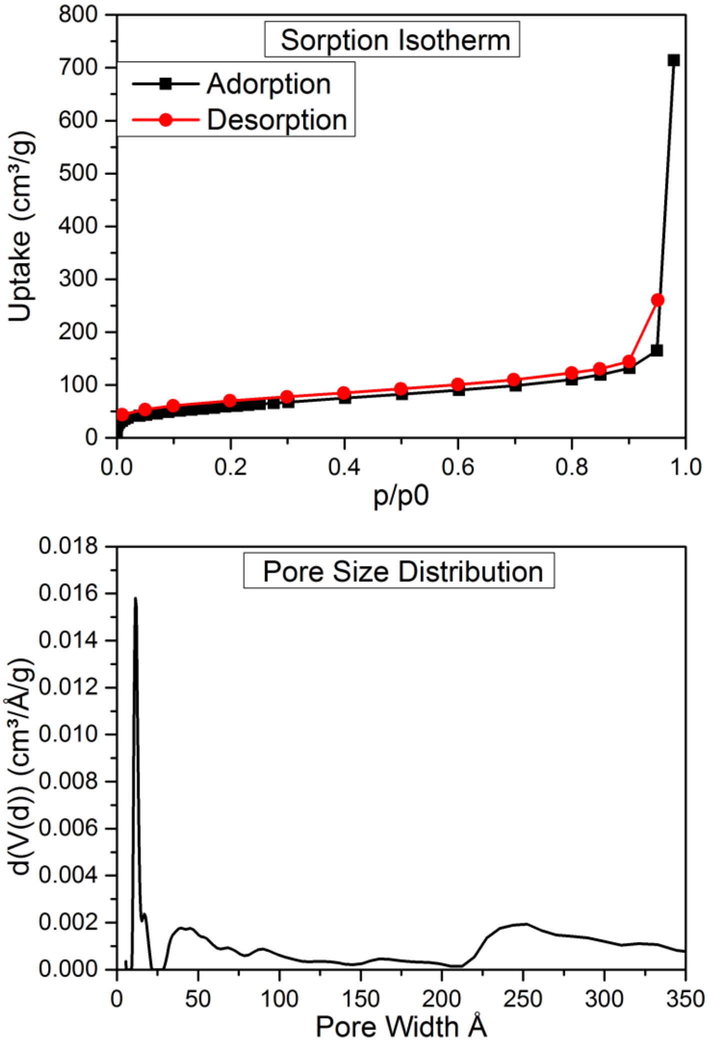

Figure S5.16. Nitrogen sorption isotherm and pore size distribution.

Table S5.2. Results of the BET analysis

Sample	**MIL-88A**
BET-surface area [m²/g]	218 m²/g
Relative pressure range used for calculation	0.11-0.23
Correlation coefficient	0.999
C-constant	Positive
Pore Size	11.44 Å

5.4.4 Stability Measurements

To investigate the stability of the particles in body relevant media, 500 µg of the coated and uncoated nanoparticles were dispersed in 1 mL ALF[5]. After a day of incubation the solutions were measured again. The solutions were clear and no particles could be recovered via centrifugation (**Figure S5.18**). The original particles seem to have been completely disassembled in the ALF media as it can be observed in the XRD and the SEM image (**Figure S5.17** and **Figure S5.19**).

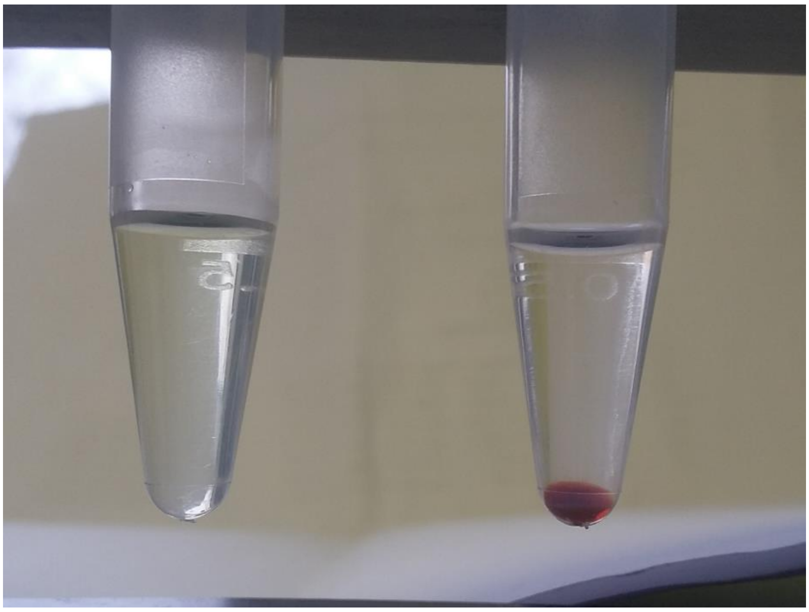

Figure S5.18. MIL-88A NPs before (right) and after (left) treatment with ALF. The particles in the untreated sample were recovered via centrifugation (14000 rpm, 5 min), while no particles could be recovered in the treated sample.

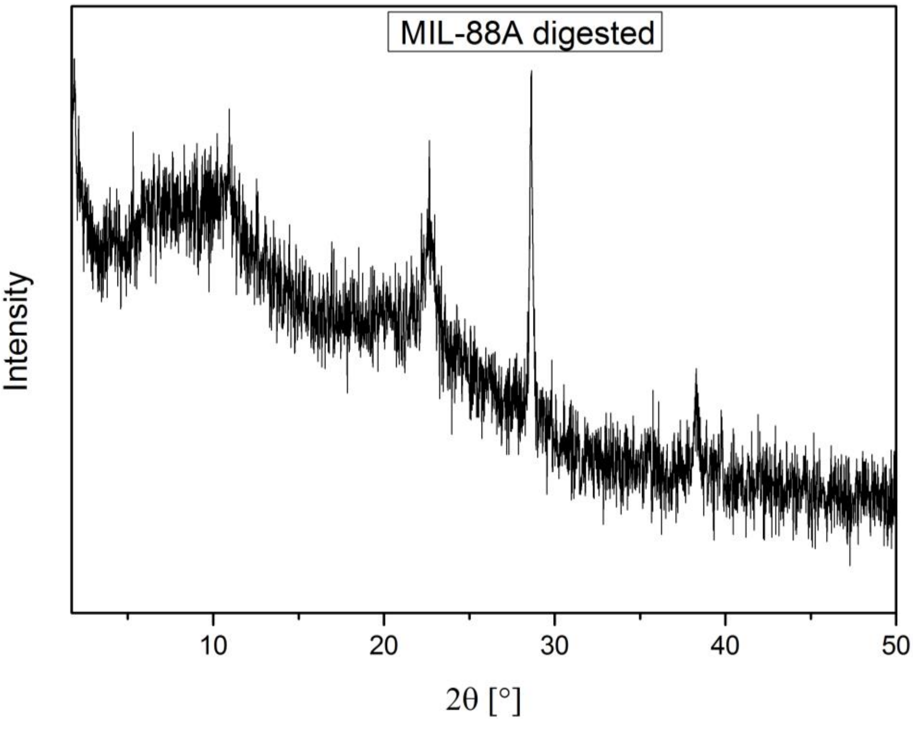

Figure S5.17. XRD of the residue after treatment of the MIL-88A nanoparticles with ALF, showing that the characteristic reflexes of MIL-88A at about 10° are no longer visible.

Figure S5.19. SEM images of the residue left after treating uncoated MIL-88A NPs with ALF,

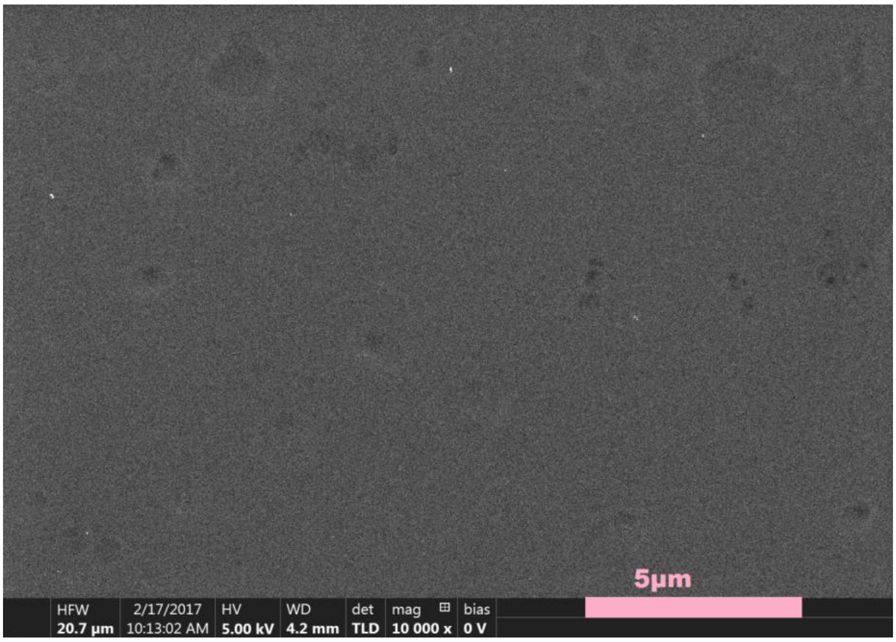

showing no discernible crystallites.

In addition to the ALF measurements the same procedures were carried out with an aqueous 10% FBS solution, showing no particle degradation after incubation overnight (**Figure S5.20**).

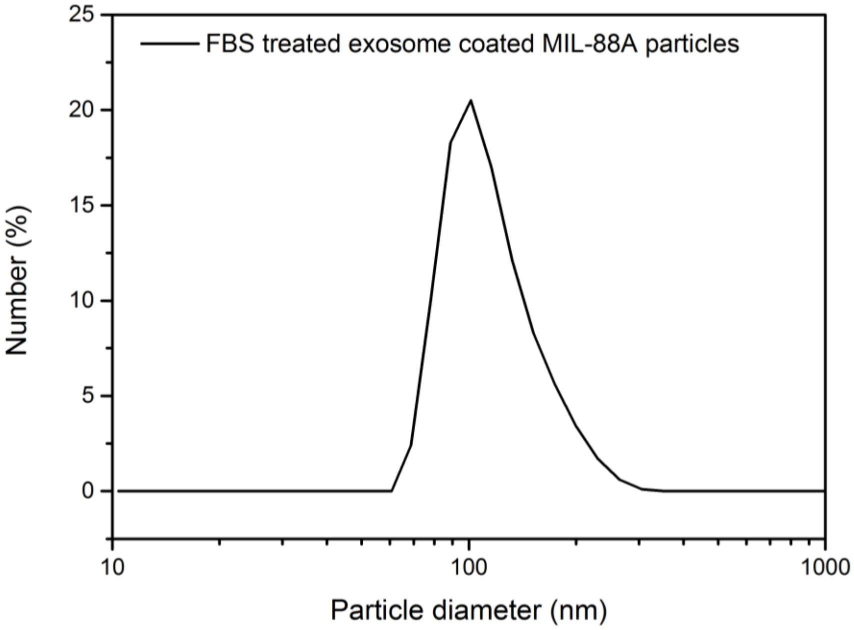

Figure S5.20. DLS size distribution of exosome coated MIL-88A NPs showing the percentage of particles for each size after overnight treatment with FBS.

5.4.5 Visualizing the Exosome coating

As proof of a successful exosome coating of the MOF nanoparticles we performed fluorescence colocalization experiments. We labeled the MOF nanoparticles (**Figure S5.21, a**) with Fluo-3, which stains the iron contained in the particles, and the exosomes with CellMaskOrange (**Figure S5.21**, **b**). Successful coating should result in a colocalization of both dyes, while they should be independently distributed in the case of failed coating. The merged image (**Figure S5.21**, **c**) of both channels shows that we indeed obtain colocalization of both dyes suggesting a successful coating. The slight offset of both channels can be explained by the time it took to switch between the different excitation wavelengths needed for the two different dyes: the particles slightly moved due to the Brownian motion preventing a complete overlap of both images in the merged channel. Careful control experiments excluded spectral overlap of the dyes and confirm that the colocalization of the signals is indeed due to successful coating.

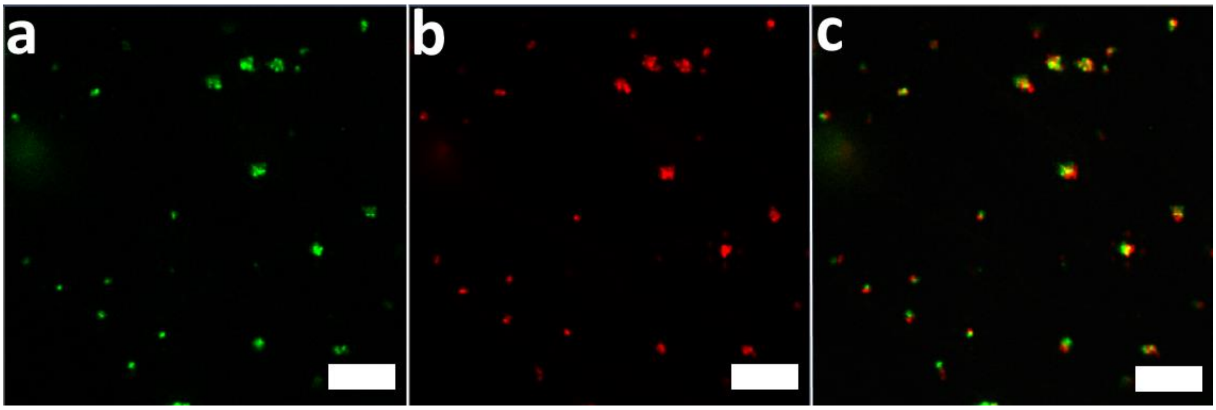

Figure S5.21. Fluorescence Cross Correlation Images of the exosome coated MIL-88A nanoparticles. The particles were marked with Fluo-3 (green, a) and iron marker, while the exosomes were marked with CellMask Orange (red, b). c shows the merged image of both channels.

5.4.6 Cell Release Experiments

For the cell release experiments 5000 HeLa cells were seeded in each well of ibidi 8-well plates and after one day 5, 10, 15 or 20 µg of the MIL-88A particles were added to each well. Incubation times of two, three and four days were investigated and can be seen in **Figure**

S5.22, **Figure S5.23**, and **Figure S5.24**, respectively. The cells were marked with CellMask Orange, by adding 1 µL masking agent, incubating for 5 minutes at 37 °C/5 % CO_2 and washing three times with DMEM to remove the remaining masking agent. The microscope images were taken with a Zeiss spinning disk microscope with an oil objective with 63x magnification. In addition to normal images Z-Stacks were also recorded, allowing for an orthogonal view of the cells, proving that the particles have entered the cell after 2 days of incubation.

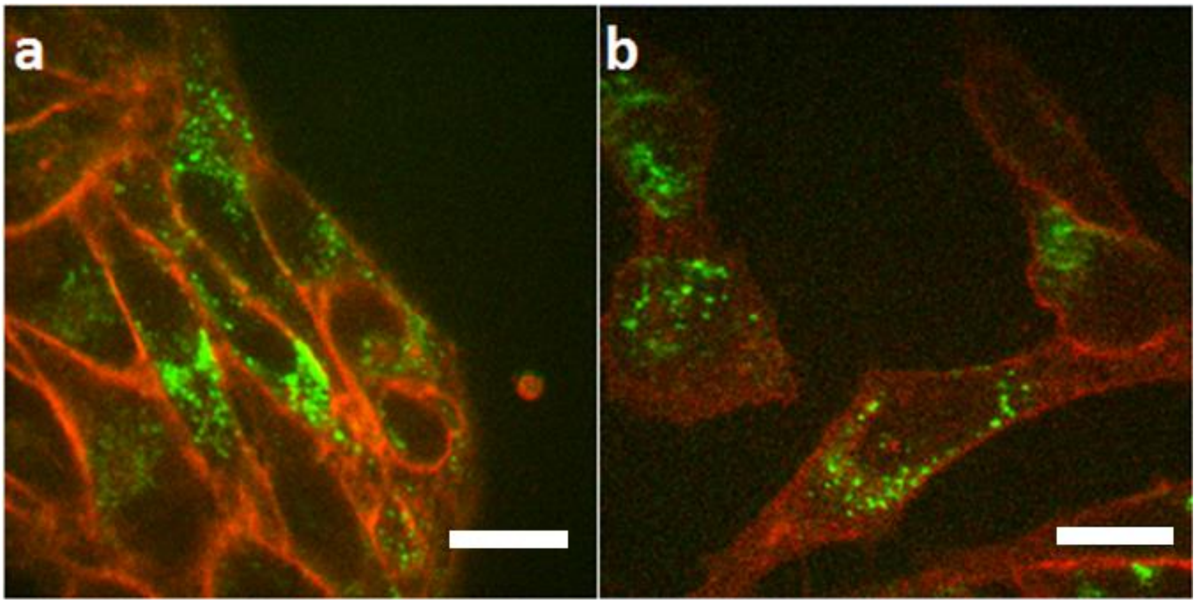

Figure S5.22. a, b) HeLa cells with exosome coated MIL-88A particles after two days of incubation. The scalebars (white) represent 20 µm.

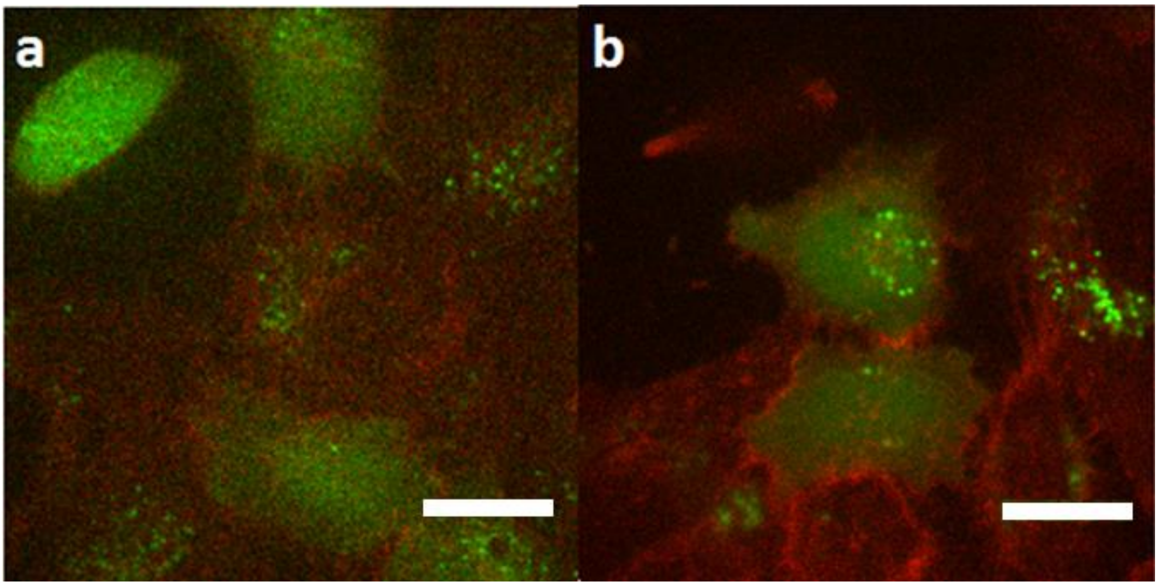

Figure S5.23. HeLa cells with exosome coated MIL-88A particles after three days of incubation. The scalebars (white) represent 20 µm.

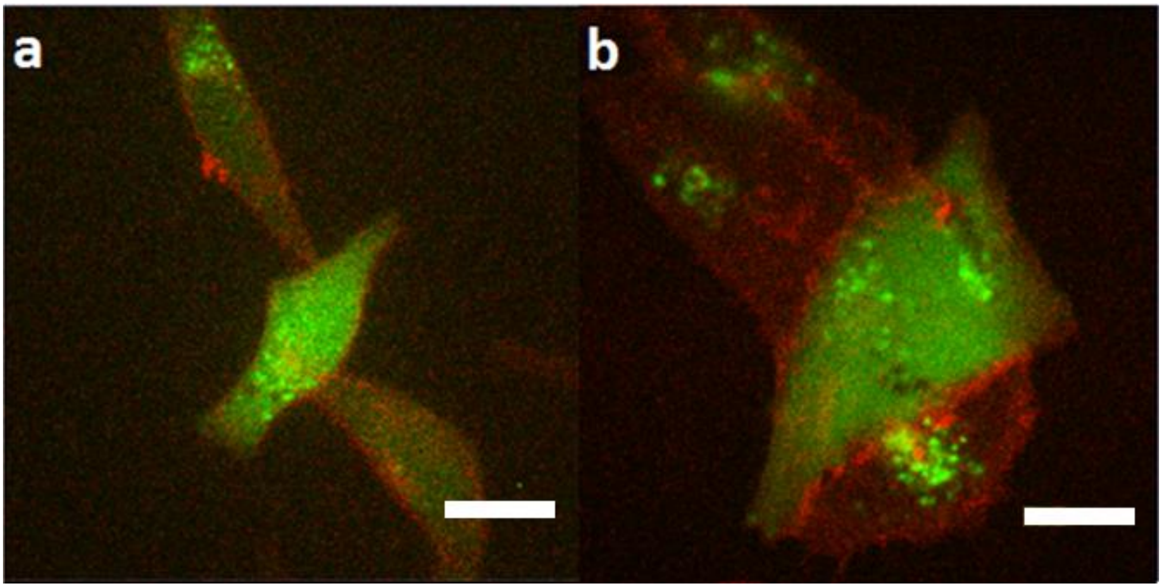

Figure S5.24. **a**, **b**) HeLa cells with exosome coated MIL-88A particles after four days of incubation. The scalebar (white) represents 20 µm.

5.4.7 Release Experiments

The release experiments were performed on a PTI fluorescence spectrometer. Hollow caps were filled with 50 µL of a 1 mg/mL particle stock solution for exosome coated and calcein loaded particles. Depending on the experiment either 150 µL water, 150 µL ALF or 90 µL water and 10 µL Triton 100-X were added. The caps were then sealed with a dialysis membrane and placed into cuvettes filled with either water or ALF and a stirring rod. The cuvettes were heated to 37 °C to simulate the cell environment. Each experiment lasted 14 h with one measurement per second. The excitation wavelength was 495 nm and the measured emission wavelength was 512 nm.

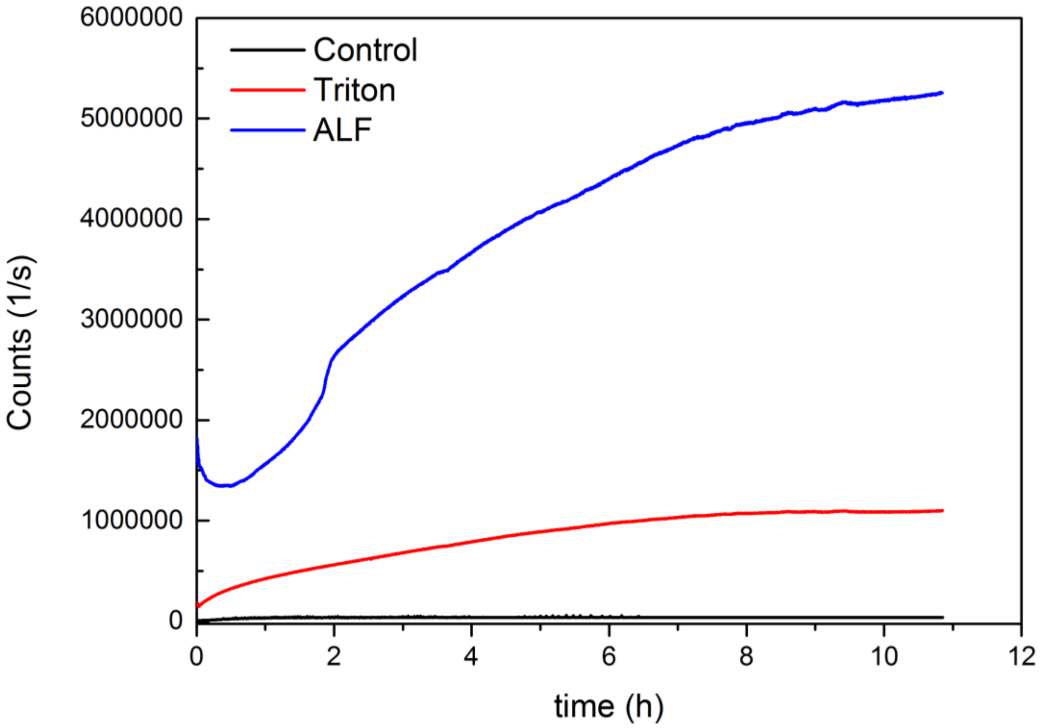

Figure S5.25. Fluorescence experiment of the exosome coated MIL-88A NPs showing that they are stable and do not release in water (black). When dissolved in ALF (blue) or Triton X-100 (red) containing media release from the particles can be observed that reaches saturation after about 10 hours.

To account for quenching 10 mL of a 1 mM solution of calcein were diluted with 990 mL PBS. Next 10 mL of this new solution were added to 4 mL water or ALF in cuvettes. In addition 10 mL triton X-100 was added to one sample. Then the fluorescence spectra of these solutions were measured to find a normalization factor between them (**Figure S5.26**). This factor was then used to calculate the offset for the individual fluorescence measurements. The normalization factor determined by comparing the measurements for water and triton X-100 to those for ALF is 2.17 and was implemented in the fluorescence experiments.

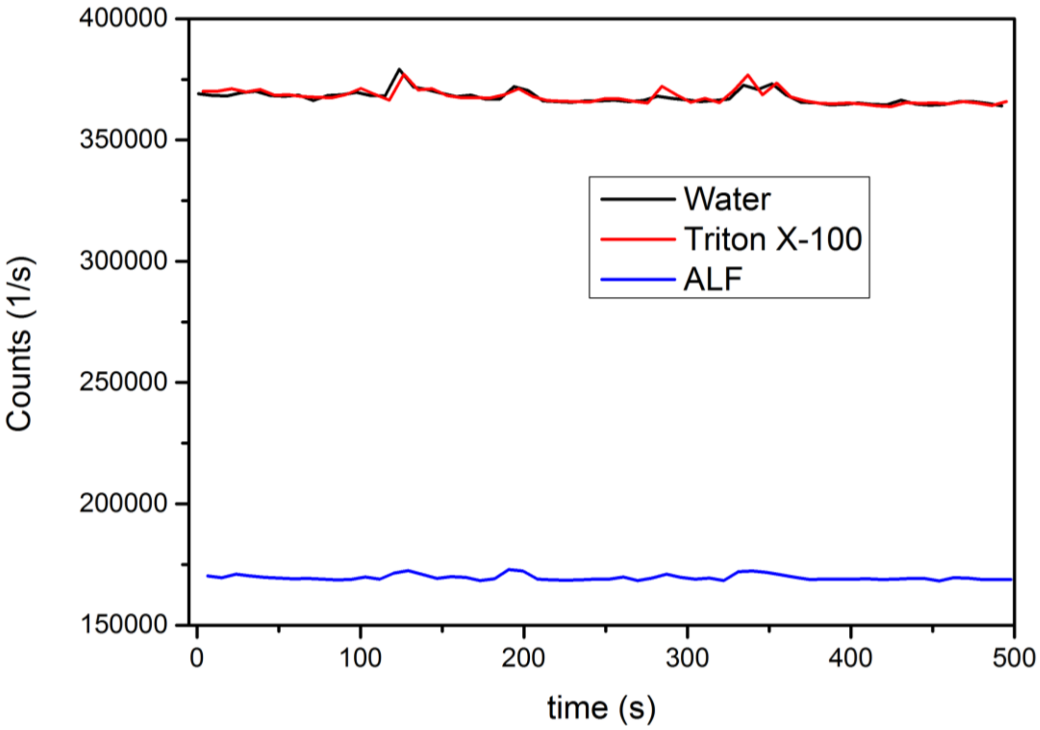

Figure S5.26. Fluorescence measurement to determine the quenching of the different media used in the fluorescence measurements.

5.4.8 UV/Vis measurements

To evaluate the loading capacity of the coated MIL-88A NPs, UV/Vis spectra of a 1 mM calcein solution, the remaining supernatant of the calcein solution after the particles were loaded, a 1 mg/mL solution of loaded particles dissolved by ALF, and a 1 mg/mL solution of coated, loaded particles were measured (**Figure S5.27**). In addition a solution containing the calculated amount of calcein loaded in the MOF was also measured. For each measurement 100 mL of the sample were diluted with 3 mL water.

The calcein loading capacity was calculated from the difference in absorbance of the measured solutions. The calcein stock solution used for loading the particles had a concentration of 1mM, i.e. 0.622 mg/mL. As 1 mL of the stock solution was used for loading, 1 mg of the particles have taken up 0.158 mg calcein or 15.8 wt%, using the ALF measurement as a basis. A quarter of the calcein was taken up by the MIL-88A particles and released. As the particles dissolve in ALF all of the loaded particles should be released. The difference in absorbance between the loaded particles and the particles dissolved in ALF can be attributed to quenching of the fluorescence as long as the calcein still resides in the MOF.

The spectrum of calcein in ALF and the sample containing the calculated amount of calcein match very well. This shows that the remains of the disintegrated MOF do not affect the UV/Vis measurements and this measurement can thus be used for determining the amount of encapsulated and released calcein.

In previous works, in which drugs like Doxorubicin and Paclitaxel were loaded into exosomes, loading efficiencies of 7.2 to 11.7% were reached.[6-8] These values are comparable but lower than those of the exosome coated MIL-88A NPs presented in this work which could reach loading capacities of up to 15.8 wt%.

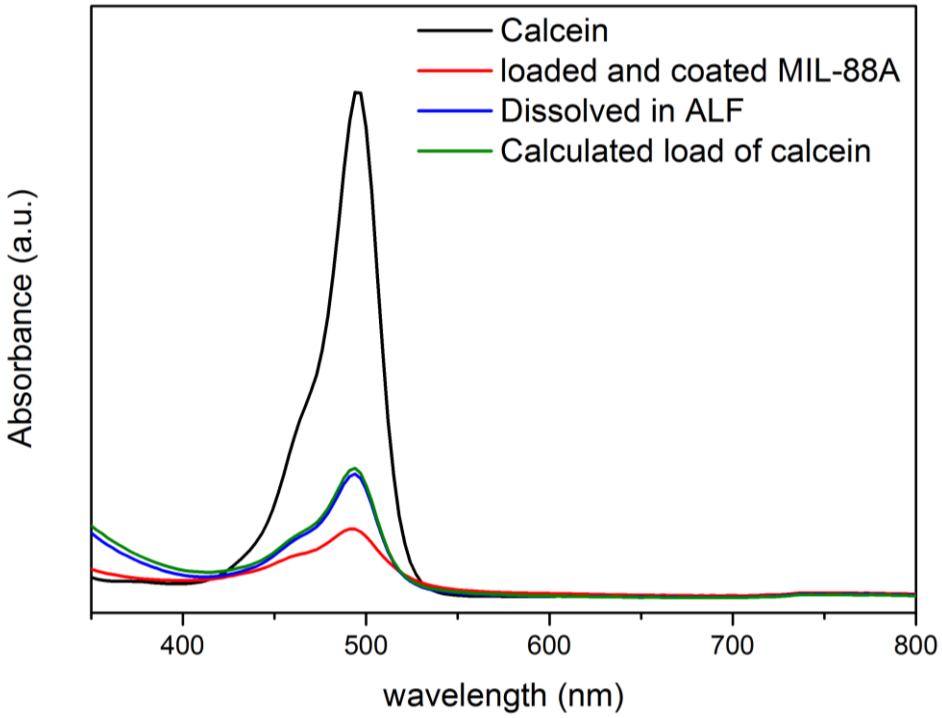

Figure S5.27. UV/Vis measurements of several different calcein and particle solutions

HDAC1 Assay to determine the SBHA loading

Due to SBHA being hardly detectable with standard analytical techniques, an HDAC1 activity assay was performed. SBHA is an inhibitor of HDAC1. The assay kit used was the HDAC1 Inhibitor Screening Assay Kit from Cayman Chemical. For the quantification different dilutions of SBHA were prepared and tested on their inhibition of HDAC1 and then compared to the inhibition of dissolved SBHA loaded particles to determine how much SBHA was loaded into the particles (

Figure S5.28).

From that we calculated the theoretical dilution at 50% inhibition for SBHA (1:42.2) and the SBHA loaded MIL-88A NPs (1:5.40). From these dilutions and the concentrations of the stock solutions we could calculate the how much SBHA (4.835 µg) and SBHA loaded particles (185 µg) were needed to inhibit 50% of the available HDAC1. By comparing these numbers we can then calculate the loading capacity: 13.1 % of the initially available 1 mM SBHA or 2.61 wt% in relation to the weight of the MOF NPs were loaded into the particles.

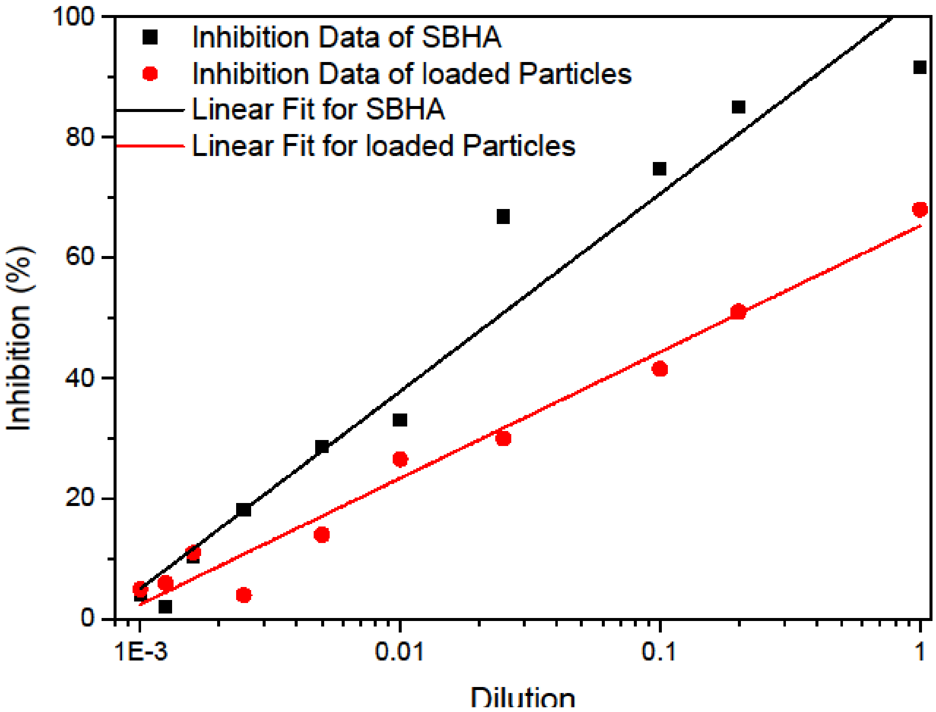

Figure S5.28. Graphical representation of the results of the HDAC1 Inhibition Assay.

5.4.9 High-Content Quantification Experiments

96-well plates from Costar were seeded with 5000 HeLa cells per well and a volume of 100 µL DMEM medium. After incubating for 1 day at 37 °C/5 % CO_2 the particles were added. Each concentration (0, 10, 20, …, 140, 150 µg/mL) was tested in three different wells. Before the measurement the plate was washed twice with 100 µL per well PBS to remove dead cells and excess calcein. Both transmission and GFP channel images were recorded. Four images were recorded per well. The images were evaluated with the MetaXpress software, by counting the number of cells showing release and the total number of cells and calculating the release percentage from these numbers.

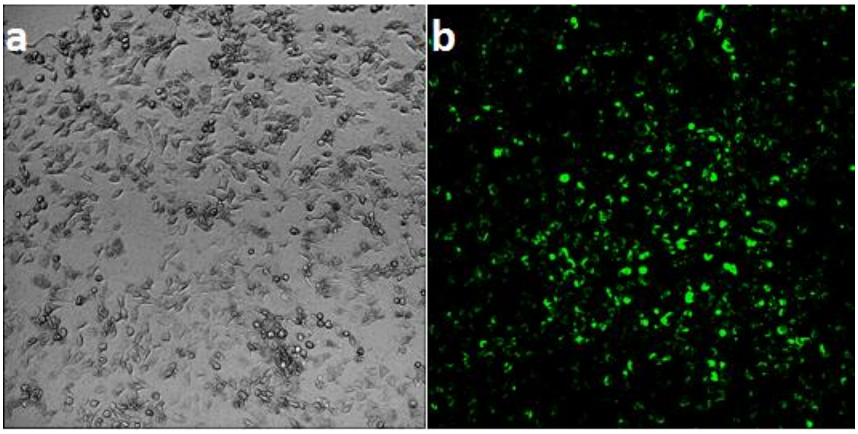

Figure S5.29. Sample images as used for the quantification measurements: **a**) Transmission image used to count the total number of cells; **b**) Fluorescence image used to count the number of cells showing release.

5.4.10 MTT-assays

5000 cells were seeded in each well of a 96-well plate and covered with 100 µL DMEM. After 1 day of incubation at 37 °C/5 % CO_2, the particles were added (0, 2, 4, 8, 20, 60, 100, 140 µg/mL). Each concentration was tested in triplicate. The supernatant was recovered via centrifugation (14000 rpm, 5 min) from a 1mg/mL loaded exosome coated MIL-88A NP stock solution after one day of incubation in PBS. The MTT-assays were performed after 3 and 4 days of incubation.

The MTT reagent concentration used was 0.5 mg reagent per 1 mL medium. The sample was washed three times with 100 µL HBSS buffer per well before 100 µL of the reagent solution was added in each well. After two hours of incubation at 37 °C/5 % CO_2 the wells were emptied and the whole plate was frozen at -80 °C for an hour. After defrosting 100 µL DMSO was added to each well and after dissolving any remaining crystals the MTT-assays were performed. MTT-assays were performed in triplicate and repeated on at least three different days.

In addition to the coated variants uncoated Mil-88A NPs were also investigated (**Figure S5.30**). They showed low toxicity with cell viabilities of over 70%.

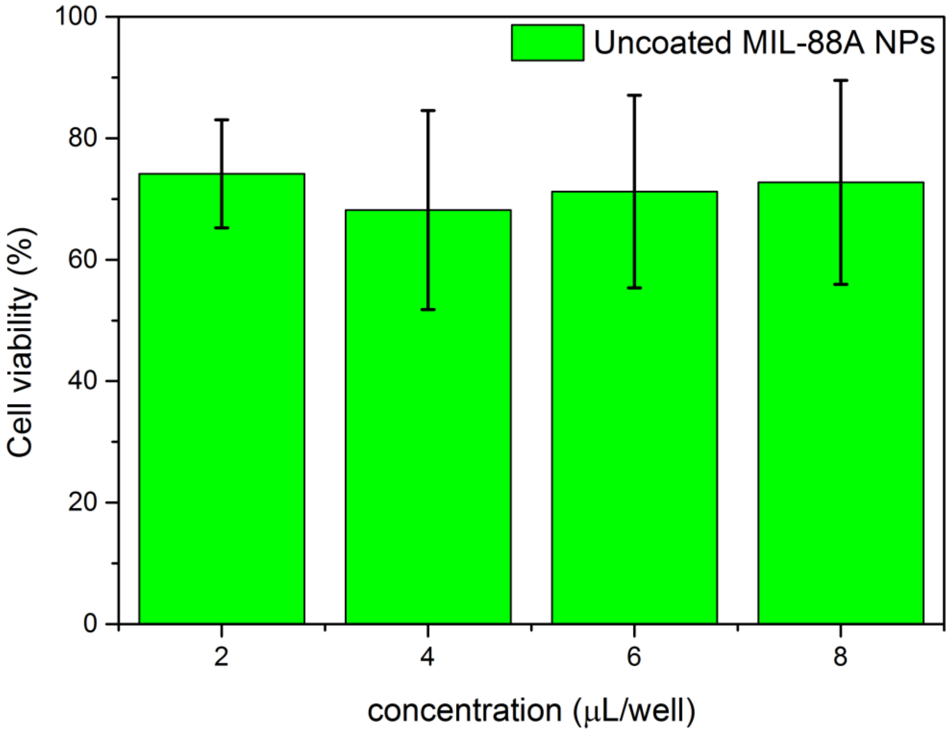

Figure S5.30. MTT Assay of HeLa cells after 3 days of incubation with uncoated MIL-88A NPs. The error bars signify the SD.

To investigate the efficacy of pure SBHA, a 1 mM solution of SBHA in PBS was added to HeLa cells in increasing amounts (**Figure S5.31**). Lower concentrations, below 20 µL/mL, proved to be nontoxic, while higher concentrations lead to very low cell viability of about 5%. Comparing the effect of free SBHA with that of transported SBHA shows that the transported SBHA possesses a higher efficacy and leads to more cell deaths. 1 µL of SBHA in PBS corresponds to 0.204 mg of pure SBHA.

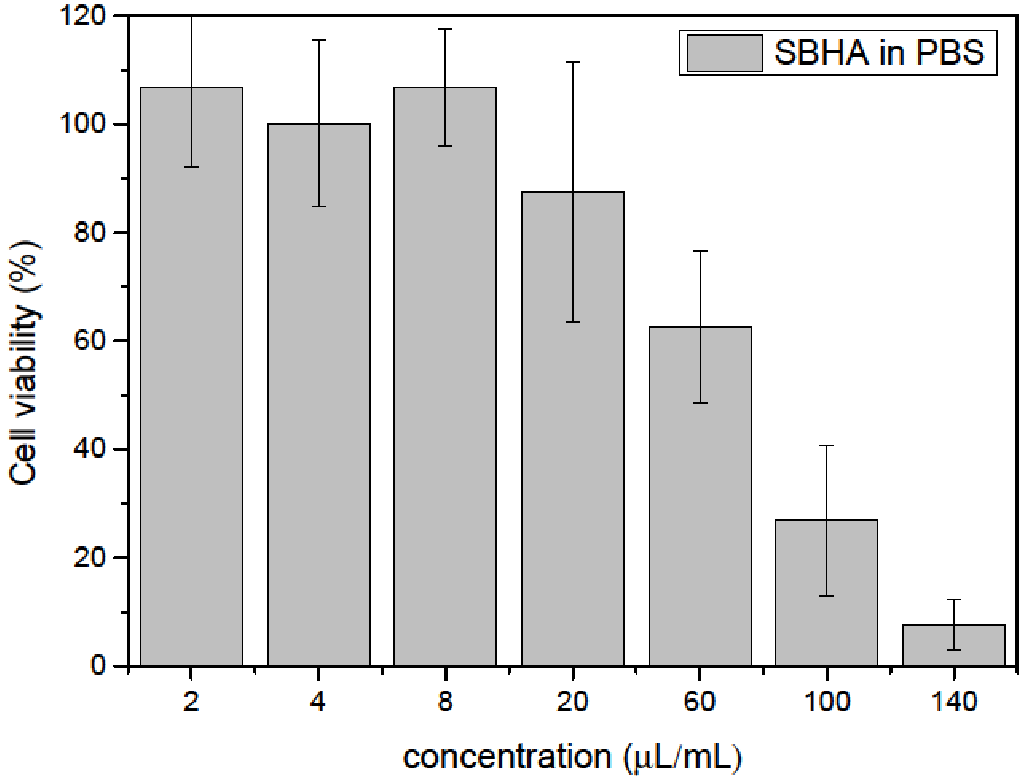

Figure S5.31. MTT Assay of HeLa cells after three days of incubation with a 1 mM solution of SBHA in PBS. The error bars signify the SD.

5.4.11 Cell targeting

Beyond potential inherent targeting through proteins naturally inserted into the exosomes, our exosome coated MOF NPs offer the option to additionally functionalize the exosome shell as has been shown earlier with liposomal coatings around NPs.[9,10] This can be done via spontaneous insertion of lipids functionalized with a targeting moiety such as folate. Folate receptors are known to be overexpressed on cancer cells and thus are a common receptor used for targeting. To show this optional targeting via inserted ligands, we added such folate functionalized lipids into the exosomal coating of the MOF NPs and performed targeting experiments

The MIL-88A NPs were loaded and coated as described previously, and then incubated overnight with 1,2-dipalmitoyl-sn-glycero-3-phosphoethanolamine-N-(6-((folate)amino)hexanoyl) to replace some of the lipds in the exosome coating.[9] The modified particles are not taken up in media saturated with folate, but are efficiently taken up in HeLa cells incubated with folate-free DMEM (**Figure S5.32**).

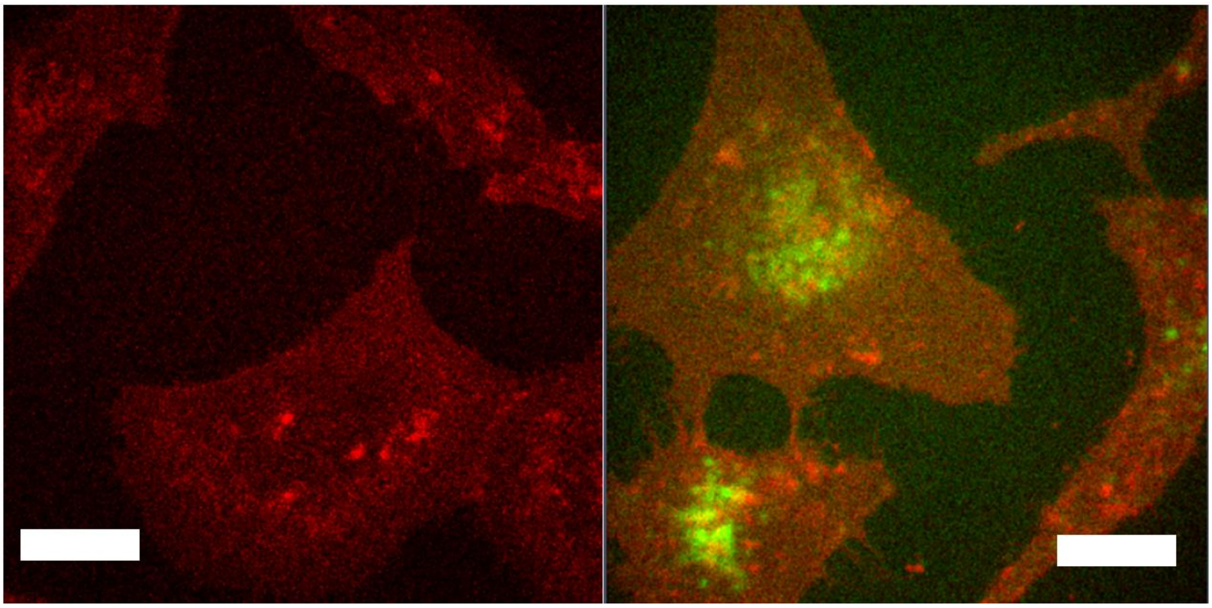

Figure S5.32. No uptake of folate modified LipMIL particles in HeLa cells incubated in a folate rich media (left). Uptake of folate modified LipMIL particles in HeLa cells in normal folate free DMEM. The scale bars in both images represent 15 µm

References

1 Chalati, T., Horcajada, P., Gref, R., Couvreur, P. & Serre, C. Optimisation of the synthesis of MOF nanoparticles made of flexible porous iron fumarate MIL-88A. *J. Mater. Chem.* **21**, 2220-2227, doi:10.1039/c0jm03563g (2011).

2 Hirschle, P. *et al.* Exploration of MOF nanoparticle sizes using various physical characterization methods - is what you measure what you get? *CrystEngComm* **18**, 4359-4368, doi:10.1039/C6CE00198J (2016).

3 Andrew Lin, K.-Y., Chang, H.-A. & Hsu, C.-J. Iron-based metal organic framework, MIL-88A, as a heterogeneous persulfate catalyst for decolorization of Rhodamine B in water. *RSC Advances* **5**, 32520-32530, doi:10.1039/C5RA01447F (2015).

4 McKinlay, A. C. *et al.* Nitric Oxide Adsorption and Delivery in Flexible MIL-88(Fe) Metal–Organic Frameworks. *Chem. Mater.* **25**, 1592-1599, doi:10.1021/cm304037x (2013).

5 Margareth R. C. Marques, R. L., and May Almukainz. Simulated Biological Fluids with PossibleApplication in Dissolution Testing. *Dissolution Technologies*, 15-28 (2011).

6 Yang, T. *et al.* Exosome Delivered Anticancer Drugs Across the Blood-Brain Barrier for Brain Cancer Therapy in Danio Rerio. *Pharmaceutical Research* **32**, 2003-2014, doi:10.1007/s11095-014-1593-y (2015).

7 Rani, S., Ryan, A. E., Griffin, M. D. & Ritter, T. Mesenchymal Stem Cell-derived Extracellular Vesicles: Toward Cell-free Therapeutic Applications. *Molecular Therapy* **23**, 812-823, doi:10.1038/mt.2015.44 (2015).

8 Tian, Y. *et al.* A doxorubicin delivery platform using engineered natural membrane vesicle exosomes for targeted tumor therapy. *Biomaterials* **35**, 2383-2390, doi:10.1016/j.biomaterials.2013.11.083 (2014).

9 Mackowiak, S. A. *et al.* Targeted Drug Delivery in Cancer Cells with Red-Light Photoactivated Mesoporous Silica Nanoparticles. *Nano Letters* **13**, 2576-2583, doi:10.1021/nl400681f (2013).

10 Ashley, C. E. *et al.* The targeted delivery of multicomponent cargos to cancer cells by nanoporous particle-supported lipid bilayers. *Nat Mater* **10**, 389-397, doi:10.1038/nmat2992 (2011).

6 Chemical Diversity in a Metal-Organic Framework revealed by Fluorescence Lifetime Imaging

This chapter is based on the following publication:

Schrimpf W, Jiang J, Ji Z, **Hirschle P**, Lamb DC, Yaghi OM, Wuttke S. Nat Commun. **2018**;9(1):1647. (DOI: 10.1038/s41467-018-04050-w)

6.1 Introduction

The central goal of materials science has always been the synthesis and characterization of materials with novel properties. Key aspects that have an impact on the properties of the material are the presence and distribution of functional groups and defects within the substance[1-6]. This chemical diversity is an unpredictable outcome of chemical synthesis conditions and arises prominently in the chemistry of metal–organic frameworks (MOFs), where the use of multiple functionalized organic linkers results in a multivariable system in which the spatial arrangement of both functionalities and defects are unknown[7-9]

Deciphering the chemical diversity in MOF crystals is an experimental challenge, because most characterization techniques rely on measuring the averaged properties of a bulk sample, such as elemental analysis, powder X-ray diffraction (PXRD), and gas adsorption isotherms. Recently, solid-state nuclear magnetic resonance (NMR) coupled with computational modeling has been shown to be extremely powerful in elucidating the distribution of different linkers and functional groups[10-13]. However, even these measurements are based on statistical of resonances emanating from many different crystals within the sample. Single-crystal X-ray diffraction, on the other hand, examines the chemical nature of defects in only one single crystal at a time.[14] Therefore, neither one of these methods provides information about the diversity of the sample as a whole. Electron microscopy, although extensively used to map defects in inorganic solids, is problematic for MOF imaging as the electron doses required to image the material with good resolution quickly damage the sample. Still, low-dose transmission electron microscopy has been very recently used to study surfaces and interfaces of the MOF ZIF-8[15] averaging. In contrast, fluorescence imaging has the advantages of spatial resolution, high throughput, and sensitivity. It was previously employed to visualize plane defects and surface functionalization in MOFs[16], and to compare the linker distribution between different methods of synthesis[13]. Extending the measured fluorescence parameters beyond the intensity, e.g., to the spectrum[13] or the lifetime[17],[18] greatly increases the information gathered about the material. Most fluorophores are highly sensitive to their immediate surroundings, so that changes in the nanoscopic environment affect their photo-physical properties, including the fluorescence lifetime. By careful analysis of the lifetime, it is therefore possible to detect and interpret spatial heterogeneities or differences between samples on length scales far below the resolution limit of a light microscope, thereby complementing the insights gained using other imaging techniques, such as electron microscopy or Raman imaging[19].

In this study, we apply fluorescence imaging combined with fluorescence lifetime analysis to examine the diversity and distribution of defects and functional groups in a MOF. Fluorescent dye modified linkers were incorporated into the UiO-67 framework, serving as both model functional group and reporter. Förster resonance energy transfer (FRET) analysis indicates a random distribution of the incorporated dyes, whereas fluorescence lifetime imaging (FLIM) revealed a correlation between fluorescence quenching and nanoscopic defects, aspects not detectable with standard bulk characterization techniques. The measurements uncovered chemical diversity in a multivariable MOF originating from different synthesis conditions, within a sample, and even within a single crystal, highlighting the potential of fluorescence based methods in decoding the state of complex porous materials.

6.2 Results

Bulk characterization. UiO-67 was chosen as a MOF prototype for this study, because it exhibits exceptional chemical and thermal stability, and has pores large enough to incorporate the dyes used for functionalization[20]. In this MOF, $Zr_6(\mu_3\text{-}O)_4(\mu_3OH)_4$ clusters are connected to 12 linear ditopic organic linkers (biphenyl-4,4′-dicarboxylic acid, BPDC), forming a network of face-centered cubic topology. A portion of the original linkers can be substituted with dye-modified versions, creating isoreticular structures without altering the topology. For this purpose, the organic linker 2-amino-BPDC was coupled to either fluorescein isothiocyanate (FITC) or rhodamine B isothiocyanate (RITC). These dye-functionalized linkers were then incorporated into the framework either de novo (i.e., added to the synthesis solution) or by post-synthetic linker exchange[21,22]. Using the lowest MMFF94 energy conformations, the maximal projection radii of the dyes attached to the linker were estimated to be 18.1 Å for FITC and 20.5 Å for RITC. This makes the dyes small enough to fit into the 23 Å wide octahedral pores of UiO-67, but not into the 11.5 Å large tetrahedral pores[23]. If the linkers are incorporated into the framework itself, the sizes of the fluorophores protruding into the pores are 14.3 Å and 17.9 Å, respectively, allowing for a better fit.

The total amount of dye-functionalized linker incorporated into the scaffold was determined by comparing the measured fluorescence signal of the digested MOFs in an aqueous solution in relation to the total amount of linker in the sample. The resulting de novo incorporation efficiencies (i.e., the ratio of the incorporated and the input fractions) were 17–27% for FITC and 2–7% for RITC (**Table S6.1**). It is likely to be that this difference is caused by the larger side groups of RITC and its positive charge. The crystallinity, porosity, and morphology of the dye-modified MOFs were investigated with PXRD (**Figure S6.5**), nitrogen adsorption/desorption isotherms (**Table S6.3**), and scanning electron microscopy (SEM, **Figure S6.9**), respectively. These bulk measurements detected no changes caused by the functionalization, independent of the incorporation method, or the type and the amount of incorporated dye.

6.2.1 Distribution of Functional Groups.

In order to determine the distribution of functional groups in the UiO-67 framework, two-color experiments were performed by incorporating both dyes into the MOF using de novo functionalization. The microscopic distribution of fluorophores is given from the fluorescence intensities within the MOFs. The nanoscale distribution of the dyes can be investigated using FRET as the fluorophores constitute a FRET pair with FITC serving as the donor and RITC as the acceptor dye. During FRET, energy is transferred nonradiatively from the excited donor fluorophore to the acceptor. This process results in quenching of the donor fluorescence, indicated by a decrease in the fluorescence lifetime, and a corresponding increase of the signal in the acceptor channel. The FRET efficiency is highly distance dependent (R^6 dependence) and can be exploited to measure the separation between fluorophores on the nanometre scale. Previous studies have already used this property in combination with FLIM to investigate the spatial distribution of fluorophores in MOFs and other porous materials[18,24,25]. The Förster radius, representing the dye separation resulting in 50% transfer efficiency, is in the range of 40–80 Å for common fluorescence dyes. It depends on the particular dye pair and the measurement conditions, most notably the spectral overlap integral between the donor emission and the acceptor absorbance, the donor fluorescence quantum yield, and the relative orientation between the dyes. Based on these properties, the Förster radius of the dye pair of FITC and RITC in water can be calculated as 55 Å. However, inside the MOF pores, these parameters can be affected in an unpredictable way, changing the Förster radius. A key factor hereby is the relative orientation between the FRET pair. Inside of the pores, it is very likely to be that the rotation of the fluorophores is restricted, resulting in a preferred orientation for each individual pair of dyes. On the other hand, the structure of UiO-67 shows high symmetry, so that the individual molecules will assume several orientations. Averaging over multiple fluorophores should give a similar result as for freely rotating dyes. Although the uncertainty regarding the Förster radius inside of the MOF makes a quantitative analysis of the inter-dye distances difficult, the presence or absence of FRET can still be used to judge the general distribution of the fluorophores.

For these investigations, the fraction of FITC was kept constant at 0.1% of the linkers during synthesis, whereas the amount of RITC was varied between 0.01% and 1%. Based on the incorporation efficiency of RITC, this concentration range should result in long average distances between the dyes and therefore produce no significant FRET signal, assuming a purely random and homogeneous nanoscale distribution of the dyes in the scaffold (**Figure 6.1a**). However, clustering, either at the surface or inside of the crystal, would create regions with higher fluorophore densities (**Figure 6.1b**), thus lowering the nearest-neighbor distances, and result in measurable FRET. From this, the presence and degree of clustering can be determined.

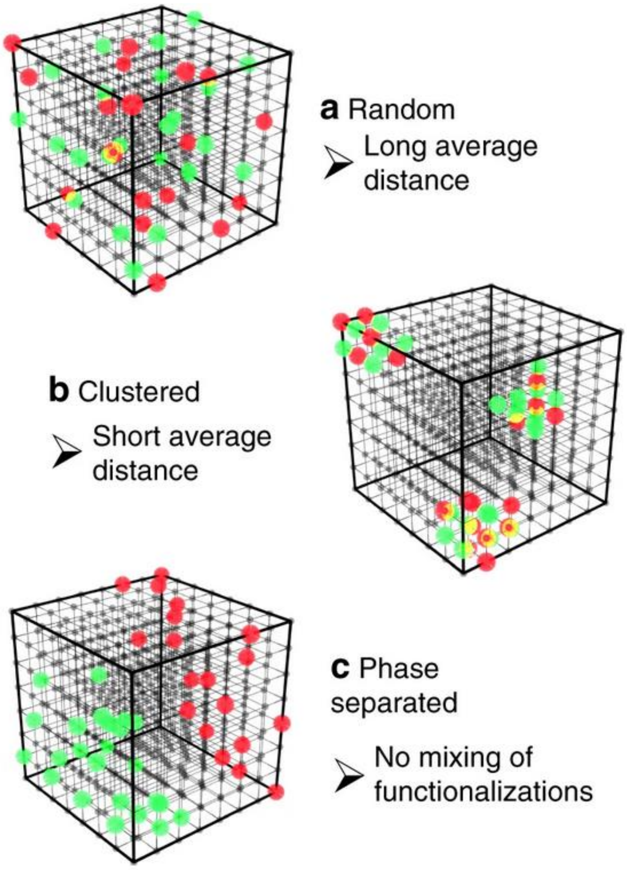

Figure 6.1. Schematic representation of the possible spatial distributions of two different functionalities within the MOF structure. **a** A random distribution with a long average separation between functional groups, green and red. **b** A clustered distribution with short average distances between functional groups. A subform of clustering is a distribution at or close to the surface. **c** A phase-separated distribution with very long distances between different functional groups. In the different phases, the individual groups themselves can be both clustered or random.

The particle shapes observed with fluorescence imaging (**Figure 6.2**) correspond well to the morphology revealed by SEM (**Figure S6.9**) for all measured samples. Furthermore, a significant, homogeneous fluorescence signal was observed for both dyes in all MOF crystallites (**Figure S6.7**), indicating that FITC and RITC are well mixed within the resolution limit of the microscope (~ 200 nm). Besides the intensity, the fluorescence lifetime of the MOFs was analysed using the phasor approach. Unlike standard fit-based lifetime analysis approaches, phasor FLIM is calculated by simple mathematical equations and is therefore not biased by the selected fit models. Instead, it uses the Fourier space to visualize the measured fluorescence lifetime in a graphical way[26,27]. This makes it very useful for a qualitative analysis of complex data with many unknown processes and contributions, as is the case for the presented data[17]. Detailed descriptions of the phasor calculations and rules are given in the supporting information and previous publications[17,26]. In short, the first cosine (g) and sine (s) Fourier coefficients of the fluorescence decay (**Figure 6.2a**) are calculated for each pixel of the corresponding FLIM image and plotted as a twodimensional histogram (**Figure 6.2b**). Hereby, all purely monoexponential decays lie on a semi-circle of radius 0.5 around the point (0.5, 0), with lifetimes decreasing in the clockwise direction. Multi-exponential decays can be treated as a vector addition of the base components and will fall inside of that circle. However, due to shot noise and the corresponding inaccuracy, the phasor of individual pixels can fall outside of the circle In this study, we plot the right-hand side of the phasor plots (i.e., the semi-circle with $0.5 < g < 1$). This means that a decrease in lifetime corresponds to a shift from the top left of the plot to the bottom right (**Figure 6.2b**).

The phasor analysis shows a clear decrease of the FITC lifetime with increasing RITC concentration, from 2.07 ± 0.18 ns at 0.01 % input RITC fraction, down to 0.83 ± 0.26 ns at 1% RITC input fraction. FRET has been previously reported as one possible quenching source for dyes incorporated into the UiO-67 scaffold[28,29]. However, a detailed analysis of the data suggests a different explanation. The RITC signal after 475 nm laser excitation (used for FITC excitation) shows the identical decay as the RITC signal after 565 nm excitation (used for direct RITC excitation), even at the highest RITC concentration (**Figure 6.2h-j**). In the case of FRET, the donor is excited first and then transfers the energy to the acceptor, leading to a delay in the fluorescence lifetime of RITC. As this is not observed, the RITC signal after 475 nm excitation is mainly caused by direct RITC fluorescence. If FRET occurs, it is, at most, a minor contribution to the fluorescence quenching of FITC and some other mechanism must be present. A similar decrease in lifetime with increasing dye concentration was also observed for samples containing only a single fluorophore type (**Figure S6.8**) that is also associated with a small spectral shift **Figure S6.6**). Although FRET between identical fluorophores is also possible, it does not directly result in a shorter lifetime and requires significantly higher dye densities to cause quenching. This further supports the argument against FRET between fluorophores as the main source of quenching.

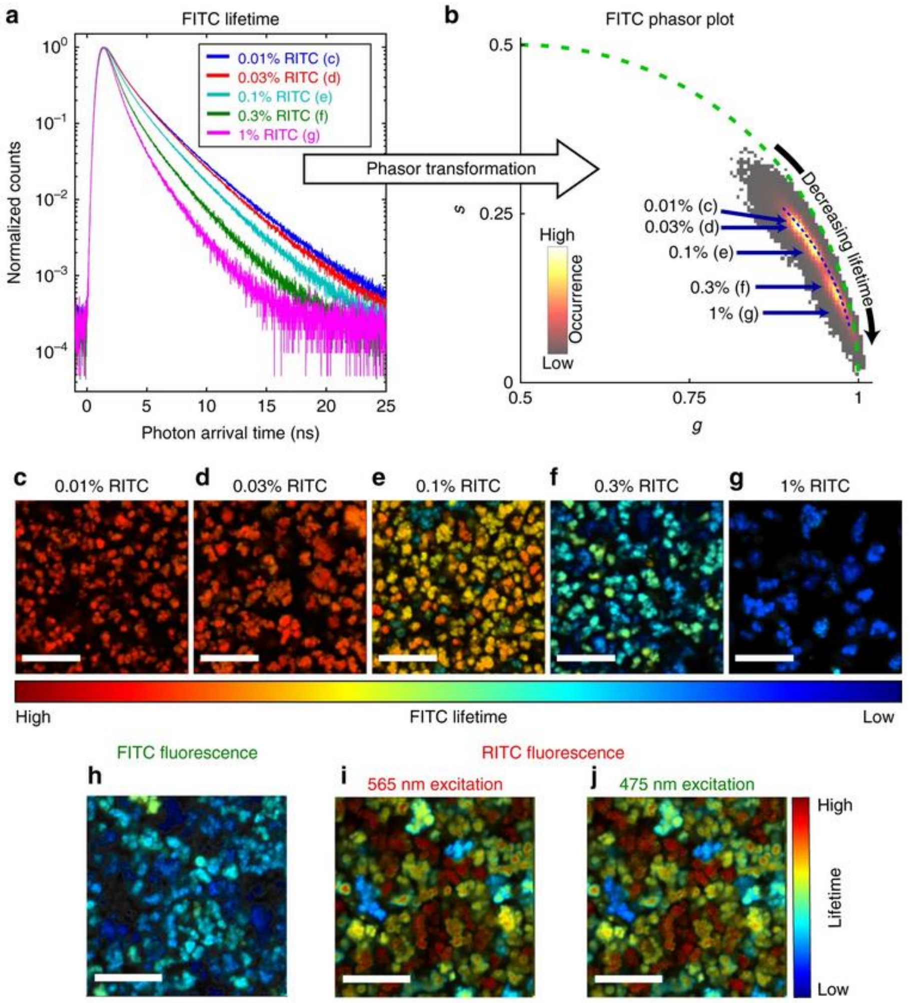

Figure 6.2. A phasor analysis of UiO-67 samples with both FITC- and RITC-labeled linkers. The fraction of labeled linkers during sample preparation was held constant at 0.1% for FITC, whereas for RITC it was varied from 0.01% to 1%. **a** Photon arrival time histogram of the FITC fluorescence for the full images shown in **c–g**. **b** The phasor histogram calculated from the pixel wise photon arrival time histograms of FITC of the images shown in **c–g**. The blue arrows point at the average phasor positions of the different samples. The green dotted line is the universal circle, indicating the possible positions of single exponential decays. **c–g** Lifetime images of FITC fluorescence of UiO-67 samples with 0.1% input FITC linker fraction and 0.01% (**c**), 0.03% (**d**), 0.1% (**e**) , 0.3% (**f**), or 1% (**g**) input RITC linker fraction. The color code represents the pixel phasor positions along the blue dotted line in **b**. **h–j** FLIM images for different excitation and detection schemes of the UiO-67 sample with 0.1% FITC and 1% RITC input fraction. The corresponding phasor plot is shown in **Figure S6.6**. h FLIM image of the green detection channel (500–540 nm) after 475 nm excitation, corresponding to the direct FITC fluorescence. **i** FLIM image of the red detection channel (570–620 nm) after 565 nm excitation corresponding to the direct RITC fluorescence. **j** FLIM image of the red detection channel after 475 nm laser excitation representing the possible FRET signal. The scale bar in all images is 10 µm.

Based on the total amount of incorporated dye in the sample with 0.1% FITC and 1% RITC, the average distance to the nearest RITC dye, assuming a purely random distribution (**Figure 6.1a**), was calculated to be 63.6 Å, a value close to the FRET range. Clustering would result in a significant decrease of the nearestneighbor distance (**Figure 6.1b**), thus causing energy transfer to occur, even when accounting for possibly shorter Förster radii inside the MOF. Thus, the absence of FRET also means the absence of clustering. At the same time, the decrease in FITC lifetime due to the incorporation of RITC indicates some interaction between the two fluorophores. As no large-scale changes were observed in the bulk characterization methods or in the fluorescence intensity, this affect must be localized within a few tens of nanometers. Thus, we can preclude phase separation (**Figure 6.1c**), suggesting that the dyes are distributed purely randomly in the framework.

6.2.2 Defects in the Scaffold Quench Fluorescence.

As FRET is the dye–dye interaction with the longest range, the absence of energy transfer suggests that a direct interaction between the fluorophores is not the source of the fluorescence quenching. At the same time, all conditions, with the exception of the fraction of dye-modified linkers, were kept constant during synthesis, meaning that the observed changes must be caused by the fluorophores themselves. The only possible explanation consistent with both observations—quenching of FITC by RITC incorporation, but no FRET—is that dye incorporation results in changes in the scaffold itself. The most likely explanation is that incorporation of dye-functionalized linkers during the formation of the MOF interferes with the crystal growth, resulting in defects. It is easy to imagine that the big and bulky dyes can sterically hinder proper scaffold formation. In addition to this steric effect, both fluorophores also have an additional carboxyl group that can interact with the zirconium clusters, further obstructing correct growth of the framework, an interference resulting in vacancies or mismatches in the crystal structure[30-33]. Considering the existing literature on zirconium-based MOFs[14,34-37], almost all types of crystal defects—missing linkers, missing clusters, or lattice mismatches—can result in coordinatively unsaturated metal sites (CUSs), and thus lead to fluorescence quenching, as has been shown earlier[38,39]. Higher dye concentrations create more defects and thus lead to more quenching. The fact that the morphology, the crystallinity, and the pore volume are unaffected indicates that these defects are very localized, extending only on the nanometer scale.

6.2.3 Measuring the Chemical Diversity between Particles.

Using both the spectral and the lifetime information, it is possible to determine the functionalization and defect level not only for the whole sample, but also for individual particles. Both the amount of dyes (**Figure 6.3a**), as well as the level of defects (**Figure 6.3b**), vary significantly between individual MOF aggregates, whereas the diversity within a single particle is much smaller. For example, the SD of the pixel lifetimes for the full image shown in **Figure 6.3b** is 0.21 ns. However, for individual particles, the SD ranges between 0.07 and 0.10 ns, more than a factor of 2 smaller.

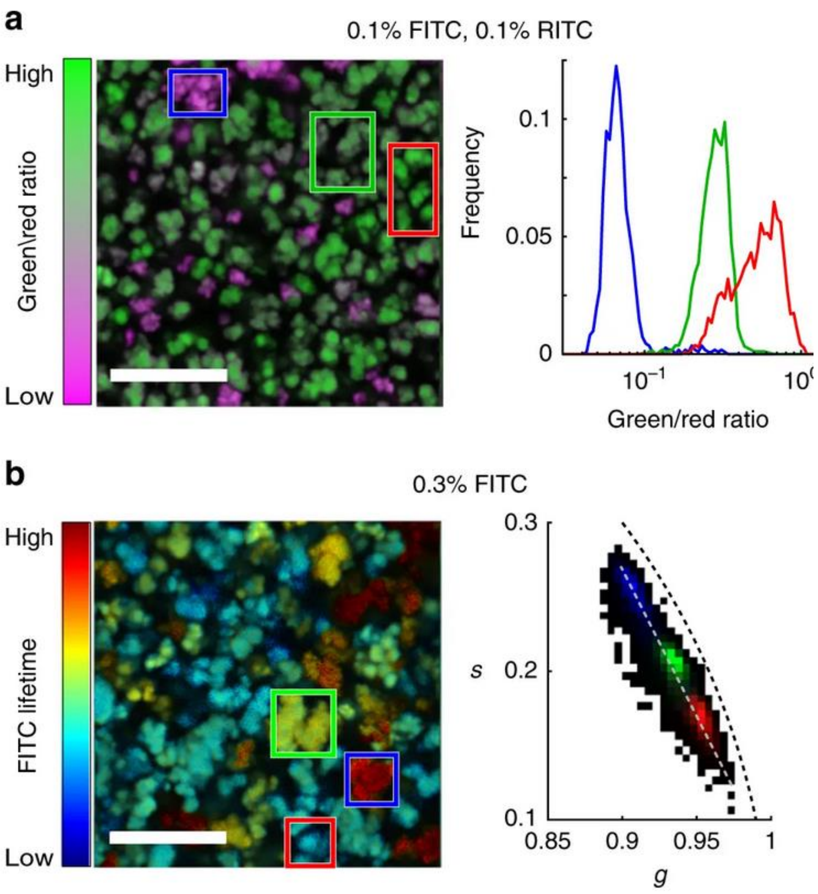

Figure 6.3. Fluorescence data for individual UiO-67 particles. **a** An image (left) and histogram (right) showing the ratio of FITC to RITC fluorescence of a UiO-67 sample with 0.1% FITC and 0.1% RITC linker input fraction. The three curves represent the regions selected with the coloured rectangles in the image. **b** A phasor FLIM image (left) and histogram (right) of the UiO67 sample with 0.3% FITC linker input fraction. The 2D colored histograms correspond to the regions highlighted with the colored rectangles in the image. The color coding of the images is based on the pixel phasor position along the gray line in the phasor histogram. The scale bar in the images is 10 µm.

One possible cause for the heterogeneity in the sample is fluctuations in the synthesis conditions, as changing the temperature or the acidity during synthesis results in small, but noticeable changes in the lifetime (**Figure S6.11a**). These parameters critically affect the rate of crystallite formation and their grow, which in turn can lead to differences in particle size, morphology, and lattice regularity, properties that all affect the inherent defect level. If aggregates already form during synthesis, their constituent crystallites are all created under similar conditions and therefore there is little variation between them. Particles that formed in different regions of the synthesis vessel at different times, on the other hand, experience stronger variations in synthesis conditions, resulting in a broader distribution in functionalization and defect level. However, analysing the phasor plots of the individual samples more closely suggests the presence of two distinct species, where the majority of particles show a shorter lifetime, whereas a small fraction exhibits longer decays (**Figure S6.11b**). This distinction is preserved for the different synthesis conditions. We further investigated whether these two species are inherent to the MOF or are induced by the dye. For this, the emission of the unfunctionalized UiO-67 was measured. Even without external fluorophores, the MOF shows luminescence, but requires much higher excitation power (~ 100–1000 ×) at a lower excitation wavelength (405 nm). Again, two populations can be distinguished, mostly via a difference in emission intensity (**Figure S6.11c**). This suggests that two species of MOF crystals are present that differ slightly in their properties. Although FLIM alone cannot determine the exact source of the observed differences, these results highlight the power of FLIM to detect small variations between different synthesis conditions and even within the sample, generally not possible with bulk measurements

6.2.4 Comparison of De novo and Post-synthetic Modification.

As the fluorescence lifetime can be used to measure the defect levels in MOFs, we can use this technique to compare de novo and linker exchange functionalization methods for incorporating modified linkers into the framework. Linker exchange is a form of post-synthetic modification, meaning that the functional groups are incorporated after the scaffold has been formed[40,41]. Therefore, it should show a different propensity for defect formation. Three different samples were functionalized via linker exchange by heating pre-formed UiO-67 crystals to 65 °C for 1 h, 6 h or 24 h in the presence of excess dye-modified linkers (**Figure 6.4**). The total number of incorporated FITC linker is nearly 1% of all linkers for all three exchange times, much higher than with de novo synthesis (**Table S6.1**). An analysis of the intensity images revealed that individual MOF particles often appear as ring-like structures with a darker core at the centre (**Figure 6.4b-d**). This heterogeneity can be attributed to the functionalization mechanism. During linker exchange, linkers labeled with dyes are added to the pre-formed MOFs and have to diffuse to the location in the framework where they exchange. The external surface of the crystals provides many CUS that are readily available for binding where the dye modified linkers do not even have to enter the pores[42]. Similar outside-in mechanisms have been previously observed for linker exchange and diffusion into MOFs[13,43,44]. Internal labelling is more difficult as the large size of the dye functionalized linkers relative to the pore and window diameters of UiO-67 make the diffusion process slow. Hence, a strong concentration gradient is created from the particles' exterior to their centre, especially for short linker exchange times. Together, these factors result in a distribution of the dyes close to the surface, reflected by the ring-like structures in the fluorescence images. For de novo functionalization, these rings are not observed, indicating that there the distribution is homogeneous throughout the crystal (**Figure 6.2 and Figure S6.8**).

The fluorescence lifetime of the post-synthetically modified samples, on the other hand, is barely affected by the high dye concentration (**Figure 6.4** and **Table S6.1**). The 1 h linker exchange MOF has an apparent lifetime of 2.11 ± 0.23 ns, very similar to the 2.28 ± 0.15 ns observed for the de novo sample with the lowest FITC concentration. The fact that the FITC concentration is more than 30 times higher but results in a similar lifetime strongly supports the hypothesis that energy transfer to defects, rather than between different fluorophores, is the main quenching mechanism for FITC. This difference in defect level is due to the fact that the MOF was first synthesized without any modification. As no dyes were present to interfere with the scaffold formation, the MOF exhibits fewer defects. Furthermore, once the framework is already fully formed, it is much harder to introduce defects that extend over nanometers. This makes the samples more resilient and the post-synthetic incorporation of the FITC modified linkers is less disruptive to the MOF backbone and less quenching is observed. Although short exchange times result in long fluorescence lifetimes, longer incubation times result in a shortening of the lifetime down to 1.40 ± 0.15 ns for an exchange time of 24 h (**Figure 6.4** and **Table S6.1**). This suggests that more defects are present after linker exchange at 65 °C for 24 h, created by prolonged incubation at higher temperature in the presence of the dye. Other possible explanations for the shorter lifetime are an increase indirect dye–dye interactions or the redistribution of the fluorophores in the crystals. Both explanations are unlikely, as the amount of fluorophores does not change (**Table S6.1**), whereas a redistribution means the dyes move toward the center of the crystals, where the fluorescence lifetime is expected to increase rather than decrease (**Figure 6.4b**).

6.2.5 Measuring Internal Heterogeneities.

With the de novo experiments, we observed that incorporation of the dye linkers into the scaffold results in the formation of defects, which, in turn, quench the fluorophores. The problem hereby is that the probe (i.e., dye) causes the defect itself rather than measuring the inherent level of defects. To perform experiments where the formation and the sensing of defect were decoupled, we used MOFs that were de novo functionalized with 0.1% or 2% FITC,

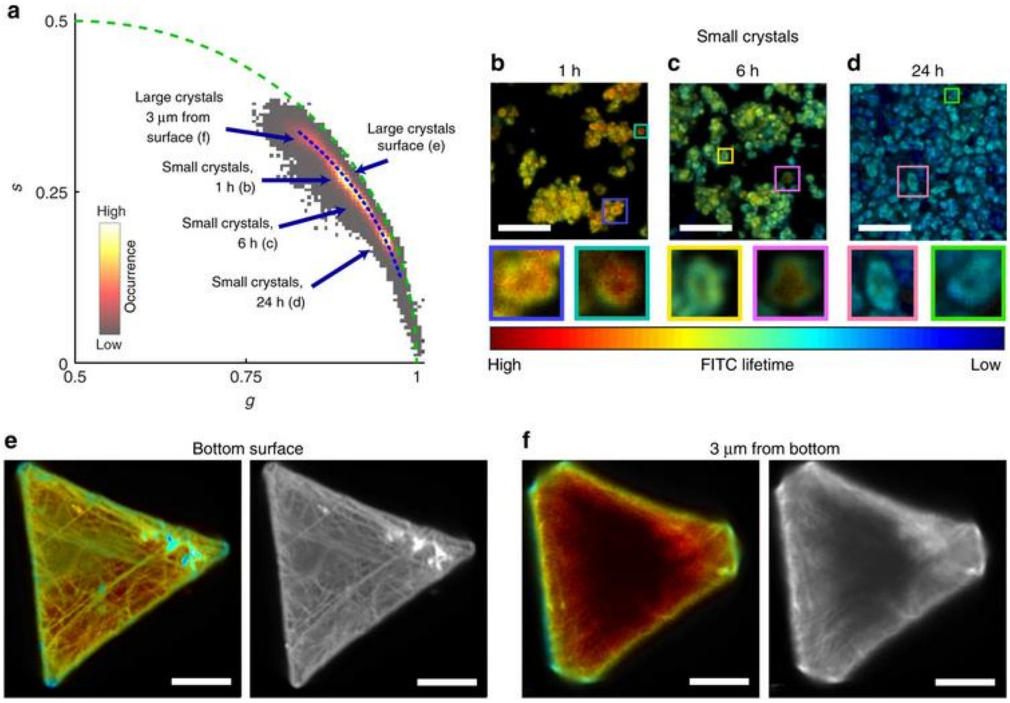

Figure 6.4. Phasor FLIM data of UiO-67 samples functionalized with FITC using linker exchange. **a** Phasor plot of the images shown in **b**-**f**. The blue arrows point at the average phasor positions of the different samples. **b**-**d** FLIM images of small crystal UiO-67 samples subjected to linker exchange with FITC-modified linkers at 65°C for 1 h (**b**), 6 h (**b**), and 24 h (**c**). The inserts below are magnifications of the coulored squares. **e**, **f** FLIM (in color) and fluorescence intensity (in gray scale) images of large crystal UiO-67 samples subjected to linker exchange with FITC-modified linkers for 24 h. **e** An image recorded at the bottom surface of a crystal. **f** an image recorded inside the crystal, 3 µmm up the bottom surface. The color coding of the images is based on the blue dotted line in panel **a** using the color table shown in **b**. The scale bar of all images in 10 µm.

and added RITC via post-synthetic treatment. Here, FITC was used to modulate the amount of defects and RITC was used to measure the defects in the crystal. RITC, this time without the linker, was added after the synthesis and diffused into the pores at 100 °C over 24 h. As both samples were treated identically, any differences in the measured RITC lifetime will be due to the different defect level introduced by the FITC.

The lifetime of the FITC signal is not affected by the incorporation of RITC (**Figure S6.12a**), showing that the post-synthetic treatment did not create additional defects. The signal for RITC, on the other hand, shows a clear correlation between the FITC concentration and the RITC lifetime (**Figure S6.12b**). The lifetime decreases from 3.26 ± 0.14 ns for the 0.1% sample to 2.71 ± 0.15 ns for the 2% sample due to the higher defect concentration. The intensity distribution again shows the ring-like structures for the dye added post-synthetically, whereas the de novo functionalization results in a more even distribution, indicating a homogeneous incorporation throughout the crystals.

6.2.6 Mapping Chemical Diversity within Single Crystals.

As the size of the individual crystallites is not much bigger that the resolution limit of the microscope, the borders between crystal surface and interior become blurred, decreasing the contrast in both fluorescence intensity and lifetime. To better distinguish these two areas, a UiO-67 sample was synthesized using an alternative protocol that yields significantly larger crystals that are ~ 30 µm in diameter (**Figure 6.4e,f and Figure S6.13**)[45]. The MOF was then functionalized with FITC-modified linkers using linker exchange at 100 °C for 24 h. Fluorescence intensity images were taken at different heights, with 500 nm separation between the different planes, showing the three-dimensional intensity distribution of the crystals (**Figure S6.13**). The lifetime was measured at the bottom surface of the crystals (**Figure 6.4e**). In addition, FLIM images were recorded 3 µm above the surface plane (**Figure 6.4f**) to limit the influence of surface bound fluorescence (axial focus size ≈ 1 µm).

Just as with the small crystallites, this functionalization method resulted in high fluorescence intensity on the outer surface and a gradual decrease of the signal toward the crystal interior (**Figure S6.13**). The edges, vertices, and cracks in the surface show even higher fluorescence intensity, indicating that these regions likely have a very high number of undercoordinated sites where the dye-modified linkers can easily bind. The fluorescence lifetime inside the crystals was found to be 2.73 ± 0.19 ns, significantly longer than for any of the other FITC functionalized samples. The value for the surface plane (2.19 ± 0.17 ns), on the other hand, corresponds well to the lifetime of the small crystal MOF modified with linker exchange for 1 h (2.11 ± 0.23 ns), as both have a similar contribution from the surface. This difference in fluorescence lifetime can either be caused by an enhancement and stabilization of the fluorophores inside of the pores, or by quenching of the fluorescence at the external surface. As the fluorescence quantum yield of FITC is already close to unity, a further enhancement is unlikely. Surface induced quenching, on the other hand, is consistent with our observation of defects as quenchers, especially when considering that the edges and cracks show a faster decay compared with the more homogeneous surface areas (**Figure 6.4e,f**).

We further investigated whether a difference between the surface and the interior of the crystal can be observed without adding fluorophores. For this, the pure UiO-67 crystals were imaged directly at the surface and 4 µm into the crystal (**Figure S6.14**). Again, the images show a clear difference between the external surface and bulk of the crystal, in both the fluorescence intensity as well as the lifetime, which is 5.08 ± 0.59 ns at the center and 3.49 ± 0.41 ns on the surface.

6.3 Discussion

In this report, we have demonstrated how to use fluorescence imaging microscopy combined with lifetime analysis to resolve the chemical diversity of a MOF in three dimensions. Specifically, we investigated the functionalization chemistry of UiO-67 and its effect on the structural features of the scaffold. The submicrometer resolution of the microscope allowed us to identify heterogeneity between individual particles in a sample and even within single crystal, e.g., between the surface and the bulk. This difference between the outside and the inside was also observed for the auto-luminescence lifetime of UiO-67 in the absence of additional fluorophores, making the methods also applicable to the study of non-fluorescent functional groups.

Based on the results we can draw several conclusions about UiO-67 and its functionalization chemistry. The FRET experiments showed no direct dye–dye interactions, indicating that de novo functionalization of the framework results in a homogeneous random distribution of the functional groups. Even though no FRET signal was detected, higher dye concentrations still led to a decrease in fluorescence lifetime. This we attribute to the creation of nanoscale defects in the scaffold caused by the incorporation of the dyes. In addition, imaging revealed a high degree of diversity in each sample for both the concentration of the dyes and the level of defects. Individual crystallites in an aggregate, on the other hand, showed a much narrower distribution of these properties. Furthermore, we compared linker exchange incorporation of the fluorophores to de novo functionalization. These experiments showed that the post-synthetic modification results in fewer defects than an incorporation during the initial synthesis. This is even more pronounced for larger crystals that tend to be more resilient to defect formation then small crystallites.

These insights highlight the power and versatility of lifetime imaging in measuring and spatially resolving the chemical diversity in porous materials. The high sensitivity of the fluorescence lifetime to the local environment of the fluorophore makes it an ideal parameter to study a variety of properties, including defects, the presence of different functional groups, or the solvent present in the pores. In addition, one can exploit the auto-luminescence of the framework without the need to modify the material in any way. Thus, we believe that advanced fluorescence microscopy has great potential in the field of material science and that a wider application of the technique will lead to a wealth of new information.

6.4 Experimental Methods

6.4.1 Chemicals and Supplies.

Anhydrous N,N-dimethylformamide (DMF), anhydrous methanol, and glacial acetic acid were obtained from EMD Millipore Chemicals. Ethyl acetate (99.9%, HPLC Plus), ethanol (≥ 99.5%, ACS Reagent), isopropyl alcohol (≥ 99.5%, BioReagent), tetrahydrofuran (THF, ≥ 99.9%, for high performance liquid chromatography (HPLC)), nitric acid (70%, ACS Reagent), sulfuric acid (95.0–98.0%, ACS Reagent), hydrochloric acid (37%, ACS Reagent), sodium bicarbonate (BioReagent), sodium sulfate (≥ 99.0, ACS Reagent), palladium on carbon (Pd/C, 10 wt.% loading), potassium hydroxide (90%), zirconium chloride (≥ 99.5%, trace metal basis), BPDC (97%), dimethyl biphenyl-4,4'dicarboxylate (99%), fluorescein-5(6)-isothiocyanate (≥ 90%), and RITC (mixed isomers) were obtained from Sigma-Aldrich. Ultra-high-purity grade H_2 gas

(Praxair, 99.999% purity) was used for the hydrogenation reaction. All starting materials, reagents, and solvents were used without further purification.

6.4.2 Synthesis of Dye-functionalized Linkers.

The dye-modified linkers were synthesized in a multi-step procedure. The synthetic approach is illustrated in **Figure S6.15**.

Dimethyl 2-nitrobiphenyl-4,4'-dicarboxylate (II)

A solution of 10 g (37 mmol) of dimethyl biphenyl-4,4'-dicarboxylate (I) in 100 ml of concentrated sulfuric acid was cooled to 0 °C and a mixture of 5 mL of 58% nitric acid and 7.5 mL of concentrated sulfuric acid was added dropwise over a period of 30 min under stirring, maintaining the temperature at 0–5 °C. The mixture was then stirred for h at 0–5 °C, diluted with 100 mL of water, and extracted with ethyl acetate. The extract was washed with water and a solution of sodium bicarbonate (7.5%), dried over anhydrous sodium sulfate, and evaporated. The residue was recrystallized from isopropyl alcohol. Yield: 9.9 g (31 mmol, 85%). ^{1}H NMR (400 MHz, $CDCl_3$) , parts per million [p.p.m.]: 3.69 (s, 3 H), 3.94 (s, 3 H), 7.55 (d, 2 H), 7.73 (d, 1 H), 8.03 (d, 2 H), 8.27 (dd, 1 H), 9.97 (d, 1 H).

Dimethyl 2-aminobiphenyl-4,4'-dicarboxylate (III)

A mixture of 9.9 g (31 mmol) of compound II, 100 mL of acetic acid, and 5 g of 10% Pd/C in a high pressure reactor was hydrogenated at room temperature and a hydrogen pressure of 10–50 atm until hydrogen was no longer consumed. The mixture was filtered and acetic acid in the filtrate was removed under vacuum. The crude product was recrystallized from ethanol. Yield: 8.8 g (29 mmol, 94%). ^{1}H NMR (400 MHz, $CDCl_3$), [p.p.m.]: 3.39 (s, 2 H), 3.83 (s, 3 H), 3.88 (s, 3 H), 7.17–8.09 (m, 7 H).

2-Aminobiphenyl-4,4'-dicarboxylic acid (NH_2-H_2BPDC, IV)

A solution of 4.95 g (20 mmol), compound III, in THF (180 mL) and methanol (130 mL) was mixed with a solution of potassium hydroxide (10 g, 178 mmol) in water (200 mL). The reaction mixture was heated to reflux overnight. After all the volatiles were removed under vacuum, it was diluted with 200 mL of water, and acidified with 6 M hydrochloric acid until pH 2. The precipitates were collected, washed with water, and dried in air. The yield was 4.3 g (17 mmol, 85%). ^{1}H NMR (400 MHz, dimethyl sulfoxide (DMSO)), [p.p.m.]: 5.15 (s, 2 H), 7.11 (d, 1 H), 7.21 (dd, 2 H), 7.41 (d, 1 H), 7.57 (m, 2 H), 8.01 (m, 2 H), 12.92 (s, 2 H).

2-Fluorescein-5(6)-isothiocyanate-biphenyl-4,4’-dicarboxylic acid (FITC-H_2BPDC, VI)

A solution of 0.50 g (1.9 mmol) of compound IV in DMF (5 mL) was added to 0.75 g (1.9 mmol) of fluorescein-5(6)-isothiocyanate (FITC, V). The reaction solution was stirred for 24 h at room temperature. The mixture was then diluted with 100 mL of 1 M hydrochloric acid. The precipitates were collected by filtration, washed with water, and dried in air. The crude product was subject to purification by preparation HPLC (stationary phase: C18; mobile phase: methanol/ water/0.1% trifluoroacetic acid (TFA). The eluent was freeze-dried and the orange solid was collected. The yield was 0.71 g (1.1 mmol, 58%). mass spectrometry (MS) (electrospray ionization (ESI-), m/z): [M-H]– calculated for C35H21O9N2S–, 645.0973; found, 645.0956.

2-RhodamineB-isothiocyanate-biphenyl-4,4’-dicarboxylic acid (RITC-H_2BPDC, VIII)

A solution of 0.25 g (0.95 mmol, VII), compound IV, in DMF (5 ml) was added to 0.51 g (0.95 mmol) of RITC (mixed isomers). The reaction solution was stirred for 24 h at room temperature. The mixture was then diluted with 100 mL of 1 M hydrochloric acid. The precipitates were collected by filtration, washed with water, and dried in air. The crude product was subject to purification by preparation HPLC (stationary phase: C18; mobile phase: methanol/water/0.1% TFA). The eluent was frozen-dried and the orange solid was collected. The yield was 0.30 g (0.36 mmol, 38%). MS (ESI-, m/z): [M-H]$^-$ calculated for $C_{45}H_{45}O_7N_4\,S^+$, 785.3003; found, 785.3005.

6.4.3 Synthesis UiO-67

Synthesis of small crystal UiO-67 and de novo functionalization.

The synthesis of pure and functionalized UiO-67 followed a modified synthesis protocol by Katz et al.[23]. BPDC (H_2BPDC) and zirconium(IV) chloride (18.2 mg, 78.1 µmol) were mixed in a 4 mL scintillation vial. In case of de novo functionalized UiO-67, some of the linker was replaced with 2-amino-BPDC modified with either FITC (FITCH_2BPDC) or rhodamineB isothiocyanate (RITC-H_2BPDC) (see **Table S6.3** and **Figure S6.15**). Dimethylformamide (DMF, 2 mL) and hydrochloric acid (0. mL, 37%) were added to this mixture. Next, the mixture was sonicated for 20 min. The vial was then heated at 90 °C for 24 h, yielding functionalized, small crystal UiO-67. The sample was then washed by immersing it in 4 mL of anhydrous DMF for 3 days. During this time, the DMF was replaced five times per day. The washing procedure was subsequently repeated with anhydrous methanol. The methanol exchanged sample was then evacuated at room temperature under vacuum for 24 h.

Synthesis of large crystal UiO-67.

Large UiO-67 single crystals are synthesized following the procedure of Ko et al[45]. A mixture of H_2BPDC (85 mg, 0.35 mmol), zirconium(IV) chloride (82 mg, 0.35 mmol), and benzoic acid (1.28 g, 10.5 mmol) was dissolved in DMF (20 mL) in a 20 mL vial. The vial was capped and heated in an isothermal oven at 120 °C for 2 days to yield octahedral-shaped crystals of ~ 30 µm diameter. The reaction mixture was allowed to cool down to room temperature and then washed with DMF (three times per day for 3 days) and acetone (three times per day for 3 days). The solvent exchanged samples were then evacuated at 120 °C to 30 mTorr.

Linker exchange functionalization. Unfunctionalized UiO-67 (12.5 mg) was placed in a 20 mL scintillation vial and a solution of FITC-H_2BPDC (2.0 mg, 3.1 µmol) in DMF (20 mL) was added. The mixture was heated to 65 °C or 100 °C, and at certain time points (1 h, 6 h, 24 h) a fraction of the suspension was removed. The extracted samples were centrifuged and the solid was subsequently washed with anhydrous DMF (10 times, 4 mL each) and anhydrous methanol (10 times, 2 mL each). The washed samples were then dried under vacuum for 24 h.

6.4.4 Dye Diffusion Incorporation.

The de novo functionalized samples with 0.1 and 2% FITC or RITC were further functionalized by letting free dye (RITC for FITClinker functionalized samples and FITC for RITC-linker functionalized samples) diffuse into the pores. For this, a suspension of the MOFs (0.625 mg mL^{-1}) in DMF with the free dye (0.58 mM) were heated to 100 °C for 24 h. Subsequently, the samples were washed three times each with DMF (1 mL) and methanol (1 mL) and dried at 70 °C in an oven.

6.4.5 Dye Concentration Measurements.

The fraction of dyes in the MOF samples was determined via fluorometry. Hereby, aliquots of the respective samples (0.3–0.6 mg) were digested in a solution of cesium fluoride (137.2 mg, 0.90 mmol) in a mixture of water (1.43 mL) and DMSO (2.57 mL). The samples were sonicated for 10 min and subsequently incubated at room temperature for 2 h, to ensure a full digestion of the framework. The stock solutions (3 mL) were then measured in a polymethylmethacrylat cuvette on a fluorescence system consisting of an 814 Photomultiplier Detector, a LPS220B

Lamp Power Supply, a Pti-MD3020 Motor Drive (all Photon Technology International) and a TC125 Temperature control (Quantum Northwest). For calibrating the conversion factors from the fluorescence signal to the concentration, different concentrations of the raw modified linker molecules were measured under identical conditions and fit with a linear function. Based on the measured dye concentration and the amount of dissolved MOF, the fraction of linkers modified with a dye were calculated in p.p.m.

6.4.6 Nearest-neighbor Calculation.

To estimate how far apart the fluorophores should be from each other, on average, assuming a perfectly random distribution in the MOFs, the nearest-neighbor distance was calculated according to:

Equation 28

$$P(r) = \frac{3}{\mathrm{a}}\left(\frac{r}{a}\right)^{2} e^{-\left(\frac{r}{a}\right)^{3}}, \text{with } a = \left(\frac{3}{4\pi n}\right)$$

Here, P(r) is the probability of finding the nearest fluorophore at distance r. The average dye density n corresponds to the number of dye molecules, *N*, per volume, *V*, and is calculated as:

Equation 29

$$n = \frac{N}{V} = \frac{24\ \cdot c}{\left(26.783\text{Å}\right)^{3}}$$

where *c* is the fraction of linkers modified with a dye. The number 24 represents the number of linkers per unit cell with a size of 26.783 Å. Based on this, we obtain a mean nearest neighbour distance $\langle r\rangle$ of:

Equation 30

$$\langle r\rangle = a\ \cdot\ \Gamma\left(\frac{4}{3}\right)$$

with Γ representing the gamma function.

6.4.7 FLIM Microscopy.

All fluorescence lifetime and intensity images were recorded on a home-built laser scanning confocal microscope equipped with pulsed interleaved excitation and time-correlated single photon counting detection, as described previously[46]. For the measurements, 20–30 µL of a suspension of the MOFs in water (1–10 mg mL^{-1}) were placed in an 8-Well LabTek I slide (VWR). Once the particles sedimented, the surface was imaged using a × 60, 1.27 numerical aperture water-immersion objective (Plan Apo IR × 60 WI, Nikon). The resolution was set to 300 by 300 pixels, resulting in a pixel size of 100 nm (30 µm total image size) or 333 nm (100 µm total image size). To ensure a good signal to noise ratio while, at the same time, minimize the influence of photon pile-up and other high signal artifacts, the count rate was kept between 50 and 500 kHz. To achieve this, the laser power (475 nm and 565 nm for FITC and RITC, respectively) was adjusted in a range of 1–20 nW for dye-functionalized samples, as measured before the objective. For autoluminescence measurements in the absence of fluorophores, a 405 nm laser was used at a power of 10 µW. Under these conditions with a total measurement time of 250–500 s, this resulted in 200–5000 photons per pixel. All analysis was performed using the software framework PAM[47].

Phasor approach to fluorescence lifetime analysis.

As there are many possible contributions to fluorescence quenching in MOFs, a fit-based quantitative analysis is difficult to perform and can even be biased when an inappropriate fit model is used. The phasor approach to FLIM[26,27], on the other hand, uses the Fourier space to visualize the measured fluorescence lifetime in a graphical way. The phasor is calculated via simple equations and is therefore not based by any fit models. This makes it very useful for a qualitative analysis of complex data with many unknown processes and contributions, as is the case for the presented data.

For each pixel, the Fourier coordinates, *g* and *s*, are calculated using **Equation 31** and **Equation 32:**

Equation 31 $$g_{i,j}(\omega) = \int_0^{2\pi} I_{i,j}(t) \cdot \cos(\omega t - \varphi_{\mathrm{Inst}})\mathrm{d}t \Bigg/ \left(M_{\mathrm{Inst}} \cdot \int_0^{2\pi} I_{i,j}(t)\mathrm{d}t \right)$$

Equation 32 $$s_{i,j}(\omega) = \int_0^{2\pi} I_{i,j}(t) \cdot \sin(\omega t - \varphi_{\mathrm{Inst}})\mathrm{d}t \Bigg/ \left(M_{\mathrm{Inst}} \cdot \int_0^{2\pi} I_{i,j}(t)\mathrm{d}t \right)$$

Here, the indices *i* and *j* define the pixel coordinates in the image and I(t) gives the photon counts of the time bin *t*. The frequency *ω* corresponds to 2π/*T*, with *T* being the full range of the photon arrival time histogram (here 40 ns). The correction terms, φ_{Instt} and M_{Inst}, account for the instrument response function (IRF) and can be calculated by measuring a reference sample with known lifetime (here Atto488 4.1 ns, Atto-Tec).

There are three main rules of the phasor space that simplify interpretation of lifetime data:

1. A convolution of a decay with a different signal (e.g., the IRF) results in a change of the coordinate system. This makes it possible to use ϕ_{Inst} and M_{Inst} to correct for the IRF without complicated convolutions.
2. All purely mono-exponential decays lie on the semi-circle of radius 0.5 cantered at (0.5,0). The lifetimes decrease clockwise from infinity at the origin to zero at the point (1,0).
3. A mixture of different lifetimes (i.e., bi- or multi-exponential decays) results in a phasor that is the weighted vector addition of the phasors of the base components. This results in the fact that any mixture of two phasors lie on a straight line connecting the original phasors. For more components, the possible space of the mixture is a polygon with the phasors of the original components at the vertices. As a consequence, all multi-exponential decays must fall inside the semi-circle.

From rules 2 and 3, it follows that curved trajectories are caused by a gradual change in the components' lifetimes, rather than a change in the relative contribution of species with constant lifetimes.

Quantitative lifetime analysis.

For each phasor position, two lifetime values can be calculated based on the phase (τ_φ) and the modulation (τ_M):

Equation 33

$$\tau_\varphi(\omega) = \frac{1}{\omega} \cdot \frac{s}{g}$$

Equation 34

$$\tau_M(\omega) = \frac{1}{\omega} \sqrt{\frac{1}{g^2 + s^2} - 1}$$

For purely mono-exponential decays, these two lifetimes are identical and correspond to the real lifetime. In the case of multi-exponential behavior, the phase and modulation lifetimes are different and do not correspond directly and unambiguously to the pure components.

To get a single apparent lifetime for each sample, first the mean τ_φ and τ_M are calculated from all pixels above a threshold of 300 photons. The arithmetic average of the mean phase and modulation lifetimes is then used to calculate an apparent lifetime. The uncertainty corresponds to the SD of the pixel distribution.

6.4.8 Additional Characterization

Powder X-ray diffraction.

PXRD measurements were conducted on a Bruker D8Venture diffractometer with a Mo-target (0.71073 Å) and Cu-target (1.54184 Å) microfocus X-ray generators. The θ–θ geometry device was equipped with a PHOTON-100 CMOS detector, measuring the samples between 2° and 50° 2θ, with a step size of 0.02° of 2θ.

Nitrogen adsorption/desorption isotherms

Gas adsorption analysis was performed on a Quantachrome Quadrasorb-SI automatic volumetric gas adsorption analyser. A liquid nitrogen bath (77 K) and ultrahigh purity grade N_2 (99.999%, Praxair) were used for the measurements. Samples were prepared and measured after being evacuated at 100 °C for 12 h. In order to calculate pore size and volume, calculations were performed using a slit-pore based N_2 on carbon QSDFT equilibrium model. To calculate the Brunauer–Emmett–Teller surface area a partial pressure range between 0.05 and 0.15 p/p_0 was used.

Scanning electron microscopy

A Zeiss NVision40 microscope was used to record SEM images. Secondary electron images were acquired using the In Lense detector at a low acceleration voltage of 5 kV. To avoid charging effects, a thin carbon film coating was applied on the samples before the measurements. The carbon deposition was performed using a BAL-TEC coating system.

References

1 Slater, A. G. & Cooper, A. I. MOFs: function-led design of new porous materials. *Science* **348**, doi:10.1126/science.aaa8075 (2015).

2 Horike, S., Shimomura, S. & Kitagawa, S. Soft porous crystals. *Nat. Chem.* **1**, doi:10.1038/nchem.444 (2009).

3 Thomas, A. Functional materials: from hard to soft porous frameworks. *Angew. Chem. Int. Ed.* **49**, doi:10.1002/anie.201000167 (2010).

4 Cölfen, H. & Antonietti, M. Mesocrystals: inorganic superstructures made by highly parallel crystallization and controlled alignment. *Angew. Chem. Int. Ed.* **44**, doi:10.1002/anie.200500496 (2005).

5 Furukawa, H., Cordova, K. E., O'Keeffe, M. & Yaghi, O. M. The Chemistry and Applications of Metal-Organic Frameworks. *Science* **341**, 1230444-1230444, doi:10.1126/science.1230444 (2013).

6 Bennett, T. D., Cheetham, A. K., Fuchs, A. H. & Coudert, F. X. Interplay between defects, disorder and flexibility in metal-organic frameworks. *Nat. Chem.* **9**, doi:10.1038/nchem.2691 (2016).

7 Osborn Popp, T. M. & Yaghi, O. M. Sequence-dependent materials. *Acc. Chem. Res.* **50**, doi:10.1021/acs.accounts.6b00529 (2017).

8 Deng, H. Multiple functional groups of varying ratios in metal-organic frameworks. *Science* **327**, doi:10.1126/science.1181761 (2010).

9 Furukawa, H., Müller, U. & Yaghi, O. M. “Heterogeneity within Order” in Metal-Organic Frameworks. *Angew. Chem. Int. Ed.* **54**, 3417-3430, doi:10.1002/anie.201410252 (2015).

10 Kong, X. Mapping of functional groups in metal-organic frameworks. *Science* **341**, doi:10.1126/science.1238339 (2013).

11 Krajnc, A., Kos, T., Zabukovec Logar, N. & Mali, G. A simple NMR-based method for studying the spatial distribution of linkers within mixed-linker metal-organic frameworks. *Angew. Chem. Int. Ed.* **54**, doi:10.1002/anie.201504426 (2015).

12 Jayachandrababu, K. C. Structure elucidation of mixed-lnker zeolitic imidazolate frameworks by solid-state 1 H CRAMPS NMR spectroscopy and computational modeling. *J. Am. Chem. Soc.* **138**, doi:10.1021/jacs.6b02754 (2016).

13 Jayachandrababu, K. C., Sholl, D. S. & Nair, S. Structural and mechanistic differences in mixed-linker zeolitic imidazolate framework synthesis by solvent assisted linker exchange and de novo routes. *J. Am. Chem. Soc.* **139**, doi:10.1021/jacs.7b01660 (2017).

14 Trickett, C. A. Definitive molecular level characterization of defects in UiO-66 crystals. *Angew. Chem. Int. Ed.* **54**, doi:10.1002/anie.201505461 (2015).

15 Zhu, Y. Unravelling surface and interfacial structures of a metal–organic framework by transmission electron microscopy. *Nat. Mater.* **16**, doi:10.1038/nmat4852 (2017).

16 Ameloot, R. Three-dimensional visualization of defects formed during the synthesis of metal-organic frameworks: a fluorescence microscopy study. *Angew. Chem. Int. Ed.* **52**, doi:10.1002/anie.201205627 (2013).

17 Schrimpf, W., Ossato, G., Hirschle, P., Wuttke, S. & Lamb, D. C. Investigation of the Co-Dependence of Morphology and Fluorescence Lifetime in a Metal-Organic Framework. *Small* **12**, 3651-3657, doi:10.1002/smll.201600619 (2016).

18 Ramachandra, S. Förster resonance energy transfer in quantum dot-dye-loaded zeolite L nanoassemblies. *Small* **7**, doi:10.1002/smll.201100010 (2011).

19 Eum, K. Highly tunable molecular sieving and adsorption properties of mixed-linker zeolitic imidazolate frameworks. *J. Am. Chem. Soc.* **137**, doi:10.1021/jacs.5b00803 (2015).

20 Cavka, J. H. A new zirconium inorganic building brick forming metal organic frameworks with exceptional stability. *J. Am. Chem. Soc.* **130**, doi:10.1021/ja8057953 (2008).

21 Deria, P. Beyond post-synthesis modification: evolution of metal–organic frameworks via building block replacement. *Chem. Soc. Rev.* **43**, doi:10.1039/C4CS00067F (2014).

22 Cohen, S. M. Postsynthetic methods for the functionalization of metal–organic frameworks. *Chem. Rev.* **112**, doi:10.1021/cr200179u (2012).

23 Katz, M. J. *et al.* A facile synthesis of UiO-66, UiO-67 and their derivatives. *Chem Commun (Camb)* **49**, 9449-9451, doi:10.1039/c3cc46105j (2013).

24 Busby, M., Kerschbaumer, H., Calzaferri, G. & Cola, L. Orthogonally bifunctional fluorescent zeolite-L microcrystals. *Adv. Mater.* **20**, doi:10.1002/adma.200702354 (2008).

25 Cucinotta, F. Energy transfer at the zeolite L boundaries: towards photo- and electroresponsive materials. *ChemPlusChem* **79**, doi:10.1002/cplu.201300272 (2014).

26 Digman, M. A., Caiolfa, V. R., Zamai, M. & Gratton, E. The phasor approach to fluorescence lifetime imaging analysis. *Biophys. J.* **94**, doi:10.1529/biophysj.107.120154 (2008).

27 Redford, G. I. & Clegg, R. M. Polar plot representation for frequency-domain analysis of fluorescence lifetimes. *J. Fluoresc.* **15**, doi:10.1007/s10895-005-2990-8 (2005).

28 Maza, W. A., Padilla, R. & Morris, A. J. Concentration dependent dimensionality of resonance energy transfer in a postsynthetically doped morphologically homologous analogue of UiO-67 MOF with a rRuthenium(II) polypyridyl complex. *J. Am. Chem. Soc.* **137**, doi:10.1021/jacs.5b03071 (2015).

29 Maza, W. A. & Morris, A. J. Photophysical characterization of a Ruthenium(II) Tris(2,2'-bipyridine)-doped zirconium UiO-67 metal–organic framework. *J. Phys. Chem. C.* **118**, doi:10.1021/jp501140r (2014).

30 Sholl, D. S. & Lively, R. P. Defects in metal–organic frameworks: challenge or opportunity? *J. Phys. Chem. Lett.* **6**, doi:10.1021/acs.jpclett.5b01135 (2015).

31 Gutov, O. V., Hevia, M. G., Escudero-Adán, E. C. & Shafir, A. Metal–organic framework (MOF) defects under control: insights into the missing linker sites and their implication in the reactivity of zirconium-based frameworks. *Inorg. Chem.* **54**, doi:10.1021/acs.inorgchem.5b01053 (2015).

32 Fang, Z., Bueken, B., De Vos, D. E. & Fischer, R. A. Defect-engineered metal-organic frameworks. *Angew. Chem. Int. Ed.* **54**, doi:10.1002/anie.201411540 (2015).

33 Cliffe, M. J. Correlated defect nanoregions in a metal–organic framework. *Nat. Commun.* **5**, doi:10.1038/ncomms5176 (2014).

34 Taddei, M. When defects turn into virtues: the curious case of zirconium-based metal-organic frameworks. *Coord. Chem. Rev.* **343**, doi:10.1016/j.ccr.2017.04.010 (2017).

35 Wu, H. Unusual and highly tunable missing-linker defects in zirconium metal–organic framework UiO-66 and their important effects on gas adsorption. *J. Am. Chem. Soc.* **135**, doi:10.1021/ja404514r (2013).

36 Valenzano, L. Disclosing the complex structure of UiO-66 metal organic framework: a synergic combination of experiment and theory. *Chem. Mater.* **23**, doi:10.1021/cm1022882 (2011).

37 Shearer, G. C. In situ infrared spectroscopic and gravimetric characterisation of the solvent removal and dehydroxylation of the metal organic frameworks UiO-66 and UiO-67. *Top. Catal.* **56**, doi:10.1007/s11244-013-0027-0 (2013).

38 Schrimpf, W., Ossato, G., Hirschle, P., Wuttke, S. & Lamb, D. C. Investigation of the co-dependence of morphology and fluorescence lifetime in a metal-organic framework. *Small* **12**, doi:10.1002/smll.201600619 (2016).

39 Wuttke, S. *et al.* Turn-on fluorescence triggered by selective internal dye replacement in MOFs. *Chem. Commun.* **50**, 3599, doi:10.1039/c3cc46591h (2014).

40 Deria, P. *et al.* Beyond post-synthesis modification: evolution of metal–organic frameworks via building block replacement. *Chem. Soc. Rev.* **43**, 5896-5912, doi:10.1039/c4cs00067f (2014).

41 Kim, M., Cahill, J. F., Su, Y., Prather, K. A. & Cohen, S. M. Postsynthetic ligand exchange as a route to functionalization of 'inert' metal–organic frameworks. *Chem. Sci.* **3**, doi:10.1039/C1SC00394A (2012).

42 Röder, R. Multifunctional nanoparticles by coordinative self-assembly of His-tagged units with metal–organic frameworks. *J. Am. Chem. Soc.* **139**, doi:10.1021/jacs.6b11934 (2017).

43 Liu, C. Establishing porosity gradients within metal–organic frameworks using partial postsynthetic ligand exchange. *J. Am. Chem. Soc.* **138**, doi:10.1021/jacs.6b07445 (2016).

44 Wang, C. & Lin, W. Diffusion-controlled luminescence quenching in metal–organic frameworks. *J. Am. Chem. Soc.* **133**, doi:10.1021/ja111197d (2011).

45 Ko, N. A significant enhancement of water vapour uptake at low pressure by amine-functionalization of UiO-67. *Dalton Trans.* **44**, doi:10.1039/C4DT02582B (2015).

46 Hendrix, J., Schrimpf, W., Höller, M. & Lamb, D. C. Pulsed interleaved excitation fluctuation imaging. *Biophys. J.* **105**, doi:10.1016/j.bpj.2013.05.059 (2013).

47 Schrimpf, W., Barth, A., Hendrix, J. & Lamb, D. C. PAM: A framework for integrated analysis of imaging, single-molecule, and ensemble fluorescence data. Biophys. J. 114, 1518–1528 (2018).

6.5 Supporting Information

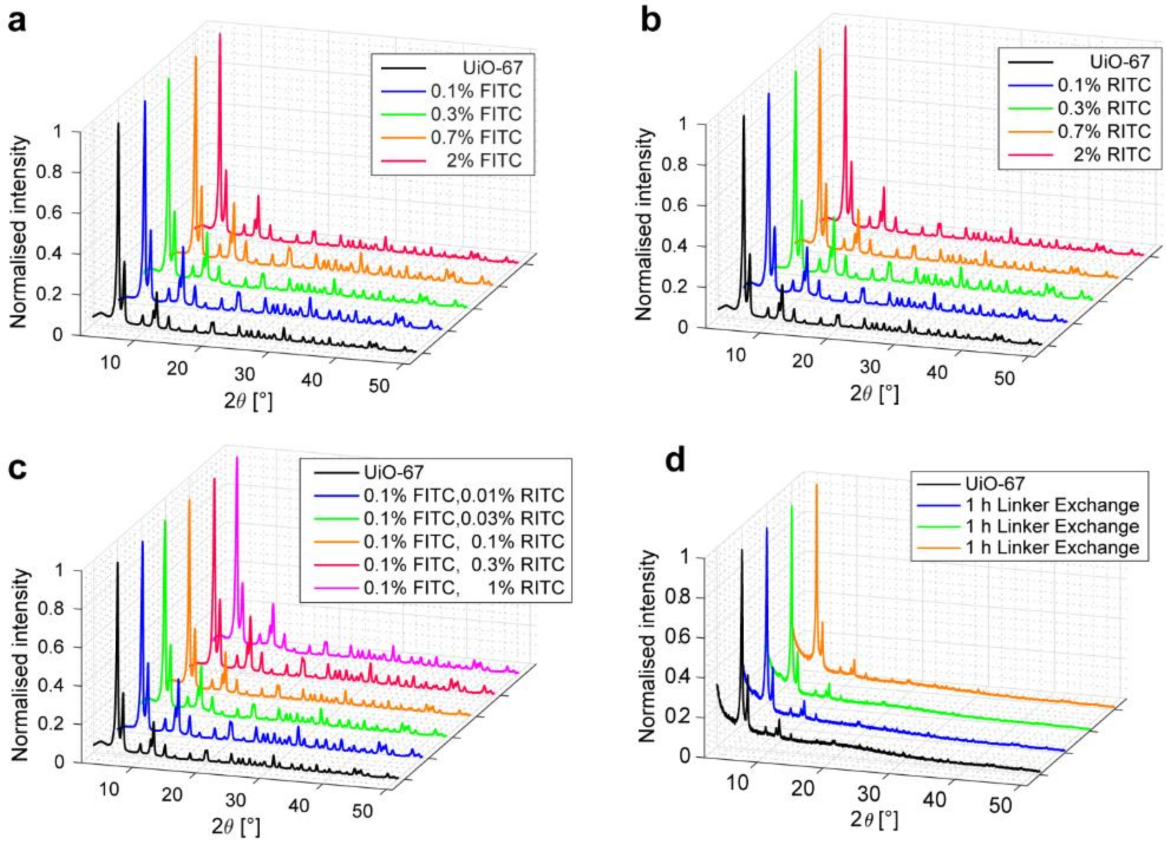

Figure S6.5. XRD patterns of small crystal UiO-67 samples with varying amounts of dye-modified linkers. **a**) *De novo* functionalization with FITC modified linker. **b**) *De novo* functionalization with RITC modified linker. **c**) De novo functionalization with both FITC and RITC modified linkers. **d**) Samples functionalized with FITC modified linker using linker exchange.

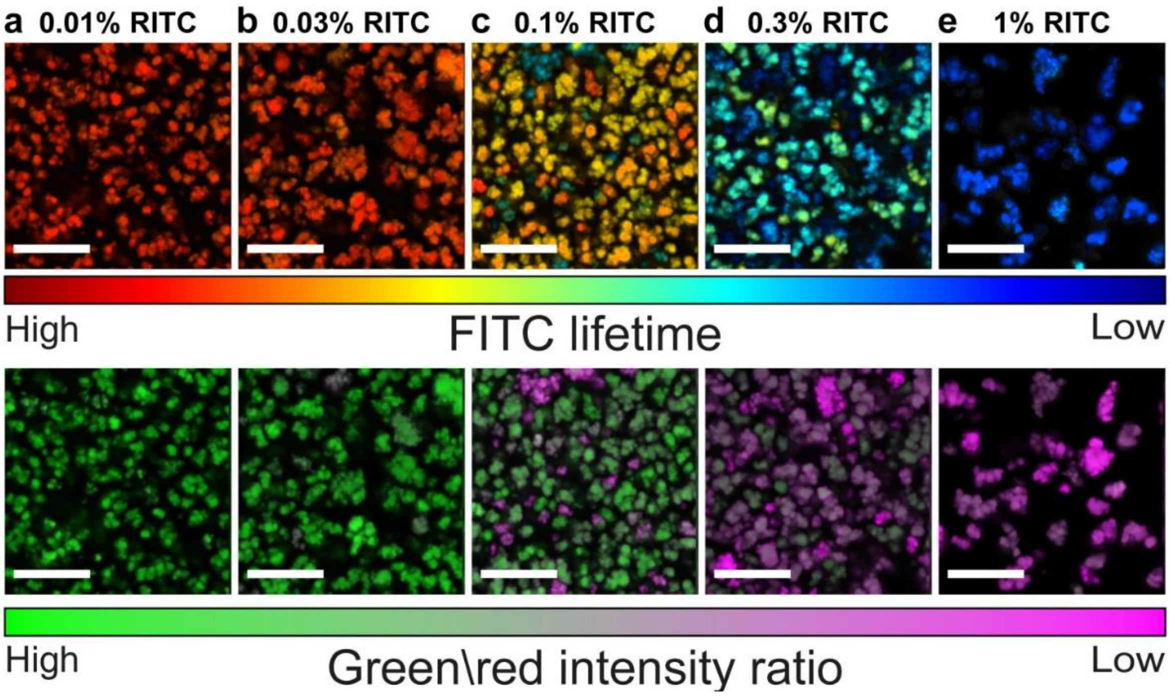

Figure S6.7. UiO-67 samples with both FITC and RITC labelled linkers. The input FITC fraction for all samples is 0.1% while the RITC content increases from left to right starting at 0.01% (**a**),0.03% (**b**), 0.1% (**c**), 0.3% (**d**), and 1% (**e**). The upper images are identical to the ones shown in **Figure 6.2**. The lower images display the intensity ratio between the green (FTIC) and the red (RITC) channels after excitation with a 475 nm laser. To optimize the contrast, the green signal was increased by a factor of 5 compared to the red channel.

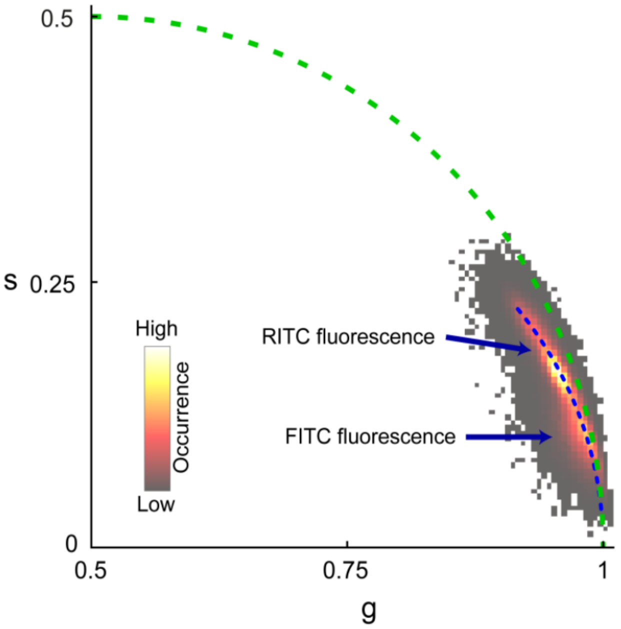

Figure S6.6 A phasor histogram of the FITC and RITC (both after 475 nm and 564 nm excitation) lifetimes of the 0.1% FITC and 1% RITC de novo modified UiO-67 sample shown in **Figure 6.1 h-k**

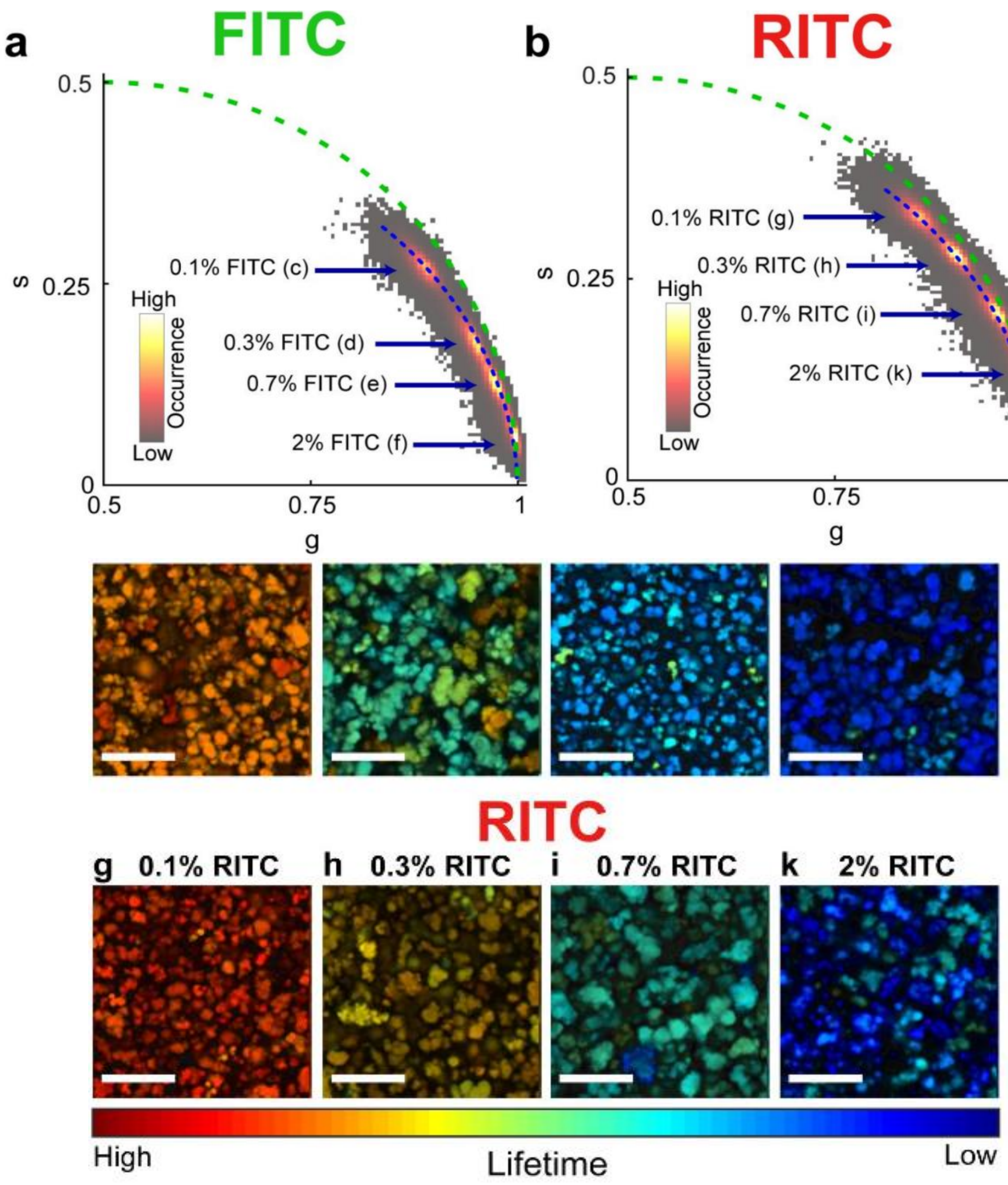

Figure S6.8. Phasor analysis of de novo UiO-67 samples with either FITC or RITC labelled linkers. **a**-**b**) Phasor plots of the FITC (**a**) and RITC (**b**) fluorescence of the full images shown in **c**-**k**. The blue arrows indicate the average phasor positions of the different samples. **c**-**f**) Lifetime images of FITC fluorescence of UiO-67 samples with 0.1% (**c**), 0.3% (**d**), 0.7% (**e**), 2% (**f**) input FITC linker fraction. **c**-**f**) Lifetime images of RITC fluorescence of UiO-67 samples with 0.1% (**c**), 0.3% (**d**), 0.7% (**e**), and 2% (**f**) input RITC linker fraction. The scale bar for all images is 10 µm.

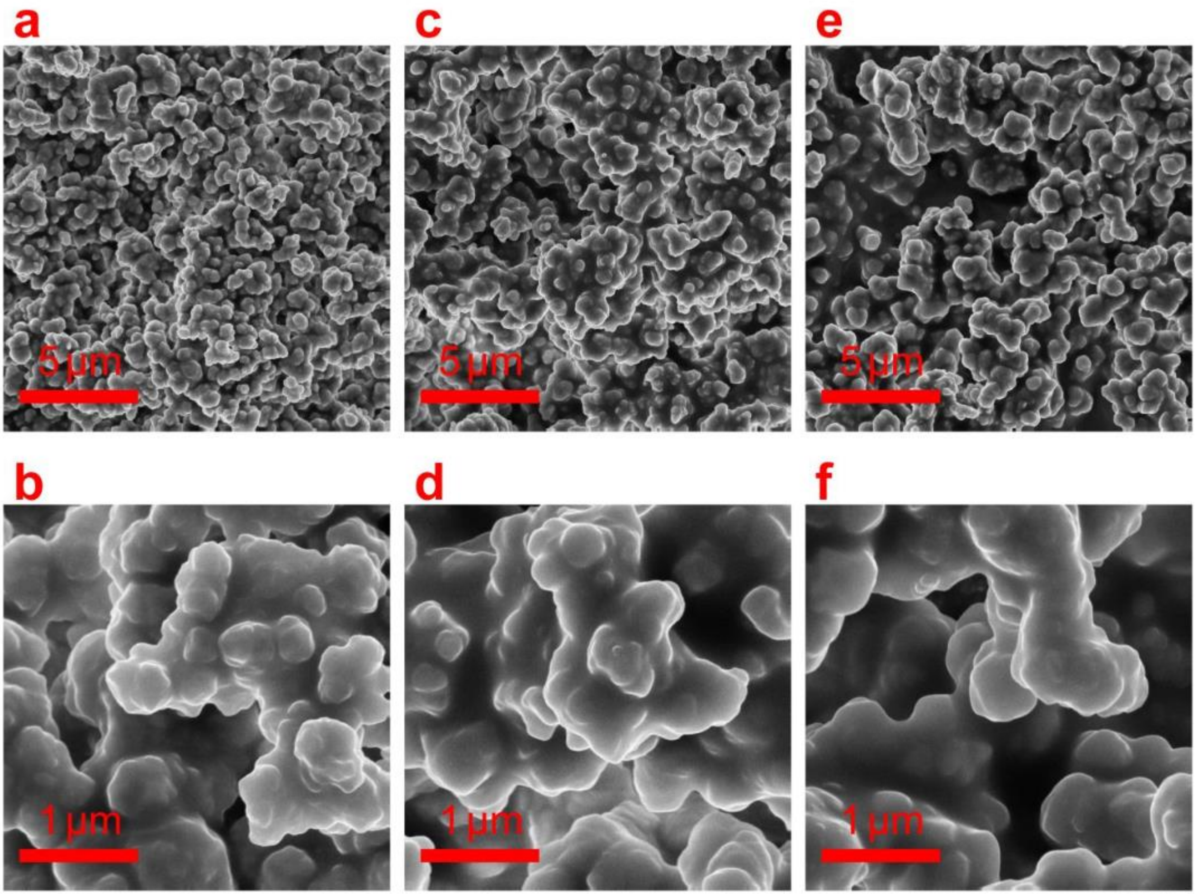

Figure S6.9. SEM images of small crystal UiO-67 samples with 0% (a and b), 0.1% (**c** and **d**) and 2% FTIC modified linker (**e** and **f**) used during synthesis.

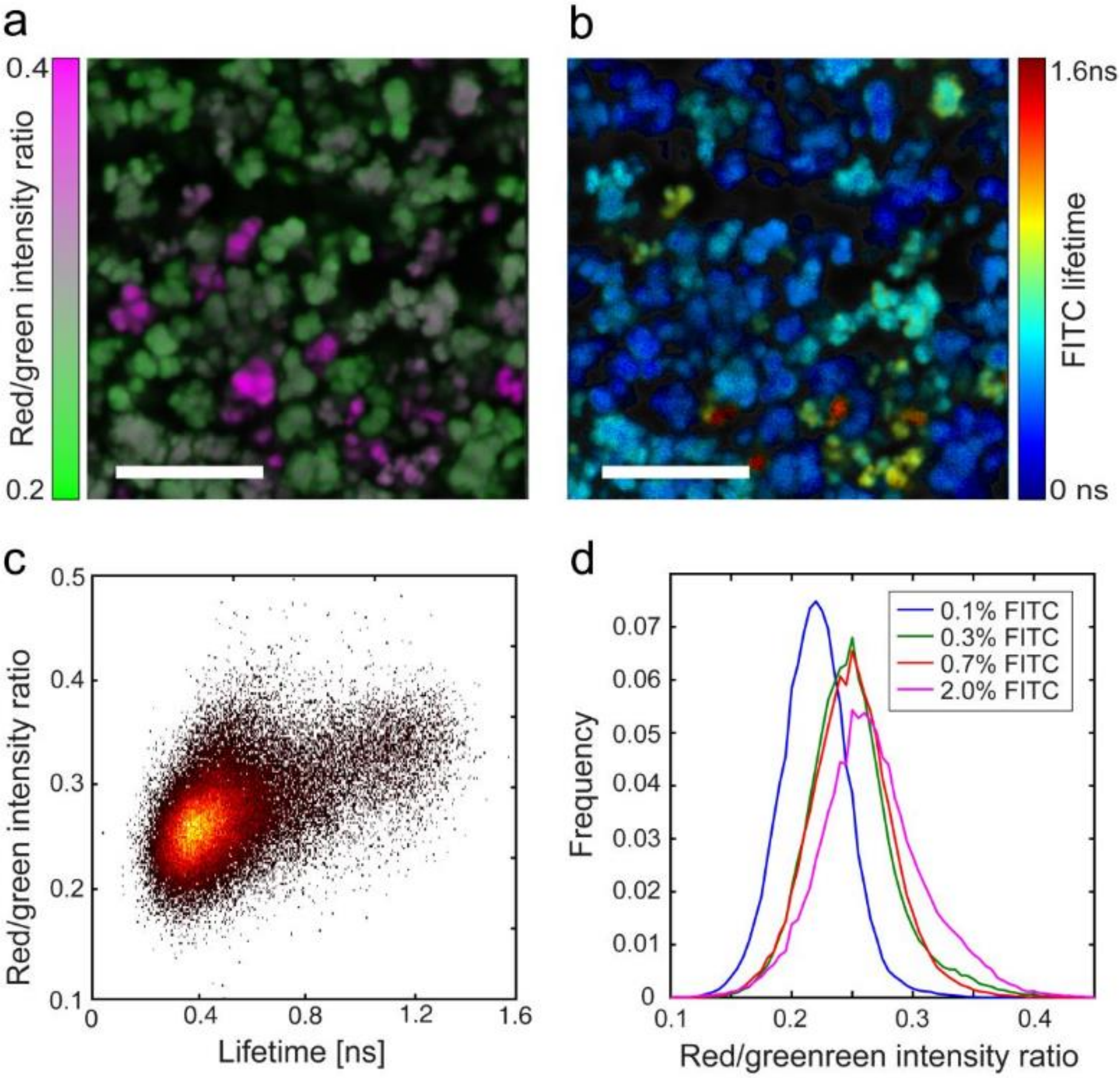

Figure S6.10. Spectral shift of UiO-67 samples *de novo* functionalized with FITC modified linkers. **a**) An intensity ratio image showing the spectral shift of FITC fluorescence for individual pixels with 2% input FITC fraction. The spectrum is indicated by the ratio between the red (570-620 nm) and the green (500-540 nm) detection channels. **b**) Fluorescence lifetime image of the same region as shown in a. **c**) Pixelwise 2D histogram of the red/green intensity ratio vs. the lifetime of *de novo* functionalized sample with 2% input FITC fraction, showing a correlation between the spectral shift and the fluorescence lifetime. **d**) Distribution of red/green intensity ratio of individual pixels for different amounts of input FITC fraction. Based on the free FITC spectrum, the difference between the 0.1% and the 2% FITC samples correspond to a red-shift of 3-6 nm. The scale bar in the images is 10 μm.

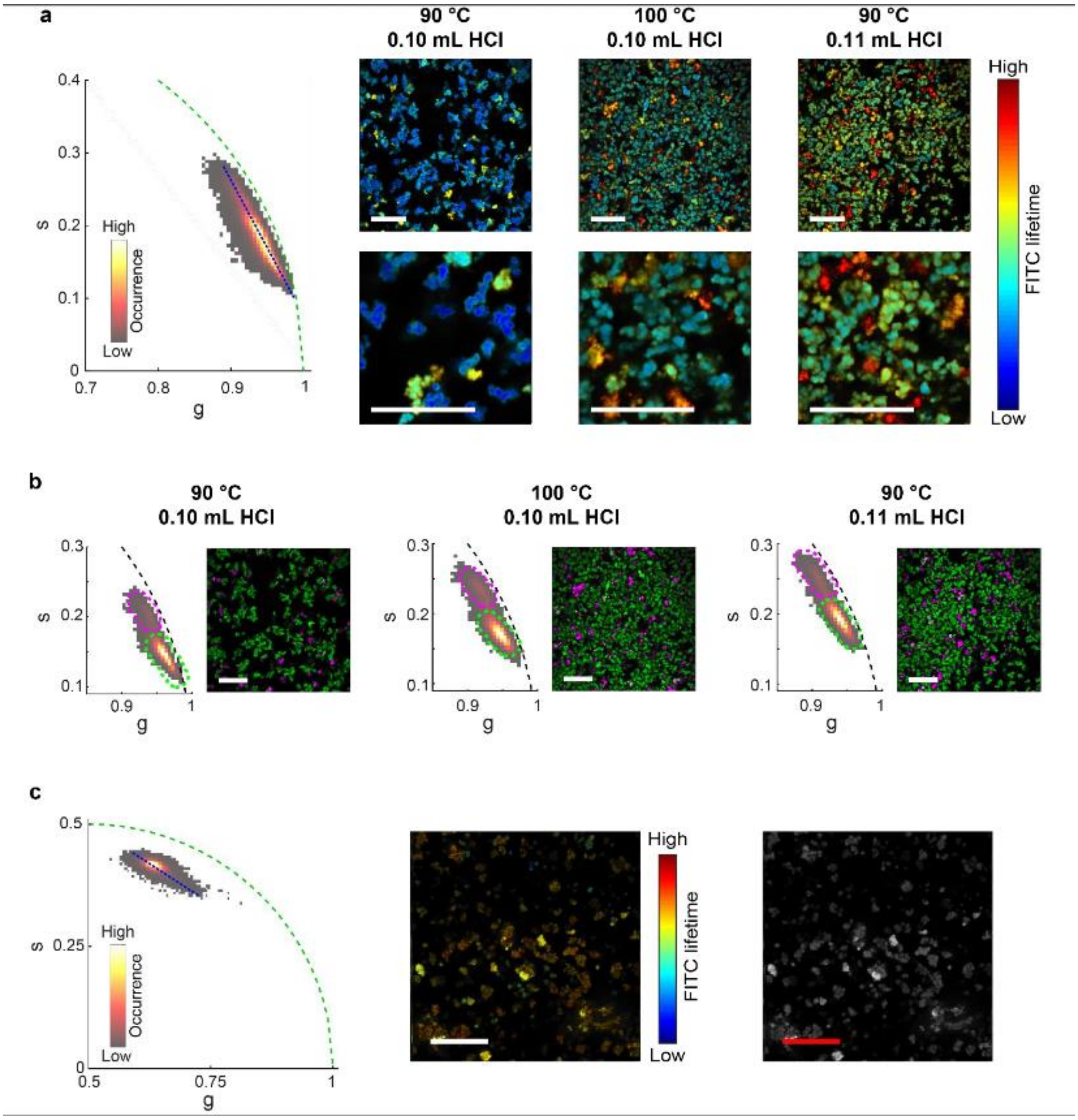

Figure S6.11. *De novo* samples at different conditions. **a**) The phasor plot and images of FITC fluorescence of 0.7% FITC *de novo* samples synthesized with standard conditions (left), at elevated temperature (middle), and higher HCl concentration (right). The blue dotted line is used to colour-code the fluorescence lifetime in the images. **b**) Separate phasor plots and FLIM images of the samples shown in a. The green and magenta ellipses indicate the two distinct particle populations and are used to colour-code the corresponding particles in the images. **c**) The phasor plot (left), FLIM image (center) and intensity image (right) of UiO-67 auto-luminescence of a sample without added fluorophores. The blue dotted line is used to colour-code the fluorescence lifetime in the FLIM image.

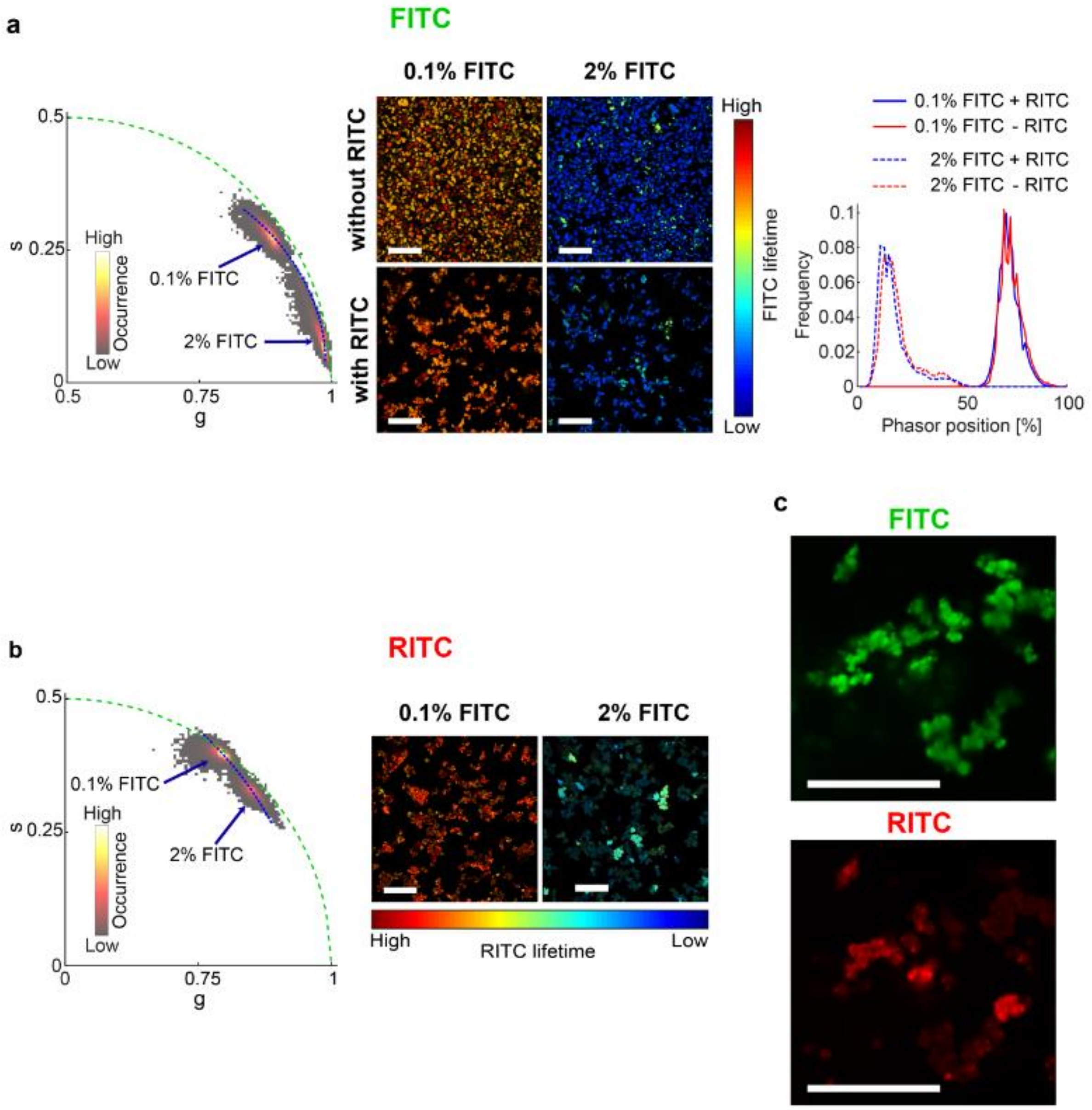

Figure S6.12. Phasor analysis of UiO-67 samples functionalized *de novo* with FITC labelled linkers and post-synthetically with RITC. **a**) Phasor histogram (left), FLIM images (centre) and phasor distribution (right) of the FITC fluorescence of the 0.1% (left images and solid lines) and 2% (right images, dotted lines) FITC *de novo* samples before (upper images, bred lines) and after (lower images, blue lines) treatment with RITC. The colour-code of the images and the phasor distribution in the line plot represent the position along the blue dotted line in the phasor histogram. **b**) Phasor plot and FLIM images of the RITC fluorescence of the 0.1% (left image) and 2% (right image) FITC *de novo* samples after treatment with RITC. **c**) Intensity images of the FITC (left, green) and RITC (right, red) fluorescence for the same region. All scale bars are 20 µm.

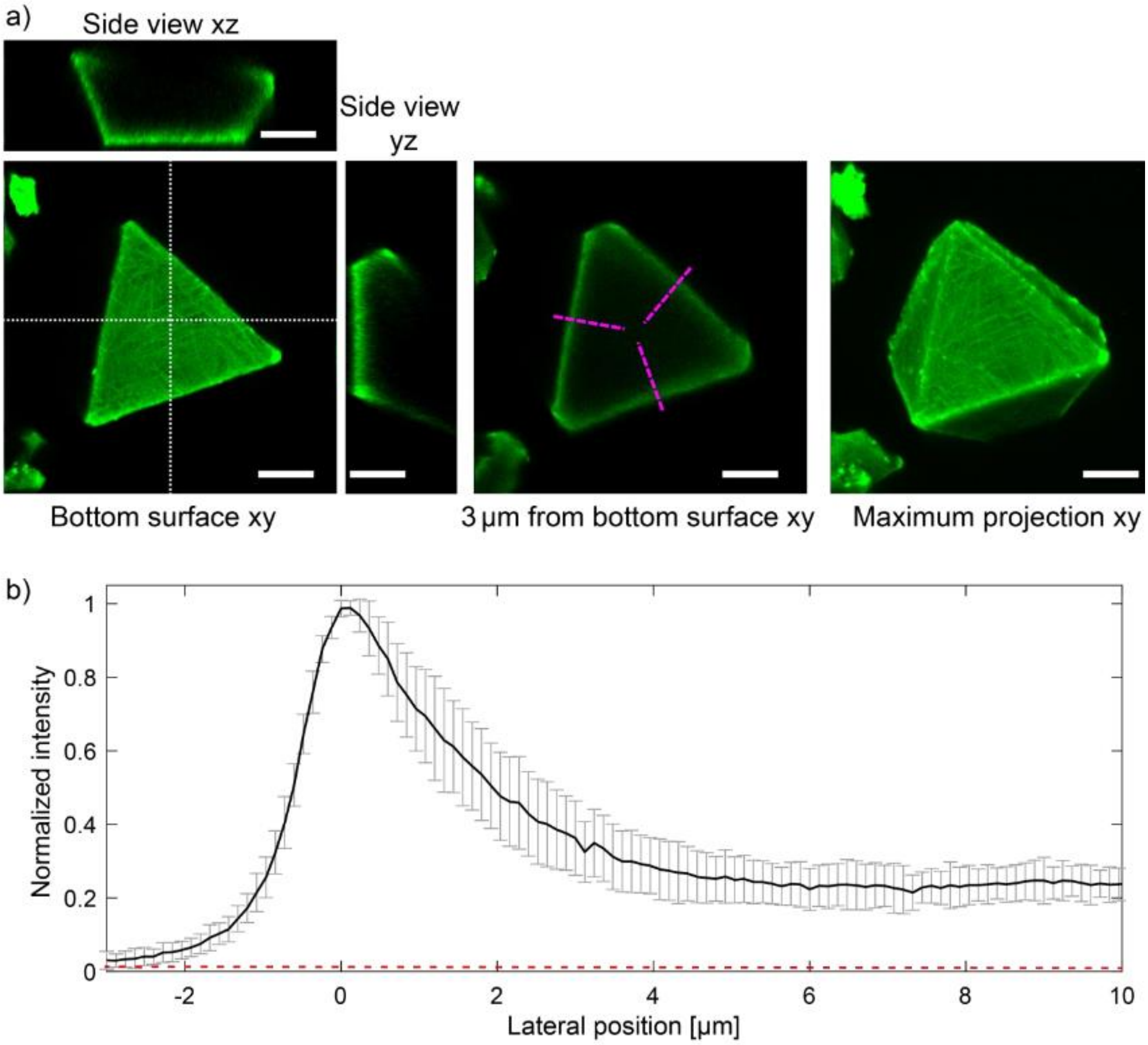

Figure S6.13. Fluorescence intensity distribution in a large UiO-67 crystal functionalized with linker exchange. **a**) Z-Scan fluorescence intensity images showing a xy slice at the bottom of the crystal (left), 3 µm up from the bottom (centre) and a xy maximum projection image for visualizing the octahedral 3D structure. The side views show the horizontal (xz) and vertical (yz) slices through the centre of the xy images highlighted by the white dotted lines. The scale bar is 10 µm. **b**) Intensity profile perpendicular to the three surfaces of the xy plane 3 µm from the bottom surface, indicated by the three dotted magenta lines in panel a. The black line shows the average and the grey error bars indicate the standard deviation of the three sides. The red dotted line indicates the intensity expected from the auto-luminescence and the background (measured outside of the crystals) and corresponds to approximately 1% of the peak intensity.

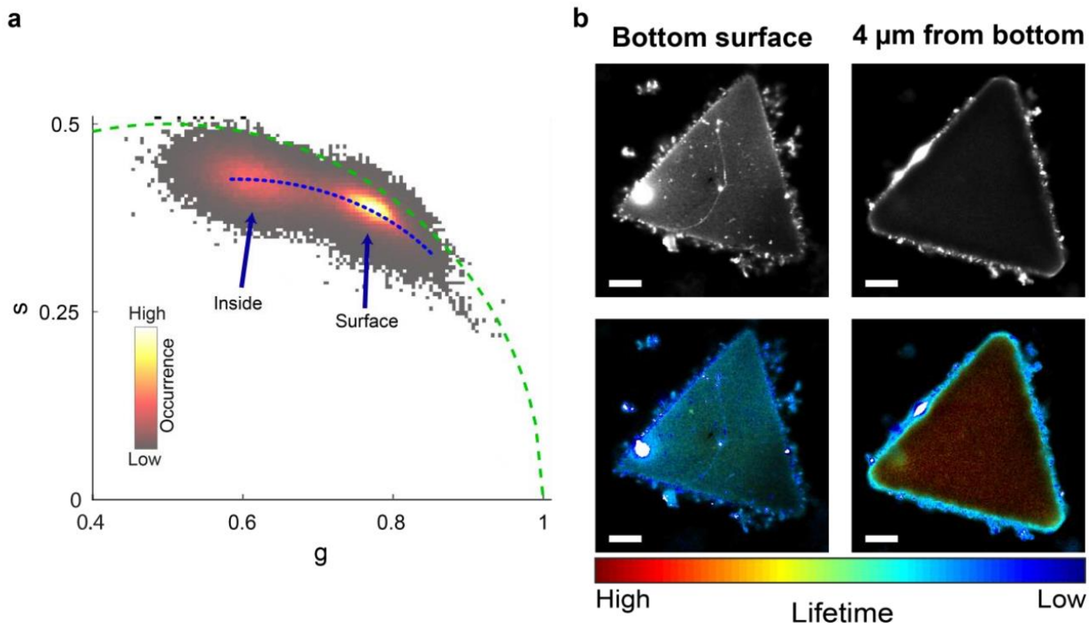

Figure S6.14. Auto-luminescence of large UiO-67 crystal. **a**) The phasor plot of the auto-luminescence of a large UiO-67 crystal at the bottom plane (surface) and 4 µm from the bottom (inside). **b**) Intensity (upper images) and FLIM (lower images) images of the auto-luminescence at the bottom surface (left images) and 4 µm from the bottom (right images). The FLIM images were color-coded according to the phasor position along the blue dotted line in **a**) using the plotted color-table. The scale bar is 10 µm.

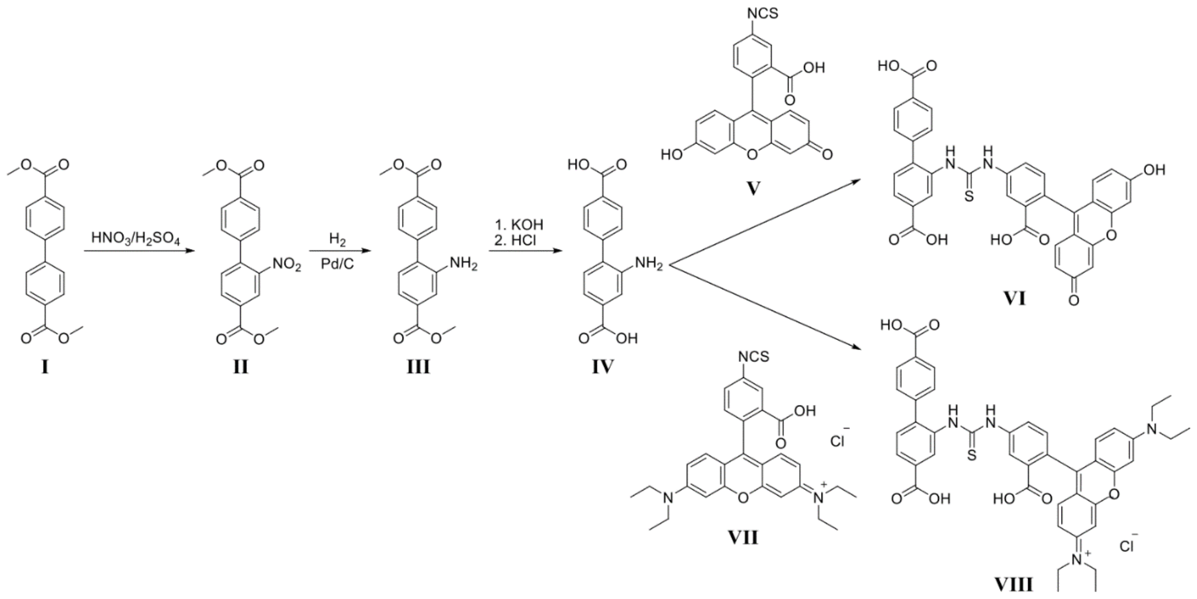

Figure S6.15. A schematic of the synthetic approach used to generate dye-functionalized linkers. For details, see the section 6.4.2.

Table S6.1. Dye incorporation and fluorescence lifetimes in FITC and RITC functionalized UiO-67 samples.

Sample	**FITC**				**RITC**			
	Conc. [ppm]	Incorp. Efficiency	Nearest Neighbour Distance [Å]	τ[ns]	Conc. [ppm]	Incorp. Efficiency	Nearest Neighbour Distance [Å]	τ[ns]
***de novo* functionalization**								
0.1% FITC	256	25.6	81.0	2.28±0.15	-	-	-	-
0.3% FITC	808	26.9	55.2	1.57±0.20	-	-	-	-
0.7% FITC	1624	23.2	43.8	1.09±0.17	-	-	-	-
2% FITC	3511	17.6	33.8	0.55±0.32	-	-	-	-
0.1% RITC	-	-	-	-	38	3.8	153	2.67±0.16
0.3% RITC	-	-	-	-	89	3.0	115	2.17±0.14
0.7% RITC	-	-	-	-	220	3.1	85.2	1.54±0.16
2% RITC	-	-	-	-	410	2.1	69.2	0.95±0.31
0.1% FITC, 0.01% RITC	212	21.2	86.3	2.06±0.18	7	7.0	269	-
0.1% FITC, 0.03% RITC	264	26.4	80.2	2.03±0.15	21	7.0	186	-
0.1% FITC, 0.1% RITC	238	23.8	83.0	1.70±0.17	64	6.4	129	-
0.1% FITC, 0.3% RITC	212	21.2	86.3	1.20±0.18	134	4.5	102	-
0.1% FITC, 1% RITC	212	21.2	86.3	0.83±0.26	529	5.3	63.6	-
linker exchange functionalization								
Small crystals, 1 h @ 65 °C	8188	-	25.5	2.11±0.23	-	-	-	-
Small crystals, 6 h @ 65 °C	7212	-	26.6	1.76±0.21	-	-	-	-
Small crystals, 24 h @ 65 °C	9561	-	24.2	1.40±0.15	-	-	-	-
Large crystals, surface	-	-	-	2.19±0.17	-	-	-	-
Large crystals, inside	-	-	-	2.73±0.19	-	-	-	-

Table S6.3. BET surface areas and pore sizes of pure and dye de novo functionalized UiO-67 samples.

Sample	Octahedral Pore Size [Å]	Tetrahedral Pore Size [Å]	Surface Area[m²/g]
UiO-67	17.5	10.5	-
0.1% FITC	17.3	10.5	2796
0.3% FITC	17.6	10.5	2195
0.7% FITC	17.7	10.6	2705
2% FITC	17.7	10.5	2451
0.1% RITC	18.1	10.5	2765
0.3% RITC	17.6	10.6	2738
0.7% RITC	17.9	10.4	2567
2% RITC	17.6	10.6	2597
0.1% FITC, 0.01% RITC	16.9	10.7	2674
0.1% FITC, 0.03% RITC	17.4	10.5	2555
0.1% FITC, 0.1% RITC	17.4	10.5	2600
0.1% FITC, 0.3% RITC	17.6	10.6	2648
0.1% FITC, 0.3% RITC	17.4	10.5	2568

Table S6.3. Amount of linkers used for *de novo* functionalization

Sample	H_2BPDC [mg]	FITC-H_2BPDC [mg]	RITC-H_2BPDC [mg]
UiO-67	18.8	-	-
UiO-67, 0.1% FITC	18.8	0.0502	-
UiO-67, 0.3% FITC	18.7	0.1506	-
UiO-67, 0.7% FITC	18.7	0.3514	-
UiO-67, 2% FITC	18.4	1.004	-
UiO-67, 0.1% RITC	18.8	-	0.0638
UiO-67, 0.3% RITC	18.7	-	0.1914
UiO-67, 0.7% RITC	18.7	-	0.4466
UiO-67, 2% RITC	18.4	-	1.276
UiO-67, 0.1% FITC, 0.01% RITC	18.8	0.0502	0.00638
UiO-67, 0.1% FITC, 0.03% RITC	18.8	0.0502	0.01914
UiO-67, 0.1% FITC, 0.1% RITC	18.5	0.0502	0.0638
UiO-67, 0.1% FITC, 0.3% RITC	18.7	0.0502	0.1914
UiO-67, 0.1% FITC, 1% RITC	18.3	0.0502	0.638

7 Conclusion and Outlook

During the course of this thesis project central aspects of the well-known MOFs MIL-101(Cr), UiO-67 and MIL-88A were investigated in detail. The physicochemical properties of these MOFs were alterated by adapting their synthesis conditions and via chemical functionalization. The resulting MOFs were characterized by many state-of-the art analytical techniques revealing new information on the frameworks' crystallinity, internal polarity, MRI activity, and their interactions at the bio-interface.

Using nanomechanical mass correlation spectroscopy, fundamental properties of MIL-101(Cr) nanoparticles were explored in the third chapter of this thesis. This newly developed microfluidic method can be used to detect mass fluctuations in nanoparticle dispersions. Using this method, it was discovered that the density of these porous particles changes drastically in solution compared to the crystallographic density of the dry MOF. In this study, we demonstrated the effect of solvents of different polarities on the MOFs' mass-density and quantified solvent uptake from mixed solvent systems. Furthermore, we influenced the polarity of the nanoparticles' inner pores by functionalizing the coordinatively unsaturated metal-sites in the frameworks with pyridine and pyrazine and quantified this polarity change by measuring the preferential solvent uptake in the MOFs' pores.

In the fourth chapter of this thesis, morphological optimization was demonstrated with iron(III) fumarate. Using different reaction conditions, (solvothermal synthesis, room temperature precipitation, microwave assisted synthesis, or microfluidics) four different particle types, each with distinct morphology and a diameter between 50 nm and 10 µm, were produced. The crystal structure of these particles was characterized extensively with different structural methods, including X-ray diffraction on the particles when suspended in dispersion, electron diffraction, and pair distribution function analysis. Using these analytical techniques, all four particle types (even including the smallest X-ray amorphous spherical nanoparticles) were found to have the MOF structure of MIL-88A. The structural and morphological variety of the particles strongly affected their biomedical potential. All iron(III) fumarate particles exhibited excellent biocompatibility, but drastic differences in their suitability for magnetic resonance imaging were noted. Morphological optimization resulted in a 3-fold increase of r_2

relaxivities and 4-fold increase of r_1 relaxivities when comparing the particles to each other rendering them in the same range as other commercially available contrast agents.

The knowledge gained regarding iron(III) fumarate synthesis was further used in chapter five for the development of a drug delivery system. Amorphous iron(III) fumarate nanoparticles were loaded with fluorescent and biologically active molecules and subsequently coated with exosomes. The combination of this hybrid nanoparticle with extracellular vesicles created carriers with high loading capacity and excellent biocompatibility. Furthermore, the uptake of these particles into cells along with facile intra-cellular release of cargo was demonstrated, a process that was not hindered by endosomal entrapment.

While chapter 3 has shown the influence of post-synthetic coordination functionalization, chapter 6 further explores the details of *in-situ* functionalization and post-synthetic linker exchange. Both of these functionalization approaches were used to create fluorescent-dye functionalized UiO-67 nanoparticles that were characterized with analytical fluorescence microscopy. This series of experiments showed that samples that appear homogenous on a bulk scale are often composed of individual particles with different degrees of functionalization. Furthermore, it correlates the addition of functional linker groups to increasing structural defects, and suggests that linker exchange is a more gentle functionalization approach compared to *de-novo* synthesis.

Additional work that was to a large extent presented in the authors masters’s thesis is shown in the appendix chapter 8. It focuses on the defining physicochemical property of nanoparticles: their size. As for other nanoparticles, MOF nanoparticle size determination is not trivial as it may depend on definition and measurement technique; there can be different “sizes” that need to be distinguished. For this purpose, Zr-fum MOF was examined with analytical techniques including electron microscopy, X-ray diffraction, dynamic light scattering, fluorescence correlation spectroscopy and atomic force microscopy. These techniques are all based on different physical principles and are used under different measurement conditions. Overall, this study shows that “size” determination will be influenced by the field of application, measurement conditions and sample preparation, and that it is often necessary to apply multiple complementary characterization techniques for particle size evaluation.

In summary, this thesis has demonstrated the significant impact of synthesis protocols and chemical modification on the functionality of MOF materials. With these approaches, well-known MOF systems were manipulated to yield great morphological and chemical variety, being easily synthesized with high reproducibility. These features were important for the application of several specialized analytical techniques and applications in the field of biomedicine. Relying on these characterization techniques, the fundamental properties of MOF nanoparticle systems were investigated from a different perspective. While being primarily focused on the nano- and meso size regime of MOF materials, the results presented in this thesis also point to the necessity of materials optimization in general as it can lead to greatly improved performance in applications.

8 Appendix: Exploration of MOF Nanoparticle Sizes using Various Physical Characterization Methods – Is what you measure what you get?

This chapter is based on the following publication:

Hirschle P, Preiß T, Auras F, Pick A, Völkner J, Valdepérez D, Witte G, Parak WJ, Rädler JO, Wuttke S. CrystEngComm. **2016**;18(23):4359-68 (DOI: 10.1039/c6ce00198j)

8.1 Introduction

Metal-organic frameworks (MOFs) are organic-inorganic hybrid crystalline compounds consisting of inorganic metallic clusters, also referred to as the nodes that are connected by organic linker molecules, *i.e*. spacers.[1-3] Owing to the many possible combinations of organic linkers and metal ions, a vast number of MOF structures, up to now more than 20,000, have been reported so far.[3] Over the last years, MOFs have attracted considerable scientific interest due to wide structural and chemical tailorability,[4-6] their high surface area,[7-10] as well as the many possible different ways to functionalize their surface[11-17]. These characteristics have allowed for a broad applications in various fields such as separation[18], storage[19-22] catalysis[23-28], sensing[29-31], drug delivery[32,33], diagnosis[32,33], and ion conduction[34]. Furthermore, it has been shown that MOF crystal size can be controlled at the nanometer level to build MOF nanoparticles (MOF NPs)[35-45]. Owing to the modular synthesis approach, together with the spatial control of chemical moieties within the crystalline framework MOF chemistry offers, MOF NPs appear as a promising new class of multifunctional NPs amongst the already existing NP material classes.

The control of MOF crystal size at the nanometer level results in MOF NPs whose properties are no longer determined by their inner surface only, but also by their outer surface properties, due to their high external surface-area-to-volume ratio.[46-50] When bulk materials are reduced to the nm size, often properties and their behavior are often size and shape dependent. Examples for MOF NPs and the resulting effects on their crystal structure and

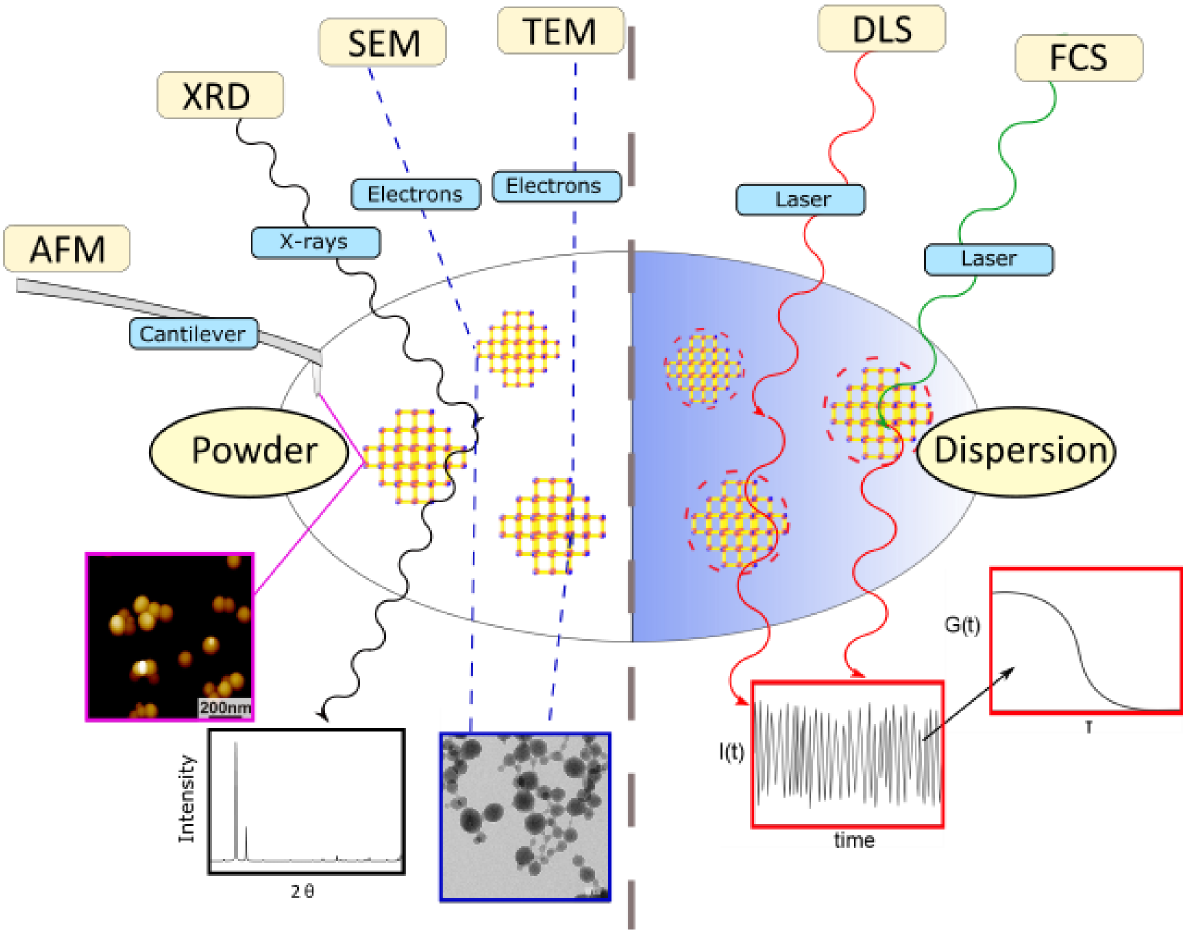

Figure 8.1. Overview of the methods used to determine the size of Zr-*fum* MOF nanoparticles (atomic-force microscopy (AFM), X-Ray diffraction (XRD), transmission electron microscopy (TEM), scanning electron microscopy (SEM), dynamic light scattering (DLS) and fluorescence correlation spectroscopy (FCS)).

sorption behavior are reported elsewhere[51-53]). Hence, the determination and knowledge of both size and shape of the NPs are of paramount importance.[54] However, the trivial but important question - *What is the "size" of a NP?* is not straightforward to answer as the size of a NP differs depending on what characterization technique is used and in which state the NP is measured[55] Various techniques, relying on different physical principles and data processing methods, are available to determine particle size and each one has its own advantages and drawbacks. In particular, once dissolved in solution, NPs interact with the solvent, e.g. by hydration, ion-adsorption[56], or agglomeration[57], and thus the effective size may significantly change[58].

8.2 Results

The Zr-*fum* NPs used in this study were synthesized using the same approach used by Behrens and co-workers.[59] The synthesis is carried out solvothermally in water using $ZrCl_4$ substrates and fumaric acid (see section 8.5 for more details). In the subsequent section, we first display the results of solid state based methods as SEM, TEM, AFM and XRD. Even for those methods conditions for measurements may be very different. While TEM requires operation in vacuum, AFM could be carried out in a fluid cell on NPs adsorbed to a surface. In addition to determination of particle size, all techniques offer some different advantages of identifying Zr-*fum* NPs, such as confirming their crystallinity and determining their 2- or 3-dimensional morphology. Thereafter, the outcomes of dispersion based methods as DLS and FCS, which need to be carried out in solvent, are showcased. Those techniques are suitable for studying NPs properties such as their aggregation behavior and their hydrodynamic diameters, which are specific to dispersions.

8.2.1 Scanning Electron Microscopy (SEM)

Scanning electron microscopy is one of the most widely used techniques to characterize nanomaterials. This method relies on the use of an electron beam, whose energy is around 5 keV, that scans the surface of a solid sample. The electrons of the incident beam impinge on the sample surface and generate secondary electrons, which are collected by a detector and used to create the sample image. SEM analyses were performed on a sample that was prepared by drying an ethanol-based dispersion of Zr-fum NPs followed by carbon-sputtering. They reveal the spherical morphology of those NPs as shown in **Figure 8.2a**. The size distribution of the Zr-fum MOF NPs was determined measuring the diameter of approximately 1000 NPs (**Figure S8.7**). The resulting values were plotted in a histogram and fitted with a Gaussian function (**Figure 8.2b**) centered on an average NPs diameter of $d^{SEM}_{Zr-fumNPs}$ = 62.0 ± 18.9 nm. Note that SEM requires conductive substrates in order to avoid charging effects, and thus a non-conductive Zr-fum NP sample should be sputtered with a conductive film before being analyzed.

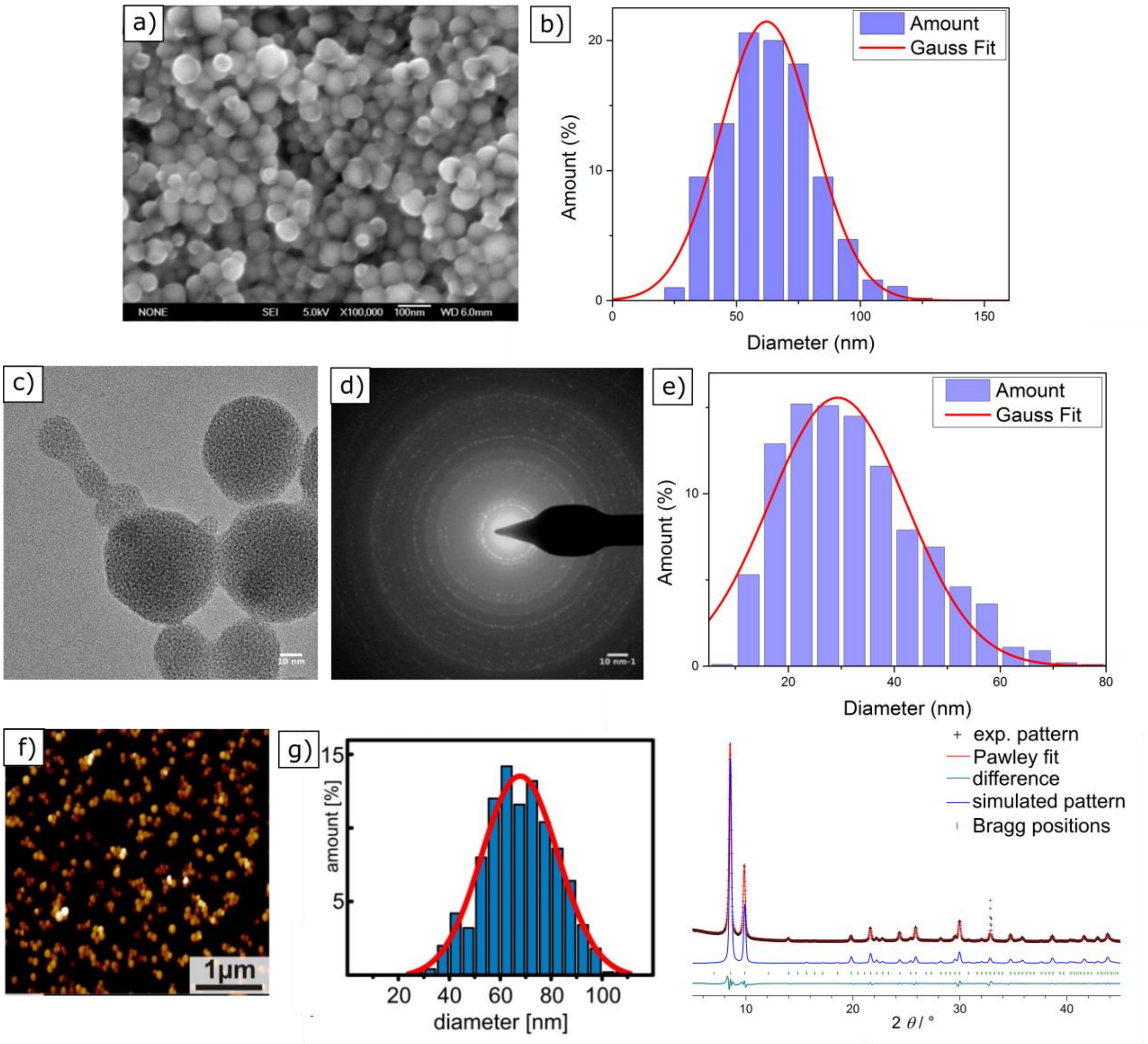

Figure 8.2. Characterization of Zr-*fum* NPs with different methods: (**a**) SEM micrograph; (**b**) particle size distributions of Zr-*fum* NPs from SEM images (**Figure S8.6**); (**c**) TEM micrograph; (**d**) electron diffraction pattern of Zr-*fum* NPs; (**e**) particle size distribution of Zr-*fum* NPs from TEM images (**Figure S8.12**-**Figure S8.16**); (**f**) AFM micrograph; (**g**) particle size distribution of Zr-*fum* NPs from AFM images; (**h**) Experimental PXRD pattern of the Zrfum-3 MOF nanoparticles (black symbols), Pawley fit (red), Bragg positions (green symbols) and the difference between the Pawley fit and experimental data (dark green). The observed reflection intensities are in very good agreement with the simulated PXRD pattern (blue) based on the *Pn*-3 symmetric Zr-*fum* MOF structure model.[53] For the simulation, a domain size of 50 nm was assumed.

8.2.2 Transmission Electron Microscopy (TEM)

In the transmission electron microscopy experiment, a high-energy electron beam (E ~200 keV) is focused on a thin sample (typically less than 200 nm) made of a carbon grid on which a droplet of the NP suspension has been evaporated. The electrons passing through the sample, in other words being transmitted, are scattered at different angles and then are focused with a lens system on the detector to achieve micrographs with a high lateral spatial resolution. TEM offers the important advantages of high magnification, ranging from 50 to 10^6 and the ability to provide both image and diffraction pattern information. The latter one is especially crucial for MOF NPs, as it proves the crystallinity of the structure. A typical TEM micrograph of Zr-fum NPs is shown in **Figure 8.2c**. and proves the spherical shape of the NPs. The histogram of **Figure 8.2e** reports the distribution of NP diameter, which was measured on approximately 1000 individual specimens (Figure S8.12-Figure S8.16). The adjustment of this distribution with a normal law gives rise to an average NPs diameter with a standard deviation of $d_{Zr-fumNPs}^{TEM}$= 62 ± 18.9 nm.

Figure 8.2d shows an electron diffraction pattern of the Zr-fum NP sample. The radial distance of the apparent spots indicates the lattice distance in reciprocal space. A comparison with tabulated values for the Zr-fum crystal structure shows very good agreement (see **Table S8.3**). Although no crystal fringes are displayed in **Figure 8.2c**, the Debye-Scherrer rings of **Figure 8.2d** prove the crystallinity of the sample. Upon prolonged exposure to the high energy electron beam (200 keV), the Debye-Scherrer rings gradually disappear over an exposure time of around 30 s (Figure S8.9-**Figure S8.11**). This indicates that the sample is damaged for the Zr-fum NPs, resulting in the loss of their crystallinity (**Figure 8.2c**). However, the electron diffraction pattern shown in **Figure 8.2d** is generated from a larger sample area, causing the rate of impinging electrons to be lower and the sample to be destroyed much slower.

8.2.3 Atomic Force Microscopy (AFM).

In atomic force microscopy, a sample is analyzed by rasterizing its surface with a sharp tip attached to a cantilever. In our case the measurements were performed in closed loop tapping mode in air, in which the cantilever is excited to vibrate close to its resonance frequency using a piezoelectric device. The interactions between the cantilever-tip and the sample surface i.e. repulsive coulomb forces and attractive van der Waals forces change the amplitude of the cantilever oscillation. A feedback loop constantly adjusts the height of the cantilever to maintain a constant oscillation amplitude, whose variations are used to generate a topographic image of the sample. **Figure 8.2f** displays an AFM micrograph of a sample of Zr-fum MOF NP sample, prepared by drying an ethanolic NP-dispersion on a SiO_2 slide. Apart from individual NPs, we also observe agglomerated NPs which can come from the sample preparation. In order to obtain the size of individual particles the measurements were realized in the outermost periphery of the dried droplet where the density of the particles is minimized. From the AFM images particle sizes have been determined statistically using the particle and pore analysis tool integrated in the Scanning Probe Image Processing (SPIP) (see section 0). The NPs height distribution is plotted in **Figure 8.2g**. The Gaussian curve fit is centered on an average NPs diameter of $d_{Zr-fumNPs}^{AFM}$ = 68 nm with a standard deviation equal to 15 nm.

8.2.4 X-ray Diffraction (XRD)

In X-ray diffraction experiments, the elastic diffraction of X-rays on the atoms of a solid sample is used to identify its atomic and molecular structure. The Scherrer equation relates the broadening of a peak in the powder diffraction pattern to the NPs size and is therefore applied to calculate NP diameter (see section 8.5) As MOFs are crystalline materials, the determination of the crystallite size and its comparison to the particle size is of interest, since it can be used to estimate if single crystals or polycrystals are dominant in the sample.

The powder X-ray diffraction (PXRD) patterns of Zr-fum MOF NP samples feature well-defined reflections across the entire measurement range, indicating the formation of well-ordered frameworks (**Figure 8.2h** and **Figure S8.17**). Moreover, the experimental reflection intensities match the simulated pattern based on the reported Zr-fum structure[59] (blue line in **Figure 8.2h**) very well, thus confirming the formation of a cubic Zr-fum MOF.

Analysis of PXRD data is commonly performed via Pawley fitting.[60] This method compares a theoretical diffraction pattern derived from a structure model to the corresponding experimental data, and varies unit cell parameters and peak profiles until the convergence criteria are reached. Unlike the Rietveld method, Pawley fitting treats peak areas as variables, thus rendering this method also applicable to patterns recorded in reflection geometry, at the cost of not being able to refine atomic positions. We used the Pawley method to extract the lattice parameter *a* from the reflection positions and the average crystal domain size d from the peak broadening (see section 0 for details).

Pawley fitting using the above mentioned structure model led to a lattice parameter *a* ranging from 17.88 ± 0.03 Å to 17.91 ± 0.03 Å for the Zr-fum NP samples (**Figure S8.17**), which are very similar to the lattice parameter of 17.91 Å that has been reported for the bulk material.[59] We then extracted the average crystal domain size *d* from the peak broadening taking into account the instrument broadening and the line shapes (see Section 2 "X-ray Diffraction" in the ESI† for details). This domain size ranges from $d_{Zr-fumNPs}^{XRD}$ = 42 ± 5 nm to 60 ± 5 nm.

In contrast to the other methods discussed above, XRD analysis provides the size of crystalline domains rather than the geometrical NP size. In the case of defect-free single-crystalline nanoparticles, these two quantities would be identical. In reality, a fraction of the NPs will feature grain boundaries or other defects that disrupt the periodicity of the crystal. The average domain size of the NP powder sample will thus be smaller than the average particle size as determined by TEM, for example.

With the presentation of the results stemming from the solid state based methods results being finished the outcomes of the dispersion based methods are broached in the following paragraphs. It is worth noting that the results of these methods may strongly depend on the solvent in which the NPs are dispersed.

8.2.5 Dynamic Light Scattering (DLS)

Dynamic light scattering is probably the most frequently used technique for determining the hydrodynamic diameter of particles, which is defined as the "size" of a hypothetical homogeneous hard sphere that diffuses in the same fashion as that of the particle being measured. The working principle of DLS relies on measuring the intensity fluctuations caused by interference of laser light that is scattered by diffusing particles. Temporal evolution of the fluctuations depends on the particle movement caused by Brownian motion. It is therefore correlated to the diffusion coefficient of the NPs, which depends on their size.

When tracing this intensity over time, it is possible to plot a second order autocorrelation function. From this autocorrelation function, the diffusion coefficient of a particle can be retrieved using a fitting model. However, caution should be taken as the resultant computed hydrodynamic diameter is dependent on the chosen fit model, which typically is hidden as a black box in the machine.[61]

In our study the average hydrodynamic diameter of Zr-fum NPs was first determined in water (see **Figure 8.3b** (black)) to have a good comparability with the similar FCS measurements (see next section). Subsequently the particles were examined in ethanol (see **Figure 8.3b** (red)) to show the reproducibility of the measurements and to show the behavior of the NPs in such a typical solvent (see section 8.5). Diluted dispersions of the NPs were analyzed, and the resulting autocorrelation function was fitted using the "method of cumulants" (for more details, see the ESI†). In water, this resulted in NPs featuring a hydrodynamic diameter of $d^{DLS}_{Zr-fumNPs}$ = 42 nm with a standard deviation of σ = 46 nm. In ethanol, their hydrodynamic diameter was equal to $d^{DLS}_{Zr-fumNPs}$ = 130 nm and a standard deviation of σ = 48 nm.

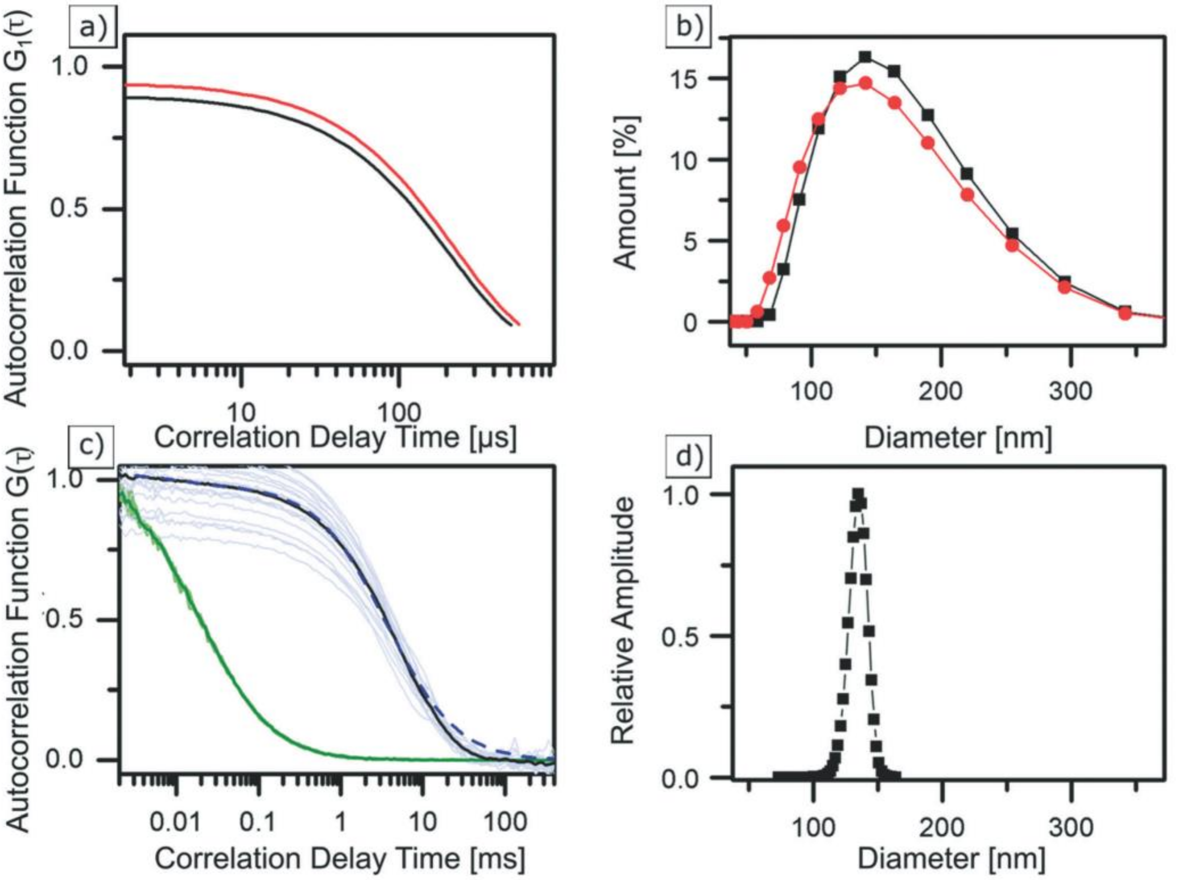

Figure 8.3. DLS correlation data (**a**) and size distribution (**b**) of Zr-fum NPs in ethanol (red) and water (black) as well as averaged and normalized FCS autocorrelation curves (**c**) of Alexa Fluor 488 (green) and labelled Zr-fum MOF NPs in water (black), greyed out curves are underlying single measurements. GDM fit (dashed blue curve) results in a size distribution (**d**) at a peak diameter of 135 nm, considering finite size correction[56]

8.2.6 Fluorescence Correlation Spectroscopy (FCS)

Fluorescence correlation spectroscopy is a fluorescence based method, which can be used to determine hydrodynamic diameter of labelled NPs[62,63]. In this method, a laser is confocally focused into the liquid sample containing fluorescently labelled NPs. The fluorescence intensity fluctuations resulting from NPs traversing the excitation volume are recorded using an avalanche photodiode and used to calculate the time autocorrelation function. FCS data analysis yields the diffusion coefficient as well as the concentration of fluorescent particles (see section 8.5). Using the Stokes Einstein relation the NP hydrodynamic is calculated from the measured diffusion coefficient. Three samples of Zr-fum NPs were labelled with the dye Alexa Fluor 488 (absorption at 488 nm and emission at 519 nm) and were examined with FCS. The normalized autocorrelation functions, shown in **Figure 8.3c**, correspond to one of the labelled Zr-fum NP samples (black). For comparison the autocorrelation of free Alexa Fluor 488 is shown in green. Normalization helps to clearly visualize that the autocorrelation function of dye-labelled NPs is shifted towards higher correlation times with respect to free Alexa Fluor 488 molecules. This indicates slower diffusion of the particles due to the larger hydrodynamic diameter of the NPs. Using single component fit model (see section 0) results in an apparent diffusion time of 3.68 ms which corresponds to a hydrodynamic diameter of $d_{Zr-fumNPs}^{FCS}$ = 135 nm after using the finite particle size correction for hollow spheres presented by Wu et al[64]. The fit (not shown) is reasonable at lag times $\tau < 10$ ms but deviations from the data show that the model of monodisperse particles is not satisfactory indicating that there is a broad distribution of the particle sizes. Thus Gaussian Distribution Model (GDM) [65,66]was used to fit the data. GDM fit (dashed blue line in **Figure 8.3c**) results (again, after finite size correction) in a peak diameter of $d_{Zr-fumNPs}^{GDMFCS}$ = 135 nm and FWHM of 17 nm (see **Figure 8.3d**).

In this article, the most widespread physical methods in the field of nanomaterials characterization, *i.e.* solid state methods, including X-ray diffraction (XRD), atomic-force microscopy (AFM), scanning electron microscopy (SEM) and transmission electron microscopy (TEM), as well as dispersion-based methods, such as dynamic light scattering (DLS) and fluorescence correlation spectroscopy (FCS), were applied to characterize and determine the size of Zr-fum MOF NPs.[67,68] **Figure 8.1** summarizes the characterization techniques that contribute to determine the size of Zr-fum MOF NPs. The Zr-*fum* NPs were synthesized based on a synthesis route reported by Behrens and co-workers (structural details of the Zr-*fum* MOF structure can be found in section 0).[59] In that report the authors showed that the particles size can be controlled with the modulator formic acid. The spherical morphology of the Zr-*fum* particles presented in this work and the associated facile definition of the particle size (*i.e.* diameter) makes the compound a prime example to showcase the various size determination methods.

In this work, we briefly discuss the physical principle of each size characterization method and show each method's practical advantages and disadvantages in NPs assessment. Then, we compare the various "sizes" obtained for Zr-*fum* NPs using the different techniques and finally, we discuss meaning and appropriateness for MOF NP characterization in general.

8.3 Discussion

As stated in the introduction, the concept of the "size" of a NP is intangible since each characterization technique provides its own NP size, which differs from one method to another. This concept becomes clearer when considering on the one hand the different physical principles governing the methods and on the other hand the state of the analyzed sample.

Herein, the employed characterization techniques were divided into two categories, depending on whether the samples were analyzed in dried state or in dispersion (**Figure 8.1**). Measuring NPs in the dry state, i.e. as a powder, has the crucial disadvantage that it is hard to distinguish between aggregated NPs resulting from the sample preparation itself or agglomerates that were already present before. The agglomeration of NPs is energetically favored as it minimizes surface area and can saturate the bonds and coordination sites.[69] Therefore, one should exercise caution when determining the NP size distribution from powder based-techniques and assuming the existence of individual NPs. In particular, in the case of the promising biomedical applications of MOF NPs as nanocarrier or diagnostic agents or even both, non-agglomerated and colloidally stable MOF NPs are required and thus, their characterization in the liquid state is mandatory to clarify their aggregation state.

SEM, TEM and AFM microscopy techniques can provide an image of NPs from which the diameter as well as the shape of the NPs are easily extracted. All microscopy techniques revealed the spherical shape of Zr-*fum* MOF NPs (**Figure 8.2**). To give a representative insight into the NPs' diameter, a statistical study must be performed on a sufficient number of NPs, independent of the used technique. In this work, the diameter of 1000 NPs for TEM and SEM and of 500 NPs for AFM has been measured on the recorded images (**Figure S8.7**, **Figure S8.12**-**Figure S8.16**). A difficulty encountered in SEM images is the identification of individual particles (see **Figure S8.7**). Small particles are easily overlooked, which might shift the resulting NP diameter distribution to higher values. TEM allows to detect smaller NPs, and thus to measure their diameter due to its larger spatial enhancement compared to the SEM.

On TEM pictures of Zr-fum MOF NPs (**Figure S8.12**), it is clearly visible that NPs are connected together *via* thin necks, which were not taken into account to evaluate the NP diameter. However, one may argue that neck-connected NPs actually originate from agglomeration. Moreover, NPs featuring diameters smaller than the diameter of the thin necks, which connect larger NPs, may be overlooked when two-dimensional TEM images are analyzed.

In high quality TEM micrographs of MOF NPs, it should be possible to detect the crystal fringes showcasing the crystallinity of the respective MOF structures.[70] In the case of Zr-*fum* MOF NPs, this was not feasible due to beam damage. However, the crystallinity of MOF NPs was unambiguously proven with HRTEM by examining the electron diffraction patterns (**Figure S8.9**-**Figure S8.11** and **Table S8.3**). Beam damage of the sample is a known problem in TEM mostly with high energy electron beams (E > 100 keV). Further, it can be stated that the Zr-*fum* MOF NPs are highly beam sensitive, since the MOF NPs lose their crystallinity over a time frame of 30s (**Figure S8.9**-**Figure S8.11**). The loss of the crystallinity of the MOF NPs goes together with shrinking, which also explains the shift of the particle size distribution to lower values, when comparing the TEM and SEM results (**Table 8.1**). Therefore, for the Zr-*fum* MOF NPs TEM analysis is not suitable for measuring the size distribution, but suitable to confirm the crystallinity of the sample (**Table S8.3**).

The NP diameter distribution gained from AFM is in good agreement with the one obtained from SEM measurements (**Table 8.1**). Contrary to SEM and TEM techniques, the contrast between the Zr-*fum* MOF NPs and the object slide (SiO_2) was sufficient to analyze the size of individual particles *via* an image software. Another advantage of AFM over SEM and TEM is the gentle nature of this method, which relies on the interaction of a cantilever tip with the particle surface instead of using a high electron energy beam.

Comparing the results of X-ray diffraction experiments to AFM and SEM results, similar diameters are measured. In contrast to SEM, TEM and AFM, which all result in NP diameter distributions, X-ray diffraction gives the average size of the sample crystalline domains, which are not necessarily equal to the NP size. Since the resulting value is an average only, no particle size distribution is obtained. The various possible NP species, which may lead to this average value, are not taken into account. In theory, the average crystalline domain size could result from two sample species, each featuring a uniform size. Alternatively, the average crystalline domain size may result from a broad particle size distribution. If all sample particles are not expected to be single crystals due to the presence of an amorphous material, one would expect the crystalline domain size to be shifted towards smaller values in comparison to NP diameter.

Additionally, defects in the crystal structure result in peak broadening. Since the crystalline domain size is calculated from the width of these peaks, this causes the former to shift towards smaller values. The good agreement among AFM, SEM and X-ray diffraction results suggests the presence of highly crystalline Zr-fum MOF NPs, whose crystal domain size is similar to the NP diameter. Finally, the sharp reflections and very small background observed in the X-ray diffraction experiments also prove the high crystallinity of the sample, complementing the results of TEM measurements.

Table 8.1. Summary of the average diameter of spherical Zr-*fum* NPs as obtained using three different microscopy tools and three different spectroscopic methods. The standard deviation is also reported.

	Method	Type of sample	What you measure	Average diameter (nm)	σ(nm)
Microscopy	SEM	Dried on carbon support	Diameter	62	18.9
	TEM	Dried on carbon grid	Diameter	29	12.9
	AFM	Dried on silica slide	Height	68	15.0
Spectroscopy	XRD	Powder	Domain Diameter	42-60	-*
	DLS	Dispersion	Hydrodynamic Diameter	142 (H_2O)	46
	FCS	Dispersion, labelled	Hydrodynamic Diameter	135 (H_2O)	17 (FWHM)

*This method does not give a particle size distribution but result in a mean size assuming a single species

The outcome of DLS and FCS is a distribution of diffusion coefficients D, which is then transformed into a distribution of hydrodynamic diameters, i.e. diameters of those spheres that yield the same D-values. Therefore, the hydrodynamic diameter does not describe the morphology of a particle but the chosen fitting model assuming a solid sphere or another ideal geometric shape, which has the same diffusion properties as the measured particle. As the Zr-fum MOF NPs feature a rather good spherical morphology, and as no additional organic surface capping is used, the values obtained from the dispersion-based methods should to some extent be comparable to those obtained from the powder methods. However, the hydrodynamic diameter of the Zr-fum MOF NPs determined using DLS and FCS is significantly larger than the NP diameters determined with powder based methods (**Table 8.1**).

In the case of DLS measurements, substantial absorption of laser light (λ = 633 nm) by the sample itself, which causes a systematic measuring error, can be ruled out by our white Zr-*fum* MOF NPs. Hence, the differences in the measured NP size values can be explained by the presence of small aggregates. FCS measurements reveal hydrodynamic diameters close to those obtained using DLS but with a narrower distribution. This can be explained by different fitting models. However, both methods disclose the presence of agglomerates of the Zr-fum MOF NPs in solution as the NP diameter determined by the solid techniques is significantly smaller. Functionalization of MOF NPs with appropriate organic surface cappings, providing either electrostatic or steric repulsion, could help reduce the amount of aggregates.

8.4 Conclusion

One of the key issues in NP research is that the product of a chemical synthesis of NPs is a colloidal dispersion, which exhibits a polydisperse distribution of sizes and shapes, rather than a collection of identical NPs. This is the main reason why the reproducibility of NP synthesis results is so difficult to ensure, even if the same person carries out the synthesis under the same experimental conditions. For this reason, a careful and extensive NP characterization is required. Moreover, future NP database will collect physical dispersion data together with the chemical composition of NPs. Such kind of database is important as it allows researchers to compare different NP data sets and also to put their own results in place. For this reason, recommendations for MOF NP characterization using standard physical characterization tools have been introduced. Zr-fum MOF NPs appeared as ideal candidates to reach this fixed target owing to their perfect spherical shape. In our work, we applied six characterization methods on Zr-fum MOF NPs and the obtained results were discussed and compared based on the underlying physical process of the characterization device.

When choosing techniques to characterize a nanomaterial, it is important to bear in mind the later usage of the respective compound. Powder characterizations with SEM, TEM or AFM are essentially sufficient when considering solid-based applications of MOF NPs. However, in solution-based applications such as drug delivery, colloidally stable NP solutions are required, which must thus be characterized in solution with DLS and/or FCS, for instance. Since these methods do not give insight into the morphology of NPs, it is therefore advantageous to complement these techniques by an image-providing technique such as TEM, SEM or AFM.

In case of MOF NPs determination of crystallinity and in particular quantification of the crystalline domains size is an important parameter. However, the XRD pattern of MOF NPs need to be carefully analyzed as high-crystallinity or even the existence of MOF structure cannot be always stated be due to the potential broadening of the peak in the XRD pattern. For example, the crystallinity of MIL-101(Cr) and MIL-100(Fe) NPs is unequivocally proven by TEM analysis only[48]. In comparison to the tested Zr-*fum* MOF NPs the respective MOF NPs in those cases were more beam stable. The difficult characterization of MOF NPs that are sensitive to the electronic beam of TEM could be overcome with the new versions of TEM instruments operating at lower voltage (*e.g.* 60 keV).

TEM analysis usually appears as the most suitable method to determine the size of isolated MOF NPs in dried state due to its high spatial resolution. However, as shown in the case of Zr-*fum* MOF NPs, beam damage can spoil the outcome, making TEM no longer appropriate. A good alternative is represented by SEM, because it operates at much lower voltage even if small NPs (< 20 nm) of a sample can be hardly detected since hidden by bigger ones. TEM and SEM pictures were used to manually determine Zr-*fum* MOF NPs size distribution. Although this is time consuming, this approach is sufficient when having spherical NPs but cannot be applied on non-spherical NPs.

Many MOF NP applications need dispersions of colloidally stable MOF NPs. Even though most researchers target solution-based NP applications (e.g. drug delivery), they often do not furnish evidence on the colloidal properties of MOF NPs. This enigma comes from agglomeration issues often met with nanomaterials. The chemistry of every NP material class, including MOF NP, faces the challenge of synthesizing colloidally stable NPs. The saturation of a MOF NP surface immediately after MOF NP nucleation, either by electrostatic repulsion or steric stabilization, can avoid this agglomeration issue. A stable MOF NP suspension can be easily characterized by DLS analysis, whereby caution should be paid to the automatic evaluation of the size distribution of the instrument. An alternative solution to DLS is FCS, as demonstrated in this article. FCS is based on evaluation of a autocorrelation function to obtain the diffusion coefficient of fluorescence-labelled NPs. Although FCS has the disadvantage of requiring dye labelled NPs, meaning that they are chemically modified, in many applications, such as drug delivery or diagnosis, NPs need to be labelled for the application itself, e.g. to carry out cell uptake studies. In these cases, FCS is an excellent characterization technique due to its high spatial and temporal resolutions and its ability to analyses extremely low NP concentrations (nM to pM concentrations) in a very small volume (∼ 0.1 fL). Consequently, a low amount of sample is needed to precisely determine the hydrodynamic diameter of labelled NPs. Moreover, FCS measurement simultaneously provides information about the concentration (inverse correlation height) of the investigated sample.

In summary, we presented comprehensive physical characterization of the size, shape and bulk properties of Zr-fum MOF NPs. Evidently, the structural properties of MOF NPs provide a large set of parameters allowing for a thorough assessment of MOF NP quality. Future applications that will exploit MOF NPs as hosts, delivery vehicles or catalytic agents rely on the full knowledge of their physical NP properties. The caveats and peculiarities in NP size characterization discussed here might help for standardization and better comparability of MOF NP properties.

References

1 Kitagawa, S., Kitaura, R. & Noro, S.-i. Functional Porous Coordination Polymers. *Angew. Chem. Int. Ed.* **43**, 2334-2375, doi:10.1002/anie.200300610 (2004).

2 Férey, G. Hybrid porous solids: past, present, future. *Chem. Soc. Rev.* **37**, 191-214, doi:10.1039/b618320b (2008).

3 Furukuwa, H., Cordova, K. E., O'Keeffe, M. & Yaghi, O. M. in *Science* Vol. 341 974-987 (2013).

4 Lu, W. *et al.* Tuning the structure and function of metal–organic frameworks via linker design. *Chem. Soc. Rev.* **43**, 5561-5593, doi:10.1039/c4cs00003j (2014).

5 Cook, T. R., Zheng, Y.-R. & Stang, P. J. Metal–Organic Frameworks and Self-Assembled Supramolecular Coordination Complexes: Comparing and Contrasting the Design, Synthesis, and Functionality of Metal–Organic Materials. *Chem. Rev.* **113**, 734-777, doi:10.1021/cr3002824 (2013).

6 Tranchemontagne, D. J., Mendoza-Cortes, J. L., O'Keeffe, M. & Yaghi, O. M. Secondary building units, nets and bonding in the chemistry of metal-organic frameworks. *Chem. Soc. Rev.* **38**, 1257-1283, doi:10.1039/b817735j (2009).

7 Yaghi, O. M. *et al.* Reticular synthesis and the design of new materials. *Nature* **423**, 705-714, doi:10.1038/nature01650 (2003).

8 Senkovska, I. & Kaskel, S. Ultrahigh porosity in mesoporous MOFs: promises and limitations. *Chem Commun (Camb)* **50**, 7089-7098, doi:10.1039/c4cc00524d (2014).

9 Grünker, R. *et al.* A new metal–organic framework with ultra-high surface area. *Chem. Commun.* **50**, 3450, doi:10.1039/c4cc00113c (2014).

10 Farha, O. K. *et al.* Metal–Organic Framework Materials with Ultrahigh Surface Areas: Is the Sky the Limit? *J. Am. Chem. Soc.* **134**, 15016-15021, doi:10.1021/ja3055639 (2012).

11 Deria, P. *et al.* Beyond post-synthesis modification: evolution of metal–organic frameworks via building block replacement. *Chem. Soc. Rev.* **43**, 5896-5912, doi:10.1039/c4cs00067f (2014).

12 Evans, J. D., Sumby, C. J. & Doonan, C. J. Post-synthetic metalation of metal–organic frameworks. *Chem. Soc. Rev.* **43**, 5933-5951, doi:10.1039/c4cs00076e (2014).

13 Cohen, S. M. Postsynthetic Methods for the Functionalization of Metal–Organic Frameworks. *Chem. Rev.* **112**, 970-1000, doi:10.1021/cr200179u (2012).

14 Furukawa, H., Müller, U. & Yaghi, O. M. "Heterogeneity within Order" in Metal-Organic Frameworks. *Angew. Chem. Int. Ed.* **54**, 3417-3430, doi:10.1002/anie.201410252 (2015).

15 Hintz, H. & Wuttke, S. Solvent-Free and Time Efficient Postsynthetic Modification of Amino-Tagged Metal–Organic Frameworks with Carboxylic Acid Derivatives. *Chem. Mater.* **26**, 6722-6728, doi:10.1021/cm502920f (2014).

16 Hintz, H. & Wuttke, S. Postsynthetic modification of an amino-tagged MOF using peptide coupling reagents: a comparative study. *Chem. Commun.* **50**, 11472-11475, doi:10.1039/c4cc02650k (2014).

17 Wuttke, S. *et al.* Turn-on fluorescence triggered by selective internal dye replacement in MOFs. *Chem. Commun.* **50**, 3599, doi:10.1039/c3cc46591h (2014).

18 Van de Voorde, B., Bueken, B., Denayer, J. & De Vos, D. Adsorptive separation on metal-organic frameworks in the liquid phase. *Chem. Soc. Rev.* **43**, 5766-5788, doi:10.1039/c4cs00006d (2014).

19 Van der Perre, S. *et al.* Experimental Study of Adsorptive Interactions of Polar and Nonpolar Adsorbates in the Zeolitic Imidazolate Framework ZIF-68 via Pulse Gas Chromatography. *J. Phys. Chem. C* **119**, 1832-1839, doi:10.1021/jp509840u (2015).

20 Van der Perre, S. *et al.* Adsorptive Characterization of the ZIF-68 Metal-Organic Framework: A Complex Structure with Amphiphilic Properties. *Langmuir* **30**, 8416-8424, doi:10.1021/la501594t (2014).

21 He, Y., Zhou, W., Qian, G. & Chen, B. Methane storage in metal–organic frameworks. *Chem. Soc. Rev.* **43**, 5657-5678, doi:10.1039/c4cs00032c (2014).

22 Canivet, J., Fateeva, A., Guo, Y., Coasne, B. & Farrusseng, D. Water adsorption in MOFs: fundamentals and applications. *Chem. Soc. Rev.* **43**, 5594-5617, doi:10.1039/c4cs00078a (2014).

23 Lee, J. *et al.* Metal–organic framework materials as catalysts. *Chem. Soc. Rev.* **38**, 1450, doi:10.1039/b807080f (2009).

24 Na, K., Choi, K. M., Yaghi, O. M. & Somorjai, G. A. Metal Nanocrystals Embedded in Single Nanocrystals of MOFs Give Unusual Selectivity as Heterogeneous Catalysts. *Nano Lett.* **14**, 5979-5983, doi:10.1021/nl503007h (2014).

25 Kuo, C.-H. *et al.* Yolk–Shell Nanocrystal@ZIF-8 Nanostructures for Gas-Phase Heterogeneous Catalysis with Selectivity Control. *J. Am. Chem. Soc.* **134**, 14345-14348, doi:10.1021/ja306869j (2012).

26 Saha, S., Das, G., Thote, J. & Banerjee, R. Photocatalytic Metal-Organic Framework from CsS Quantum Dot Incubated Luminescent Metallohydrogel. *J. Am. Chem. Soc.* **136**, 14845-14851 (2014).

27 Xu, H.-Q. H., Jiahua; Wang, Dengke; Li, Zhaohui; Zhang, Qun; Luo, Yi; Yu, Shu-Hong; Jiang, Hail-Long. Visible-Light Photoreduction of CO_2 in a Metal-Organic Framework Boosting Electron-Hole Separation via Electron Trap States. *J. Am. Chem. Soc.* **137**, 13440-13443 (2015).

28 Li, Y., Xu, H., Ouyang, S. & Ye, J. Metal-organic frameworks for photocatalysis. *Phys. Chem. Chem. Phys.* **18**, 7563-7572, doi:10.1039/c5cp05885f (2016).

29 Kreno, L. E. *et al.* Metal–Organic Framework Materials as Chemical Sensors. *Chem. Rev.* **112**, 1105-1125, doi:10.1021/cr200324t (2012).

30 Hinterholzinger, F. M., Rühle, B., Wuttke, S., Karaghiosoff, K. & Bein, T. Highly sensitive and selective fluoride detection in water through fluorophore release from a metal-organic framework. *Sci. Rep.* **3**, doi:10.1038/srep02562 (2013).

31 Nickerl, G., Senkovska, I. & Kaskel, S. Tetrazine functionalized zirconium MOF as an optical sensor for oxidizing gases. *Chem Commun (Camb)* **51**, 2280-2282, doi:10.1039/c4cc08136f (2015).

32 Horcajada, P. *et al.* Metal–Organic Frameworks in Biomedicine. *Chem. Rev.* **112**, 1232-1268, doi:10.1021/cr200256v (2012).

33 He, C., Liu, D. & Lin, W. Nanomedicine Applications of Hybrid Nanomaterials Built from Metal–Ligand Coordination Bonds: Nanoscale Metal–Organic Frameworks and Nanoscale Coordination Polymers. *Chem. Rev.* **115**, 11079-11108, doi:10.1021/acs.chemrev.5b00125 (2015).

34 Horike, S., Umeyama, D. & Kitagawa, S. Ion Conductivity and Transport by Porous Coordination Polymers and Metal–Organic Frameworks. *Acc. Chem. Res.* **46**, 2376-2384, doi:10.1021/ar300291s (2013).

35 Chevreau, H. *et al.* Synthesis of the biocompatible and highly stable MIL-127(Fe): from large scale synthesis to particle size control. *CrystEngComm*, doi:10.1039/c5ce01864a (2016).

36 Carné-Sánchez, A., Imaz, I., Cano-Sarabia, M. & Maspoch, D. A spray-drying strategy for synthesis of nanoscale metal–organic frameworks and their assembly into hollow superstructures. *Nature Chemistry* **5**, 203-211, doi:10.1038/nchem.1569 (2013).

37 Schaate, A. *et al.* Modulated Synthesis of Zr-Based Metal-Organic Frameworks: From Nano to Single Crystals. *Chemistry - A European Journal* **17**, 6643-6651, doi:10.1002/chem.201003211 (2011).

38 Tsuruoka, T. *et al.* Nanoporous Nanorods Fabricated by Coordination Modulation and Oriented Attachment Growth. *Angew. Chem. Int. Ed.* **48**, 4739-4743, doi:10.1002/anie.200901177 (2009).

39 Liang, K. *et al.* Biomimetic mineralization of metal-organic frameworks as protective coatings for biomacromolecules. *Nature Communications* **6**, 7240, doi:10.1038/ncomms8240 (2015).

40 Furukawa, S., Reboul, J., Diring, S., Sumida, K. & Kitagawa, S. Structuring of metal–organic frameworks at the mesoscopic/macroscopic scale. *Chem. Soc. Rev.* **43**, 5700-5734, doi:10.1039/c4cs00106k (2014).

41 Falcaro, P. *et al.* MOF positioning technology and device fabrication. *Chem. Soc. Rev.* **43**, 5513-5560, doi:10.1039/c4cs00089g (2014).

42 Ameloot, R. *et al.* Direct Patterning of Oriented Metal-Organic Framework Crystals via Control over Crystallization Kinetics in Clear Precursor Solutions. *Adv. Mater.* **22**, 2685-2688, doi:10.1002/adma.200903867 (2010).

43 Lu, G. *et al.* Imparting functionality to a metal–organic framework material by controlled nanoparticle encapsulation. *Nature Chemistry* **4**, 310-316, doi:10.1038/nchem.1272 (2012).

44 Falcaro, P. *et al.* A new method to position and functionalize metal-organic framework crystals. *Nature Communications* **2**, 237, doi:10.1038/ncomms1234 (2011).

45 Ameloot, R. *et al.* Interfacial synthesis of hollow metal–organic framework capsules demonstrating selective permeability. *Nature Chemistry* **3**, 382-387, doi:10.1038/nchem.1026 (2011).

46 Carné, A., Carbonell, C., Imaz, I. & Maspoch, D. Nanoscale metal–organic materials. *Chem. Soc. Rev.* **40**, 291-305, doi:10.1039/c0cs00042f (2011).

47 Li, P. *et al.* Synthesis of nanocrystals of Zr-based metal-organic frameworks with csq-net: significant enhancement in the degradation of a nerve agent simulant. *Chem Commun (Camb)* **51**, 10925-10928, doi:10.1039/c5cc03398e (2015).

48 Wuttke, S. *et al.* MOF nanoparticles coated by lipid bilayers and their uptake by cancer cells. *Chem. Commun.* **51**, 15752-15755, doi:10.1039/c5cc06767g (2015).

49 Xu, G., Otsubo, K., Yamada, T., Sakaida, S. & Kitagawa, H. Superprotonic Conductivity in a Highly Oriented Crystalline Metal–Organic Framework Nanofilm. *J. Am. Chem. Soc.* **135**, 7438-7441, doi:10.1021/ja402727d (2013).

50 McGuire, C. V. & Forgan, R. S. The surface chemistry of metal-organic frameworks. *Chem Commun (Camb)* **51**, 5199-5217, doi:10.1039/c4cc04458d (2015).

51 Sakata, Y. *et al.* Shape-Memory Nanopores Induced in Coordination Frameworks by Crystal Downsizing. *Science* **339**, 193-196, doi:10.1126/science.1231451 (2013).

52 Hijikata, Y. *et al.* Differences of crystal structure and dynamics between a soft porous nanocrystal and a bulk crystal. *Chem. Commun.* **47**, 7632, doi:10.1039/c1cc10983a (2011).

53 Tanaka, D. *et al.* Rapid preparation of flexible porous coordination polymer nanocrystals with accelerated guest adsorption kinetics. *Nature Chemistry* **2**, 410-416, doi:10.1038/nchem.627 (2010).

54 Jiang, J. O., G.; Biswas, P. Characterisation of size, surface charge and agglomeration state of nanoparticle dispersions for toxicological studies. *J. Nanopart. Res.* **11**, 77-89 (2009).

55 Sperling, R. A. L. T. D., S.; Kudera, S.; Zanella, M.; Lin, C.-A. J.; Chang, W.; Braun, D.; Parak, W. J. Size determination of (bio-)conjugated water-soluble colloidal nanoparticles - a comparison of different techniques. *J. Phys. Chem. C* **111**, 11552-11559 (2007).

56 Zhang, F. *et al.* Ion and pH sensing with colloidal nanoparticles: influence of surface charge on sensing and colloidal properties. *Chemphyschem* **11**, 730-735, doi:10.1002/cphc.200900849 (2010).

57 Caballero-Díaz, E. P., C.; Kastl, L.; Rivera-Gil, P.; Simonet, B.; Valcárel, M.; Jiménez-Lamana, J.; Laborda F.; Parak, W. J. The Toxicity of Silver Nanoparticles Depends on Their Uptake by Cells and Thus on Their Surface Chemistry. *Particle & Particle Systems Characterization* **30**, 1079-1085 (2013).

58 Rivera-Gil, P. J. d. A., D.; Wulf, V.; Pelaz, B.; del Pino, P.; Zhao, Y.; de la Fuente, I.; Ruiz de Larramendi, I.; Rojo, T.; Liang, X.-J.; Parak, W. J. The Challenge To Relate the Physicochemical Properties of Colloidal Nanoparticles to Their Cytotoxicity. *Account of Chemical Research* **46**, 743-749 (2013).

59 Wißmann, G. *et al.* Modulated synthesis of Zr-fumarate MOF. *Microporous Mesoporous Mater.* **152**, 64-70, doi:10.1016/j.micromeso.2011.12.010 (2012).

60 Pawley, G. S. Unit-cell refinement from powder diffraction scans. *J. Appl. Crystallogr.* **14**, 357-361, doi:10.1107/s0021889881009618 (1981).

61 Tay, C. Y., Setyawati, M. I., Xie, J., Parak, W. J. & Leong, D. T. Back to Basics: Exploiting the Innate Physico-chemical Characteristics of Nanomaterials for Biomedical Applications. *Adv. Funct. Mater.* **24**, 5936-5955, doi:10.1002/adfm.201401664 (2014).

62 Pellegrino, T. M., L.; Kudera, S.; Liedl, T.; Koktysh, D.; Rogach, A. L.; Keller, S.; Rädler, J.; Natile, G.; Parak, W. J. Hydrophobic nanocrystals coated with an amphiphilic polymer shell: a general route to water soluble nanocrystals. *Nanoletters* **4**, 703-707 (2004).

63 Liedl, T. K., S.; Simmel, F. C.; Rädler, J. O.; Parak, W. J. Fluorescent Nanocrystals as Colloidal Probes in Complex Fluids measured by Fluorescence Correlation Spectroscopy. *Small* **1**, 997-1003 (2005).

64 Wu, B. C., Yan, Müller, Joachim D. Fluorescence correlation spectroscopy for finite-sized particles. *Biophys. J.* **7**, 2800-2808 (2008).

65 Mittag, J. J., Milani, S., Walsh, D. M., Radler, J. O. & McManus, J. J. Simultaneous measurement of a range of particle sizes during Abeta1-42 fibrillogenesis quantified using fluorescence correlation spectroscopy. *Biochem. Biophys. Res. Commun.* **448**, 195-199, doi:10.1016/j.bbrc.2014.04.088 (2014).

66 Pal, N., Dev Verma, S., Singh, M. K. & Sen, S. Fluorescence correlation spectroscopy: an efficient tool for measuring size, size-distribution and polydispersity of microemulsion droplets in solution. *Anal. Chem.* **83**, 7736-7744, doi:10.1021/ac2012637 (2011).

67 Zahn, G. *et al.* A water-born Zr-based porous coordination polymer: Modulated synthesis of Zr-fumarate MOF. *Microporous Mesoporous Mater.* **203**, 186-194, doi:10.1016/j.micromeso.2014.10.034 (2015).

68 Zahn, G. *et al.* Insight into the mechanism of modulated syntheses: in situ synchrotron diffraction studies on the formation of Zr-fumarate MOF. *CrystEngComm* **16**, 9198-9207, doi:10.1039/c4ce01095g (2014).

69 Goesmann, H. & Feldmann, C. Nanoparticulate Functional Materials. *Angew. Chem. Int. Ed.* **49**, 1362-1395, doi:10.1002/anie.200903053 (2010).

70 Ameloot, R. *et al.* Interfacial synthesis of hollow metal-organic framework capsules demonstrating selective permeability. *Nat Chem* **3**, 382-387, doi:10.1038/nchem.1026 (2011).

8.5 Supplementary Information

8.5.1 Experimental Methods

Thermogravimetry (TG): A dried sample of Zr-*fum* (6.3 mg) was examined on a *TASC 414/4* (*Netzsch*). The thermogravimetric experiment was performed with a heating rate of 10 °C/min up to 900 °C. The results were evaluated using the included software Proteus v4.3.

Nitrogen Sorption: Dried powder of Zr-fum (6.3 mg) was degassed for 12 h at 120 °C in high vacuum. Subsequently, nitrogen sorption was performed on the sample using an Autosorb-1 (Quantachrome). The results were evaluated using the software ASiQwin v3.0. Brunauer-Emmett-Teller (BET) surface areas[1] were calculated by using the linearized form of the BET equation. A correlation coefficient of r = 0.999755 was achieved. The pore size distribution of the sample was determined by using the software`s non-local density functional theory (NLDFT) equilibrium model based on slit and cylindrical pores.

Scanning Electron Microscopy (SEM): The experiments, which are presented here, were performed on a *Jeol JSM-6500F* with EDX-Detektor and *Inca*-software (*Oxford Instruments*). For sample preparation, an ethanolic dispersion of the Zr-*fum* nanoparticles was dried and subsequently sputtered with carbon. The resulting micrographs were evaluated manually using the software *ImageJ v1.49*.

Transmission Electron Microscopy (TEM): All of the experiments were performed on a *Tecnai G2* (*Fei*) with an acceleration voltage of 200 kV. For sample preparation, a dispersion of the Zr-*fum* nanoparticles in ethanol was dried on a carbon-coated copper grid. The resulting micrographs were evaluated manually by using the software *ImageJ v1.49*. The micrographs shown in **Figure S8.8** and **Figure S8.12**-**Figure S8.16** have been measured in imaging mode. The electron diffraction patterns shown in **Figure S8.9**-**Figure S8.11** have separately been recorded in separately diffraction mode.

Atomic Force Microscopy (AFM): Epi-ready silicon wafers coated with a native oxide (Siegert Wafer GmbH) were used as ultraflat supporting substrates. Initially, all supports were cleaned in an ultrasonic bath in ethanol and subsequently blown dry in a nitrogen stream. 2 µL of the nanoparticle solution were pipetted onto a substrate. Slow evaporation of the solvent at room temperature led to a concentric density gradient of the nanoparticles deposited on the surface. The morphology of nanoparticles was characterized by means of atomic force microscopy using a SPM5500-AFM instrument (Agilent) operated in closed loop tapping mode at ambient conditions, and using HQ:NSC15/AlBS cantilevers (MikroMasch; resonance frequency, 325 kHz). The z-range of the scanner had been carefully calibrated using a standard silicon grating with a step height of 84.3 nm and an accuracy of 1.5 nm.

X-Ray Diffraction (XRD): Powder X-ray diffraction (PXRD) measurements were performed using a Bruker D8 Discover with Ni-filtered Cu K_α radiation and a LynxEye position-sensitive detector. In order to reduce the peak broadening caused by the instrument to a minimum, 0.05 mm and 3 mm slits were installed at the X-ray tube assembly and the detector, respectively. In conjunction with a detector opening of 0.8 °, the instrument broadening was thus reduced to 0.05 ° 2ϑ (calibrated against LaB_6). The Pawley fitting[2,3] of the resulting data treats peak areas as variables. Hence, they were not being used for atom-position refinement. Only the unit cell size *a* and the crystallite size *d* were refined. The reflections were assumed to feature a Pseudo-Voigt profile and peak asymmetry was corrected using the Berar-Baldinozzi function.

Dynamic Light Scattering (DLS): During the experiments, all DLS measurements were performed on a *Zetasizer Nano Series* (Nano-ZS, *Malvern*). The employed laser operated at a wavelength λ = 633 nm. The measurement of Zr-*fum* was conducted directly after washing the freshly synthesized nanoparticles. For the respective measurement, the sample dispersion in ethanol was diluted in ethanol (1:200) or water (1:200).

Fluorescence Correlation Spectroscopy (FCS): All experiments were conducted on an Axiovert 200M equipped with a ConfoCor2 unit (Carl Zeiss), using a 40x NA1.2 water immersion objective and an argon ion laser at 488 nm wavelength. Emitted light was separated from excitation light with a dichroic mirror and a bandpass emission filter (505 – 550 nm). Samples were prepared and measured in Nunc 8 well plates (Thermo Scientific). The focal width w = 0.2 µm was determined by a calibration measurement using Alexa Fluor 488 with a known diffusion coefficient of $D = 435\ \mu m^2/s$. [4] Samples of three individually produced batches of Zr-*fum* were investigated with FCS. For this purpose Zr-*fum* nanoparticles were fluorescently labeled by adding 20 µL of Zr-*fum* dispersed in ethanol suspension to 200 µL of an Alexa Fluor 488 solution. After 10 minutes of incubation FCS measurements were performed. To avoid singe particle aggregates, which would distort the correlation curves, the so called dust filter of the instrument's software (70%) was used. By this the fluorescence fluctuations are analysed prior to correlation and spikes caused by agglomerated particles having a deviation of more than 70% from the average count rate within a binned count rate time are cut out and not used for the correlation analysis similar to the method described by Persson *et al.* (2009).[5]

8.5.2 Chemicals

The chemicals Zr(IV) chloride (≥ 95 %, Aldrich), formic acid (> 85 %, Aldrich), fumaric acid (≥ 99.5 %, Fluka) and ethanol (99.9 %, VWR) were all used without further purification.

8.5.3 Synthesis of Zr-*fum* Samples

$ZrCl_4$ and Fumaric acid (**Table S8.2**) were put into a glass reactor (25 mL). A mixture of water (10 mL) and formic acid (975 µL) was added to the educts. The reactor was then sealed and placed in an oven at 120 °C for 24 h.

After cooling down, the resulting white precipitate was washed. The dispersion was divided into 8 vials (1.5 mL), and then centrifuged (14000 rpm, 5 min). After discarding the supernatants, the precipitates were redispersed in water (1.25 mL per precipitate) via sonication. The dispersions were centrifuged (14000 rpm, 5 min) and the supernatants removed. The precipitates were redispersed in ethanol (1.25 mL per precipitate). After repeating this last washing cycle for an additional washing cycle the ethanol-based dispersions were unified.

Table S8.2. Weight-ins of the respective Zr-*fum* batches.

Sample	**m($ZrCl_4$) [mg]**	**m(fumaric acid) [mg]**
Zrfum-1	120.9	180.4
Zrfum-2	120.4	180.2
Zrfum-3	120.6	180.4
Zrfum-4	120.5	180.3

8.5.4 Structure of Zr-fum

As reported by Wißman *et al.*[6] the microporous, cubic structure of Zr-*fum* featuring the formula $Zr_6O_4(OH)_4(O_2C\text{-}(CH)_2\text{-}CO_2)_6$ displays the space group $Pn\overline{3}$. The X-ray diffraction experiments conducted in this work (see **Figure S8.17**) have resulted in a lattice parameter of a = (17.91 ± 0.03) nm to (17.88 ± 0.03) nm.

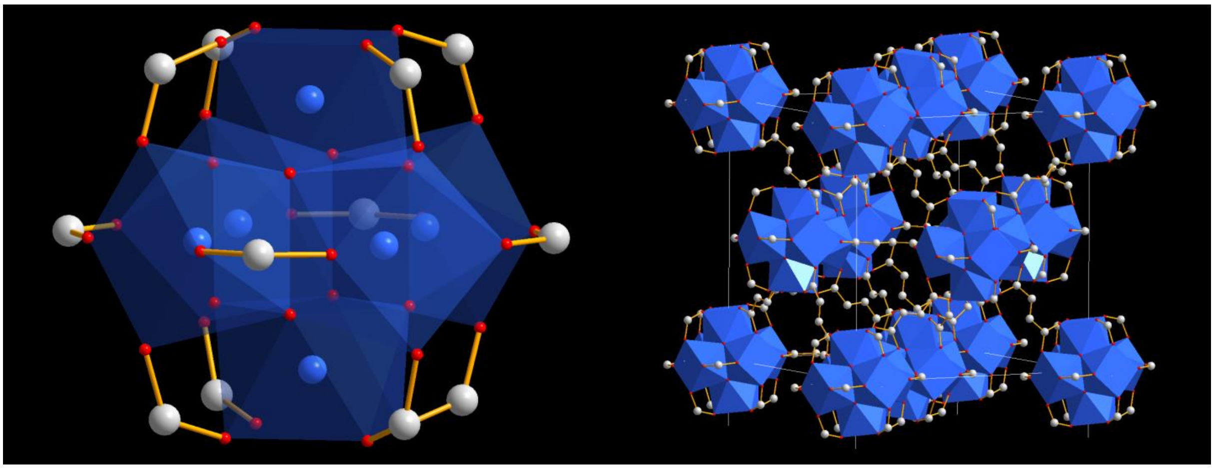

Figure S8.4. Secondary building unit (left) and architecture (right) of Zr-*fum*; Zr (*blue*), O (*red*), C (*grey*).

Figure S8.4 shows the composition of the structure and the position of the secondary building units (SBUs) on the vertices and faces of a cubic cell. Each SBU comprises of 6 Zr-atoms (*blue*) that are octahedrally aligned and coordinated by 8 oxygen-atoms (*red*). The carbon atoms (*grey*) are the first segment of the emerging fumaric acid linker chains, which are arranged cuboctahedrally and thereby connecting each SBU to 12 neighboring clusters.

8.5.5 Nitrogen Sorption

The Zr-*fum* nanoparticles displayed a specific BET surface area of 408 $m^2 \cdot g^{-1}$. The pore size distribution (see **Figure S8.5**) was determined to feature a maximum at the pore with d = 0.57 nm. The corresponding nitrogen sorption graph (see **Figure S8.5**) can be identified as an IUPAC Type I microporous adsorption isotherm.[7]

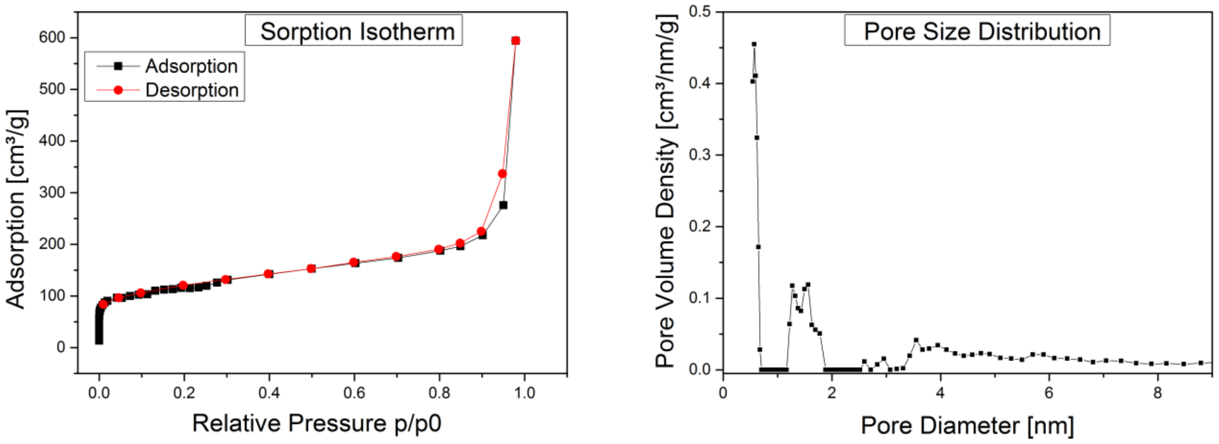

Figure S8.5. Nitrogen sorption isotherm showing the adsorption of nitrogen in dependency of its relative pressure (**left**) and the differential pore size distribution in dependency of the pore-diameter (**right**).

8.5.6 Thermogravimetry

From 48 °C to 250 °C a mass loss occurred which was probably caused by desorption of water from the framework. At 260 °C the decomposition of the organic linker began, similar to the decomposition of pure fumaric acid at 200 °C as reported by Wißman *et al.*[6] This decomposition-step was finished at 480 °C. Subsequently at around 600 °C a final mass loss occurred, which was finished at around 750 °C. Comparing the TG measurement with the data published by Wißman *et al.*, similarities can be seen: they report a similar decomposition range for the linker starting at 250 °C and ending at 400 °C. Wißman *et al.* also provide an explanation for the final mass loss: CO_2 is released from the decomposition of carboxylate groups. Overall, this mass loss caused by the sample during the decomposition of the linker and release of CO_2 is at 47.5 %, which is in a good agreement with the calculated results at 45.8 %.[6] The corresponding graph is shown in **Figure S8.6**.

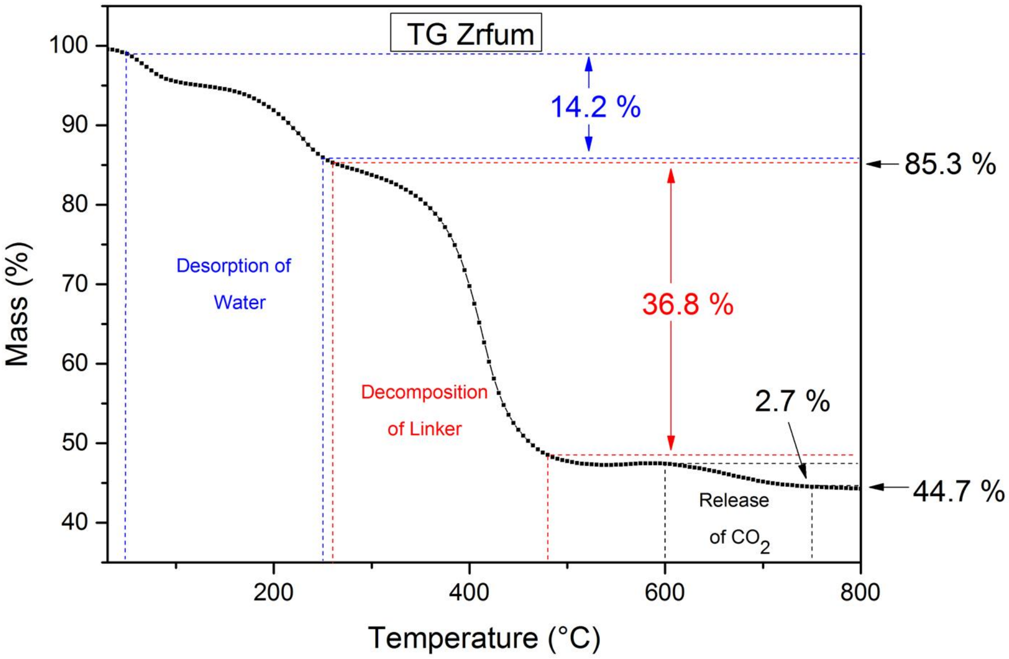

Figure S8.6. Thermogravimetric evaluation of Zr-*fum.*

8.5.7 Scanning Electron Microscopy

The image, which is used to obtain the SEM size distribution, is shown in **Figure S8.7**.

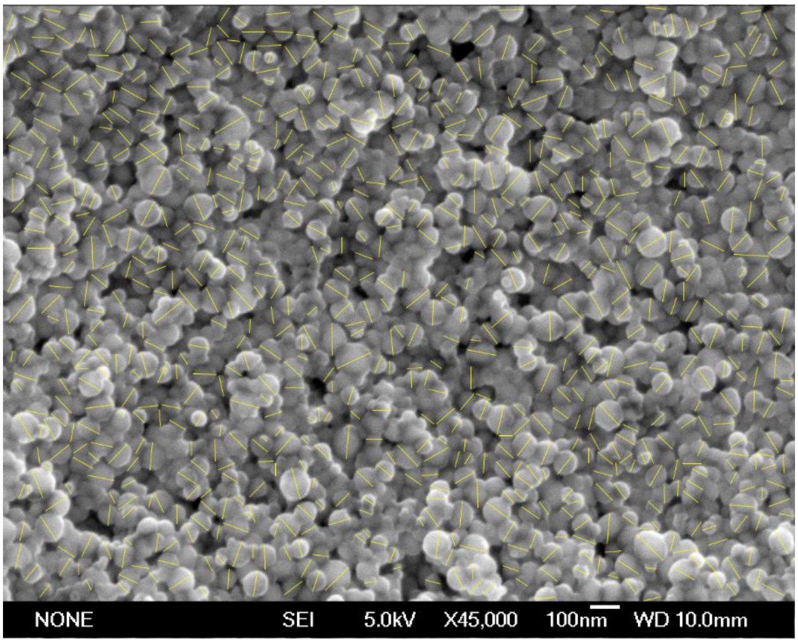

Figure S8.7. Zr-*fum* particles measured for SEM size determination

8.5.8 Transmission Electron Microscopy

An overview picture of dried Zr-*fum* nanoparticles is shown in **Figure S8.8**.

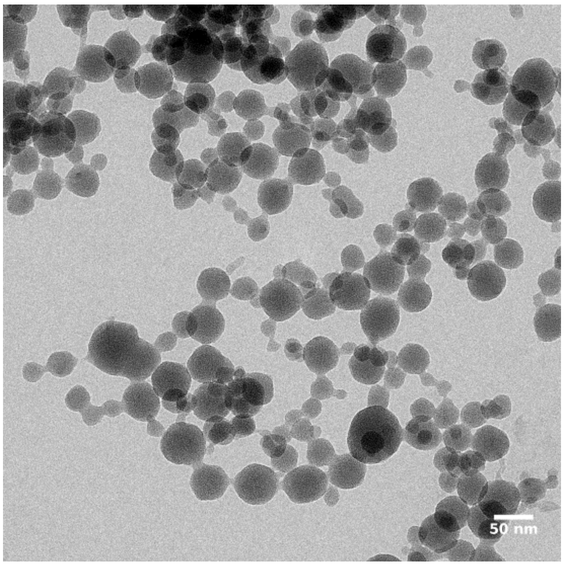

Figure S8.8. Overview picture of Zr-*fum.*

Figure S8.9, **Figure S8.10**, and **Figure S8.11** show Zr-fumarate when exposed to an electron beam (200 keV) for a prolonged period of time. The Debye-Scherrer rings, which are initially still recognizable after an exposure time of 6.5 s, gradually disappear indicating the damage the sample is taking from the electron beam.

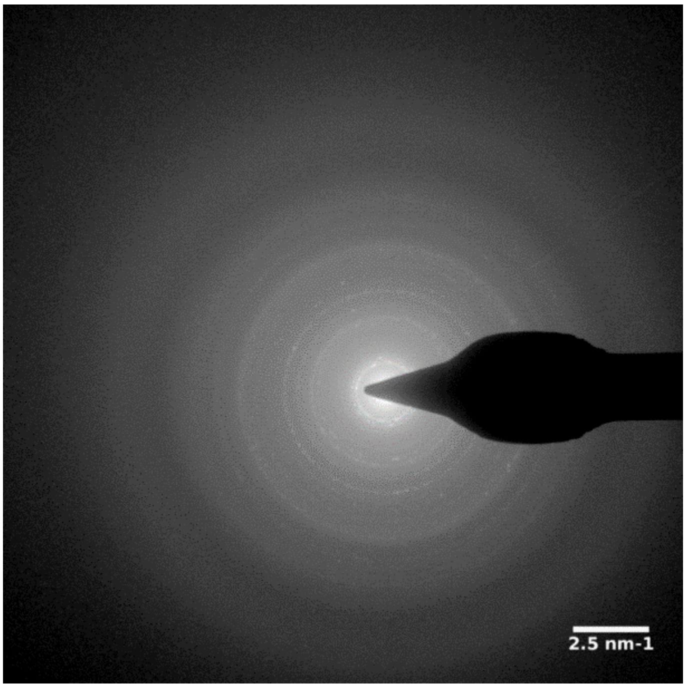

Figure S8.9. Electron diffraction pattern of sample Zr-*fum* after 6.5 seconds in a 200 kV electron beam.

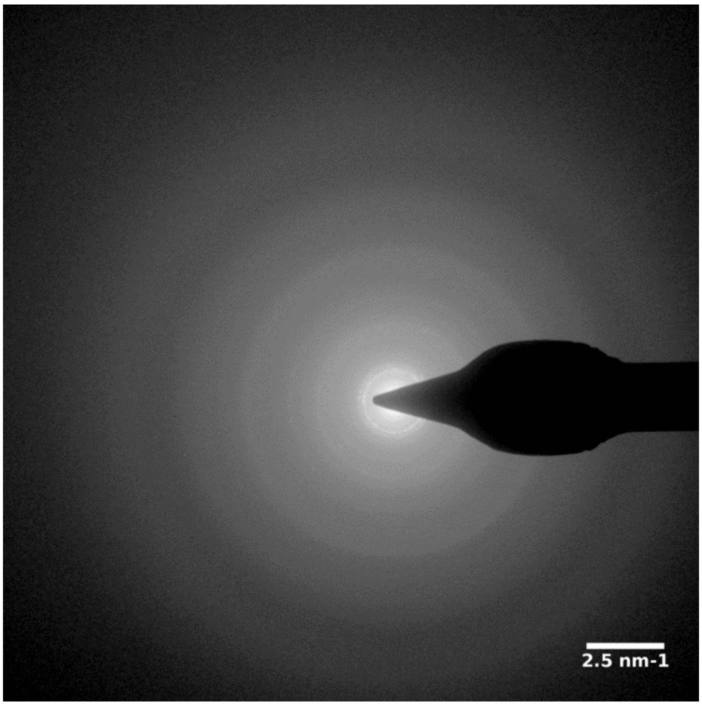

Figure S8.10. Electron diffraction pattern of sample Zr-*fum* after 13 seconds in a 200 kV electron beam.

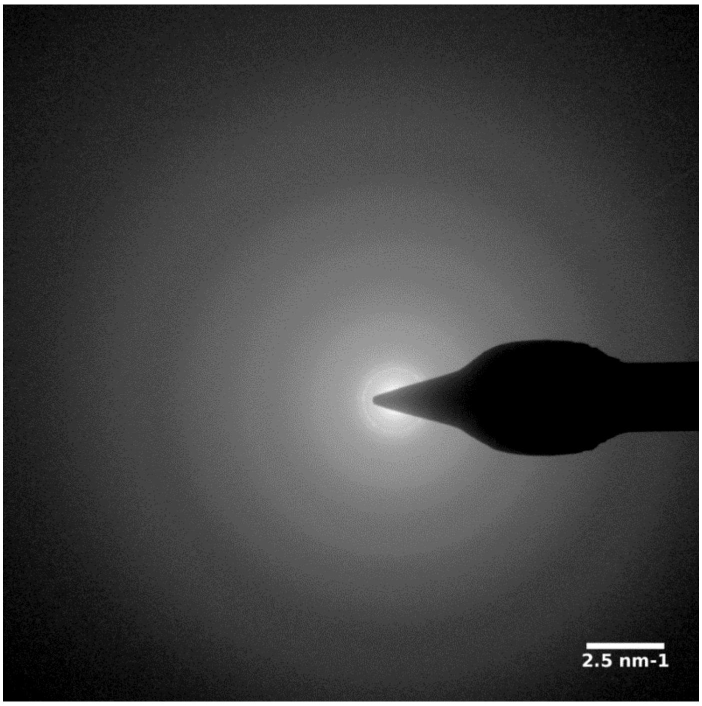

Figure S8.11. Electron diffraction pattern of sample Zr-*fum* after 26 seconds in a 200 kV electron beam.

In **Table S8.3** the Debye-Scherrer rings of Zr-*fum* shown in **Figure S8.9** are shown along with their corresponding HKL indices and interplanar spacings *d*. They are in good agreement with the crystallographic data published by Wißmann *et al.*[6], which verifies the successful synthesis of Zr-fumarate MOF nanoparticles.

Table S8.3. Diffraction rings of Zr-*fum* with their indices and interplanar spacing.

Diffraction Ring	*d (experiment)* [Å]	HKL	d (literature)[4] [Å]	deviation [%]
1	10.1365	(111)	10.3591	2.1
2	8.7538	(200)	8.9545	2.2
3	4.3961	(400)	4.4776	1.8
4	4.0201	(331)	4.1084	2.1

5	3.5727	(422)	3.6554	2.3
6	3.3966	(333)	3.4466	1.5
7	2.9373	(600)	2.9847	1.6
8	2.6755	(533)	2.7312	2.0
9	2.5374	(444)	2.5850	1.8
10	2.4732	(551)	2.5081	1.4
11	2.2804	(553)	2.3315	2.2

The particles that were measured to determine the TEM size distribution are shown in **Figure S8.12**, **Figure S8.13**, **Figure S8.14**, **Figure S8.15**, and **Figure S8.16**.

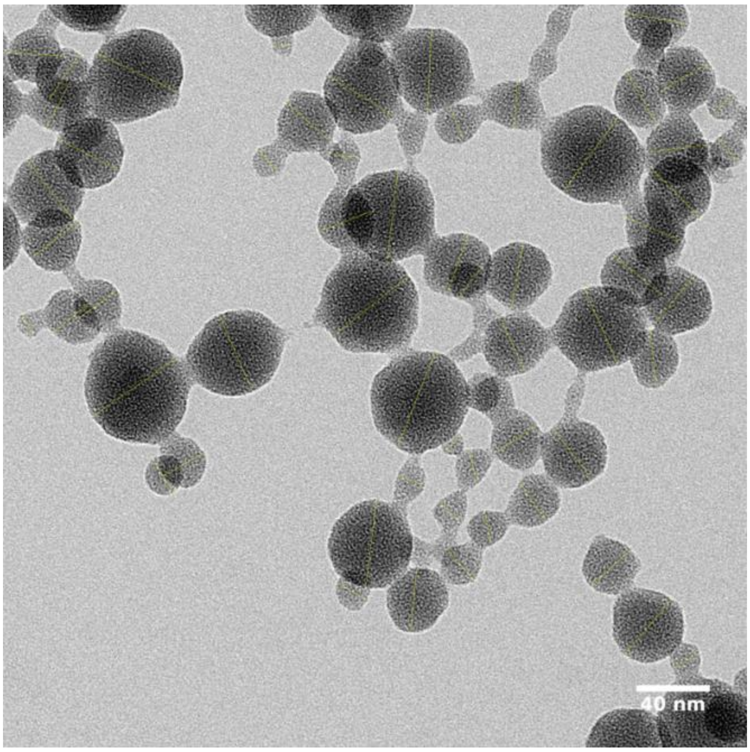

Figure S8.12. Zr-*fum* particles measured for TEM size determination.

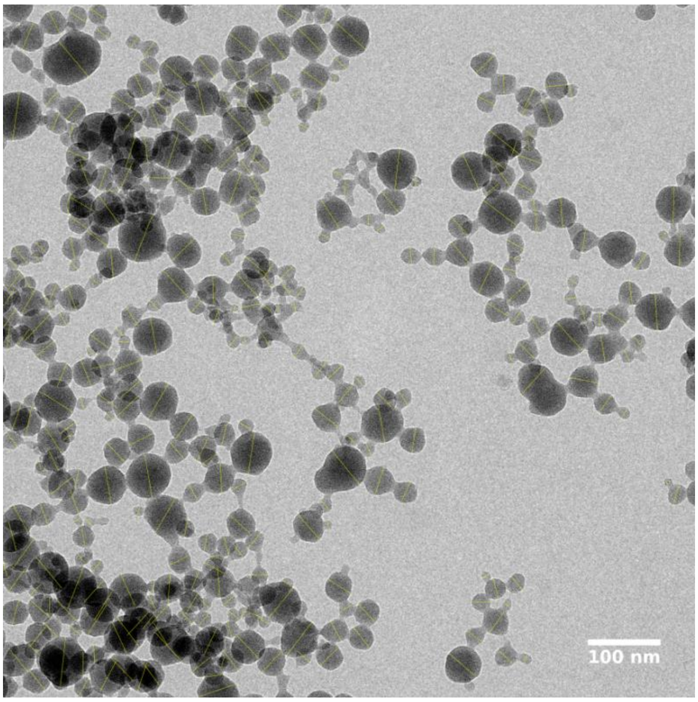

Figure S8.13. Zr-*fum* particles measured for TEM size determination.

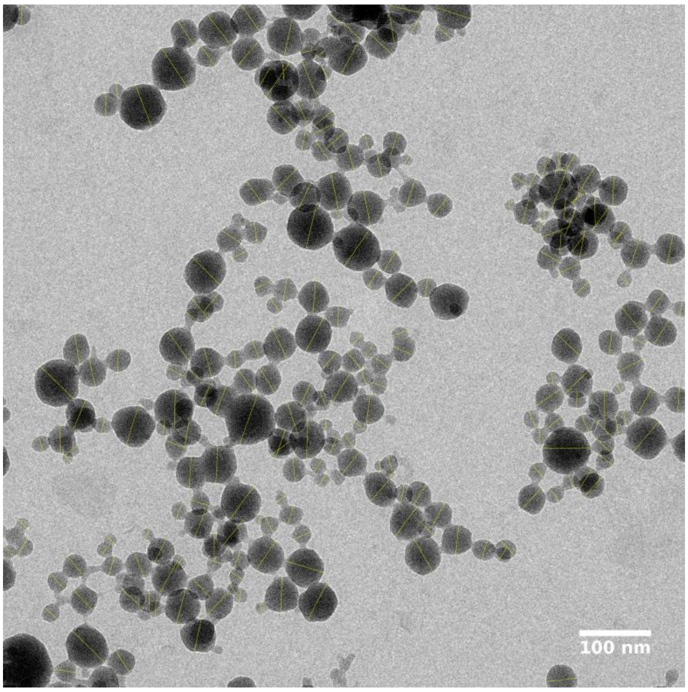

Figure S8.14. Zr-*fum* particles measured for TEM size determination.

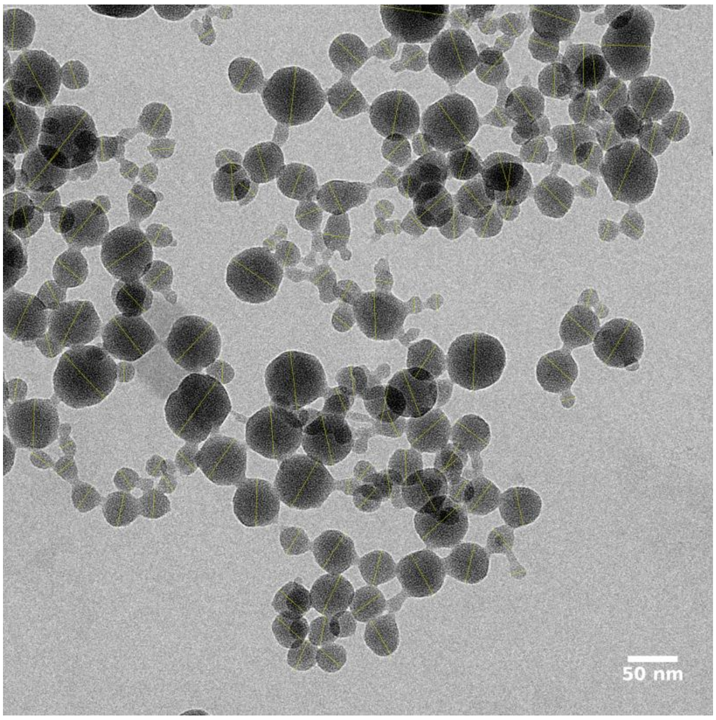

Figure S8.15. Zr-*fum* particles measured for TEM size determination.

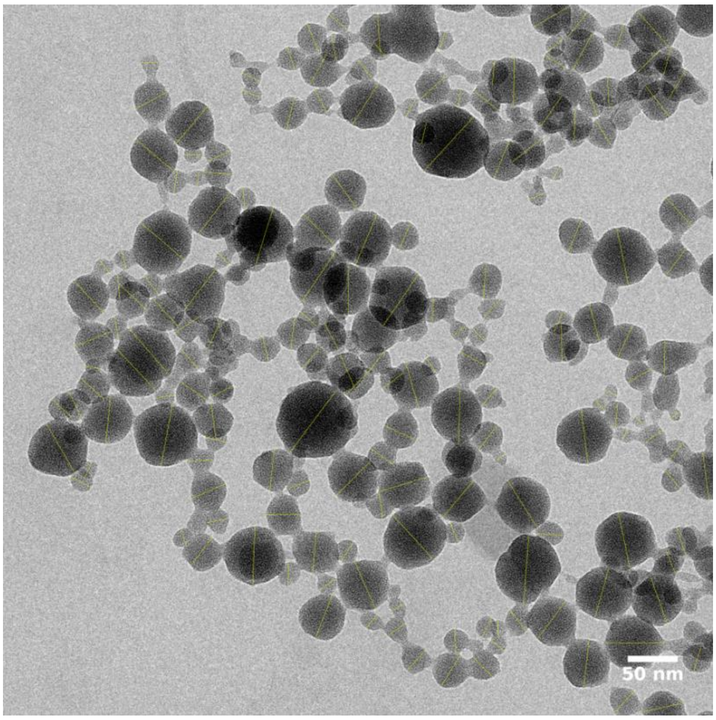

Figure S8.16. Zr-*fum* particles measured for TEM size determination.

8.5.9 X-ray Diffraction

The theoretical PXRD pattern of the Zr-*fum* MOF was simulated using the structure model and atomic coordinates reported by Wißmann *et al.*[6] and assuming a domain size of 50 nm.

The results of the X-ray diffraction experiments for samples Zrfum-1, Zrfum-2, Zrfum-3 and Zrfum-4 are shown in **Figure S8.17**. The corresponding average size of the crystalline domains is shown in **Table S8.4**. Besides slightly smaller crystalline domains for sample Zrfum-3, the crystalline domains of the sample generally feature a similar size, which confirms the good reproducibility of the aqueous synthesis.

Pawley fitting of the experimental PXRD data was carried out using in the Reflex module of the Accelrys Materials Studio software and refining the unit cell parameter *a* and the domain size *d*. We used Pseudo-Voigt peak shape functions with fixed profile parameters (determined from measurements of a LaB_6 micropowder sample). Peak asymmetry was corrected using the Berar-Baldinozzi function. Overlay of the observed and refined profiles shows very good correlation with small deviations at low angles, where the peak asymmetry is more pronounced.

Table S8.4. Lattice parameters and average domain sizes of the Zrfum-1-4 samples.

Sample	Lattice parameter *a* [Å]	Average domain size *d* [nm]
Zrfum-1	17.91 ± 0.03	60 ± 5
Zrfum-2	17.89 ± 0.03	55 ± 5
Zrfum-3	17.89 ± 0.03	42 ± 5
Zrfum-4	17.88 ± 0.03	54 ± 5

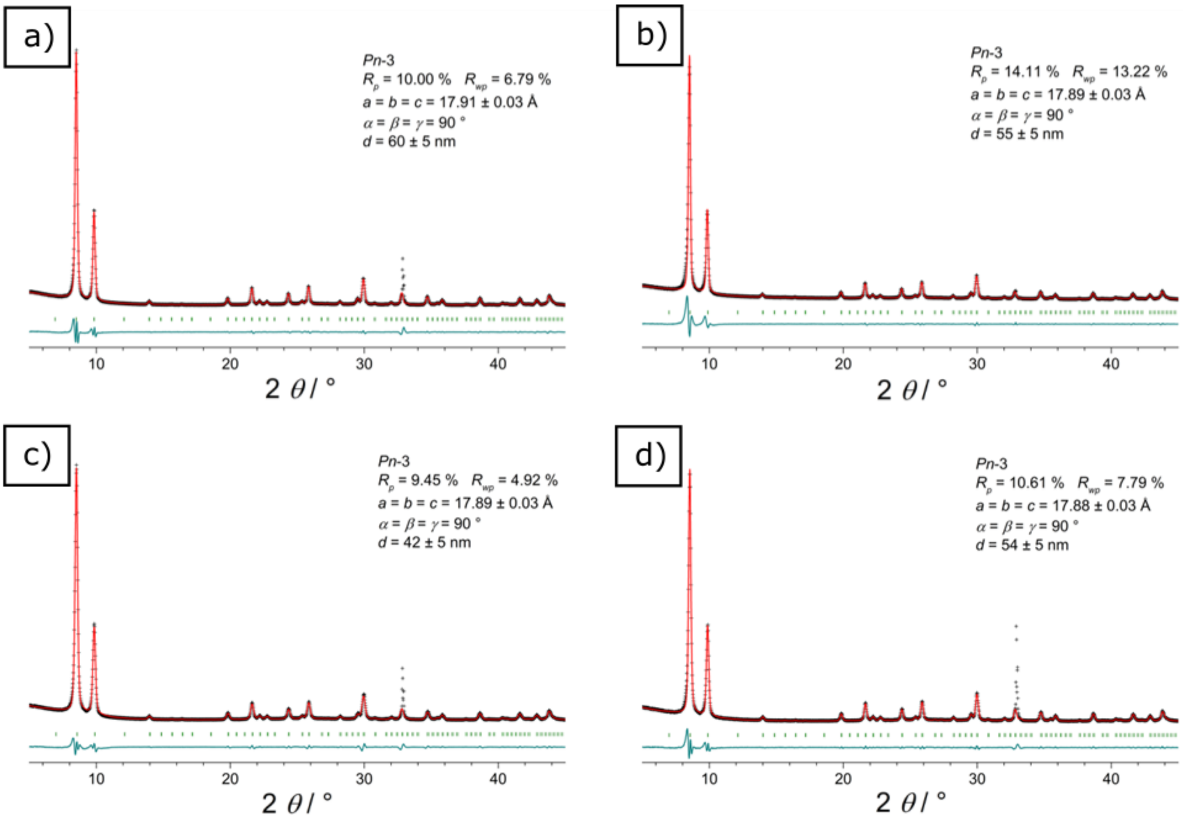

Figure S8.17. PXRD patterns of the Zrfum-1 (a), Zrfum-2 (b), Zrfum-3 (c), and Zrfum-4 (d). The experimental data are shown in black, corresponding Pawley fits in red, Bragg positions as green symbols, and the difference between the experimental pattern and the fits as dark green lines. All four experimental patterns were found to feature an additional peak at 31.5 ° of variable intensity, which could not be attributed to any of the starting materials or the MOF. This reflection was masked during the Pawley fitting.

8.5.10 Atomic Force Microscopy

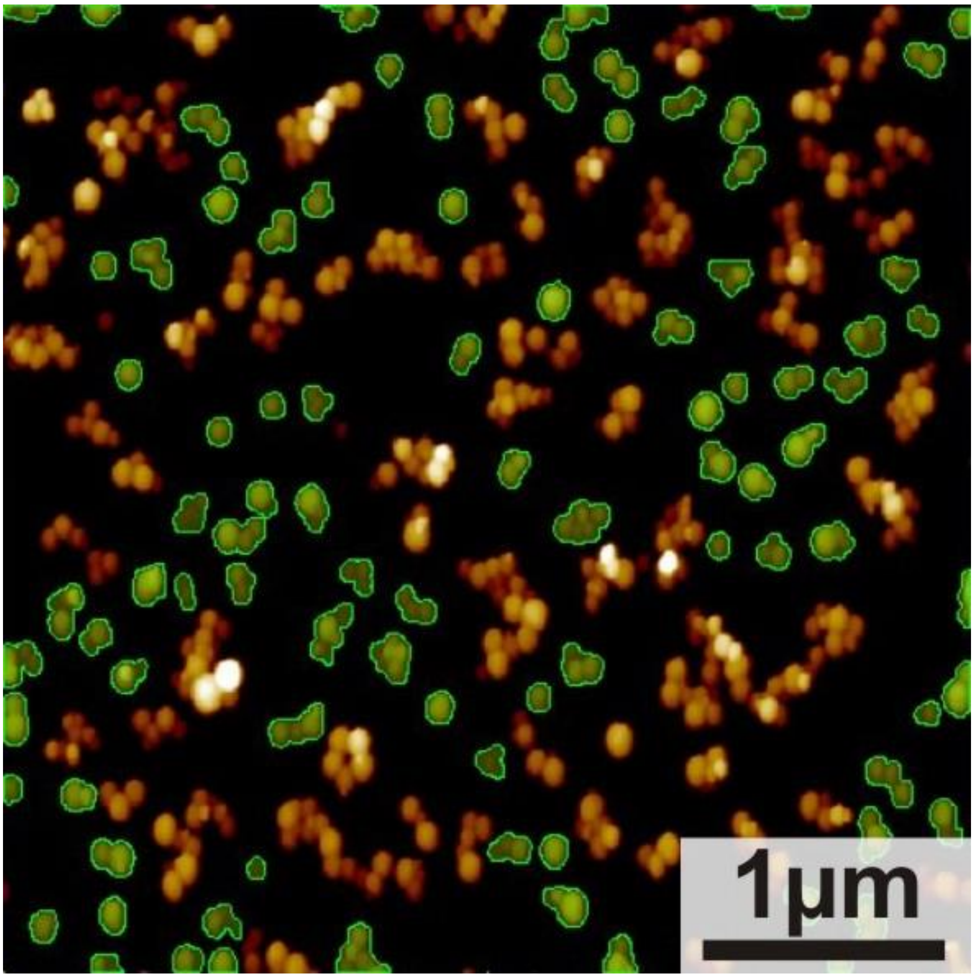

Figure S8.18. AFM image of MOFs after performing particle and pore analysis in Scanning Probe Image Processing (SPIP). The maximum height of green coloured areas was determined with respect to the surrounding substrate (black). Among chosen particles agglomeration in image plane is clearly observable. However, data indicated no stacking in evaluated z-direction.

In **Figure S8.19** a zoom-in is shown (**a**), together with an exemplary topographical cross-section of a single particle (**b**). For a quantitative particle size analysis, only the height was used, since the lateral extension is mainly given by the apex of the AFM tip and thus appears larger than the height (cf. **Figure S8.19 b**).

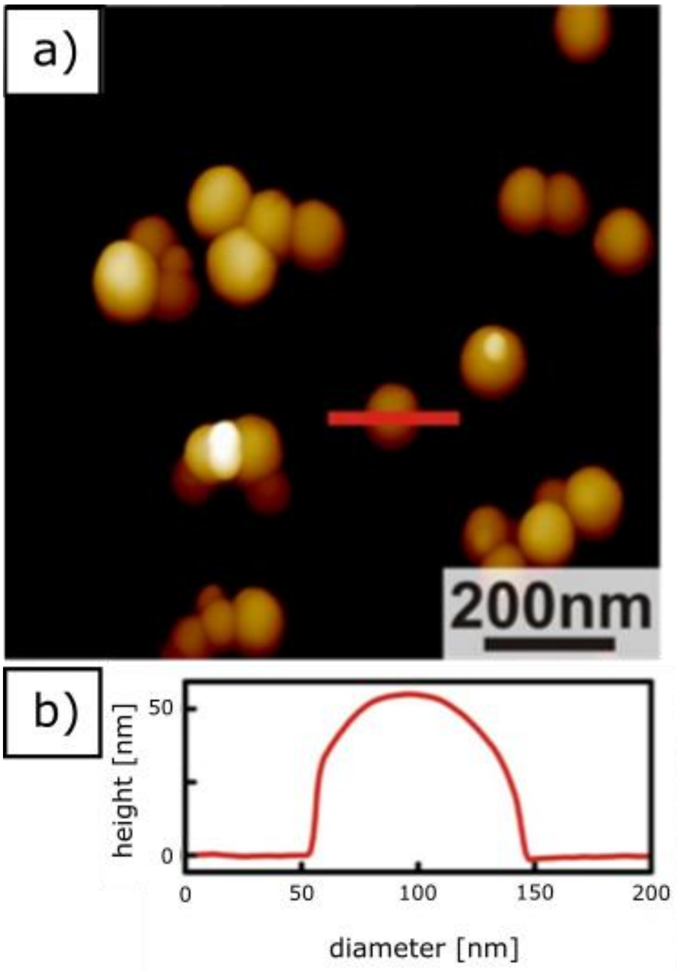

Figure S8.19. Zoomed-in AFM micrograph (**a**) with corresponding cross section of one single particle (**b**).

8.5.11 Ensuring Reproducibility

To ensure reproducibility in the synthesis of the Zr-*fum* nanoparticles, multiple batches (Zrfum-1 to Zrfum-4) were synthesized and examined for their size attributes. This was done with X-ray diffraction, additionally with dynamic light scattering in ethanol.

8.5.12 Dynamic Light Scattering

The particle size distribution of samples Zrfum-1, Zrfum-2, Zrfum-3, and Zrfum-4 were determined *via* dynamic light scattering in ethanol. The results are shown in **Table S8.5**. Each sample was measured two consecutive times after finishing the washing steps of the synthesis. The similarities in the resulting diameters ranging from 129 nm to 136 nm show the good reproducibility of the synthesis of the particles. However, there are fluctuations regarding the polydispersity index (PDI), even for two consecutive measurements of the same sample, which shows, that the PDI can only be used as a rough estimation for the polydispersity of the sample.

Table S8.5. Results (intensity distribution) of the DLS measurements of samples Zrfum-1 to Zrfum-4 in ethanol.

Sample	Measurement	Diameter(Cumulants) [nm]	PDI
Zrfum-1	1	130	0.135
	2	129	0.168
Zrfum-2	1	135	0.094
	2	132	0.136
Zrfum-3	1	135	0.098
	2	135	0.111
Zrfum-4	1	136	0.117
	2	134	0.086

8.5.13 Fluorescence Correlation Spectroscopy

The particle size and size distribution of samples Zrfum-1, Zrfum-2, Zrfum-3 were determined with FCS. The results are shown in **Table S8.6**. The similarities in the resulting diameters show the good reproducibility of the synthesis of the particles.

Table S8.6. Results of the FCS measurements of samples Zrfum-1 to Zrfum-3 labeled with Alexa Fluor 488 in water. FWHM = full width at half maximum

Sample	Diameter (single component Fit) [nm]	Diameter & FWHM (GDM Fit, see calculations) [nm]
Zrfum-1	127	133, 12
Zrfum-2	136	133, 18
Zrfum-3	136	135, 17

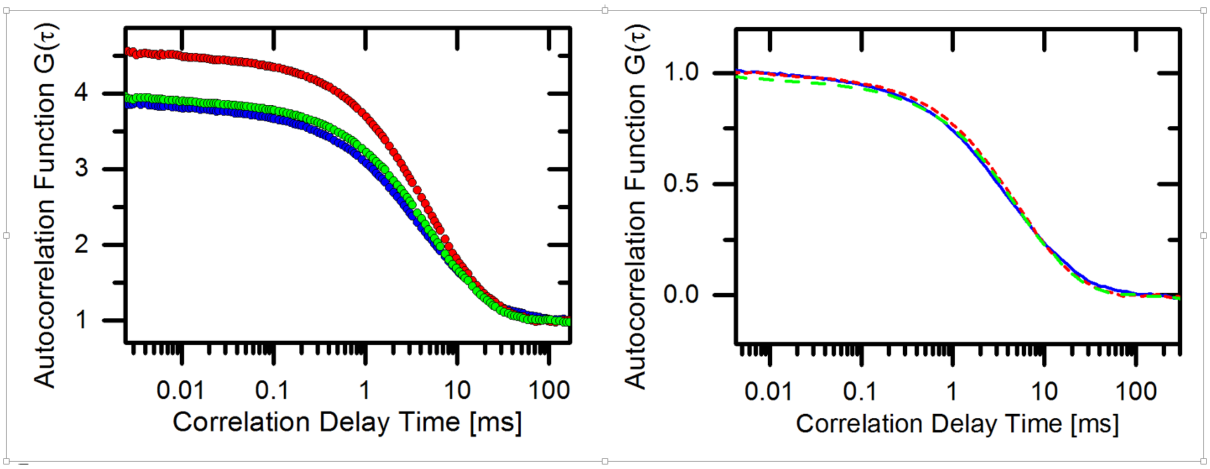

Figure S8.20. left: FCS Autocorrelation functions of labelled Zr-fum particles sample 1(blue), 2(red) and 3(green). Original correlation curves (left) show slightly different correlation heights implying slightly different concentrations of the three nanoparticle samples. The same data after normalization (**right**) shows small variation in the diffusion times of the Zr-fum samples denoting small batch to batch variations in the hydrodynamic diameter which was also confirmed by single component and GDM fit.

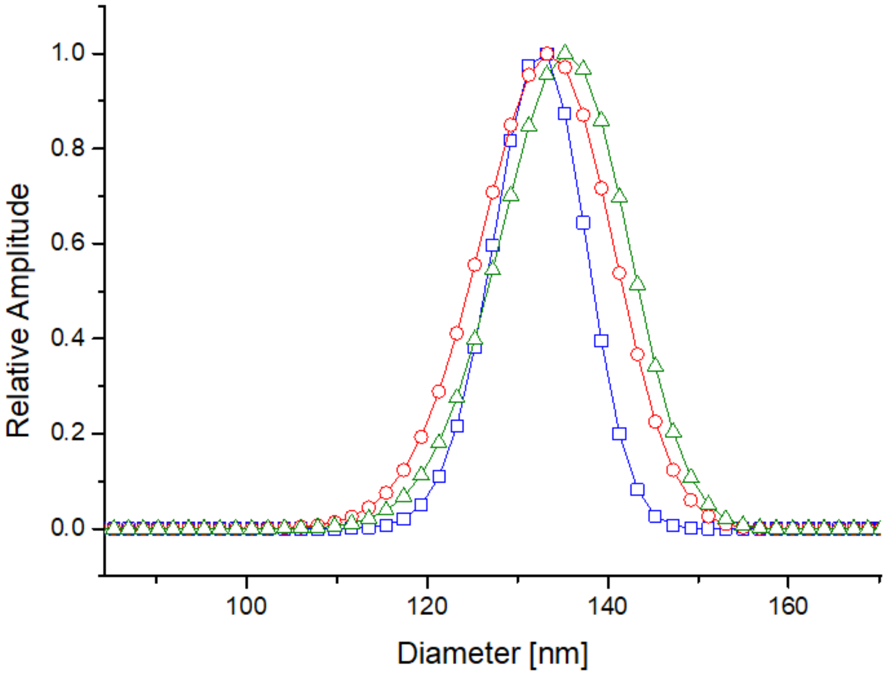

Figure S8.21. FCS size distribution of three measured nanoparticle batches 1(blue), 2(red) and 3(green) obtained from GDM Fit. The similarities in the resulting diameters show the great reproducibility of the synthesis of the particles.

8.5.14 Calculations

Dynamic Light Scattering

The data received during the DLS measurements was evaluated using the "method of cumulants"[8], which is shortly described in the following section. It introduces a polydispersity index (PDI, see **Equation 40**) as an indicator of the size distribution of the particles. Generally, DLS uses the time-dependent intensity fluctuations of a sample-scattered laser. These intensity fluctuations can be described with a second order intensity-autocorrelation function as shown in **Equation 35**:

Equation 35

$$G^{(2)}(\tau) = \frac{\langle I(t)I(t+\tau)\rangle}{\langle I(t)\rangle^2}$$

The intensity-autocorrelation function is linked by the Siegert relation[9] to a field-correlation function as presented in **Equation 36** using the baseline B and a geometry factor β.

Equation 36
$$G^{(2)}(\tau) = B + \beta[g^{(1)}(\tau)]^2$$

This field-correlation function of monodisperse particles can be described with **Equation 37** featuring the decay rate Γ and the passed time τ:

Equation 37
$$G^{(1)}(\tau) = \exp(-\Gamma\tau)$$

The decay rate $\Gamma = Dq^2$ includes the diffusion coefficient *D* and the magnitude of the scattering vector *q*, which is given by **Equation 38**:

Equation 38
$$q = \frac{4\pi n}{\lambda_0}\sin\left(\frac{\theta}{2}\right)$$

Here, *n* is the refractive index of the solvents, θ is the angle at which the scattered intensity was measured (θ = 173 °), and λ_0 is the wavelength of the laser in vacuum (λ_0 = 633 nm).

For polydisperse samples, the “method of cumulants” can be used. Here, the intensity-autocorrelation function is described by **Equation 39**:

Equation 39
$$G^{(2)} = B + \beta\exp(-2\bar{\Gamma}\tau)\left(1 + \frac{\mu_2}{2!}\tau - \frac{\mu_3}{3!}\tau^2 \ldots\right)^2$$

With this method, the correlation function was fitted up to the point, where the amplitudes are 10% of the initial amplitude. The term $\left(1 + \frac{\mu_2}{2!}\tau - \frac{\mu_3}{3!}\tau^2 \ldots\right)$ was cut off at its second segment. Using this method of cumulants, it is possible to take into account multiple species in dispersion. It introduces a polydispersity index (PDI, see **Equation 40**) as an indicator of the size distribution of the particles.

Equation 40
$$PDI = \frac{\mu_2}{\bar{\Gamma}^2}$$

This polydispersity index was used to determine the standard deviation σ of the particle size distribution using **Equation 41** with the average hydrodynamic particle diameter *d.*

Equation 41

$$PDI = \left(\frac{\sigma}{d}\right)^2$$

Fluorescence Correlation Spectroscopy

Fluorescence correlation spectroscopy (FCS) is a versatile technique that makes use of fluorescence intensity fluctuations to characterize the dynamics of a low number of particles (e.g. single molecules or nanoparticles) diffusing through a very small confocal detection volume. It has been used in plentiful biophysical studies and many applications in analytical chemistry and Biochemistry were found.[10-13] FCS is ideal for measuring molecular diffusion and, thus, the molecular size in highly dilute solutions without any need to perturb the system.[14,15]

Since Magde *et al.* demonstrated the principles of FCS in 1972 and improvements of Rigler *et al.* using confocal microscopy, FCS evolved immensely in terms of its applicability, sensitivity and versatility.[16,17]

In FCS, information is extracted by determination of the autocorrelation function (**Equation 42**)

Equation 42

$$(\tau) = \frac{\langle F(t)F(t+\tau)\rangle}{\langle F\rangle^2}$$

of the fluctuating fluorescence signal F(t) and fitting an physical model to the resulting correlation curve. In the case of free diffusion the correlation is given by **Equation 43**,

Equation 43

$$G(\tau) = 1 + G(0)\frac{1}{1+\frac{\tau}{\tau_D}}\frac{1}{\sqrt{1+\frac{\tau}{S^2\tau_D}}}$$

where $G(0)$ is the correlation's amplitude, S is the ratio between the lateral and the axial confocal volume radius, while τ_D is the mean time a particle needs to diffuse across the focal volume[18]. Knowing the width ω of the confocal volume, the hydrodynamic radius is given by **Equation 44**

Equation 44

$$R_H = \frac{2k_B T \tau_D}{3\pi\eta\omega^2}$$

using the Boltzmann constant k_B as well as the temperature $T = 295$ K and viscosity $\eta = 0.958$ mPas of the measured aqueous suspension.

In order to obtain a size distribution from FCS fits a Gaussian Distribution Model (GDM) fit[12] was also applied. The underlying concept of GDM is that the sample is not monodisperse with a single value for the diffusion time, τ_D, but a Gaussian distribution on a fixed logarithmic diffusion time-scale with a peak diffusion time τ_P. The fit to the autocorrelation function is described by **Equation 45**

Equation 45

$$G(\tau) = 1 + \sum_{i=1}^{n} a_i(\tau_{Di}) \frac{1}{1 + \frac{\tau}{\tau_{Di}}} \frac{1}{\sqrt{1 + \frac{\tau}{S^2 \tau_{Di}}}}$$

where $a_i(\tau_{Di}) = \mathrm{A} \exp\left[-\left(\frac{\ln\left(\frac{\tau_{Di}}{\tau_P}\right)}{b}\right)^2\right]$ with relative amplitude *A* and a distribution width of *b*.

Taking into account that Zr-fum nanoparticles have radii comparable to the beam waist ω, the measured diffusion time has a larger value than it would have if point particles with the same diffusive behavior were observed. Due to the fact that Alexa Fluor 488 labeling was applied at the outer surface of the nanoparticles they are fluorescing hollow spheres from the FCS view. The equation $\tau_{measured} = \tau_{D_{pointparticle}} \cdot (1 + \frac{8R^2}{3\omega^2})$, taken from Wu et al. [19] was used to correct this finite particle size effect of hollow spheres.

References

1 Brunauer, S. E., P. H.; Teller, E. Adsorption of Gases in Multimolecular Layers. *J. Am. Chem. Soc.* **60**, 309-319 (1938).

2 Pawley, G. S. Unit-cell refinement from powder diffraction scans. *J. Appl. Crystallogr.* **14**, 357-361, doi:10.1107/s0021889881009618 (1981).

3 Pawley, G. S. in *J. Appl. Crystallogr.* Vol. 14 357-361 (1981).

4 Zdenek Petrásek, P. S. in *Biophys. J.* Vol. 94 1437-1448 (2008).

5 Persson, G., Thyberg, P., Sande, T. & Widengren, J. in *J. Phys. Chem. B* Vol. 113 8752-8757 (2009).

6 Wißmann, G. *et al.* in *Microporous Mesoporous Mater.* 64-70 (2012).

7 Sing, K. S. W. E., D. H. ; Haul, R. A. W.; Moscou, L.; Pierotti, R. A.; Rouquérol, J.; Siemieniewska, T. Reporting Physisorption Data for Gas/Solid Systems: with Special Reference to the Determination of Surface Area and Porosity. *Pure & Appl. Chem.* **57**, 603-619 (1985).

8 Frisken, B. J. in *Appl. Opt.* Vol. 40 4087-4091 (2001).

9 Schätzel, K. *"Single-photon correlation techniques" in Dynamic Light Scattering, W. Brown*. (Oxford University, 1993).

10 Digman, M. A. & Gratton, E. in *Annual Review of Phyiscal Chemistry* Vol. 62 645-668 (2011).

11 Haustein Elke, P. S. in *Annu. Rev. Biophys. Biomol. Struct.* Vol. 26 151-169 (2007).

12 Mittag, J. J., Milani, S., Walsh, D. M., Radler, J. O. & McManus, J. J. Simultaneous measurement of a range of particle sizes during Abeta1-42 fibrillogenesis quantified using fluorescence correlation spectroscopy. *Biochem. Biophys. Res. Commun.* **448**, 195-199, doi:10.1016/j.bbrc.2014.04.088 (2014).

13 Lippok, S. *et al.* in *Biophys. J.* Vol. 105 1208-1216 (2013).

14 Kuyper, C. L., Budzinski, K. L., Lorenz, R. M., Chiu & T., D. in *J. Am. Chem. Soc.* Vol. 128 730-731 (2006).

15 Pal, N., Dev Verma, S., Singh, M. K. & Sen, S. Fluorescence correlation spectroscopy: an efficient tool for measuring size, size-distribution and polydispersity of microemulsion droplets in solution. *Anal. Chem.* **83**, 7736-7744, doi:10.1021/ac2012637 (2011).

16 Douglas, M., Elson, E. & Webb, W. W. in *Phys. Rev. Lett.* Vol. 29 705-708 (1972).

17 Rigler, R., Mets, Ü., Widengren, J. & Kask, P. in *European Biophysics Journal 22* Vol. 22 169-175 (1993).

18 Schwille, P. & Hausstein, E. in *Spectroscopy* Vol. 94 1-33 (2009).

19 Wu, B. C., Yan, Müller, Joachim D. Fluorescence correlation spectroscopy for finite-sized particles. *Biophys. J.* **7**, 2800-2808 (2008).